

**Structural Investigations of Hydroxylase Proteins and Complexes in Bacterial
Multicomponent Monooxygenase Systems**

by

Michael S. McCormick
B.S. Chemistry (2003)
B.S. Biochemistry (2003)
The University of Michigan – Ann Arbor

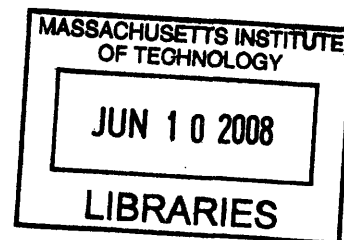
SUBMITTED TO THE DEPARTMENT OF CHEMISTRY IN PARTIAL FULFILLMENT
OF THE REQUIREMENTS FOR THE DEGREE OF

DOCTOR OF PHILOSOPHY IN INORGANIC CHEMISTRY
AT THE
MASSACHUSETTS INSTITUTE OF TECHNOLOGY

May 2008

[June 2008]

© 2008 Massachusetts Institute of Technology
All rights reserved




ARCHIVES

Signature of Author: _____
Department of Chemistry
May 19, 2008

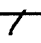
Certified by: _____
Stephen J. Lippard
Arthur Amos Noyes Professor of Chemistry
Thesis Supervisor

Accepted by: _____
Robert W. Field
Chairman, Departmental Committee on Graduate Studies


This doctoral thesis has been examined by a committee of the Department of Chemistry as follows:



Christopher C. Cummins
Professor of Chemistry
Committee Chair



Stephen J. Lippard
Arthur Amos Noyes Professor of Chemistry
Thesis Supervisor



Catherine L. Drennan
Professor of Chemistry and Biology

Structural Investigations of Hydroxylase Proteins and Complexes in Bacterial Multicomponent Monooxygenase Systems

by

Michael S. McCormick

Submitted to the Department of Chemistry on May 19, 2008

In Partial Fulfillment of the Requirements for the Degree of
Doctor of Philosophy in Inorganic Chemistry

Abstract

Bacterial multicomponent monooxygenases (BMMs) such as toluene/*o*-xylene monooxygenase (ToMO), phenol hydroxylase (PH), and soluble methane monooxygenase (sMMO) catalyze hydrocarbon oxidation reactions at a carboxylate-bridged non-heme diiron center common to many systems in biology, as discussed in the first and subsequent chapters of this document. Chapter 1 provides a summary of various relationships between structure and activity in BMMs, as they have been determined through decades of research into BMM hydrocarbon catalysis.

Presented in Chapter 2 are the structures of the native (ToMOH) and manganese(II)-reconstituted (Mn(II)-ToMOH) ToMO hydroxylase, at 1.85 Å and 2.20 Å resolution, respectively. The structure of Mn(II)-ToMOH reveals an active site coordination and geometry similar to that in diferrous and manganese(II)-reconstituted MMOH, indicating that it represents an analog of the diferrous ToMOH structure. Through comparison of the native ToMOH and Mn(II)-ToMOH structures, a collection of metal site oxidation state dependent conformational changes in conserved residues on the surface of the hydroxylase α -subunit are observed, suggesting a relationship between active site oxidation state and component interactions in BMMs. Through analysis of the 1.85 Å ToMOH structure, a series of hydrophobic cavities through the α -subunit connecting the active site to the protein surface analogous to those previously noted in MMOH were also discovered as part of this work.

Chapter 3 describes three X-ray crystal structures of ToMOH T201X mutants, and four structures of ToMOH N202X mutants at resolutions ranging from 1.90 to 2.90

Å. These data reveal alterations in the ToMOH active site pocket surface topology and malformed hydrogen bonding interactions resulting from the various mutations that may respectively be responsible for substrate hydroxylation regiospecificity and proton translocation differences observed of the mutant proteins in future biochemical studies when compared to the wild-type system.

Reported in Chapter 4 is a 1.95 Å X-ray crystal structure of the xenon gas pressurized PH hydroxylase (Xe-PHH), along with computational analyses of the various surface-to-diiron center cavities, channels, and pores in the α -subunits of all three structurally characterized BMM hydroxylase proteins. The structure of Xe-PHH reveals extensive xenon binding in the conserved α -subunit hydrophobic cavities and suggests a role for the pathway in dioxygen transport to the active site during catalysis. Computational analyses of surface-to-diiron center cavities, channels, and pores in the BMM hydroxylase α -subunits supports findings from the Xe-PHH structure, and provides insight into how the various molecular substrate transport pathways may have been carved into the different hydroxylase proteins through evolution.

Thesis Supervisor: Stephen J. Lippard

Title: Arthur Amos Noyes Professor of Chemistry

To Julie and my parents, who have always enabled my success.

Acknowledgements

Pursuing a Ph.D. at MIT has been the most difficult experience of my life. The past five years have been filled with stress, anxiety, and countless nights without sleep. In exchange for these challenges, however, I have accomplished things I had only imagined in the past, and experienced educational growth I never knew I was capable of. I could not have made it this far without the insight, assistance, and support of certain individuals in my life that I would like to take this opportunity to thank.

First and foremost I want to acknowledge my thesis advisor, Steve Lippard, for his undying support, colorful personal character, and fantastic ability to turn willing students into highly functional and scholarly scientists. Steve's approach in research is absolutely amazing, and one that I strive to model in my own work. He fears no experiment, and proceeds through the scientific process time and time again as if it were his first and most eager day on the job. He truly loves the work, the questions, and the answers that together make science exciting. Using his many great qualities he has constructed an institution characterized by a long list of enlightening results and a wonderful legacy of people that I am proud to be a part of.

Among the many bright and talented colleagues that I have had the fortune to work with throughout the pursuit of my Ph.D. there are a handful that I am particularly indebted. Above all is Matt Sazinsky, my mentor and friend. Matt has been a source of helpful advice since before I even joined Steve's group all the way through writing and defending this very thesis. He taught me almost everything I know about macromolecular crystallography, rescued me from countless crises in my student life, and introduced me to the true spirit of a fulfilling synchrotron run, all while maintaining an environment of hilarious cynicism and instilling in me his many fine qualities as a teacher. Alongside Matt in my early days in the Lippard Lab were some other great scientists and people, namely, Liz Cadieux, Dong Xu, Viviana Izzo, Jessica Blazyk, and Laurance Beauvais. Each of these individuals was as essential to my development as an experimental biochemist as they were in creating an interesting and eventful place to work. In the latter half of my tenure in the lab, I was joined by other fine colleagues, Christine Tinberg, Ryan Todd, Woon Ju Song, and Erik Dill who all further enabled my progression through graduate school and enjoyment of the lab environment. I admire all of these colleagues as people and scientists and will forever appreciate their contributions to my growth and experience at MIT.

In addition to my graduate student and postdoctoral colleagues, I have had the great fortune of working with Karen Condon, Diana Matthes, and Mihai Duduta, as students of mine during my tenure at MIT. Karen was my first and longest-running UROP student, whom I remember most fondly for her incredible ambition and drive, which enabled her to achieve excellent results in her research, earn the respect of myself and many senior individuals in the lab, and currently, her rapid progress toward the medical degree that she began pursuing after graduating from MIT. After having worked with Karen for three years I had developed into a better instructor than ever, and just in time to take on Diana for six months as a full-time student while she pursued a Diploma thesis from her home institution in Berlin, Germany, and almost simultaneously, Mihai as a new UROP student. Diana's passion for science was a breath of fresh air in my then long-developed research projects that I was happy to reinforce by teaching her everything I could during her tenure at MIT, which ended in

her achieving the Diploma she first set out for. Mihai has undoubtedly been one of the brightest individuals that I have ever had worked with, who's extremely professional yet uniquely relaxed approach to science I found both inspiring and refreshing. He operates at an unusually high level, even for an MIT undergraduate, and I am sure that he will find much success in his future pursuits in science and in life.

Throughout my graduate student career at MIT I was also able to make some good friends. The first of which was Evan Guggenheim, whom I met during the visitation weekend, sat beside me in classes and as an undergraduate laboratory TA in the early years, and then endured the full breadth of research alongside me as a fellow member of Steve's lab. We have been through every step of the whole progress together, and I can honestly say that it would have been a dull experience without his friendly presence at my side to share in the highs and lows of the whole MIT experience. Also critical in my graduate student career was my friendship with Jeremy Kodanko, who was at the same time an awesome person to be in the lab with as he was to get out of the lab with. Since first meeting in Steve's lab, Jeremy and I have become great friends and I'm sure that that will be the case for years and years to come. Later in my days in the lab I became friends with Ryan Todd, who also accompanied me on many long synchrotrons and has since become a true friend and accomplished crystallographer himself. Also a late friend in the lab was Matt Wallace, who was really the first person to remind me of the importance of using one's breaks from the science to do something physical, and as a result I regained both my strength and love for fitness during his time in the lab that I had somehow lost in my previous years. Lastly, I must acknowledge Andy Tennyson, a classmate of mine along with Evan, who's seemingly constant presence in the lab was always great to have when I wanted to take a moment away from work to pick his brain, exchange quotes from *The Simpsons*, or just plain gripe about something.

In addition to my lab mates and student co-workers I am indebted to Cathy Drennan and the many helpful members of her lab, who collectively enabled me to accomplish many important aspects of the crystallographic work that I conducted while at MIT. As the lone full-time macromolecular crystallographer in the Lippard Lab for most of my tenure I was fortunate to have such a helpful group of scientists, and Cathy herself, to refer to for advice and the answers to countless questions in my research. I am particularly thankful for the advice of Paul Hubbard, Leah Blasiak, Jessica Vey, Ainsley Davis, and Luke Higgins. Along these same lines I would also like to thank another Drennan group alumnus, Tzanko Doukov, who provided assistance and moral support during virtually all of my data collection trips to SSRL.

I also must mention the most significant people from my undergraduate education at the University of Michigan, who helped me reach MIT in the first place. Most notable is my undergraduate research advisor Vincent Pecoraro, who first introduced me to bioinorganic chemistry and laid the foundations for my interest in scientific research. Also key in my early research and scholarly development were Wen-Yuan Hsieh, Manolis Matzapetakis, and Daniel Pursche who were graduate student mentors, and professor Brian Coppola who's friendly guidance I will never forget.

Last but certainly not least I want to acknowledge my girlfriend Julie, and the many friends of mine who supported me during the seemingly never-ending process of obtaining my degree. Without their much needed distractions and reminders of the real world, I think I may have gone absolutely crazy. Cheers to all – I'm finally finished!

Table of Contents

Abstract.....	3
Dedication.....	5
Acknowledgements.....	6
List of Tables.....	14
List of Figures.....	16
Chapter 1: Relationships Between Structure and Activity in Bacterial Multicomponent Monooxygenases.....	22
Research Overview and Potential Applications.....	23
Hydrocarbon Catalysis in Methane Monooxygenase.....	27
Structural Characterization of BMM Hydroxylases.....	31
BMM Component Protein Structures and Interactions.....	37
The State of BMM Structural Research Prior to the Present Work.....	39
References.....	45
Chapter 2: Manganese(II) Reconstituted and Native Toluene/<i>o</i>-Xylene Monooxygenase Hydroxylase X-ray Crystal Structures Reveal Conformational Shifts in Conserved Residues and an Enhanced View of the Protein Interior.....	54
Introduction.....	55
Results and Discussion.....	56
Materials and Methods.....	61

Preparation of apo ToMOH.....	61
Crystallization.....	61
Crystal Annealing.....	62
Data Collection and Refinement.....	62
Acknowledgement.....	63
References.....	73

Chapter 3: X-ray Crystallographic Characterization of Various Mutants of the

Conserved Residues T201 and N202 in the α -subunit of Toluene/*o*-Xylene

Monooxygenase Hydroxylase from <i>Pseudomonas</i> sp. OX1.....	77
Introduction.....	78
Experimental.....	80
Crystallization.....	80
Diffraction Data Collection and Crystal Structure Determination.....	80
Results and Discussion.....	82
Crystallization.....	82
Diffraction Data Collection and Crystal Structure Determination.....	82
Structural Effects of the T201 Mutations.....	83
Structural Effects of the N202 Mutations.....	84
Conclusions.....	85
References.....	102

Chapter 4: Exploring Voids in BMM Hydroxylase α -subunits: X-ray Crystallographic Characterization of the Xenon-Pressurized Hydroxylase Component of Phenol Hydroxylase from *Pseudomonas sp.* OX1, and Computational Analyses of the Hydroxylase Components of Phenol Hydroxylase, Toluene/*o*-Xylene Monooxygenase, and Methane Monooxygenase.....105

Introduction.....106

Experimental Methods.....111

 General Considerations.....111

 Crystallization.....111

 Structure Determination and Refinement.....113

 PH Michaelis-Menten Kinetics with Dioxygen and Xenon.....113

 Analysis of BMM Hydroxyase Voids Using PyMOL.....115

 Analysis of BMM Hydroxylase Voids Using CAVER.....115

 BMM Hydroxylase α -subunit Protein Sequence Alignments.....116

Results and Discussion.....116

 Iron Content and Activity.....116

 Crystallization, Xenon Pressurization, and Data Collection.....116

 Structure Determination and Refinement.....117

 PH Michaelis-Menten Kinetics with Dioxygen and Xenon.....120

 Analysis of BMM Hydroxyase Voids Using PyMOL.....120

 BMM Hydroxylase α -subunit Protein Sequence Alignments.....122

 Analysis of BMM Hydroxylase Voids Using CAVER.....123

Conclusions.....125

Acknowledgements.....	127
References.....	150

Appendix 1: X-ray Structure of a Hydroxylase-Regulatory Protein Complex from a Hydrocarbon-Oxidizing Multicomponent Monooxygenase, *Pseudomonas sp.* OX1

Phenol Hydroxylase.....	156
Author Contribution.....	156
Abstract.....	157
Introduction.....	157
Materials and Methods.....	158
Purification of Phenol Hydroxylase.....	158
Activity and Iron Content.....	158
Crystallization and Collection of X-ray Diffraction Data.....	158
Structure Determination.....	159
Results and Discussion.....	159
PHH Global Fold.....	159
PHM Fold and Binding Site on the Hydroxylase.....	159
Diiron Center.....	159
Second-Sphere Hydrogen Bonding Patterns.....	162
A Conserved Mononuclear Zn ²⁺ Site.....	162
Conserved Active Site Residues and Changes in Helix E.....	163
Structural Changes in Helix F.....	163

Possible Consequences of Regulatory Protein Binding on Transfer of Electrons to the Hydroxylase.....	163
Access of Substrate to the Diiron Center.....	165
Active Site Pocket and Substrate Specificity.....	166
Conclusions and Prospects.....	167
Acknowledgement.....	167
References.....	167
Supporting Information.....	170
Appendix 2: Experimental Procedures for the Expression and Purification of Monoclonal Antibodies to MMOH from Hybridoma Cell Lines.....	180
Introduction.....	181
Monoclonal Antibody Structure and Technology.....	181
Experimental Methods.....	183
General Considerations.....	183
MAb Expression: Growth and Harvest of Antibody Cell Lines.....	184
MAb Purificaiton: DEAE Sepharose Ion-Exchange Chromatography.....	185
MAb Purificaiton: Protein-G Affinity Chromatography.....	186
MAb Fragmentation: Soluble Papain.....	187
Fab Fragment Purificaiton: MonoQ Ion-Exchange Chromatography.....	188
Results and Discussion.....	188
MAb Expression: Growth and Harvest of Antibody Cell Lines.....	188
MAb Purificaiton: DEAE Sepharose Ion-Exchange Chromatography.....	189

MAb Purificaiton: Protein-G Affinity Chromatography.....	189
MAb Fragmentation: Soluble Papain.....	189
Fab Fragment Purificaiton: MonoQ Ion-Exchange Chromatography.....	189
References.....	196

Appendix 3: Dioxygen Activation at Non-Heme Diiron Centers: Oxidation of a Proximal Residue in the I100W Variant of Toluene/o-Xylene Monooxygenase Hydroxylase.....

Author Contribution.....	197
Introduction.....	198
Experimental Methods.....	199
Crystallization and Data Collection.....	200
Structure Determination and Refinement.....	200
Results.....	202
X-ray Crystal Structure of ToMOH I100W.....	202
Conclusions.....	210
Acknowledgement.....	210
References.....	211

Biographical Note.....

Curriculum Vitae.....

List of Tables

Table 2.1	Angstrom Distances between atoms and ions in the active sites of 2.15 Å ToMOH _{ox} , 1.85 Å ToMOH _{ox} , 1.96 Å MMOH _{ox} , and 1.70 Å MMOH _{ox}	64
Table 2.2	X-ray Data Collection and Refinement Statistics for 1.85 Å ToMOH _{ox} and Mn(II)-reconstituted ToMOH.....	65
Table 3.1	Percentages of Residues in Ramachandran Plot Favored, Allowed, and Outlier Regions.....	88
Table 3.2	B-factors for Metal Ions and Non-Protein Ligands in Structures of ToMOH.....	89
Table 3.3	X-ray Data Collection and Refinement Statistics for ToMOH T201G, T201S, and T201V.....	90
Table 3.4	X-ray Data Collection and Refinement Statistics for ToMOH N202A, N202D, N202L, and N202Y.....	91
Table 4.1	Size and Polarizability of Dioxygen, Xenon, and Methane Gas.....	128
Table 4.2	X-ray Data Collection and Refinement Statistics for Xenon-Pressurized PHH.....	129
Table 4.3	Xenon Atom Details from 1.95 Å Xenon-Pressurized PHH X-ray Structure.....	130
Table 4.4	Fe—Xe and Xe—Xe Distances in 1.95 Å Xenon-Pressurized PHH X-ray Structure.....	131
Table 4.5	Residues Contributing to the van der Waals Surfaces of Voids in the Crystallographically Characterized BMM Hydroxylases.....	132

Table A1.1	X-ray Data Collection, Phasing, and Refinement Statistics for Native and SeMet PHH-PHM.....	159
Table A1.2	Heavy Atom Anomalous Peak Intensities for PHH-PHM.....	163
Table A1.3	Residues Comprising the BMM Active Site Substrate Binding Pocket.....	167
Table A3.S2	Data Collection and Refinement Statistics for ToMOH I100W.....	221
Table A3.S3	Distances Between W100 Side Chain Atoms and the Diiron Active Site.....	222

List of Figures

Figure 1.1	Select Dioxygen Activated Carboxylate Bridged Diiron Sites in Biology.....	41
Figure 1.2	Biological Reactions of Four BMM Subclasses.....	42
Figure 1.3	The Reaction Cycle of Soluble Methane Monooxygenase.....	43
Figure 1.4	Global Folds, Active Site Access Routes, Histidine-Linked Hydrogen Bonding Networks, and Iron Center Coordination in the Structurally Characterized BMM Hydroxylases.....	44
Figure 2.1	Overlaid 1.85 Å ToMOH _{ox} and 2.20 Å Mn(II)-ToMOH Structures.....	66
Figure 2.2	Active Site Coordination and Geometry 1.85 Å ToMOH _{ox} and 2.20 Å Mn(II)-ToMOH.....	67
Figure 2.3	Active Site Density Stereo Images of 1.85 Å ToMOH _{ox} and 2.20 Å Mn(II)-ToMOH.....	68
Figure 2.4	Active Site Geometries of 2.15 Å ToMOH _{ox} , 1.85 Å ToMOH _{ox} , 2.20 Å Mn(II)-ToMOH, 1.70 Å MMOH _{ox} , 2.15 Å MMOH _{red} , and 2.30 Å Mn(II)-MMOH.....	69
Figure 2.5	Metal Center Oxidation State Dependent Conformational Shifts in ToMOH and MMOH.....	70
Figure 2.6	Interior Surface Renderings of ToMOH and MMOH α -subunits.....	71
Figure 2.7	Hexaethylene Glycol Molecules Modeled into the ToMOH Channel in 1.85 Å ToMOH _{ox} and 2.20 Å Mn(II)-ToMOH.....	72

Figure 3.1	Active Site Coordination and Geometry in ToMOH T201G, ToMOH T201S, ToMOH T201V, ToMOH N202A, ToMOH N202D, ToMOH N202L, and ToMOH N202Y, as Compared to that in Wild-type ToMOH, Mn(II)-reconstituted ToMOH, and Wild-type MMOH.....	92
Figure 3.2	Stereo Views of the Active Site Electron Density in ToMOH T201G, ToMOH T201S, ToMOH T201V.....	93
Figure 3.3	Stereo Views of the Active Site Electron Density in ToMOH N202A, ToMOH N202D, ToMOH N202L, and ToMOH N202Y.....	94
Figure 3.4	Views of the Various Side Chain Conformations, Hydrogen-Bonding Interactions, and Electron Density for Residues E197, T201X, N202, and Q228 from ToMOH T201G, ToMOH T201S, and ToMOH T201V as Compared to Wild-Type and Mn(II)-reconstituted ToMOH.....	95
Figure 3.5	Stereo View of the Overlaid Structures of Wild-type ToMOH, Mn(II)-reconstituted ToMOH, ToMOH T201G, ToMOH T201S, and ToMOH T201V.....	96
Figure 3.6	Space-filling View of the Active Site Cavity in Wild-type ToMOH, ToMOH T201G, ToMOH T201S, and ToMOH T201V.....	97
Figure 3.7	Effects of the Mutation on the van der Waals Surface Topology of the ToMOH Channel and Pore Region in ToMOH T201G, ToMOH T201S, and ToMOH T201V as Compared to Wild-type ToMOH.....	98
Figure 3.8	Views of the Various Side Chain Conformations, Hydrogen-Bonding Interactions, and Electron Density for Residues E197, T201, N202X, and	

	Q228 from ToMOH N202A, ToMOH N202D, ToMOH N202L, and ToMOH N202Y as Compared to Wild-Type and Mn(II)-reconstituted ToMOH.....	99
Figure 3.9	Stereo View of the Overlaid Structures of Wild-type ToMOH, Mn(II)-reconstituted ToMOH, ToMOH N202A, ToMOH N202D, ToMOH N202L, and ToMOH N202Y.....	100
Figure 3.10	Effects of the Mutation on the van der Waals Surface Topology of the ToMOH Channel and Pore Region in ToMOH N202A, ToMOH N202D, ToMOH N202L, and ToMOH N202Y as Compared to Wild-type and Mn(II)-reconstituted ToMOH.....	101
Figure 4.1	A View of the Active Site Pocket and Four-Helix Bundle PHH, MMOH, and ToMOH.....	133
Figure 4.2	Global View of the Dimer Structure, and Comparison of the α -subunits and Four-Helix Bundle in Xe-PHH.....	134
Figure 4.3	SDS-PAGE Analysis of Purified PHM and PHH Expression Products, and Native PAGE Analysis of Purified PHM.....	135
Figure 4.4	Active Site Coordination and Geometry in Xe-PHH.....	136
Figure 4.5	Composite Omit Map Electron Density in the Iron Coordination Environments of Xe-PHH Protomers A and B.....	137
Figure 4.6	Zinc and Copper Binding Sites in Xe-PHH.....	138
Figure 4.7	Composite Omit Map Electron Density in the Zinc and Copper Coordination Environments of Xe-PHH Protomers A and B.....	139
Figure 4.8	Overview of the Xenon-Binding Locations in Xe-PHH.....	140
Figure 4.9	Detailed View of Xenon-Binding Sites in the α -subunit of Xe-PHH.....	141

Figure 4.10	Michaelis-Menten Plot of PH Activity at Various Concentrations of Dioxygen and Xenon Gas.....	142
Figure 4.11	Surface-to-Active Site Voids in the α -subunit of PHH.....	143
Figure 4.12	Surface-to-Active Site Voids in the α -subunit of MMOH.....	144
Figure 4.13	Surface-to-Active Site Voids in the α -subunit of ToMOH.....	145
Figure 4.14	Results from BMM Hydroxylase α -subunit Sequence Alignments.....	146
Figure 4.15	Diiron Center Access Routes in PHH, PHH-PHM, MMOH, and ToMOH as Calculated by CAVER.....	148
Figure 4.16	Overview of the Xenon-Binding Locations in MMOH Form I and Form II Crystals.....	149
Figure A1.1	Global Structure of the PHH-PHM Complex and Enlarged View of PHM in the PHH Canyon.....	160
Figure A1.2	Structures of the Diiron Center in Native and SeMet PHH as Compared to Mixed-Valent MMOH.....	161
Figure A1.3	Hydrogen-Bonding Network in the Second Coordination Sphere of PHH in the PHH-PHM Complex.....	161
Figure A1.4	Zinc Binding Site in the C-terminal Domain of the PHH α -subunit.....	161
Figure A1.5	Structural Differences in Conserved Helix E Residues.....	164
Figure A1.6	Structural Changes in α -subunit Helix F in the SeMet PHH Structure, and the PHH-PHM Binding Interface at α -subunit Helices E and F.....	164
Figure A1.7	Cavities and Pores in the PHH α -subunit, and Stereo View of the Conserved Residues and Water Molecules Contributing to the Pore Through the α -subunit Four-Helix Bundle in the PHH-PHM Complex....	165

Figure A1.8	Access of the Substrate to the Diiron Center at the PHH-PHM Interface.....	166
Figure A1.9	Stereo View of the PHH and ToMOH Substrate Binding Pockets.....	167
Figure A1.S1	Structure and Electrostatic Surfaces of PHH, ToMOH, and MMOH.....	171
Figure A1.S2	Structures of the PHH and ToMOH γ -subunits.....	172
Figure A1.S3	Interaction of the PHH β -subunit N-terminus with α -subunit helices E and F on the Hydroxylase Surface in which PHM is not Bound.....	173
Figure A1.S4	Structural Comparisons Between BMM Regulatory Proteins.....	174
Figure A1.S5	Sequence Alignments of BMM Regulatory Proteins within their Specific Subfamilies.....	175
Figure A1.S6	Stereo View of the $2F_o-F_c$ Simulated Annealing Omit Electron Density Maps Surrounding the Native PHH Diiron Active Sites from Chain A and PHM Bound Chain B contoured to 1.2σ	177
Figure A1.S7	Sequence Alignment of the C-terminal Portion of the PH Hydroxylase α -subunit Depicting the Conserved Cysteines Contributing to the Zinc Binding Site in PHH.....	178
Figure A1.S8	Structural Changes in Helix F.....	179
Figure A2.1	Monoclonal Antibody Structure.....	191
Figure A2.2	MMOH MAb Expressing Hybridoma Cells at 63X and 100X Magnification.....	192
Figure A2.3	A_{280} and Conductivity Traces from DEAE Sepharose Purification of MAb 49 TCS.....	193

Figure A2.4	MAB and BSA Containing Fractions from DEAE Sepharose Purification of MAb 49 TCS.....	193
Figure A2.5	A ₂₈₀ and pH Traces from Protein-G Affinity Purification of MAb 7 TCS.....	194
Figure A2.6	MAB Containing Fractions from Protein-G Affinity Purification of MAb 7 TCS.....	194
Figure A2.7	MAB Fragmentations Using Soluble Papain.....	195
Figure A3.1	View of the Active Site Pocket of ToMOH from the Substrate Access Channel.....	199
Figure A3.2	Substrate Access Channel Extending from the Protein Surface to the Active Site.....	199
Figure A3.3	Conformations Adopted by W100 in the ToMOH I100W Crystal Structure.....	202
Figure A3.4	Diiron Center Blocking Effect of W100 in ToMOH I100W in Comparison to MMOH and Native ToMOH.....	202

CHAPTER 1

Relationships Between Structure and Function in Bacterial Multicomponent Monooxygenase Enzyme Systems

Research Overview and Potential Applications. The non-heme diiron active site in bacterial multicomponent monooxygenases (BMMs) is a perfect example of a functional inorganic unit utilized in nature for multiple processes in biology.(1, 2) In BMMs, it is employed in the hydroxylase protein component for the formation of oxygenated intermediates responsible for hydrocarbon oxidation reactions. Beyond this, it performs diverse and important functions in many other enzymes including tyrosyl radical generation in ribonucleotide reductase,(3) iron storage in ferritins,(4) fatty acid desaturation in Δ^9 desaturase,(5) dioxygen transport in hemerythrin,(6) and oxidative stress protection in rubrerythrin.(7) In all of these cases the diiron site is located within another biologically common motif, a four-helix bundle, where its coordination environment includes a glutamate carboxylate that bridges the iron atoms, and two histidine imidazoles oriented in a syn fashion with respect to the iron-iron vector (Figure 1.1).(2) Moreover, in all but hemerythrin, the remaining protein-derived ligands are three monodentate carboxylate side chains from glutamate or aspartate residues. Given these observations alone, it is clear that the various functions accomplished by the diiron site in these systems are made possible by the surrounding protein matrices, and specifically, the sequences and geometries adopted in the outer coordination spheres as well as the various cavities and channels in their respective structures that collectively dictate the chemistry occurring in the primary coordination environment. Due to this fact, knowledge of the protein structures that contain carboxylate-bridged diiron sites is required for a complete understanding of the mechanisms employed to perform their biological functions. Fortunately, due to advances in synchrotron science during recent decades, such knowledge is rapidly becoming a reality. The present thesis

describes the most current macromolecular crystallographic work on BMM hydroxylases and their component complexes, as well as the insight that this work provides into the mechanisms of biological hydrocarbon oxidation chemistry that they foster at the diiron site, within in the context of previous structural, spectroscopic, and solution biochemical studies.

The BMM class of enzymes is capable of catalytically oxidizing a formidable range of hydrocarbons, including various linear, branched, saturated, unsaturated, halogenated, and aromatic hydrocarbons up to C₈ in size, to yield corresponding alcohol and epoxide products.(8) Independent of their wide substrate range, many BMMs are able to site-specifically oxidize substrates with regio- and/or enantio-selectivity. All confer upon their host bacteria the ability to maintain their carbon and energy requirements through hydrocarbon metabolism, which begins with BMM catalysis. As a result, the individual BMM subclasses exhibit specific substrate preferences that enable their host bacteria to survive on their primary hydrocarbon food stocks, and to that end each has evolved from their common ancestor to specialize in particular oxidation reactions, often in exchange for the inability to oxidize other substrates that may be turned over by BMMs outside their subclass.(9) The subclass to which each BMM belongs is therefore assigned on the basis of their observed substrate preferences, and the result of this classification approach are six established subclasses: soluble methane monooxygenases (sMMOs), alkene monooxygenases (AMOs), phenol hydroxylases (PHs), four-component toluene monooxygenases (TMOs), hyperthermophilic toluene monooxygenases (SsoMOs), and tetrahydrofuran monooxygenases (THMOs).(9, 10) Currently, the focus of the BMM research

community is on the first four of these subclasses (Figure 1.2). The research presented herein pertains to members of the TMO and PH subclasses, with heavy reference and comparison to the sMMOs.

The best-studied BMM is soluble methane monooxygenase (sMMO) from *Methylococcus capsulatus* (Bath) and *Methylosinus trichosporium* OB3b, which is of particular interest because it is the only member of the class able to activate and subsequently hydroxylate the strong C—H bond in methane, at ambient temperatures and pressures.(11, 12) Second and third on the list of well-studied BMMs are toluene/*o*-xylene monooxygenase (ToMO) and phenol hydroxylase (PH) from *Pseudomonas sp.* (OX1).(13) These two systems are notable in that they are members of the TMO and PH subclasses, which specialize in aromatic hydrocarbon oxidation, and in the case of the former, perform various regio- and enantio-selective oxidations on said aromatics.(13, 14) The reason for this breakdown in the level of study on the various BMMs is, first and foremost, to elucidate the mechanism of methane hydroxylation in sMMO and the detailed reasons for which biology employs the common non-heme diiron unit in accomplishing that remarkable chemistry at ambient temperature and pressure. Second, it is due to the attractive applications that studies of all three aforementioned classes offer.

Modern biological research has revealed, since its inception, that life forms inhabit any and all environments that can potentially support them, and BMM containing bacteria are clearly no exception. These bacteria thrive in countless environments of varying degrees of general life inhabitability including within sewers and polluted waters, outside deep-sea ocean vents and active volcanoes, and even in the human mouth.(15,

16) So not only do BMMs accomplish hydrocarbon oxidation chemistry catalytically, selectively, and on a wide substrate scope at a diiron center that is not by any means unique in biology, they can do so in a diverse range of environments including the very harsh. Moreover, methanotrophs such as sMMO hosts play a significant role in regulating global methane levels, an observation that further supports the notion that their metabolic chemistry has a marked and positive influence on the composition of the earth's atmosphere.(17)

Findings from BMM research are ripe for application in many areas including alternative fuel research, bioremediation, and the development of green catalysts for use in industrial organic synthetic procedures. Bioremediation of chlorinated compounds(18, 19) and petroleum components(20, 21) using monooxygenase-containing bacteria is currently established, and some BMMs with high substrate hydroxylation regiospecificities have already been prepared through active site engineering.(22-29) These uses only represent the surface of a much deeper potential for the application of BMM-related science, however. Provided with enough knowledge about their hydroxylase protein structures, for example, one can envision countless possibilities for enzyme engineering that could catalytically effect generation of regio- or enantio-selective starting materials for pharmaceutical research, using environmentally friendly buffer solutions for the reaction solvents. Possibly of greater importance is the potential application of this research in alternative fuel technology where catalysts could be developed on basis of BMM studies that could allow for the environmentally friendly conversion of methane from natural gas sources to liquid methanol that could be subsequently transferred around the globe with greater ease than its gaseous starting

material. Due to this fantastic possibility, said catalyst development is already an active area of research in synthetic modeling chemistry.(11, 30-38)

None of these applications, or the many yet to be conceived, can be brought to fruition without intimate knowledge of the protein structures, component interactions, and mechanisms involved in BMM catalysis. The previous and presently reported structural studies were conducted to this end and are discussed below and in the chapters and appendices that follow. The overarching result of this research into the structural biology of BMMs is significant insight into the spectroscopic, theoretical, and solution biochemical findings obtained to date and potentially in future work as well. The collective mechanistic information obtained through BMM research may eventually facilitate the development of novel technologies that can assist in propelling humankind closer to a time in which we may continue to accelerate the development of culture, while simultaneously exerting an elevated level of care for the global environment in which we thrive.

Hydrocarbon Catalysis in Methane Monooxygenase. The study of BMM catalysis is best developed in the case of sMMO, as mentioned above, so it is logical to begin a discussion of BMM substrate oxidation with a brief review of key findings from that work, with focus on results from the study of that from *Methylococcus capsulatus* (Bath). In particular, the catalytic cycle and involved chemistry are far better understood in sMMO than the other BMMs, and have resulted in establishment of the basic reaction scheme presented below (Figure 1.3). Critical to hydrocarbon catalysis in sMMO is interaction of the accessory Fe₂S₂ and FAD-containing reductase, and cofactorless regulatory protein with the carboxylate-bridged diiron site containing hydroxylase (vide infra).(8, 12, 39,

40) The reductase protein functions to transfer electrons from NADH oxidation to the diiron center, presumably in connection with proton transfer from bulk solvent, to convert it from the resting diferric state to the two-electron reduced diferrous state.(39, 41, 42) Upon said reduction, which is also possible to accomplish chemically using dithionite and mediators, hydroxylase-regulatory protein complex formation is required for dioxygen activation and the subsequent generation of the oxygenated intermediates utilized for hydrocarbon oxidation.(40, 43)

Extensive spectroscopic and theoretical studies of intermediate formation and structure in sMMO have provided considerable insight into structure of the hydrocarbon-oxidizing intermediate species employed by the system. Namely, the formation and decay of a peroxodiiron(III) intermediate has been observed following the reaction of dioxygen with the reduced hydroxylase, as a quadrupole doublet with $\delta=0.66 \text{ mm s}^{-1}$ and $\Delta E_Q=1.51 \text{ mm s}^{-1}$ using Mössbauer spectroscopy, and by stopped flow optical spectroscopy at 420 nm ($\epsilon = 4,000 \text{ M}^{-1} \text{ cm}^{-1}$) and 725 nm ($\epsilon = 1,800 \text{ M}^{-1} \text{ cm}^{-1}$). (12) The geometry of the peroxide coordination in this intermediate is believed to be either cis- μ -1,2, or μ - η^2 : η^2 on the basis of sMMO DFT calculations(44, 45), model complex geometries, and Raman spectroscopy on related diiron carboxylate proteins.(46, 47) The μ - η^2 : η^2 geometry is notably favored in recent theoretical calculations, however, because it exhibits lower energy than the other possibilities.(48) Although the peroxo intermediate is known to be competent for substrate turnover, at least in the case of certain vinyl ethers,(49) it first decays to yield a more reactive high-valent diiron(IV) species deemed intermediate Q prior to product formation when methane is the substrate.(50) Like the peroxo intermediate, the formation and decay of intermediate Q

is observable by Mössbauer spectroscopy, as quadrupole doublets with $\delta=0.21 \text{ mm s}^{-1}$ and $\Delta E_Q=0.68 \text{ mm s}^{-1}$ for Fe1, and $\delta=0.14 \text{ mm s}^{-1}$ and $\Delta E_Q=0.55 \text{ mm s}^{-1}$ for Fe2, as well as by stopped flow optical spectroscopy at 350 nm ($\epsilon = 3,600 \text{ M}^{-1} \text{ cm}^{-1}$) and 420 nm ($\epsilon = 7,200 \text{ M}^{-1} \text{ cm}^{-1}$).⁽¹²⁾ Also as in the case of the peroxo intermediate, the geometry of the intermediate Q has been assigned on the basis of DFT calculations and analogy to model compounds and similar diiron carboxylate intermediates, as a di- μ -oxo species.⁽⁵⁰⁾ This established geometry is further supported by results from EXAFS spectroscopy that indicate a $\sim 2.5 \text{ \AA}$ Fe—Fe distance as well as short Fe—O distances of 1.8 and 2.0 \AA for the structure of intermediate Q that are indicative of a di- μ -oxo diamond core motif.⁽⁵¹⁾ Upon reaching intermediate Q, substrate hydroxylation takes place at the diiron center, product is released, and the system returns to the resting diferric state at which time it is again poised for reduction and the next round of catalysis.

When considering the reaction schemes adopted by sMMO and other BMMs (Figure 1.2), and particularly when one is concerned with the structures of the hydroxylase and its component protein complexes, understanding the means by which the four substrates (electrons, protons, dioxygen, and a hydrocarbon) reach the diiron site is important in elucidating the mechanisms of catalysis employed by these systems. Accordingly, substrate trafficking is a major focus in current BMM research and is only beginning to be understood.⁽⁵²⁾

Electrons are unique among the substrates that must reach the diiron site during *in vivo* catalysis because they are transferred from NADH oxidation through covalent and hydrogen bonds in the component proteins, and furthermore, because this process

undoubtedly involves the formation of a complex between the hydroxylase and reductase proteins.(39, 40) In sMMO, reductase protein binding induces a structural change in the hydroxylase protein,(39) and an analogous effect is presumed to occur in all BMMs. Moreover, this process is markedly different in TMO catalysis, because in that BMM subclass an additional Rieske-type ferredoxin mediates electron transfer between the Fe_2S_2 and FAD-containing reductase component common to all BMM systems and the hydroxylase protein. This difference in the component interaction scheme adopted by TMOs implies a marked variation in the means of electron transfer into the hydroxylase with respect to that adopted by the remaining, three-component BMMs (vide infra).

In contrast to electron transfer, the translocation of protons, dioxygen, and hydrocarbons into the vicinity of the active site does not necessarily require a component protein binding event, but instead involves the physical translocation of molecular species. Protons are most likely brought to the active site in the form of H_3O^+ cations, and may require conformational changes in the hydroxylase protein. Structural evidence for such a conformational shift occurring in concert with proton translocation has already been noted for sMMO,(53) and is discussed in the context of all BMMs in Chapters 2 and 3 on the basis of similar results from studies of ToMO. The movement of dioxygen and hydrocarbons into the active site environment is also not theoretically restricted to involve component protein binding, and furthermore, may also not require any concomitant conformational changes in the hydroxylase.

Provided with a basic framework for substrate trafficking in BMM systems, one can anticipate that the access pathways for the various substrates in the hydroxylase

protein comprise: a static network of polar residues linking the diiron site to the protein surface for electron transfer, a proton translocation route that may be flexible in conformation, and separate or shared molecular access route(s) traversing open-space pathway(s) from the active site cavity to bulk solvent. Substance to this basic framework is duly provided by analysis of the hydroxylase and hydroxylase-regulatory protein structures, as well as from results of component interaction studies and the structural bases for their associated conclusions, which brings this discussion to the important findings from said research.

Structural Characterization of BMM Hydroxylases. Considering the amount of mechanistic data obtained to date on the sMMO system, it is not surprising that structural characterization of the sMMO hydroxylase (MMOH) is also considerably more developed than that of the remaining BMM hydroxylases. Accordingly, X-ray crystallographic characterization of MMOH is extensive,(8) and includes data on the resting diferric,(54-57) one-electron reduced Fe(II)Fe(III) mixed-valent,(53) two-electron reduced diferrous,(53, 58, 59) divalent metal-reconstituted,(60) xenon- and haloalkane-bound,(61) product-bound,(62) and product analog-bound(63) states. The first MMOH structure revealed, among other things, the global fold and orientation of the protein subunits (Figure 1.4) in addition to the geometry and location of the diiron center.(55) The $(\alpha\beta\gamma)_2$ heterodimeric protein was observed as primarily α -helical in fold, and that the dimer interface gives rise to a canyon region centered about the pseudo- C_2 symmetry axis that separates the two protomers, which was proposed at that time to be a potential site for component protein binding.(55)

In addition, this early structure indicated that the diiron center is located in a four-helix bundle within the α -subunits, and adopts a geometry and first coordination sphere strikingly similar to that observed in other enzymes containing carboxylate-bridged diiron centers (vide supra). Specifically, the geometry observed was one that oriented the iron atoms 3.4 Å from one another through protein side chain coordination from a bridging glutamate carboxylate, histidine imidazoles in a syn disposition with respect to the Fe—Fe vector, and three additional monodentate glutamate carboxylates (Figure 1.4). The remainder of the pseudo-octahedral coordination environment of both iron atoms was found to consist of a solvent derived μ -hydroxo bridge, a terminal water molecule on Fe1, and a bidentate bridging acetate anion. These results on the MMOH diiron center geometry were consistent with early spectroscopic data on the protein,(64, 65) and provided for the first time a visual depiction of the methane-oxidizing active site at atomic resolution. In addition to these insightful findings this structure revealed that the active site is located in a cavity entirely hydrophobic in nature save a single threonine residue, and was linked to the exterior solvent environment via a series of additional hydrophobic cavities and a short but constricted pathway between helices E and F in the α -subunit.

Not long after determination of the first structure of MMOH in its oxidized resting state, the structure of the reduced diferrous form was similarly characterized.(59) The most significant findings from this structure all pertained to the diiron center coordination in geometry. Foremost was the observation of a “carboxylate shift”(66) in the coordination of the E243 side chain, which changed ligation mode from monodentate to bidentate on Fe2, and μ -carboxylato bridging with respect to both irons. This

coordination change in the active site was adopted as result of a significant reorientation in the position of the dangling oxygen atom of the E243 carboxylate with respect to that in the oxidized structure and additionally resulted in the displacement of the μ -hydroxo anion observed in the resting state of the enzyme. Another feature of note in this early structure of diferrous MMOH was the presence of a μ -OH₂ ligand occupying the position of the bidentate bridging acetate anion reported in the first structure. These coordination changes in the active site, which collectively resulted in reduction of the coordination number on Fe₂ from six to five, provided insight into the mechanism of intermediate formation in MMO catalysis because they indicated how two-electron reduction of the iron atoms was accommodated by the protein such to open a site for dioxygen coordination on Fe₂ while maintaining charge-neutrality in the active site.

Following determination of the diferric and diferrous structures of MMOH, additional crystallographic data were reported on these forms of the protein at improved resolutions, along with the characterization of the one-electron reduced Fe(II)Fe(III) mixed-valent form.⁽⁵³⁾ The mixed-valent data provided a depiction of the diiron site when partially reduced, and accordingly, a partial carboxylate shift in E243 was adopted in this structure wherein the side chain coordination was bidentate on Fe₂ as in the case of the reduced diiron site but not bridging both irons as in the case of the oxidized form. Although these observations regarding the mixed-valent active site are interesting, the bulk of the insightful results from this work came from comparative analysis of the updated diferric and diferrous structures. This comparative work revealed an unanticipated series of conformational changes on the protein surface of the iron-ligating helices E and F, in the vicinity of the active site pocket. Of particular note among

the observed conformational changes was a significant rotamer shift in the side chain of an asparagine residue strictly conserved among BMMs, which was proposed at that time to potentially relate to hydroxylase-regulatory complex formation because of its location near the active site on the α -subunit surface, and because of the nature of the shift and side-chain functional group (Chapters 2 and 3).

MMOH has also been characterized in the apo form, and following reconstitution of the apo protein with manganese(II) and cobalt(II).⁽⁶⁰⁾ The structural results from characterization of the apo protein indicated that proper folding and organization of the α -subunit residues and helices that comprise the active site coordination environment require the presence of bound metal ions. The structures reconstituted with manganese(II) and cobalt(II) revealed that the active site coordination and geometry in these forms of MMOH strongly resemble that in the diferrous protein, save slight perturbations in the metal—ligand distances, and led to their assignment as structural analogs for the reduced hydroxylase. Experimental procedures for the extraction and reconstitution of the active site metal ions in MMOH were also established as part of this work. Additional, kinetic analysis of iron extraction and metal reconstitution processes via these methods in the presence and absence of the regulatory protein indicated that it serves to block active site metal ion movement from and into the coordination environment.

In effort to elucidate a role for the hydrophobic cavities found in the MMOH α -subunit, multiple xenon- and product analog-bound structures of MMOH were determined and analyzed in detail following characterization of various forms of the diiron site.^(61, 63) In all of these structures, a large majority of the bound xenon atoms

(Chapter 4) and product analogs were located in the hydrophobic cavities initially suggested to act as the route of hydrocarbon access to MMOH active site cavity, thereby providing further evidence for that hypothesis. Moreover, in the structure of bromohexanol-bound MMOH, significant alterations in the backbone and side chain conformations of residues in helices E and F were observed and suggested to be a result of the presence of this relatively large (with respect to methane) hydrocarbon inside the α -subunit cavities.⁽⁶³⁾ The effect of these conformational alterations in the iron ligating and surface-exposed helices E and F was an extension in the π -helical conformation of helix E, and greater active site cavity solvent exposure via the access pathway traversing a route to the α -subunit surface between the two helices, which was identified in the initial structure of MMOH (*vide supra*) and deemed the “pore” upon this observation. This finding, in the context of results from the component interaction studies described below, led to the conclusion that a similar effect on the helix conformations and pore route accessibility might occur upon regulatory protein binding to the hydroxylase. Provided that regulatory protein binding exerts a similar effect on the hydroxylase α -subunit protein structure, then it would be reasonable to conclude that it may act as the means by which dioxygen reactivity is conferred upon the hydroxylase when in complex with the catalytically-required component, through resulting conformational changes in the active site cavity or coordination environment.

Last in the series of X-ray crystallographic studies of BMM hydroxylases conducted prior to the work reported herein by the author, was characterization of the ToMO hydroxylase (ToMOH) in the diferric, azide-bound, and bromophenol-bound states.⁽⁶⁷⁾ This milestone in the study of BMM structure was most significant in that it

represented the only BMM hydroxylase protein other than MMOH to be structurally characterized at the time. Analysis of the ToMOH structure revealed numerous similarities and differences to MMOH that gave rise to important conclusions regarding their substrate reactivity differences including critical insight into various reasons why ToMO hydroxylates aromatic substrates but is not capable of oxidizing methane whereas the converse is true for MMO. The diiron sites in ToMOH and MMOH were found to be essentially identical but the relative solvent accessibility of the two active sites was noted as significantly different because of the presence of a large, non-conserved and open-channel bulk solvent access route traversing a pathway from the protein surface to the active site cavity in ToMOH. Also immediately clear upon comparison of the MMOH and ToMOH dimer structures was a different overall fold and orientation of the protein γ -subunits, which has recently been ascribed as another possible reason for the different reactivity trends that characterize the two systems, on the basis of theoretical calculations.(68) The structure of ToMOH additionally facilitated the discovery of a surface-to-active site histidine imidazole linked hydrogen-bonding network that is conserved in MMOH and ToMOH, and proposed to be the route of electron transfer to the diiron site by analogy to a similar network known to function for electron transfer in the R2 subunit of ribonucleotide reductase (Figure 1.4).

Just prior to accomplishing crystallographic structural characterization of ToMOH, the recombinant expression of this hydroxylase in appreciable yield and with high enzymatic activity was established.(69) Due to the fact that this is not yet possible for MMOH, and considering the significant structural homology between the two systems, the combined structural and genetic results were particularly exciting because it opened

the door to site-directed mutagenesis studies of ToMOH from which the results could be extended to MMOH by analogy. Along the same lines, the structural determination of ToMOH mutants became relatively straightforward upon characterization of the native protein, because phasing of the diffraction data from mutant samples could be expedited through the use of molecular replacement and the native coordinates.

BMM Component Protein Structures and Interactions. A handful of BMM component proteins other than the hydroxylase have been structurally characterized. In the MMO system, NMR structures of the 16 kDa regulatory protein (MMOB)(70, 71) as well as the individual Fe₂S₂ ferredoxin(72) and flavin(73) domains of the 39 kDa reductase protein (MMOR) have been obtained. The structure of MMOB from *Methylococcus capsulatus* (Bath) revealed its novel fold and the presence of lengthy unstructured N- and C-termini.(70) Moreover, perturbations in ¹⁵N-labeled MMOB heteronuclear single-quantum coherence spectra occurred upon titration of MMOH into the NMR samples, and provided for accurate (Appendix 1) determination of the hydroxylase binding face of MMOB.(70) In subsequent mutagenesis work and related structural analysis it was determined that the N-terminus of MMOB is involved in binding the hydroxylase, and is essential to the protein function.(74) The individual structures of the ferredoxin and flavin domains of the reductase protein, which were determined as such because of the large size of the full-length protein for NMR structural determination, exhibit structural properties similar to those of other reductase proteins with analogous functions in biology.

Outside the sMMO system, the regulatory protein components of toluene-4-monooxygenase (T4MOD) from *Pseudomonas mendocina*(75) and phenol hydroxylase

(DmpM) from *Pseudomonas* sp CF600(76) have been structurally characterized by NMR spectroscopy, and the former by X-ray crystallography as well.(77) These structures collectively indicate that although the novel fold first noticed in the structure of MMOB is conserved among BMM systems, the lengths of the unstructured termini vary significantly. N-terminal deletion studies of T4MOD have shown that it is not important for catalysis in contrast to the aforementioned results regarding this structural feature in MMOB. The structure of the 10 kDa Rieske-type ferredoxin component of toluene-4-monooxygenase (T4MOC) from *Pseudomonas mendocina* has been determined by NMR(78) and X-ray crystallographic methods.(79) The structures resulting from this work indicate that the electrostatic surface of the protein deviates from that in other Rieske proteins, leading to the conclusion this electrostatic difference may relate to its interaction with the T4MO hydroxylase.

Since early work on sMMO, the relationship between efficient catalysis and component interactions in BMM systems has been well established. The interaction of the reductase and Rieske proteins with the hydroxylase in BMMs for electron transfer to the diiron center seems relatively straightforward, because the accessory proteins in this case are common in biology and are accordingly well characterized. Recent work on the MMOH-MMOR interaction(39) and the identification of complex formation between T4MOD and T4MOC during T4MO catalysis(80) have indicated that despite the observation that BMM reductase and Rieske proteins are structurally homologous to those utilized in many other biological systems, their involvement in BMM component interactions may be more complicated than originally anticipated. Moreover, the simple fact that BMMs in the TMO subclass require a Rieske component for electron transfer in

addition to the universally employed reductase gives rise to the notion that the reductase component interaction scheme utilized in TMOs is directly related to their specialized ability to site-specifically hydroxylate aromatic compounds.

Undeniably more complicated than the hydroxylase-reductase interactions in BMMs, however, are the details and roles for the hydroxylase-regulatory component interactions in these systems. The regulatory protein is relatively small in comparison with the remaining component proteins, exhibits an unusual core protein fold and the presence of unstructured termini of varying lengths and necessity for catalysis, and contains no cofactors. In addition to these fascinating observations, BMM regulatory proteins have been implicated in numerous roles in BMM catalysis including the facilitation of hydroxylase dioxygen activation and reaction coupling efficiency, gating metal ion and small molecule access to the active site cavity, and altering hydrocarbon oxidation regioselectivity.^(8, 81-83) To date, the exact role of the regulatory protein in BMMs remains unclear.

The State of BMM Structural Research Prior to the Present Work. Prior to the start of the presently reported work on the crystallographic characterization of BMM hydroxylases, the structural questions in the forefront of BMM research primarily revolved around elucidating the nature of the hydroxylase-regulatory protein complex, probing the roles of various residues in the active site cavity and substrate-binding channel of ToMOH, and understanding the means of proton and electron transport to the active site during catalysis. The first structure of ToMOH had very recently been determined, and like the channel within its structure, the hydrophobic cavities in MMOH were considered unique among BMM hydroxylases. Structural characterization of the

hydroxylase component of phenol hydroxylase seemed a distant, although obtainable reality. The following chapters and appendices describe the author's contribution to the structural characterization of BMM hydroxylases and their component complexes that has been accomplished during the past five years.

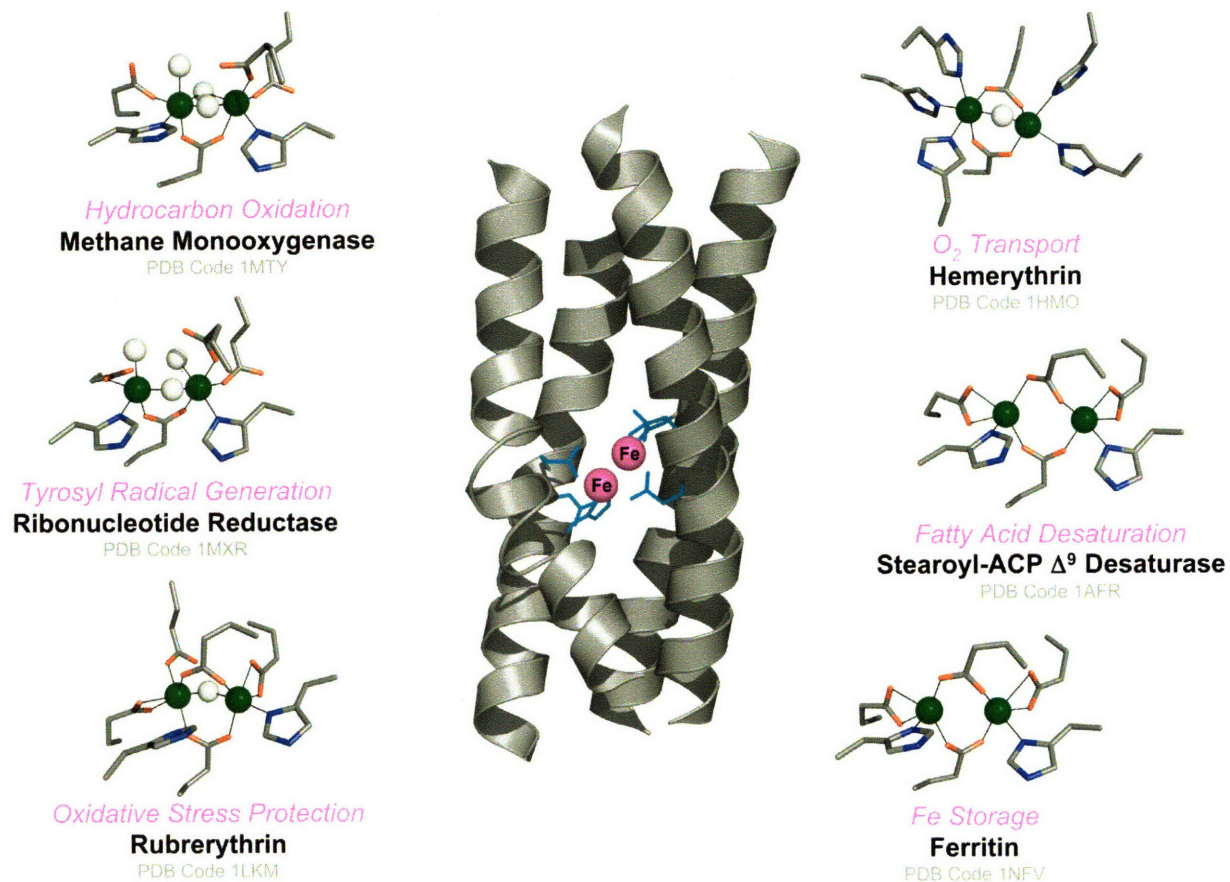


Figure 1.1. Select dioxygen activated carboxylate bridged diiron sites in biology. Protein ligands are shown as sticks in grey (carbon), blue (nitrogen), and red (oxygen). Iron atoms and solvent ligands are shown as spheres in green and white, respectively. A typical (MMOH shown) iron site ligating four-helix bundle is represented as ribbons (grey) with ligand side chains as sticks (cyan) and iron atoms as spheres (magenta).

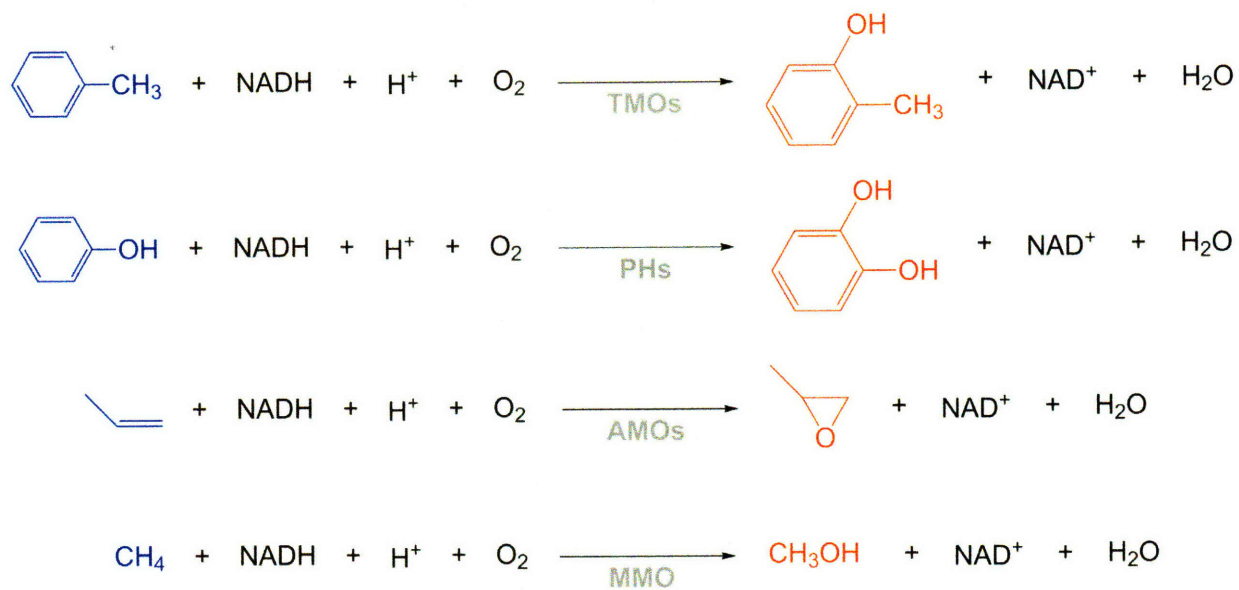


Figure 1.2. Biological reactions of four BMM subclasses. Hydrocarbon substrates and products are shown in blue and red, respectively.

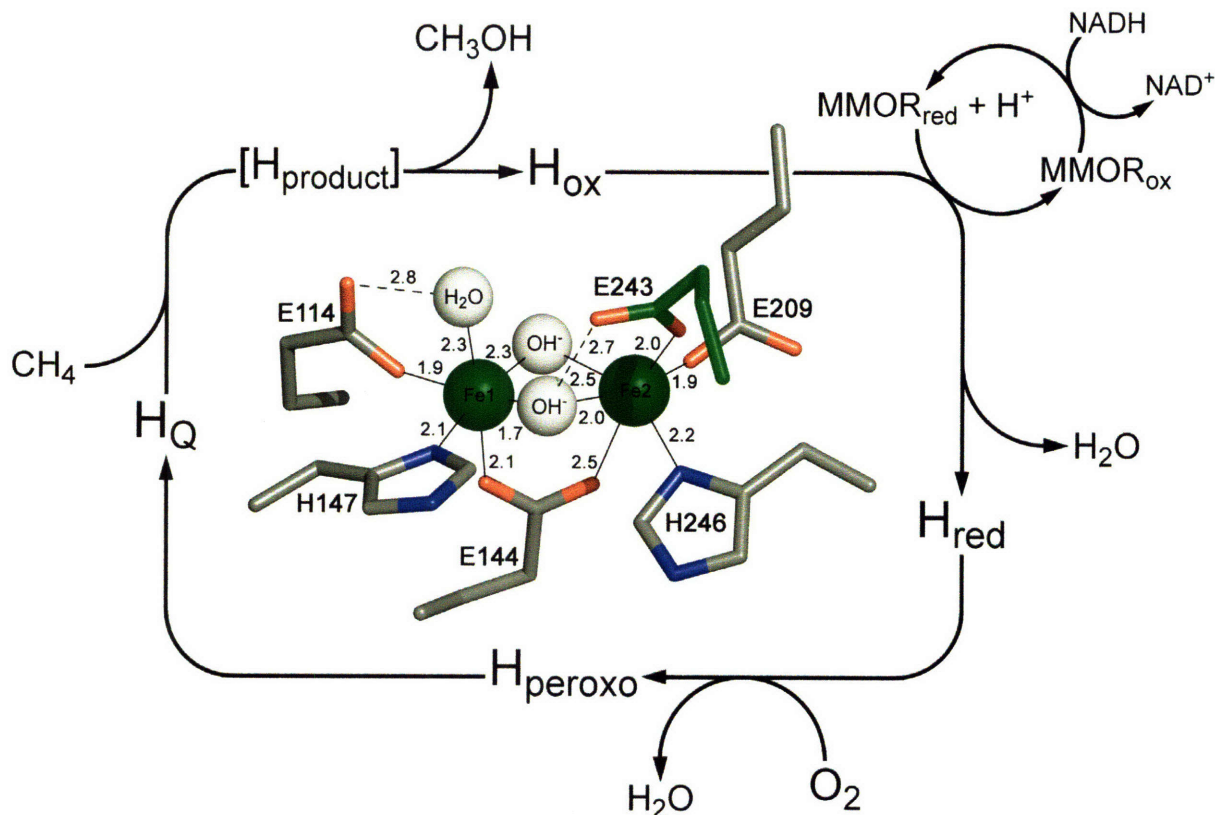
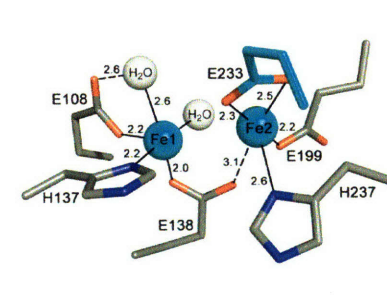
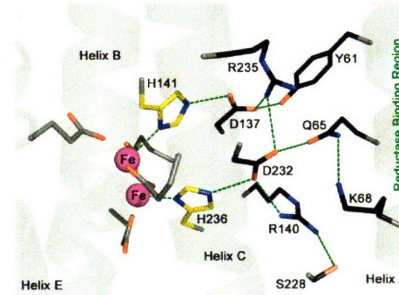
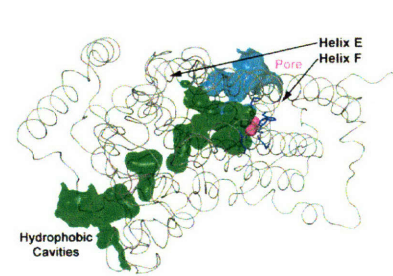
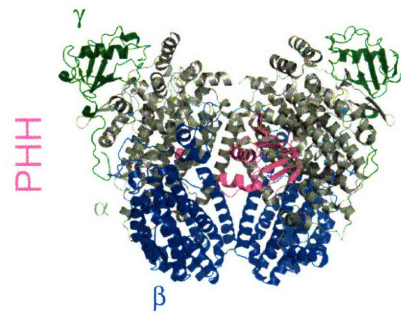
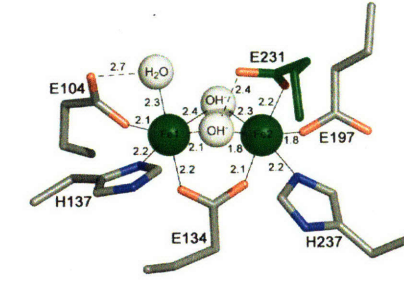
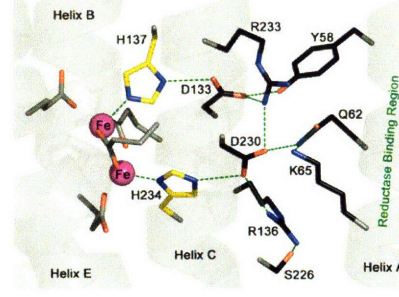
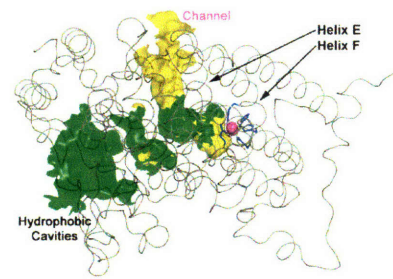
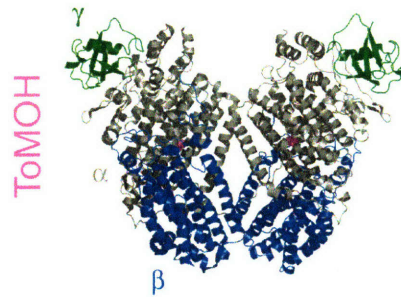
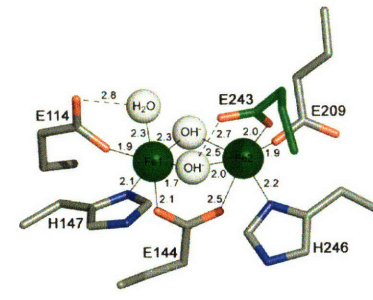
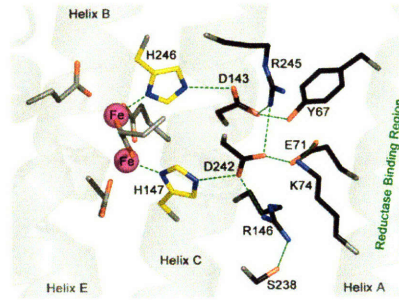
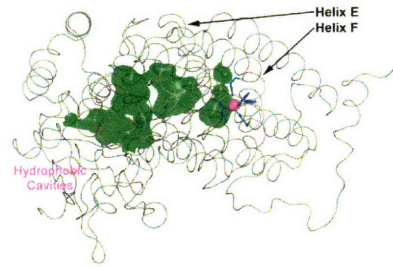
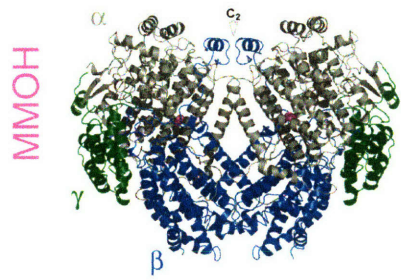


Figure 1.3. The reaction cycle of soluble methane monooxygenase, indicating the resting diferric (H_{ox}), reduced diferrous (H_{red}), peroxy intermediate (H_{peroxo}), and intermediate Q (H_Q) states. The diferric active site coordination and geometry is shown in the center of the reaction cycle. Iron atoms and solvent ligands are shown as spheres in green and white, respectively. Protein ligands are represented as sticks in grey (carbon), green (E243 carbon), red (oxygen), and blue (nitrogen). Interatomic distances are provided in angstroms.

Figure 1.4. (next page) Global folds, active site access routes, histidine-linked hydrogen bonding networks, and iron center coordination (left to right) in the structurally characterized BMM hydroxylases. Alpha (grey), beta (blue), and gamma (green) subunits are shown as ribbons in the hydroxylase dimer images. Alpha subunit C_α trace is represented as ribbons in grey, and interior van der Waals surfaces are shown in green (hydrophobic cavities), yellow (ToMOH channel), and cyan (PHH pore) in the α -subunit interior images. Iron atoms are represented as spheres in magenta, select helices as grey ribbons, and protein side chains as sticks in grey (carbon), yellow (histidine carbon), black (hydrogen-bonding network carbon), red (oxygen), and blue (nitrogen) in the hydrogen-bonding network images. Iron atoms are represented as spheres in green and cyan, solvent ligands as spheres in white, and protein ligands as sticks in grey (carbon), green or cyan (carboxylate shift residue carbon), red (oxygen), and blue (nitrogen) in the images of the diiron sites.



References

1. Lippard, S. J., and Berg, J. M., Editors (1994) *Principles of Bioinorganic Chemistry*, University Science Books, Mill Valley, CA.
2. Nordlund, P., and Eklund, H. (1995) Di-iron-carboxylate proteins. *Curr. Opin. Struct. Biol.* 5, 758-766.
3. Stubbe, J. (2003) Di-iron-tyrosyl radical ribonucleotide reductases. *Curr. Opin. Chem. Biol.* 7, 183-188.
4. Carrondo, M. A. (2003) Ferritins, iron uptake and storage from the bacterioferritin viewpoint. *EMBO J.* 22, 1959-1968.
5. Lindqvist, Y., Huang, W., Schneider, G., and Shanklin, J. (1996) Crystal structure of delta9 stearyl-acyl carrier protein desaturase from castor seed and its relationship to other di-iron proteins. *EMBO J.* 15, 4081-4092.
6. Stenkamp, R. E. (2001) Hemerythrin. *Handb. Metalloproteins* 2, 687-698.
7. Kurtz, D. M., Jr., and Coulter, E. D. (2004) Bacterial nonheme iron proteins and oxidative stress. *Chemtracts* 17, 127-155.
8. Sazinsky, M. H., and Lippard, S. J. (2006) Correlating structure with function in bacterial multicomponent monooxygenases and related diiron proteins. *Acc. Chem. Res.* 39, 558-566.
9. Leahy, J. G., Batchelor, P. J., and Morcomb, S. M. (2003) Evolution of the soluble diiron monooxygenases. *FEMS Microbiol. Rev.* 27, 449-479.
10. Notomista, E., Lahm, A., Di Donato, A., and Tramontano, A. (2003) Evolution of bacterial and archaeal multicomponent monooxygenases. *J. Mol. Evol.* 56, 435-445.
11. Lippard, S. J. (2005) Hydroxylation of C-H bonds at carboxylate-bridged diiron centers. *Philos. Trans. R. Soc. London* A363, 861-877.
12. Merckx, M., Kopp, D. A., Sazinsky, M. H., Blazyk, J. L., Muller, J., and Lippard, S. J. (2001) Dioxygen activation and methane hydroxylation by soluble methane monooxygenase: a tale of two irons and three proteins. *Angew. Chem., Int. Ed.* 40, 2782-2807.

13. Cafaro, V., Izzo, V., Scognamiglio, R., Notomista, E., Capasso, P., Casbarra, A., Pucci, P., and Di Donato, A. (2004) Phenol hydroxylase and toluene/*o*-xylene monooxygenase from *Pseudomonas stutzeri* OX1: interplay between two enzymes. *Appl. Environ. Microbiol.* 70, 2211-2219.
14. McClay, K., Fox, B. G., and Steffan, R. J. (2000) Toluene monooxygenase-catalyzed epoxidation of alkenes. *Appl. Environ. Microbiol.* 66, 1877-1882.
15. Sazinsky, M. H. (2004) *Structural Studies of Bacterial Multicomponent Monooxygenases: Insights into Substrate Specificity, Diiron Center Tuning and Component Interactions*, Doctoral thesis, Massachusetts Institute of Technology, Cambridge, MA.
16. Anesti, V., McDonald, I. R., Ramaswamy, M., Wade, W. G., Kelly, D. P., and Wood, A. P. (2005) Isolation and molecular detection of methylotrophic bacteria occurring in the human mouth. *Environ. Microbiol.* 7, 1227-1238.
17. Hanson, R. S., and Hanson, T. E. (1996) Methanotrophic bacteria. *Microbiol. Rev.* 60, 439-471.
18. Adriaens, P., and Vogel, T. M. (1995) Biological treatment of chlorinated organics. *Microb. Transform. Degrad. Toxic Org. Chem.*, 435-486.
19. Young, L. Y., and Cerniglia, C. E., Editors (1995) *Microbial Transformation and Degradation of Toxic Organic Chemicals*, Wiley-Liss, New York, NY.
20. Huesemann, M. H. (2004) Biodegradation and bioremediation of petroleum pollutants in soil. *Soil Biol.* 1, 13-34.
21. Atlas, R. M. (1995) Bioremediation of petroleum pollutants. *Int. Biodeterior. Biodegrad.* 35, 317-327.
22. Feingersch, R., Shainsky, J., Wood, T. K., and Fishman, A. (2008) Protein engineering of toluene monooxygenases for synthesis of chiral sulfoxides. *Appl. Environ. Microbiol.* 74, 1555-1566.
23. Vardar, G., and Wood, T. K. (2005) Protein engineering of toluene-*o*-xylene monooxygenase from *Pseudomonas stutzeri* OX1 for enhanced chlorinated ethene degradation and *o*-xylene oxidation. *Appl. Microbiol. Biotechnol.* 68, 510-517.
24. Tao, Y., Bentley, W. E., and Wood, T. K. (2005) Regiospecific oxidation of naphthalene and fluorene by toluene monooxygenases and engineered

- toluene 4-monooxygenases of *Pseudomonas mendocina* KR1. *Biotechnol. Bioeng.* 90, 85-94.
25. Fishman, A., Tao, Y., Rui, L., and Wood, T. K. (2005) Controlling the Regiospecific Oxidation of Aromatics via Active Site Engineering of Toluene para-Monooxygenase of *Ralstonia pickettii* PKO1. *J. Biol. Chem.* 280, 506-514.
 26. Vardar, G., Ryu, K., and Wood, T. K. (2005) Protein engineering of toluene-*o*-xylene monooxygenase from *Pseudomonas stutzeri* OX1 for oxidizing nitrobenzene to 3-nitrocatechol, 4-nitrocatechol, and nitrohydroquinone. *J. Biotechnol.* 115, 145-156.
 27. Fishman, A., Tao, Y., Bentley, W. E., and Wood, T. K. (2004) Protein engineering of toluene 4-monooxygenase of *Pseudomonas mendocina* KR1 for synthesizing 4-nitrocatechol from nitrobenzene. *Biotechnol. Bioeng.* 87, 779-790.
 28. Tao, Y., Fishman, A., Bentley, W. E., and Wood, T. K. (2004) Altering toluene 4-monooxygenase by active-site engineering for the synthesis of 3-methoxycatechol, methoxyhydroquinone, and methylhydroquinone. *J. Bacteriol.* 186, 4705-4713.
 29. Vardar, G., and Wood, T. K. (2004) Protein engineering of toluene-*o*-xylene monooxygenase from *Pseudomonas stutzeri* OX1 for synthesizing 4-methylresorcinol, methylhydroquinone, and pyrogallol. *Appl. Environ. Microbiol.* 70, 3253-3262.
 30. Costas, M., Mehn, M. P., Jensen, M. P., and Que, L., Jr. (2004) Dioxygen Activation at Mononuclear Nonheme Iron Active Sites: Enzymes, Models, and Intermediates. *Chem. Rev.* 104, 939-986.
 31. Jackson, T. A., and Que, L., Jr. (2006) Structural and functional models for oxygen-activating nonheme iron enzymes. *Concepts Models Bioinorg. Chem.*, 259-286.
 32. Lee, D., and Lippard, S. J. (1998) Structural and Functional Models of the Dioxygen-Activating Centers of Non-Heme Diiron Enzymes Ribonucleotide Reductase and Soluble Methane Monooxygenase. *J. Am. Chem. Soc.* 120, 12153-12154.
 33. Lee, D., and Lippard, S. J. (2002) Modeling Dioxygen-Activating Centers in Non-Heme Diiron Enzymes: Carboxylate Shifts in Diiron(II) Complexes

Supported by Sterically Hindered Carboxylate Ligands. *Inorg. Chem.* **41**, 2704-2719.

34. Lee, D., Pierce, B., Krebs, C., Hendrich, M. P., Huynh, B. H., and Lippard, S. J. (2002) Functional Mimic of Dioxygen-Activating Centers in Non-Heme Diiron Enzymes: Mechanistic Implications of Paramagnetic Intermediates in the Reactions between Diiron(II) Complexes and Dioxygen. *J. Am. Chem. Soc.* **124**, 3993-4007.
35. Que, L., Jr., and Dong, Y. (1996) Modeling the oxygen activation chemistry of methane monooxygenase and ribonucleotide reductase. *Acc. Chem. Res.* **29**, 190-196.
36. Rohde, J.-U., Bukowski Michael, R., and Que, L., Jr. (2003) Functional models for mononuclear nonheme iron enzymes. *Curr. Opin. Chem. Biol.* **7**, 674-682.
37. Shan, X., and Que, L., Jr. (2006) High-valent nonheme iron-oxo species in biomimetic oxidations. *J. Inorg. Biochem.* **100**, 421-433.
38. Tshuva, E. Y., and Lippard, S. J. (2004) Synthetic Models for Non-Heme Carboxylate-Bridged Diiron Metalloproteins: Strategies and Tactics. *Chem. Rev.* **104**, 987-1011.
39. Blazyk, J. L., Gassner, G. T., and Lippard, S. J. (2005) Intermolecular Electron-Transfer Reactions in Soluble Methane Monooxygenase: A Role for Hysteresis in Protein Function. *J. Am. Chem. Soc.* **127**, 17364-17376.
40. Gassner, G. T., and Lippard, S. J. (1999) Component interactions in the soluble methane monooxygenase system from *Methylococcus capsulatus* (Bath). *Biochemistry* **38**, 12768-12785.
41. Blazyk, J. L., and Lippard, S. J. (2004) Domain Engineering of the Reductase Component of Soluble Methane Monooxygenase from *Methylococcus capsulatus* (Bath). *J. Biol. Chem.* **279**, 5630-5640.
42. Blazyk, J. L., and Lippard, S. J. (2002) Expression and Characterization of Ferredoxin and Flavin Adenine Dinucleotide Binding Domains of the Reductase Component of Soluble Methane Monooxygenase from *Methylococcus capsulatus* (Bath). *Biochemistry* **41**, 15780-15794.
43. Fox, B. G., Liu, Y., Dege, J. E., and Lipscomb, J. D. (1991) Complex formation between the protein components of methane monooxygenase from

- Methylosinus trichosporium* OB3b. Identification of sites of component interaction. *J. Biol. Chem.* 266, 540-550.
44. Gherman, B. F., Baik, M.-H., Lippard, S. J., and Friesner, R. A. (2004) Dioxygen Activation in Methane Monooxygenase: A Theoretical Study. *J. Am. Chem. Soc.* 126, 2978-2990.
 45. Siegbahn, P. E. M. (2001) O-O bond cleavage and alkane hydroxylation in methane monooxygenase. *J. Biol. Inorg. Chem.* 6, 27-45.
 46. Moenne-Loccoz, P., Baldwin, J., Ley, B. A., Loehr, T. M., and Bollinger, J. M., Jr. (1998) O₂ activation by non-heme diiron proteins: identification of a symmetric μ -1,2-peroxide in a mutant of ribonucleotide reductase. *Biochemistry* 37, 14659-14663.
 47. Moenne-Loccoz, P., Krebs, C., Herlihy, K., Edmondson, D. E., Theil, E. C., Huynh, B. H., and Loehr, T. M. (1999) The ferroxidase reaction of ferritin reveals a diferric μ -1,2 bridging peroxide intermediate in common with other O₂-activating non-heme diiron proteins. *Biochemistry* 38, 5290-5295.
 48. Rinaldo, D., Philipp, D. M., Lippard, S. J., and Friesner, R. A. (2007) Intermediates in Dioxygen Activation by Methane Monooxygenase: A QM/MM Study. *J. Am. Chem. Soc.* 129, 3135-3147.
 49. Beauvais, L. G., and Lippard, S. J. (2005) Reactions of the Peroxo Intermediate of Soluble Methane Monooxygenase Hydroxylase with Ethers. *J. Am. Chem. Soc.* 127, 7370-7378.
 50. Baik, M.-H., Newcomb, M., Friesner, R. A., and Lippard, S. J. (2003) Mechanistic Studies on the Hydroxylation of Methane by Methane Monooxygenase. *Chem. Rev.* 103, 2385-2419.
 51. Shu, L., Nesheim, J. C., Kauffmann, K., Munck, E., Lipscomb, J. D., and Que, L., Jr. (1997) An Fe₂IVO₂ diamond core structure for the key intermediate Q of methane monooxygenase. *Science* 275, 515-518.
 52. Murray, L. J., and Lippard, S. J. (2007) Substrate trafficking and dioxygen activation in bacterial multicomponent monooxygenases. *Acc. Chem. Res.* 40, 466-474.
 53. Whittington, D. A., and Lippard, S. J. (2001) Crystal Structures of the Soluble Methane Monooxygenase Hydroxylase from *Methylococcus capsulatus*

(Bath) Demonstrating Geometrical Variability at the Dinuclear Iron Active Site. *J. Am. Chem. Soc.* 123, 827-838.

54. Rosenzweig, A. C., Frederick, C. A., and Lippard, S. J. (1992) Crystallization and preliminary x-ray analysis of the methane monooxygenase hydroxylase protein from *Methylococcus capsulatus* (Bath). *J. Mol. Biol.* 227, 583-585.
55. Rosenzweig, A. C., Frederick, C. A., Lippard, S. J., and Nordlund, P. (1993) Crystal structure of a bacterial non-heme iron hydroxylase that catalyzes the biological oxidation of methane. *Nature* 366, 537-543.
56. Rosenzweig, A. C., and Lippard, S. J. (1994) Determining the Structure of a Hydroxylase Enzyme That Catalyzes the Conversion of Methane to Methanol in Methanotrophic Bacteria. *Acc. Chem. Res.* 27, 229-236.
57. Elango, N., Radhakrishnan, R., Froland, W. A., Wallar, B. J., Earhart, C. A., Lipscomb, J. D., and Ohlendorf, D. H. (1997) Crystal structure of the hydroxylase component of methane monooxygenase from *Methylosinus trichosporium* QB3b. *Protein Sci.* 6, 556-568.
58. Rosenzweig, A. C., Brandstetter, H., Whittington, D. A., Nordlund, P., Lippard, S. J., and Frederick, C. A. (1997) Crystal structures of the methane monooxygenase hydroxylase from *Methylococcus capsulatus* (Bath): implications for substrate gating and component interactions. *Proteins* 29, 141-152.
59. Rosenzweig, A. C., Nordlund, P., Takahara, P. M., Frederick, C. A., and Lippard, S. J. (1995) Geometry of the soluble methane monooxygenase catalytic diiron center in two oxidation states. *Chem. Biol.* 2, 632.
60. Sazinsky, M. H., Merckx, M., Cadieux, E., Tang, S., and Lippard, S. J. (2004) Preparation and x-ray structures of metal-free, dicobalt and dimanganese forms of soluble methane monooxygenase hydroxylase from *Methylococcus capsulatus* (Bath). *Biochemistry* 43, 16263-16276.
61. Whittington, D. A., Rosenzweig, A. C., Frederick, C. A., and Lippard, S. J. (2001) Xenon and Halogenated Alkanes Track Putative Substrate Binding Cavities in the Soluble Methane Monooxygenase Hydroxylase. *Biochemistry* 40, 3476-3482.
62. Whittington, D. A., Sazinsky, M. H., and Lippard, S. J. (2001) X-ray Crystal Structure of Alcohol Products Bound at the Active Site of Soluble Methane Monooxygenase Hydroxylase. *J. Am. Chem. Soc.* 123, 1794-1795.

63. Sazinsky, M. H., and Lippard, S. J. (2005) Product Bound Structures of the Soluble Methane Monooxygenase Hydroxylase from *Methylococcus capsulatus* (Bath): Protein Motion in the alpha-Subunit. *J. Am. Chem. Soc.* **127**, 5814-5825.
64. DeRose, V. J., Liu, K. E., Kurtz, D. M., Jr., Hoffman, B. M., and Lippard, S. J. (1993) Proton ENDOR identification of bridging hydroxide ligands in mixed-valent diiron centers of proteins: methane monooxygenase and semimet azidohemerythrin. *J. Am. Chem. Soc.* **115**, 6440-6441.
65. DeWitt, J. G., Bentsen, J. G., Rosenzweig, A. C., Hedman, B., Green, J., Pilkington, S., Papaefthymiou, G. C., Dalton, H., Hodgson, K. O., and Lippard, S. J. (1991) X-ray absorption, Moessbauer, and EPR studies of the dinuclear iron center in the hydroxylase component of methane monooxygenase. *J. Am. Chem. Soc.* **113**, 9219-9235.
66. Rardin, R. L., Tolman, W. B., and Lippard, S. J. (1991) Monodentate carboxylate complexes and the carboxylate shift: implications for polymetalloprotein structure and function. *New J. Chem.* **15**, 417-430.
67. Sazinsky, M. H., Bard, J., Di Donato, A., and Lippard, S. J. (2004) Crystal Structure of the Toluene/*o*-Xylene Monooxygenase Hydroxylase from *Pseudomonas stutzeri* OX1: Insight Into the Substrate Specificity, Substrate Channeling, And Active Site Tuning of Multicomponent Monooxygenases. *J. Biol. Chem.* **279**, 30600-30610.
68. Gherman, B. F., Lippard, S. J., and Friesner, R. A. (2005) Substrate Hydroxylation in Methane Monooxygenase: Quantitative Modeling via Mixed Quantum Mechanics/Molecular Mechanics Techniques. *J. Am. Chem. Soc.* **127**, 1025-1037.
69. Cafaro, V., Scognamiglio, R., Viggiani, A., Izzo, V., Passaro, I., Notomista, E., Dal Piaz, F., Amoresano, A., Casbarra, A., Pucci, P., and Di Donato, A. (2002) Expression and purification of the recombinant subunits of toluene/*o*-xylene monooxygenase and reconstitution of the active complex. *Eur. J. Biochem.* **269**, 5689-5699.
70. Walters, K. J., Gassner, G. T., Lippard, S. J., and Wagner, G. (1999) Structure of the soluble methane monooxygenase regulatory protein B. *Proc. Natl. Acad. Sci. USA* **96**, 7877-7882.
71. Chang, S. L., Wallar, B. J., Lipscomb, J. D., and Mayo, K. H. (1999) Solution structure of component B from methane monooxygenase derived through heteronuclear NMR and molecular modeling. *Biochemistry* **38**, 5799-5812.

72. Mueller, J., Lugovskoy, A. A., Wagner, G., and Lippard, S. J. (2002) NMR structure of the [2Fe-2S] ferredoxin domain from soluble methane monooxygenase reductase and interaction with its hydroxylase. *Biochemistry* 41, 42-51.
73. Chatwood, L. L., Mueller, J., Gross, J. D., Wagner, G., and Lippard, S. J. (2004) NMR Structure of the Flavin Domain from Soluble Methane Monooxygenase Reductase from *Methylococcus capsulatus* (Bath). *Biochemistry* 43, 11983-11991.
74. Brandstetter, H., Whittington, D. A., Lippard, S. J., and Frederick, C. A. (1999) Mutational and structural analyses of the regulatory protein B of soluble methane monooxygenase from *Methylococcus capsulatus* (Bath). *Chem. Biol.* 6, 441-449.
75. Hemmi, H., Studts, J. M., Chae, Y. K., Song, J., Markley, J. L., and Fox, B. G. (2001) Solution Structure of the Toluene 4-Monooxygenase Effector Protein (T4moD). *Biochemistry* 40, 3512-3524.
76. Qian, H., Edlund, U., Powlowski, J., Shingler, V., and Sethson, I. (1997) Solution structure of phenol hydroxylase protein component P2 determined by NMR spectroscopy. *Biochemistry* 36, 495-504.
77. Lountos, G. T., Mitchell, K. H., Studts, J. M., Fox, B. G., and Orville, A. M. (2005) Crystal Structures and Functional Studies of T4moD, the Toluene 4-Monooxygenase Catalytic Effector Protein. *Biochemistry* 44, 7131-7142.
78. Skjeldal, L., Peterson, F. C., Doreleijers, J. F., Moe, L. A., Pikus, J. D., Westler, W. M., Markley, J. L., Volkman, B. F., and Fox, B. G. (2004) Solution structure of T4moC, the Rieske ferredoxin component of the toluene 4-monooxygenase complex. *J. Biol. Inorg. Chem.* 9, 945-953.
79. Moe, L. A., Bingman, C. A., Wesenberg, G. E., Phillips, G. N., Jr., and Fox, B. G. (2006) Structure of T4moC, the Rieske-type ferredoxin component of toluene 4-monooxygenase. *Acta Crystallogr. D* 62, 476-482.
80. Moe, L. A., McMartin, L. A., and Fox, B. G. (2006) Component Interactions and Implications for Complex Formation in the Multicomponent Toluene 4-Monooxygenase. *Biochemistry* 45, 5478-5485.
81. Zhang, J., and Lipscomb, J. D. (2006) Role of the C-Terminal Region of the B Component of *Methylosinus trichosporium* OB3b Methane Monooxygenase in the Regulation of Oxygen Activation. *Biochemistry* 45, 1459-1469.

82. Zhang, J., Wallar, B. J., Popescu, C. V., Renner, D. B., Thomas, D. D., and Lipscomb, J. D. (2006) Methane Monooxygenase Hydroxylase and B Component Interactions. *Biochemistry* 45, 2913-2926.
83. Zheng, H., and Lipscomb, J. D. (2006) Regulation of Methane Monooxygenase Catalysis Based on Size Exclusion and Quantum Tunneling. *Biochemistry* 45, 1685-1692.

CHAPTER 2

Manganese(II) Reconstituted and Native Toluene/*o*-xylene Monooxygenase Hydroxylase X-ray Crystal Structures Reveal Conformational Shifts in Conserved Residues and an Enhanced View of the Protein Interior

This chapter has been reproduced in part with permission from *J. Am. Chem. Soc.* **2006**, *128*, 15108-15110. Copyright 2006 American Chemical Society.

Introduction

Non-heme diiron enzymes perform important functions in biology,(1) including the selective oxidation of hydrocarbons by bacterial multicomponent monooxygenases (BMMs).(2,3) Dioxygen activation and the conversion of C–H to C–OH bonds is accomplished at carboxylate-bridged diiron units within the α -subunits of the hydroxylase components of these enzymes.(4) The active oxidant in some of these reactions has been trapped as a kinetically competent intermediate that forms upon reaction of the diiron(II) core with O₂.(5) The binding of a small effector protein(6) to the hydroxylase facilitates this process. The evolutionarily related(2) toluene/*o*-xylene monooxygenase (ToMO)(7) and soluble methane monooxygenase (sMMO)(3) hydroxylases ToMOH and MMOH have nearly identical resting diiron(III) active site structures,(4,8-10) but ToMO cannot hydroxylate methane. Since crystallographic characterization of ToMOH has thus far been limited to a native, oxidized structure at 2.15 Å resolution,(8) and in order to expand our structural characterization and mechanistic understanding of the ToMO system, we have determined X-ray crystal structures of native ToMOH to 1.85 Å resolution and of ToMOH reconstituted with Mn(II) as an analog of the reduced, diiron(II) enzyme.(11) The results, which provide important insights that significantly advance our knowledge about the BMM family of enzymes, are that (i) formation of the dimetal(II) center is accompanied by a carboxylate shift and opening of a site for dioxygen binding and activation; (ii) a strategically placed, conserved asparagine residue in the dimetal(II) form of the enzyme undergoes a rotameric shift; and (iii) there exists a previously unidentified series of hydrophobic cavities analogous to those in MMOH. A technical discovery of note in this study is the

use of an annealing procedure during data collection, improving the resolution from 2.55 to 1.85 Å.

Since a suitable crystal of the diiron(II) form of ToMOH was unavailable, the dimanganese(II) derivative was prepared from the apo protein and MnCl_2 and structurally characterized to 2.20 Å. A 1.85 Å resolution structure of native ToMOH_{ox} was determined using crystals grown in an identical manner. Detailed information about sample preparation, Mn reconstitution, crystal annealing, data collection, and structure solution and statistics are described in materials and methods below.

Results and Discussion

Although the overall topology and fold of the native protein are essentially identical to those of the previously published structure of ToMOH_{ox} ,⁽⁸⁾ the active site differs (Figures 2.1 through 2.4). Foremost is the absence of a thioglycolate molecule bridging the two iron atoms, which was not present in the current purification buffer (vide infra). Instead, the iron atoms are linked either by a hydroxide anion, as observed in MMOH structures,⁽¹²⁾ or the terminal hydroxyl group of the polyethylene glycol molecule found in the product-binding channel (vide infra).⁽⁸⁾ Additional differences between the diiron centers of the previously reported and the present higher resolution structure of ToMOH_{ox} are minor and are summarized in Table 2.1.

The structure of the Mn(II)-ToMOH derivative is quite revealing. The carboxylate group of E231, which is analogous to E243 in MMOH, undergoes a shift from its terminal, monodentate coordination mode in ToMOH to a bidentate-terminal, monodentate-bridging position (Figure 2.2). In conjunction with this carboxylate shift, the bridging hydroxide syn to the coordinate histidine ligands is displaced while the one in

the anti position becomes protonated and is semi bridging, being 2.8 Å from Mn1. This structure closely resembles the core geometry of reduced and of dimanganese(II) reconstituted MMOH (Figure 2.4).(11, 12) The results are consistent with Mn being in the divalent state and strongly suggest that ToMOH_{red} will have the same configuration. As in the structures of MMOH_{ox}, MMOH_{red}, and Mn(II)-MMOH, an increase in the metal-metal distance accompanies the carboxylate shift and oxidation state change.

The present Mn(II)-ToMOH results are nicely consistent with recently reported X-ray absorption spectroscopy (XAS) data for ToMOH_{red}.(13) This study indicated that the reduced active site is similar to that of MMOH_{red}, both having iron coordination numbers between 5 and 6, and average Fe-Fe distances of 3.3-3.4 Å. Moreover, in the presence of their respective regulatory proteins MMOB and ToMOD, the XAS spectra of the diferrous hydroxylases closely resemble one another, as well as those for hydroxylases in the absence of the regulatory protein. Thus, it is probable that the active site structures of ToMOH and MMOH immediately prior to O₂ activation are very similar, based on the results reported here and the XAS data. Differences in reactivity, therefore, are likely to reflect the nature of the oxygenated intermediates and/or the surrounding protein scaffolds.

In this regard it is noteworthy that accompanying changes in the oxidation state of the dimetallic center are conformational shifts analogous to those first discovered in a comparison of the MMOH_{red} to MMOH_{ox} structures.(12) Precisely the same features can be identified by comparing the Mn(II)-ToMOH and 1.85 Å ToMOH_{ox} structures. Conformational shifts in MMOH residues N214, E240, L244, and R245 in MMOH(12) are reflected in the analogous N202, Q228, S232, and R233 amino acid side chains of ToMOH (Figure 2.5). These residues are located on surface-exposed regions of helices

E and F, adjacent to the diiron center, where the regulatory protein is postulated to bind in the MMO system(10,12,14) and known to bind in the phenol hydroxylase (PH) system. (Chapter 4) The shift in ToMOH N202 (Figures 2.1 and 2.5) is most significant because (i) this residue is strictly conserved among BMMs; (ii) the structures reported here reveal the dependence of the side chain orientation on oxidation state in ToMOH and MMOH; and (iii) the amide group in the analogous residue N204 in PHH is in hydrogen bond contact with the side chain hydroxyl group of S72 (S111 in MMOB; S82 in T4MOD) of the PH regulatory component (PHM) in the PHH-PHM complex X-ray structure. (Chapter 4)

In the ToMOH_{ox} structure the N202 side chain points away from the diiron center and faces bulk solvent. In Mn(II)-ToMOH the side chain rotates inward, toward the active site. The resulting 80° rotameric shift in the N202 side chain occurs exclusively about the C_α-C_β bond and is the largest among the ToMOH oxidation state-dependent rotamer shifts thus far encountered. As with MMOH, the asparagine side-chain rotamer shift affects the local electrostatics and topology of the protein surface between helices E and F directly above the active site. In the oxidized protein the N202 carboxamide group protrudes from the protein surface and in this manner can serve as a hydrogen bond donor or acceptor. Upon reduction of the active site, this carboxamide group is directed into the “pore” region directly above the active site and is centered between helices E and F. The effect of this change on the topology of the protein surface is to create a crevice with less electrostatic character than for the oxidized protein.

Collectively, these observations reinforce prior claims that the conserved hydroxylase asparagine(12) and regulatory component serine(15) residues are key players in the interaction between the hydroxylase and regulatory protein components.

They further suggest that regulatory component protein binding to the hydroxylase is linked to the asparagine rotamer shift, which in turn, depends on the diiron center oxidation state.

The morphology of the protein interior distinguishes MMOH and ToMOH. Xenon pressurization, as well as halogenated substrate and product binding experiments, with MMOH crystals reveal that both Xe and hydrocarbons can reside in a series of variably interconnected hydrophobic cavities in the α -subunit (Figure 2.6).^(14,16) The cavities, or pockets, trace a pathway from the active site to the protein surface and are postulated to be the means of substrate access to, or product access from, the diiron center. Homologous pockets exist in ToMOH (Figure 2.6) but were not proposed as a link from the surface to the diiron center because of the occurrence of a 35-40 Å channel that connects the active site to the protein exterior via a divergent pathway. The hydrophobic pockets that traverse the interior of the ToMOH α -subunit are the active site pocket (cavity 1), an intermediate space located between helices B and D (cavity 2), and a solvent-exposed cavity found near the interface of the α - and γ -subunits (cavity 3). Cavity 1 is structurally homologous to cavity 1 in MMOH and cavities 2 and 3 are homologous to cavity 2 and a combination of cavities 3 and 4 in MMOH, respectively. It is possible that the hydrophobic pockets in ToMOH convey hydrocarbon access to the active site, but an alternative scenario is that in ToMOH the cavities are a consequence of its evolutionary relationship to MMOH. If the latter is the case, then the ToMOH channel may have evolved in the protein scaffold to tune its reactivity and favor hydroxylation of aromatic substrates.

In the ToMOH_{ox} and Mn(II)-ToMOH structures presented here, electron density in the channel has been modeled as a molecule of hexaethylene glycol, a component of

polyethylene glycol (PEG) 400 in the crystallization buffer (Figure 2.7). Attempts to model water molecules into the density led to unreasonable interatomic distances. In both structures, hexaethylene glycol is disordered as evidenced by high B-factors exhibited in the refinement, which generally increase with distance from the active site. Although our model indicates that the PEG chain ends at the channel fork we believe that in reality its molecular weight is greater than as shown, and that the remainder of the PEG chain in the channel is positionally disordered between the two forks of the channel. Moreover, for both structures it was possible to model the hexaethylene glycol molecule as bound to the active site metal ions as a bridging alkoxide ligand or simply in hydrogen bond contact with a bridging hydroxide ion. The two models afforded similar refinement statistics and could not be distinguished. For presentation purposes we have chosen the latter of these two possibilities in our refined model but note that either option is a likely representation for the channel electron density.

The present Mn-ToMOH and ToMOH_{ox} structures add significantly to the mounting structural evidence implicating BMM protein scaffolds as determinants of inter-system reaction diversity. The active sites of ToMOH and MMOH are highly homologous in both the reduced and resting states. Control of conformational shifts by the redox state of the protein, first noted in MMOH, is conserved in ToMOH. Experimentally, we show here that ToMOH is susceptible to iron extraction and Mn reconstitution by methods established in identical experiments with MMOH.⁽¹¹⁾ Crystal annealing by careful cryostream control at SSRL induced a dramatic resolution increase in crystalline samples of ToMOH, a procedure that should prove useful in future studies. The resulting resolution increase in the ToMOH_{ox} X-ray structure has allowed us to

improve our view of the protein interior and diiron center, leading to an enhanced description of the protein scaffold, active site ligation, and core geometry.

Materials and Methods

Preparation of apo ToMOH. ToMOH was expressed and purified as previously described,(8) except that thioglycolate was not included in the purification buffers. Apo ToMOH was prepared as previously described for MMOH,(11) with slight modifications as described below. A 2.8 mL solution of 50 μ M ToMOH, 4 mM 1,10-phenanthroline, 1 mM methyl viologen, 100 mM NaCl, 5% (v/v) glycerol, and 25 mM MOPS at pH 7.0 was degassed by repeated vacuum purge /N₂ backfill cycles. A 20 μ L aliquot of 400 mM sodium dithionite was added to the ToMOH solution in an anaerobic chamber and the solution was incubated overnight at 4 °C. Apo protein was separated from the iron extraction reagents with an EconoPac 10DG (Bio-Rad) desalting column and contained 0.03 ± 0.01 Fe atoms per ToMOH dimer as determined by the ferrozine assay.(17)

Crystallization. Crystallization of Mn(II)-ToMOH was accomplished by the hanging drop vapor diffusion method at 20 °C, with slight modification of the previously described conditions,(8) as described below. Precipitant solution contained 100 mM HEPES at pH 7.5, 2.1 - 2.5 M (NH₄)₂SO₄, 2-4 % (v/v) polyethylene glycol 400, and 10 or 20 mM MnCl₂·4H₂O. Hanging drops contained 2 μ L 50 μ M apo ToMOH in 10 mM MES, 10% (v/v) glycerol, pH 7.1 buffer, 1 μ L precipitant solution, and 1 μ L microseed stock solution (native ToMOH microcrystals in 100 mM HEPES at pH 7.5, 2.3 M (NH₄)₂SO₄, 2% (v/v) polyethylene glycol 400 buffer). Microseeds of the native protein insignificantly comprise less than 0.1% of the final diffraction data set. Crystals did not form in the absence of MnCl₂, suggesting that active site metals stabilize ToMOH. Crystals of

native ToMOH were grown using conditions identical to those employed in obtaining Mn(II)-ToMOH crystals, with exception that $\text{MnCl}_2 \cdot 4\text{H}_2\text{O}$ was not present in the crystallization buffer, and the incubation temperature was 18 °C instead of 20 °C.

Crystal Annealing. Crystal annealing was conducted at the Stanford Synchrotron Radiation Laboratory (SSRL) on beam line 9-2 directly before data collection. Utilizing the flow control feature within the SSRL BLU-ICE(18) data collection software suite, native ToMOH crystals were subject to 5 s annealing times directly before and after irradiating with 10 s 12.7 keV X-ray pulse. The crystal used to obtain the native ToMOH data reported here saw the most dramatic increase in resolution, from 2.55 Å to 1.85 Å following one round of annealing. Using a cryo pin mounted thermocouple, analysis of this procedure indicated that the crystal temperature increases from 100 to 233 K before returning to 100 K during a 5 s annealing time period.

Data Collection and Refinement. Mn(II)-ToMOH X-ray diffraction data were collected at SSRL on beam line 9-2 at 100 K. Data were indexed, integrated, and scaled by using the HKL 2000 software suite,(19) and initial phases were determined by rigid body refinement molecular replacement in CNS.(20) Molecular replacement was conducted in CNS using the fully refined native ToMOH coordinates (PDB code 1T0Q) with coordinating ligand side chains and all non-protein atoms removed as a starting model. Subsequent models were built in XtalView(21) and refined using CNS. Data collection and refinement statistics can be found in Table 2.2.

X-ray diffraction data on native ToMOH were similarly collected at SSRL on BL 9-2 at 101K. Data were indexed, integrated, and scaled by using the HKL 2000 software suite. Phasing of the native ToMOH data was accomplished by using EPMR(22) and ToMOH coordinates (PDB code 1T0Q) in which all non-protein atoms and the side

chains of the coordinating ligands and residues I100, T201, N202, Q228, and S232 removed as a starting model. Subsequent models were built in Coot(23) and refined using REFMAC5(24) in CCP4.(25) MSDchem ideal coordinates, CNS parameters, and CNS topology files for the polyethylene glycol component (residue name P6G) were obtained from the HIC-Up database.(26)

Statistical and geometrical analyses of Mn(II)-ToMOH and 1.85 Å ToMOH_{ox} using PROCHECK(27) indicated that 99.8% of the residues in each structure occupied allowed regions of their respective Ramachandran plots. The complete data collection and refinement statistics can be found in Table 2.2.

Acknowledgement

This work was supported by a grant from the National Institutes of Health (GM32134 to S.J.L.). M.H.S. was supported under a NIH Biotechnology Training Grant. X-ray data were collected at the Stanford Synchrotron Radiation Laboratory (SSRL), funded by the Department of Energy (BES, BER) and the NIH (NCRR, NIGMS). Crystallographic coordinates are in the RCSB databank, accession numbers 2INC and 2IND. All figures were generated using PyMOL.(28)

Table 2.1. Angstrom distances between atoms and ions in the active sites of 2.15 Å resolution ToMOH_{ox} (PDB code 1T0Q), 1.85 Å resolution ToMOH_{ox}, 1.96 Å resolution MMOH_{ox} (PDB code 1FZ1), and 1.70 Å resolution MMOH_{ox} (PDB code 1MTY).

2.15 Å ToMOH _{ox}			1.85 Å ToMOH _{ox}			1.96 Å MMOH _{ox}			1.70 Å MMOH _{ox}		
Atom	Atom	Dist.	Atom	Atom	Dist.	Atom	Atom	Dist.	Atom	Atom	Dist.
Fe1	Fe2	3.1	Fe1	Fe2	3.1	Fe1	Fe2	3.2	Fe1	Fe2	3.1
Fe1	E104 OE1	2.2	Fe1	E104 OE1	2.1	Fe1	E114 OE1	2.0	Fe1	E114 OE1	1.9
Fe1	H137 ND1	2.1	Fe1	H137 ND1	2.3	Fe1	H147 ND1	2.2	Fe1	H147 ND1	2.1
Fe1	E134 OE2	2.1	Fe1	E134 OE2	2.2	Fe1	E144 OE2	2.2	Fe1	E144 OE2	2.1
Fe1	μOH1	2.2	Fe1	μOH1	2.1	Fe1	μOH1	1.8	Fe1	μOH1	1.7
Fe1	μOH2	2.2	Fe1	μOH2	2.4	Fe1	μOH2	2.7	Fe1	μOH2	2.3
Fe1	H2O1	2.0	Fe1	H2O1	2.3	Fe1	H2O1	2.4	Fe1	H2O1	2.3
Fe2	E197 OE2	1.9	Fe2	E197 OE2	1.8	Fe2	E209 OE2	2.2	Fe2	E209 OE2	1.9
Fe2	H234 ND1	2.2	Fe2	H234 ND1	2.2	Fe2	H246 ND1	2.2	Fe2	H246 ND1	2.2
Fe2	E231 OE1	2.3	Fe2	E231 OE1	2.2	Fe2	E243 OE1	2.3	Fe2	E243 OE1	2.0
Fe2	E134 OE1	2.2	Fe2	E134 OE1	2.1	Fe2	E144 OE1	2.5	Fe2	E144 OE1	2.5
Fe2	μOH-TG*	2.0	Fe2	μOH1	1.8	Fe2	μOH1	2.0	Fe2	μOH1	2.0
Fe2	μOH2	2.1	Fe2	μOH2	2.3	Fe2	μOH2	2.8	Fe2	μOH2	2.5
μOH1	E231 OE2	2.3	μOH1	E231 OE2	2.4	μOH1	E243 OE2	2.8	μOH1	E243 OE2	2.7
H2O1	E104 OE2	2.5	H2O1	E104 OE2	2.7	H2O1	E114 OE2	2.6	H2O1	E114 OE2	2.8

*Thioglycolate

Table 2.2. Data Collection and Refinement Statistics for 1.85Å resolution ToMOH_{ox} and 2.20 Å resolution Mn(II)-ToMOH.

	ToMOH _{ox}	Mn(II)-ToMOH
Data Collection		
Beamline	SSRL 9-2	SSRL 9-2
Wavelength (Å)	0.979	0.979
Space Group	P3 ₁ 21	P3 ₁ 21
Unit Cell Dimensions (Å)	182.6 x 182.6 x 68.1	182.5 x 182.5 x 67.8
Resolution Range (Å)	50 - 1.85	30 - 2.20
Total Reflections	1,064,847	385,987
Unique Reflections	99,695	64,565
Completeness (%) ^a	90.4 (78.9)	98.0 (91.9)
I/σ(I) ^a	55.8 (5.5)	17.5 (4.5)
R _{sym} (%) ^{a,b}	8.7 (43.0)	6.9 (43.1)
Phasing Method	Molecular Replacement	Molecular Replacement
Refinement		
R _{cryst} (%) ^c	19.5	21.5
R _{free} (%) ^d	22.9	24.4
No. Protein Atoms	7335	7346
No. Non-Protein Atoms	421	201
R.m.s Deviation Bond Length (Å)	0.018	0.007
R.m.s Deviation Bond Angles (deg)	1.70	1.26
Average B-value (Å ²)	41.8	50.8

^aValues in parentheses are for the highest resolution shell. ^bR_{sym} = $\sum_i \sum_{hkl} |I_i(hkl) - \langle I(hkl) \rangle| / \sum_{hkl} \langle I(hkl) \rangle$, where $I_i(hkl)$ is the *i*th measured diffraction intensity and $\langle I(hkl) \rangle$ is the mean intensity for the Miller index (hkl). ^cR_{cryst} = $\sum_{hkl} ||F_o(hkl)| - |F_c(hkl)|| / \sum_{hkl} |F_o(hkl)|$. ^dR_{free} = R_{cryst} for a test set of reflections (5% in each case).

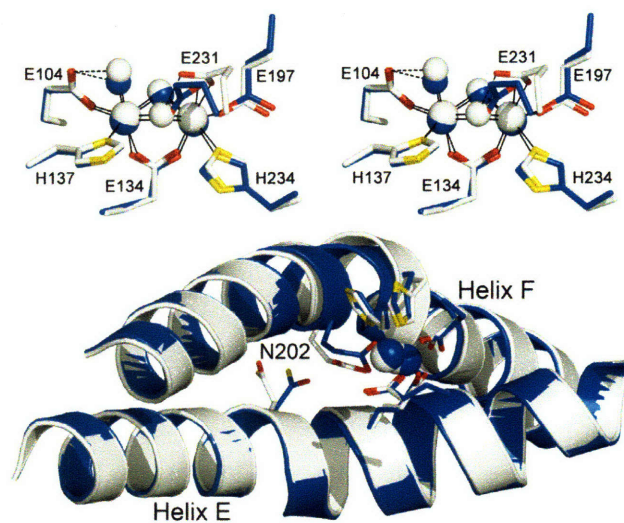


Figure 2.1. Overlaid 1.85 Å resolution ToMOHox (white) and 2.20 Å resolution Mn(II)-ToMOH (blue) structures. Top: stereo view of the active sites. Bottom: helices E and F, active site ligands and metals, and N202. Fe(III) ions, Mn(II) ions, and solvent ligands are represented as white or blue spheres. Side chain ligands are represented as sticks in white or blue (carbon), red (oxygen) and yellow (nitrogen).

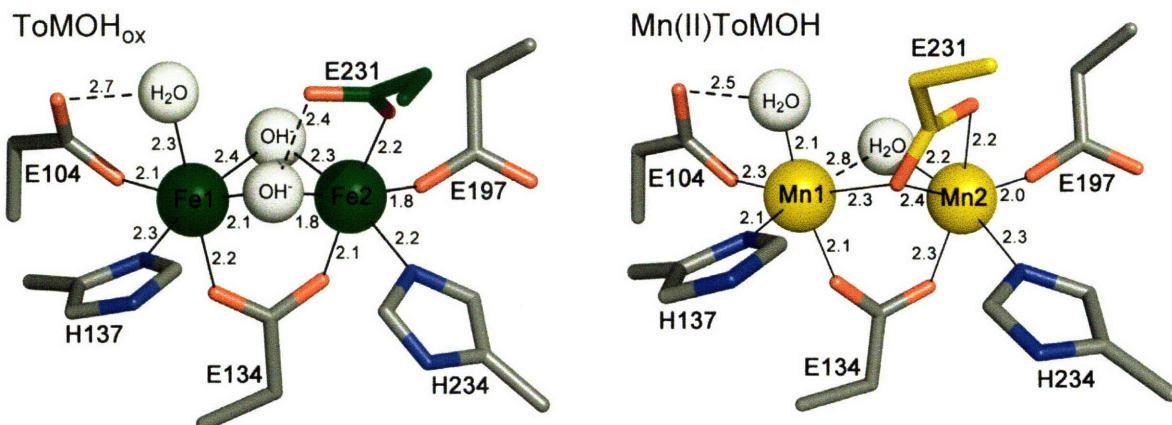


Figure 2.2. Active site geometries of 1.85 Å resolution ToMOH (left), and 2.20 Å resolution Mn(II)-ToMOH (right). All distances are provided in Å. Fe(III) ions, Mn(II) ions, and solvent ligands are represented as green, yellow, and white spheres, respectively. Side chain ligands are represented as sticks in grey (carbon), red (oxygen), and blue (nitrogen).

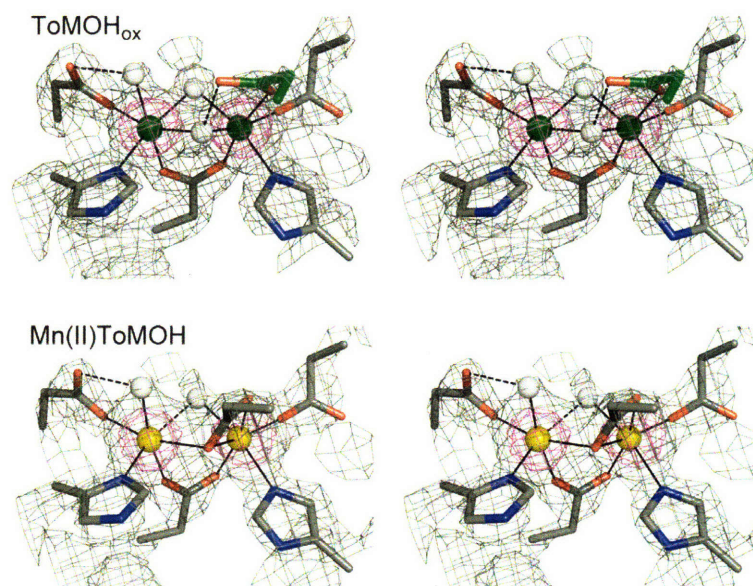


Figure 2.3. Active site density stereo images of 1.85 Å resolution ToMOH_{ox} (top), and 2.20 Å resolution Mn(II)-ToMOH (bottom). Fe(III) ions, Mn(II) ions, and oxygen atoms are represented as green, yellow, and white spheres, respectively. Side chain ligands are portrayed as sticks in grey (carbon), red (oxygen), and blue (nitrogen). $2F_o - F_c$ composite omit electron density maps contoured to 1σ and 3σ are shown in grey and magenta, respectively.

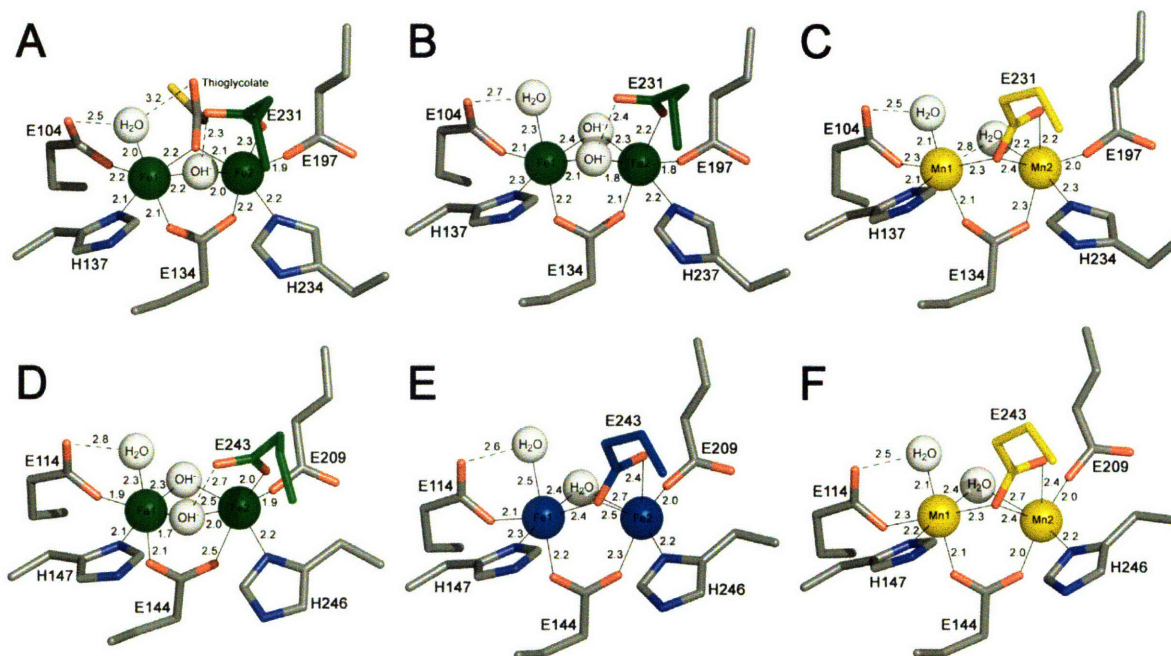


Figure 2.4. Active site geometries of (A) 2.15 Å resolution ToMOH_{ox} (PDB code 1T0Q), (B) 1.85 Å resolution ToMOH_{ox}, (C) 2.20 Å resolution Mn(II)-ToMOH, (D) 1.70 Å resolution MMOH_{ox} (PDB code 1MTY), (E) 2.15 Å resolution MMOH_{red} (PDB code 1FYZ), and (F) 2.30 resolution Å Mn(II)-MMOH (PDB code 1XMF). All distances are provided in angstroms. Fe(III) ions, Fe(II) ions, Mn(II) ions, and solvent ligands are represented as green, blue, yellow, and white spheres, respectively. Side chain ligands are represented as sticks in grey (carbon), red (oxygen), and blue (nitrogen).

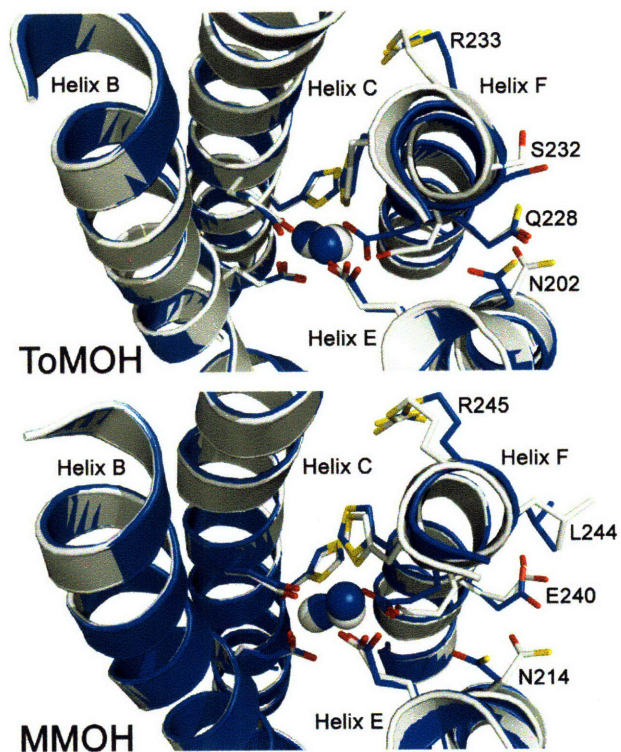


Figure 2.5. Metal center oxidation state dependent conformational shifts in ToMOH and MMOH. Top: 1.85 Å resolution ToMOH_{ox} (white) and 2.20 Å resolution Mn(II)-ToMOH (blue). Bottom: MMOH_{ox} (white; PDB code 1MTY) and MMOH_{red} (blue; PDB code 1FYZ). The metal-binding four-helix bundle, active site ligands and ions, and select side chains are shown as overlaid structures. Metal ions and helix backbones are represented as spheres and cartoons, respectively. Amino acid side chains are shown as sticks in blue/white (carbon), red (oxygen), and yellow (nitrogen).

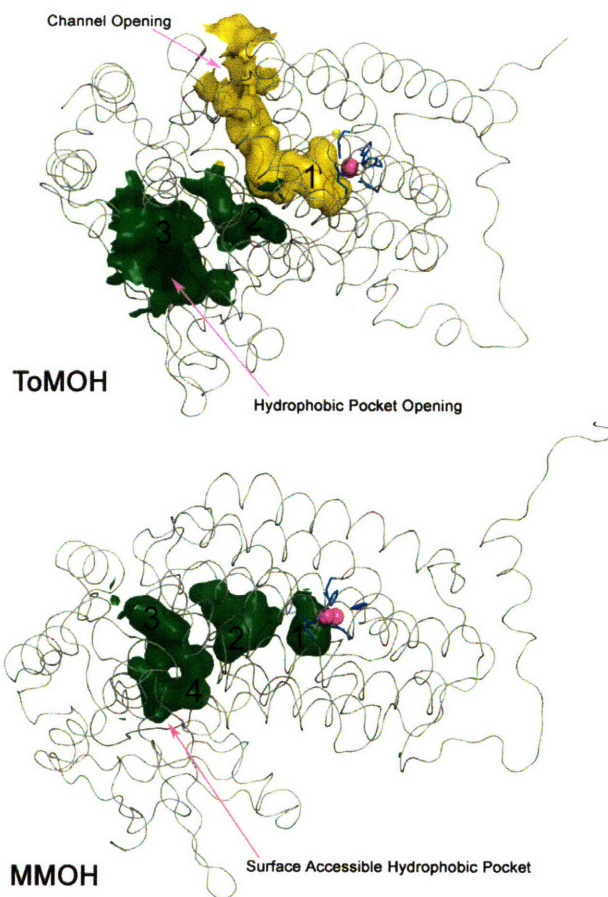


Figure 2.6. Interior surface renderings of ToMOH (top) and MMOH (bottom) α -subunits. ToMOH channel van der Waals surface is shown in yellow; hydrophobic pockets in ToMOH and MMOH are shown in green. Protein backbones (C_{α} trace) are represented as grey ribbons, active site iron atoms as magenta spheres, and side chain ligands as blue sticks.

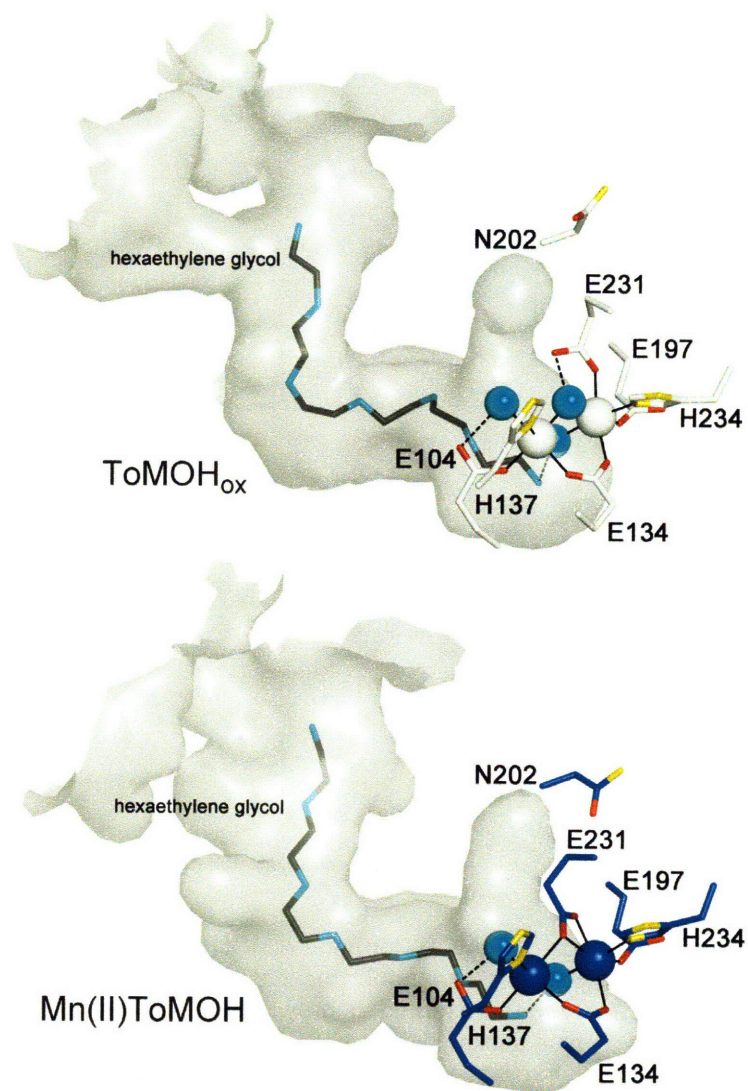


Figure 2.7. Hexaethylene glycol molecules modeled into the ToMOH channel in 1.85 Å ToMOH_{ox} (top) and 2.20 Å Mn(II)-ToMOH (bottom). Fe(III) ions (white), Mn(II) ions (blue), and solvent ligands (cyan) are represented as spheres. Hexaethylene glycol is shown as sticks in cyan (oxygen) and black (ethylene) in the channel interior. Ligating amino acid and N202 side chains are represented as sticks in white/blue (carbon), yellow (nitrogen), and red (oxygen); the protein interior van der Waals surface is shown in translucent grey.

References

- (1) Tshuva, E. Y.; Lippard, S. J. (2004) Synthetic Models for Non-Heme Carboxylate-Bridged Diiron Metalloproteins: Strategies and Tactics. *Chem. Rev.* **104**, 987-1011, and refs. cited therein.
- (2) (a) Notomista, E.; Lahm, A.; Di Donato, A.; Tramontano, A. (2003) Evolution of bacterial and archaeal multicomponent monooxygenases. *J. Mol. Evol.* **56**, 435-445. . (b) Leahy, J. G.; Batchelor, P. J.; Morcomb, S. M. (2003) Evolution of the soluble diiron monooxygenases. *FEMS Microbiol. Rev.* **27**, 449-479.
- (3) Merkx, M.; Kopp, D. A.; Sazinsky, M. H.; Blazyk, J. L.; Müller, J.; Lippard, S. J. (2001) Dioxygen activation and methane hydroxylation by soluble methane monooxygenase: a tale of two irons and three proteins. *Angew. Chem. Int. Ed.* **40**, 2782-2807.
- (4) Sazinsky, M. H.; Lippard, S. J. (2006) Coorelating Structure with Function in Bacterial Multicomponent Monooxygenases and Related Diiron Proteins. *Acc. Chem. Res.* **39**, 558-566.
- (5) (a) Murray, L. J.; García-Serres, R.; Naik, S.; Huynh, B. H.; Lippard, S. J. (2006) Dioxygen Activation at Non-Heme Diiron Centers: Characterization of Intermediates in a Mutant Form of Toluene/o-Xylene Monooxygenase Hydroxylase. *J. Am. Chem. Soc.* **128**, 7458-7459. . (b) Beauvais, L. G.; Lippard, S. J. (2005) Reactions of the Peroxo Intermediate of Soluble Methane Monooxygenase Hydroxylase with Ethers. *J. Am. Chem. Soc.* **127**, 7370-7378. . (c) Brazeau, B. J.; Lipscomb, J. D. (2000) Kinetics and Activation Thermodynamics of Methane Monooxygenase Compound Q Formation and Reaction with Substrates. *Biochemistry* **39**, 13503-13515. . (d) Valentine, A. M.; Stahl, S. S.; Lippard, S. J. (1999) Mechanistic studies of the reaction of reduced methane Monooxygenase hydroxylase with dioxygen and substrates. *J. Am. Chem. Soc.* **121**, 3876-3887. . (e) Shu, L.; Nesheim, J. C.; Kauffmann, K.; Münck, E.; Lipscomb, J. D.; Que, L., Jr. (1997) An Fe₂IVO₂ diamond core structure for the key intermediate Q of methane monooxygenase. *Science* **275**, 515-518. . (f) Liu, K. E.; Wang, D.; Huynh, B. H.; Edmondson, D. E.; Salifoglou, A.; Lippard, S. J. (1994) Spectroscopic detection of intermediates in the reaction of dioxygen with the reduced methane monooxygenase/hydroxylase from *Methylococcus capsulatus* (Bath). *J. Am. Chem. Soc.* **116**, 7465-7466. . (g) Lee, S. K.; Nesheim, J. C.; Lipscomb, J. D. (1993) Transient intermediates of the methane monooxygenase catalytic cycle. *J. Biol. Chem.* **268**, 21569-21577.
- (6) (a) Zhang, J.; Wallar, B. J.; Popescu, C. V.; Renner, D. B.; Thomas, D. D.; Lipscomb, J. D. (2006) Methane Monooxygenase Hydroxylase and B Component Interactions. *Biochemistry* **45**, 2913-2926, and refs. cited therein. . (b) Lountos, G. T.; Mitchell, K. H.; Studts, J. M.; Fox, B. G.; Orville, A. M. (2005) Crystal Structures and Functional Studies of T4moD, the Toluene 4-Monooxygenase Catalytic Effector Protein. *Biochemistry* **44**, 7131-7142. . (c) Scognamiglio, R.;

- Notomista, E.; Barbieri, P.; Pucci, P.; Dal Piaz, F.; Tramontano, A.; Di Donato, A. (2001) Conformational analysis of putative regulatory subunit D of the toluene/o-xylene-monooxygenase complex from *Pseudomonas stutzeri* OX1. *Protein Sci.* 10, 482-490. . (d) Walters, K. J.; Gassner, G. T.; Lippard, S. J.; Wagner, G. (1999) Structure of the soluble methane monooxygenase regulatory protein B. *Proc. Natl. Acad. Sci. U.S.A.* 96, 7877-7882. . (e) Liu, Y.; Nesheim, J. C.; Lee, S.-K.; Lipscomb, J. D. (1995) Gating effects of component B on oxygen activation by the methane monooxygenase hydroxylase component. *J. Biol. Chem.* 270, 24662-24665.
- (7) Cafaro, V.; Izzo, V.; Scognamiglio, R.; Notomista, E.; Capasso, P.; Casbarra, A.; Pucci, P.; Di Donato, A. (2004) Phenol hydroxylase and toluene/o-xylene monooxygenase from *Pseudomonas stutzeri* OX1: interplay between two enzymes. *Appl. Environ. Microbiol.* 70, 2211-2219, and refs. cited therein.
- (8) Sazinsky, M. H.; Bard, J.; Di Donato, A.; Lippard, S. J. (2004) Crystal Structure of the Toluene/o-Xylene Monooxygenase Hydroxylase from *Pseudomonas stutzeri* OX1: Insight Into the Substrate Specificity, Substrate Channeling, And Active Site Tuning of Multicomponent Monooxygenases. *J. Biol. Chem.* 279, 30600-30610.
- (9) (a) Rosenzweig, A. C.; Brandstetter, H.; Whittington, D. A.; Nordlund, P.; Lippard, S. J.; Frederick, C. A. (1997) Crystal structures of the methane monooxygenase hydroxylase from *Methylococcus capsulatus* (Bath): implications for substrate gating and component interactions. *Proteins* 29, 141-152. . (b) Elango, N.; Radhakrishnan, R.; Froland, W. A.; Wallar, B. J.; Earhart, C. A.; Lipscomb, J. D.; Ohlendorf, D. H. (1997) Crystal structure of the hydroxylase component of methane monooxygenase from *Methylosinus trichosporium* OB3b. *Protein Sci.* 6, 556-568. . (c) Rosenzweig, A. C.; Nordlund, P.; Takahara, P. M.; Frederick, C. A.; Lippard, S. J. (1995) Geometry of the soluble methane monooxygenase catalytic diiron center in two oxidation states. *Chem. Biol.* 2, 409-418.
- (10) Rosenzweig, A. C.; Frederick, C. A.; Lippard, S. J.; Nordlund, P. (1993) Crystal structure of a bacterial non-heme iron hydroxylase that catalyzes the biological oxidation of methane. *Nature* 366, 537-543.
- (11) Sazinsky, M. H.; Merx, M.; Cadieux, E.; Tang, S.; Lippard, S. J. (2004) Preparation and X-ray Structures of Metal-Free, Dicobalt and Dimanganese Forms of Soluble Methane Monooxygenase Hydroxylase from *Methylococcus capsulatus* (Bath). *Biochemistry* 43, 16263-16276.
- (12) Whittington, D. A.; Lippard, S. J. (2001) Crystal Structures of the Soluble Methane Monooxygenase Hydroxylase from *Methylococcus capsulatus* (Bath) Demonstrating Geometrical Variability at the Dinuclear Iron Active Site. *J. Am. Chem. Soc.* 123, 827-838.

- (13) Rudd, D. J.; Sazinsky, M. H.; Lippard, S. J.; Hedman, B.; Hodgson, K. O. (2005) X-ray Absorption Spectroscopic Study of the Reduced Hydroxylases of Methane Monooxygenase and Toluene/o-Xylene Monooxygenase: Differences in Active Site Structure and Effects of the Coupling Proteins MMOB and ToMOD. *Inorg. Chem.* **44**, 4546-4554.
- (14) Sazinsky, M. H.; Lippard, S. J. (2005) Product Bound Structures of the Soluble Methane Monooxygenase Hydroxylase from *Methylococcus capsulatus* (Bath): Protein Motion in the alpha-Subunit. *J. Am. Chem. Soc.* **127**, 5814-5825.
- (15) Zheng, H.; Lipscomb, J. D. (2006) Regulation of Methane Monooxygenase Catalysis Based on Size Exclusion and Quantum Tunneling. *Biochemistry* **45**, 1685-1692.
- (16) Whittington, D. A.; Rosenzweig, A. C.; Frederick, C. A.; Lippard, S. J. (2001) Xenon and Halogenated Alkanes Track Putative Substrate Binding Cavities in the Soluble Methane Monooxygenase Hydroxylase. *Biochemistry* **40**, 3476-3482.
- (17) Gibbs, C. R. (1976) Characterization and application of FerroZine iron reagent as a ferrous iron indicator. *Anal. Chem.* **48**, 1197-1201.
- (18) McPhillips, T. M.; McPhillips, S. E.; Chiu, H.-J.; Cohen, A. E.; Deacon, A. M.; Ellis, P. J.; Garman, E.; Gonzalez, A.; Sauter, N. K.; Phizackerley, R. P.; Soltis, S. M.; Kuhn, P. (2002) Blu-Ice and the Distributed Control System: software for data acquisition and instrument control at macromolecular crystallography beamlines. *J. Synchrotron Rad.* **9**, 401-406.
- (19) Otwinowski, Z.; Minor, W. (1997) Processing of x-ray diffraction data collected in oscillation mode. *Method. Enzymol.* **276**, 307-326.
- (20) Brünger, A. T.; Adams, P. D.; Clore, G. M.; DeLano, W. L.; Gros, P.; Grosse-Kunstleve, R. W.; Jiang, J.-S.; Kuszewski, J.; Nilges, M.; Pannu, N. S.; Read, R. J.; Rice, L. M.; Simonson, T.; Warren, G. L. (1998) Crystallography & NMR System: a new software suite for macromolecular structure determination. *Acta Crystallogr. D* **54**, 905-921.
- (21) McRee, D. E. (1999) XtalView/Xfit-A Versatile Program for Manipulating Atomic Coordinates and Electron Density. *J. Struct. Biol.* **125**, 156-165.
- (22) Kissinger, C. R.; Gehlhaar, D. K.; Fogel, D. B. (1999) Rapid automated molecular replacement by evolutionary search. *Acta Crystallogr. D* **55**, 484-491.
- (23) Emsley, P.; Cowtan, K. (2004) Coot: model-building tools for molecular graphics. *Acta Crystallogr. D* **60**, 2126-2132.

- (24) Murshudov, G. N.; Vagin, A. A.; Dodson, E. J. (1997) Refinement of macromolecular structures by the maximum-likelihood method. *Acta Crystallogr. D* 53, 240-255.
- (25) Anonymous (1994) The CCP4 suite: programs for protein crystallography. *Acta Crystallogr. D* 50, 760-763.
- (26) Kleywegt, G. J.; Jones, T. A. (1998) Databases in protein crystallography. *Acta Crystallogr. D* 54, 1119-31.
- (27) Laskowski, R. A.; MacArthur, M. W.; Moss, D. S.; Thornton, J. M. (1993) PROCHECK: A program to check the stereochemical quality of protein structures. *J. Appl. Cryst.* 26, 283-291.
- (28) DeLano, W. L. *The PyMOL Molecular Graphics System*, DeLano Scientific: San Carlos, CA, USA, 2002.

CHAPTER 3

X-ray Crystallographic Characterization of Various Mutants of the Conserved Residues T201 and N202 in the α -subunit of Toluene/*o*-Xylene Monooxygenase Hydroxylase from *Pseudomonas* sp. OX1

Introduction

The toluene monooxygenases (TMOs) are a unique subset of BMMs that perform regio- and enantio-selective hydroxylation and epoxidation reactions on aromatic substrates.(1) TMOs are also special among BMMs in that they employ a Rieske protein component in addition to the Fe_2S_2 and ferredoxin containing reductase utilized in all BMMs.(2) Moreover, it has been established that electrons are transferred to TMO hydroxylases from NADH by the interaction with the Rieske protein, following its reduction by the NADH-oxidizing Fe_2S_2 reductase protein.(1) Due to the difference in the TMO component interaction scheme with respect to other BMMs, it is evident that the TMO hydroxylase reduction may, therefore, deviate significantly in the mechanism of protein interaction from that of other BMMs.

In addition to receiving electrons from the reductase protein(s) in BMMs and forming oxygenated intermediates after dioxygen binding, the activity of the hydroxylase requires proton translocation into the diiron site cavity. The movement of protons into the active site coordination environment, presumably in the form of H_3O^+ cations,(3) is therefore a subject of interest in the study of BMMs. Results from experimental work on heme-containing cytochrome P450 enzymes(4, 5) and the carboxylate bridged diiron enzyme Δ^9 desaturase(6) have indicated that a conserved threonine in the active site cavity is responsible for proton transfer to the metal center during catalysis. A similarly positioned and strictly conserved threonine is located in the active site cavity of BMM hydroxylases near the protein surface, and is in fact the only polar residue found in the hydrophobic environment surrounding the diiron site in the three BMM hydroxylases crystallographically characterized to date.(2) Moreover, theoretical studies of soluble

methane monooxygenase further implicate this conserved residue in the proton transfer step during catalysis.

The working hypothesis that the conserved threonine in the active site of BMM was generated primarily because of its position with respect to the diiron site and protein surface, and also by the physical properties of its side chain (ie. pK_a , polarity, volume, and geometry). Prior to the current work, this conserved threonine was investigated in the toluene-4-monooxygenase (T4MO) TMO system from *Pseudomonas mendocina* KR1, by site-directed mutagenesis and a series of solution biochemical studies.⁽⁷⁾ Studies of the T4MO threonine mutants indicated that the wild-type residue is not important for hydrocarbon catalysis in that system, but did influence the T4MO hydroxylation regiospecificity. These studies were limited, however, to include only steady-state activity, coupling efficiency, and product distribution analyses, the results of which may not completely reflect the influence of this conserved residue on TMO catalysis.

The conserved threonine in the active site cavity of BMMs is directly adjacent to an equally conserved asparagine on the surface of the hydroxylase, just ~ 12 Å from the diiron site.⁽²⁾ Recent structural work on the dimanganese(II) form of ToMOH, an analog of the diferrous form (Chapter 2), revealed that this asparagine is among a group of surface exposed residues that undergo active site oxidation state dependent conformational shifts. The shift adopted by this strictly conserved residue is most notable because it moves the carboxamide side chain from bulk solvent exposure in the oxidized form of the enzyme to a position in which it is buried between two of the iron-ligating helices in the dimanganese(II) form. In the latter, it points toward the diiron

site and is relatively less available for inter-protein hydrogen-bond formation. This movement was previously observed for the analogous asparagine residue in structures of MMOH,(8) thereby providing further evidence for the generalization that the conserved residue is important for catalysis and may be critical in mediating protein component interactions.

Following the attainment of these results in ToMOH and MMOH, the structure of the hydroxylase-regulatory protein complex in the PH system was determined (Appendix 1). It revealed the presence of an inter-protein hydrogen bond between the conserved asparagine side chain and that of an equally conserved serine residue on the regulatory protein surface. Collectively, these observations implicate a role for the conserved asparagine residue in catalysis and the hydroxylase-regulatory component interaction, with the added notion that there may be a relationship between active site oxidation state and regulatory protein binding events.

The universally conserved BMM hydroxylase α -subunit threonine and asparagine residues (T201 and N202, respectively) are individually under current investigation in the ToMO system through site-directed mutagenesis and subsequent biochemical analysis.(9) The results of these studies will eventually be compared with identical analyses of the wild-type hydroxylase, and additionally in the case of the threonine mutants, with that from the aforementioned analogous work on the T4MO system. To help with interpretation of the solution biochemical studies of the mutant ToMOH proteins, the author has structurally characterized the glycine, serine, and valine mutants of T201, as well as the alanine, aspartate, leucine, and tyrosine mutants of N202, by X-ray crystallography. These structural results are described herein.

Experimental

Crystallization. Hydroxylase protein samples for crystallization were prepared as described previously.(9) Protein crystallization and cryogenic sample preparation for X-ray diffraction data collection on the ToMOH mutants were also conducted as previously described, including the concentrations of protein and precipitant solution components and microseeding technique used (Chapter 2).

Diffraction Data Collection and Crystal Structure Determination. X-ray diffraction data were collected at 100K at SSRL on BL 9-2 (N202L) and BL 11-1 (T201G, T201S, T201V, N202A, and N202Y) as well as at APS on the NE-CAT 8-BL (N202D). Data collected at SSRL were obtained using the BLU-ICE data collection software suite(10) and that collected at APS were obtained using the CONSOLE data collection software suite. In all cases diffraction data indexing, integration, and scaling were performed in HKL2000.(11) Similarly, molecular replacement phasing was accomplished for all mutant proteins by using EPMR(12) and 1.85 Å resolution ToMOH coordinates (PDB code 2INC) in which all non-protein atoms and the side chains of the coordinating ligands and residues I100, T201, N202, Q228, S232, and R233 removed in the starting model. Model fitting and refinement were performed using Coot(13) and REFMAC5(14) in CCP4(15), respectively. Final rounds of refinement as well as the calculation of simulated annealing composite omit maps were conducted using CNS.(16) MSDchem ideal coordinates as well as CNS topology and parameter files for glycerol and PEG heterocompounds were obtained from the HIC-UP database (residue codes GOL and

P6G, respectively).(17) Proper backbone and side chain geometries were confirmed with PROCHECK.(18)

Results and Discussion

Crystallization. Crystallization time for all ToMOH mutants matched that observed for the native protein when seeded with small quantities of high-quality native ToMOH crystal fragments, at 24 – 48 hours (Chapter 2). Moreover, the size and morphology of the mutant protein crystals also matched that for the native protein, with approximate dimensions of 0.5 x 0.5 x 0.5 mm and an octahedral shape (Chapter 2).

Diffraction Data Collection and Crystal Structure Determination. Diffraction data collection and processing on the ToMOH T201G, T201S, and T201V mutants resulted in the 2.10, 2.90, and 1.90 Å resolution data sets, respectively, with statistics reported in Tables 3.1, 3.2, and 3.3. That for the ToMOH N202A, N202D, N202L, and N202Y resulted in the 2.36, 2.70, 2.40, and 1.95 Å resolution data sets, respectively, with statistics reported in Tables 3.1, 3.2, and 3.4. Global folds of the α -, β -, and γ -subunits of the mutant hydroxylase structures obtained by molecular replacement phasing of the individual data sets were isomorphous with the native protein, and all exhibit hydroxylase C $_{\alpha}$ -to-C $_{\alpha}$ atom RMSDs of < 0.3 Å³ with respect to wild-type (PDB Code 2INC). Similarly, diiron site coordination and geometry in all of the mutants are essentially identical to that in the wild-type ToMO (Chapter 2) and MMO(19) hydroxylases (Figures 3.1, 3.2, and 3.3). The previously observed (Chapter 2) bound PEG-400 fragments from the crystallization buffer asymmetrically bridging the iron atoms in place of one of the hydroxo ligands, delineates the channel pathway toward

the protein surface in all cases as well.

Structural Effects of the T201 Mutations. The mutant T201X side chains and surrounding residue orientations are clearly evident in the composite omit map electron density (Figure 3.4). Due to this, the structural effects of the various mutations are readily observed upon analysis of the three structures. The results of said analysis indicate that the protein backbone geometry at and in the vicinity of the mutated side chain is not perturbed in any of the crystallographically characterized T201 mutants. Conformations of the neighboring N202 and Q228 residues, however, deviate from their respective orientations in the wild-type protein, with exception of that for N202 in the T201V mutant (Figure 3.5). In wild-type ToMOH, the T201 side chain is held in position via hydrogen-bonding interactions with the backbone carbonyl oxygen atoms of residues E197 and T201, as well as with the backbone nitrogen of N202. This effectively also locks the threonine side chain methyl group in a non-flexible position in the active site cavity. The orientation of the serine hydroxyl group in ToMOH T201S matches that for the threonine hydroxyl group in the wild-type protein through hydrogen-bonding interactions identical to that observed in the native protein.

In ToMOH T201G and T201V, side chain hydrogen-bonding interactions with the surrounding backbone are not possible due to the lack of a hydroxyl group on the mutant side chains. ToMOH T201G completely lacks a side chain in position 201, which results in a larger and slightly more hydrophobic active site cavity. The valine side chain, on the other hand, has approximately the same shape and size as the threonine side chain so the mutation does not result in a significant change in the overall size of the active site cavity but does cause a marked decrease in the local hydrophobicity in

the region of residue 201. Presumably as a result of the polarity difference between the wild type and mutant side chains in ToMOH T201V is a notable $\sim 90^\circ$ rotation about the C_α - C_β bond in the orientation of the valine side chain with respect to the orientation of the threonine side chain in wild-type ToMOH. The valine side chain is hydrophobic, and adopts this orientation to avoid the polar environment that the serine and threonine side chains occupy in the wild-type and T201S proteins, and because the surrounding space within the active site cavity sterically allows it. Regarding the morphology of the active site cavity, position 201 in the ToMOH α -subunit exhibits a significant influence on its size and shape, as indicated by space filling views and van der Waals surface depictions of this region in the mutant proteins (Figures 3.6 and 3.7, respectively). Of particular note is the effect of the mutations on the PHH-like pore region above the diiron site,(20) which is significantly occluded in ToMOH T201S because of the rotamer position adopted by N202 in that structure, and similarly in ToMOH T201V because of the orientation adopted by the mutated side chain for the reasons discussed above.

Structural Effects of the N202 Mutations. As in the case of the T201 mutations, the orientations of the mutant N202X side chains and surrounding residues are clearly indicated in the composite omit map electron density (Figure 3.8). Analysis of the resulting models indicates significant alterations on the surface of the mutant hydroxylase α -subunits with respect to wild-type as well as malformed hydrogen bonding interactions with the surrounding residues (Figures 3.9 and 3.10). In native ToMOH, the hydrogen bonding interaction between N202 and Q228 occurs between the carboxamide side chains of the two residues as well as between the Q228 side chain and the N202 backbone carbonyl oxygen. In the ToMOH N202A and N202Y mutants,

hydrogen-bonding between the side chains is not possible, so the resulting hydrogen bond between the Q228 carboxamide group and the N202X backbone is shorter, which actually pulls helix F slightly closer to helix E, causing the pore region above the diiron to constrict significantly (Figure 3.10). The same hydrogen bonding shift in the N202X-Q228 interaction takes place in Mn(II) reconstituted ToMOH and ToMOH N202L but the pore remains open because of the 202 side chain in these structures is sterically blocking its closure. In the ToMOH N202D mutant, the pore is constricted as in the case of the N202A and N202Y mutants, but in that case it is due to stronger interactions between Q228 and the D202 side chain resulting from its full negative charge.

Conclusions

The structure of the ToMOH protein is most notably distinguished from that of the well-characterized MMOH in that the hydroxylase γ -subunits exhibit a different overall fold and position with respect to α - and β -subunits when compared to MMOH, and the presence of large solvent accessible channel that traverses a pathway in the α -subunit between helices B and E from the active site pocket to the protein surface (Figure 1.4).(21) The difference in the γ -subunit fold and orientation in ToMOH with respect to that of MMOH in terms of its influence on the hydroxylase function is only beginning to be understood(22) and is not likely relevant to the current discussion. The presence of the solvent-accessible channel in ToMOH, on the other hand, is undoubtedly of functional significance in the activity of the ToMO system relative to other BMMs such as MMOH. This structural feature in ToMOH probably affects the formation of active site intermediates relative to those in MMOH (for example), because of the increased

availability of bulk solvent to the active site cavity.(23) Moreover, the residues lining the ToMOH channel are known to influence hydrocarbon substrate oxidation regiospecificity on the basis of mutagenesis work.(24, 25) In light of findings from the aforementioned mutagenesis studies, and detailed analysis of the channel geometry (Chapter 4), it is logical to conclude that the identities and orientations of the various the channel-lining residues effectively steer the substrate as it approaches the diiron site. Residue 201 in the ToMOH α -subunit is among those that contribute to the ToMOH channel surface (Figures 3.5 and 4.12). Furthermore, it sits directly at the interface between the active site pocket and the remainder of the channel pathway to the protein surface. Regardless of the fact that it may not be the primary function of the conserved threonine residue in ToMO, these observations strongly implicate the side chain orientation in influencing substrate hydroxylation regiospecificity.

Insight into potential effects of the various T201 and N202 mutations on interactions between the hydroxylase and component proteins, as well as that on electron and proton transfer is provided by the current structural results. Of particular note are the various orientations of the N202 and Q228 side chains in these structures, which differ from those of wild-type ToMOH structures in most of the mutants (Figure 3.4). These two residues, which are also conserved in BMMs, are located on the protein surface in close vicinity to residue 201, and both are known to change conformation in concert with active site reduction and the associated Fe² coordination carboxylate shift in ToMOH and MMOH (Chapter 1 and Chapter 2). Moreover, the strictly conserved asparagine has already been implicated in component interactions and/or proton transfer in BMMs, upon observing the conformational shift that it adopts when the

oxidized and reduced structures of MMOH(8), and later ToMOH (Chapter 2), were compared. The results of the alternate N202 and Q228 side chain conformations on the structure of the mutant proteins are malformed intra-protein residue-residue hydrogen bonding interactions and surface topologies relative to wild-type. Considering this and the previously suggested involvement of the conserved asparagine in electron/proton transfer event in BMMs, it is not unreasonable to conclude that the effects of the T201 and N202 mutations on the orientations and hydrogen-bonding schemes adopted by Q228 may be responsible for any electron transfer and substrate turnover reactivity trends observed for the mutant proteins relative to wild-type in future biochemical studies.

Table 3.1. Percentages of Residues in Ramachandran Plot Favored, Allowed, and Outlier Regions

Structure	Favored Regions	Allowed Regions	Outlier Regions	Resolution
<i>Native ToMOH</i>	97.4	2.2	0.3	1.85
<i>Mn(II)-ToMOH</i>	95.5	4.3	0.2	2.20
<i>ToMOH I100W</i>	92.4	6.9	0.8	2.10
<i>ToMOH T201G</i>	97.1	2.8	0.1	2.10
<i>ToMOH T201S</i>	94.4	4.8	0.8	2.90
<i>ToMOH T201V</i>	97.4	2.5	0.1	1.90
<i>ToMOH N202A</i>	94.0	4.9	1.0	2.36
<i>ToMOH N202D*</i>	84.9	12.8	2.2	2.70
<i>ToMOH N202L</i>	93.7	5.4	0.9	2.40
<i>ToMOH N202Y</i>	97.0	2.8	0.2	1.95
<i>Xe-PHH</i>	98.0	1.9	0.1	1.95

*Non-ideal geometry statistics in this structure are the result of low resolution, and outliers are heavily concentrated in the protein γ -subunit.

Table 3.2. B-factors for Metal Ions and Non-Protein Ligands in Structures of ToMOH

	<i>Average B-factors (\AA^2) in ToMOH Structures</i>								
	<i>Native</i>	<i>Mn(II)</i>	<i>T201G</i>	<i>T201S</i>	<i>T201V</i>	<i>N202A</i>	<i>N202D</i>	<i>N202L</i>	<i>N202Y</i>
All Atoms	41.7	50.7	46.7	24.1	52.1	48.6	45.6	42.4	56.1
Fe 1	34.8	-	31.3	24.3	33.6	69.3	57.2	52.7	44.4
Fe 2	36.5	-	37.4	29.5	30.3	63.8	62.2	55.6	39.0
Mn 1	-	40.4	-	-	-	-	-	-	-
Mn 2	-	39.0	-	-	-	-	-	-	-
PEG 1 ^a	70.4	81.1	68.7	58.5	66.7	57.8 ^b	89.3	87.5	77.7
PEG 2	-	-	60.9	54.4	54.0	-	-	-	74.3
PEG 3	-	-	-	-	80.1	-	-	-	-
PEG 4	-	-	-	-	82.9	-	-	-	-
Glycerol 1	-	-	65.2	45.3	60.7	82.0	65.9	74.7	65.5
Glycerol 2	-	-	53.1	40.2	48.3	81.3	49.7	68.8	61.8
Glycerol 3	-	-	-	30.0	43.6	63.9	55.5	63.6	48.6
Glycerol 4	-	-	-	-	45.5	71.5	81.7	71.0	48.2
Glycerol 5	-	-	-	-	-	91.7	85.7	81.5	71.6
Glycerol 6	-	-	-	-	-	77.5	74.8	-	65.8
Glycerol 7	-	-	-	-	-	91.3	-	-	67.3

^aPEG 1 is the polyethylene glycol fragment that is bound in the interior of the ToMOH channel.

^b50% occupancy.

Table 3.3. X-ray Data Collection and Refinement Statistics for ToMOH T201G, T201S, and T201V

	ToMOH T201G	ToMOH T201S	ToMOH T201V
Data Collection			
Beamline	SSRL 11-1	SSRL 11-1	SSRL 11-1
Wavelength (Å)	0.979	0.979	0.979
Space Group	P3 ₁ 21	P3 ₁ 21	P3 ₁ 21
Unit cell dimensions (Å)	183.0 x 183.0 x 68.7	182.8 x 182.8 x 68.9	182.9 x 182.9 x 68.6
Resolution range (Å)	50.0 - 2.10	50.0 - 2.90	50.0 - 1.90
Total Reflections	1151797	223666	1801358
Unique Reflections	74572	29616	98258
Completeness (%)*	96.7 (92.9)	100 (99.9)	95.5 (84.6)
I/σ(I)	30.8 (3.8)	22.7 (7.7)	36.8 (2.9)
R _{sym} (%)	10.3 (56.0)	10.4 (31.2)	9.8 (66.0)
Refinement			
R _{cryst} (%)	22.3	18.4	20.6
R _{free} (%)	23.5	22.5	21.8
Average B-value (Å ²)	46.7	24.1	52.1
RMSD Bond Length (Å)	0.007	0.008	0.006
RMSD Bond Angles (°)	1.36	1.54	1.36
No. Protein Atoms	7335	7337	7338
No. Non-Protein Atoms	248	159	699
Fe Atoms	2	2	2
Water Molecules	196	101	597
PEG-400 Fragments	2	2	4
Glycerol Molecules	2	3	4
RMSD to Wild-Type ToMOH	0.136	0.170	0.114
PDB Code	XXXX	XXXX	XXXX

Table 3.4. X-ray Data Collection and Refinement Statistics for ToMOH N202A, N202D, N202L, and N202Y

	ToMOH N202A	ToMOH N202D	ToMOH N202L	ToMOH N202Y
Data Collection				
Beamline	SSRL 11-1	APS NE-CAT 8-BM	SSRL 11-1	SSRL 9-2
Wavelength (Å)	0.979	0.983	0.979	0.979
Space Group	P3 ₁ 21	P3 ₁ 21	P3 ₁ 21	P3 ₁ 21
Unit cell dimensions (Å)	182.6 x 182.6 x 67.7	182.5 x 182.5 x 67.0	182.5 x 182.5 x 67.7	182.4 x 182.4 x 68.0
Resolution range (Å)	50.0 - 2.36	50.0 - 2.70	50.0 - 2.40	50.0 - 1.95
Total Reflections	1092212	214302	1018546	451216
Unique Reflections	53293	35039	49725	91024
Completeness (%)*	99.3 (97.4)	98.8 (97.3)	98.0 (90.8)	96.6 (89.5)
I/σ(I)	69.4 (6.1)	16.9 (3.6)	57.5 (6.5)	35.0 (3.7)
R _{sym} (%)	9.8 (49.5)	7.6 (30.9)	10.9 (44.3)	6.5 (45.7)
Refinement				
R _{cryst} (%)	23.7	25.7	22.3	22.5
R _{free} (%)	26.1	29	24.8	24
Average B-value (Å ²)	48.6	45.6	42.4	56.1
RMSD Bond Length (Å)	0.008	0.01	0.008	0.006
RMSD Bond Angles (°)	1.50	1.71	1.46	1.31
No. Protein Atoms	7335	7338	7338	7342
No. Non-Protein Atoms	161	129	184	577
Fe Atoms	2	2	2	2
Water Molecules	98	72	115	495
PEG-400 Fragments	1	1	1	2
Glycerol Molecules	7	6	5	7
RMSD to Wild-Type ToMOH	0.184	0.291	0.172	0.107
PDB Code	XXXX	XXXX	XXXX	XXXX

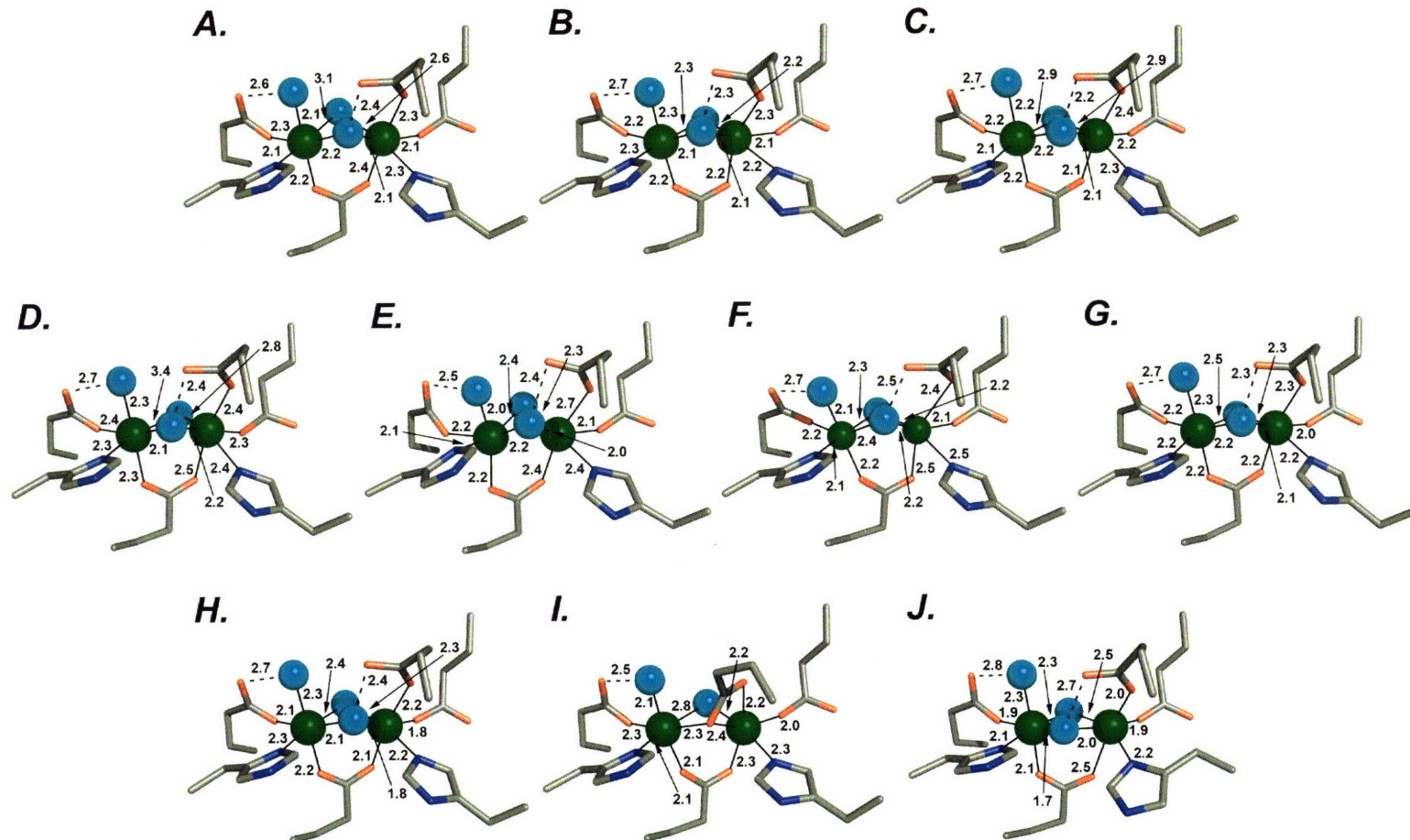


Figure 3.1. Active site coordination and geometry in ToMOH T201G (A), ToMOH T201S (B), ToMOH T201V (C), ToMOH N202A (D), ToMOH N202D (E), ToMOH N202L (F), and ToMOH N202Y (G), as compared to that in wild-type ToMOH (H), Mn(II)-reconstituted ToMOH (I), and wild-type MMOH (J). Active site metal ions are shown as green spheres, solvent and PEG terminal oxygen derived ligands as cyan spheres, and amino acid side chain ligands as sticks in grey (carbon), blue (nitrogen), and red (oxygen). Interatomic distances are provided in angstroms.

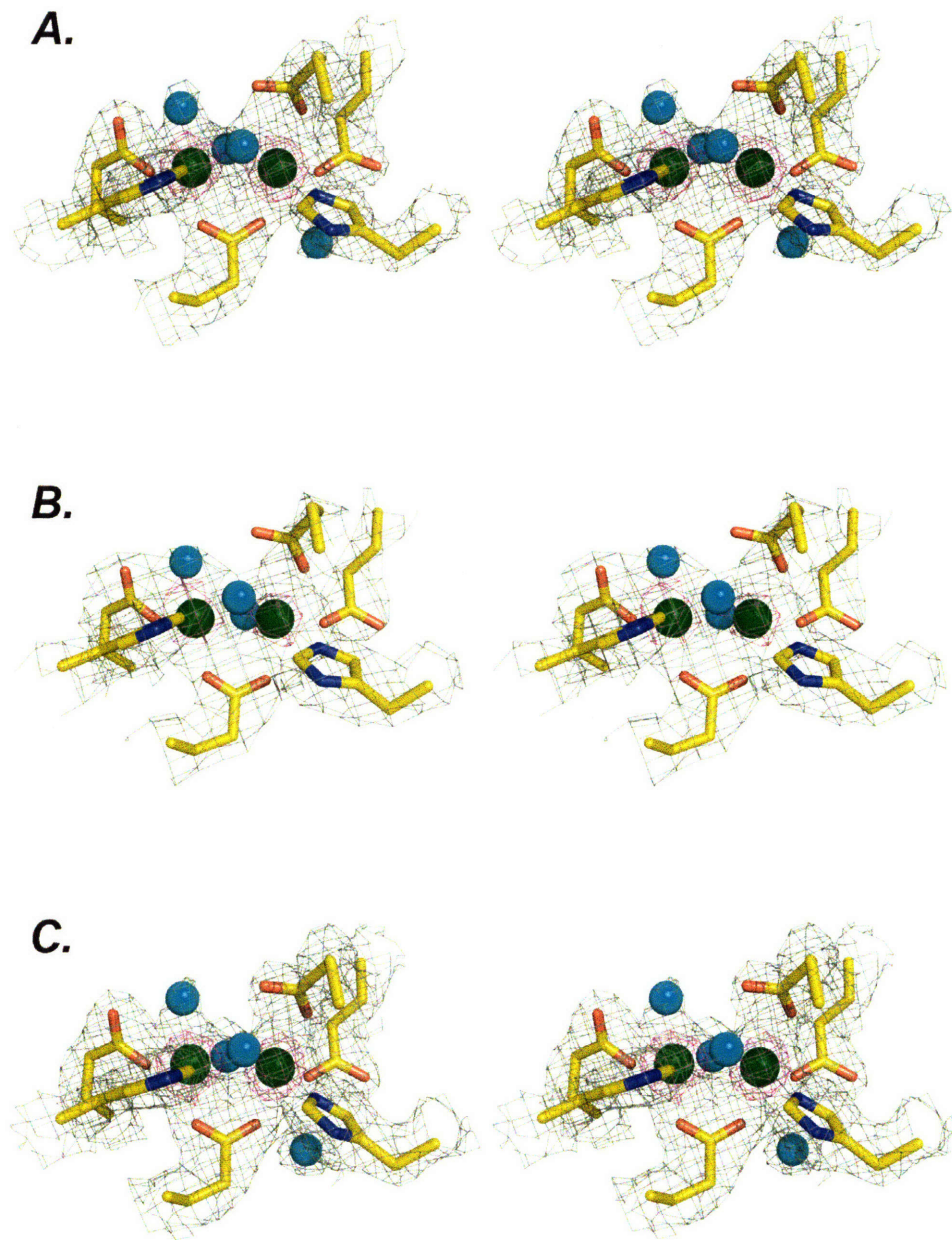


Figure 3.2. Stereo views of the active site electron density in ToMOH T201G (A), ToMOH T201S (B), and ToMOH T201V (C). Iron atoms are shown as green spheres. Solvent derived ligands, the coordinated oxygen atom from the PEG fragment, and a water molecule in hydrogen bond contact with E104 (A and C only) are all shown as cyan spheres. Amino acid side chain ligands are represented as sticks in yellow (carbon), blue (nitrogen), and oxygen (red). Composite omit map electron density is shown in magenta (contoured to 5.0 sigma) and grey (contoured to 1.5 sigma).

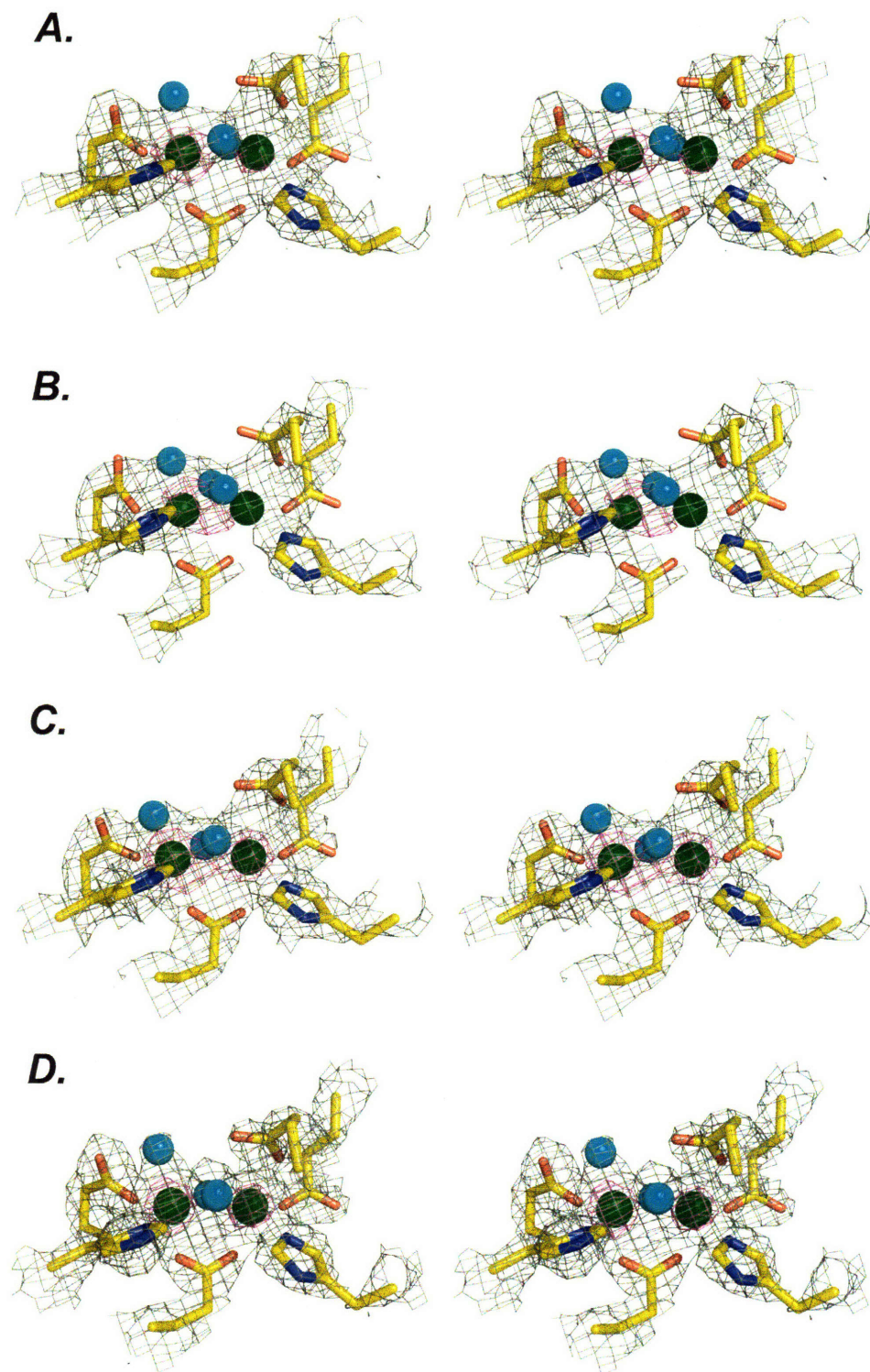


Figure 3.3. Stereo views of the active site electron density in ToMOH N202A (A), ToMOH N202D (B), ToMOH N202L (C), and ToMOH N202Y (D). Iron atoms are shown as green spheres. Solvent derived ligands and coordinated oxygen atoms from PEG fragments are shown as cyan spheres. Amino acid side chain ligands are represented as sticks in yellow (carbon), blue (nitrogen), and oxygen (red). Composite omit map electron density is shown in magenta (contoured to 5.0 sigma) and grey (contoured to 1.0 sigma).

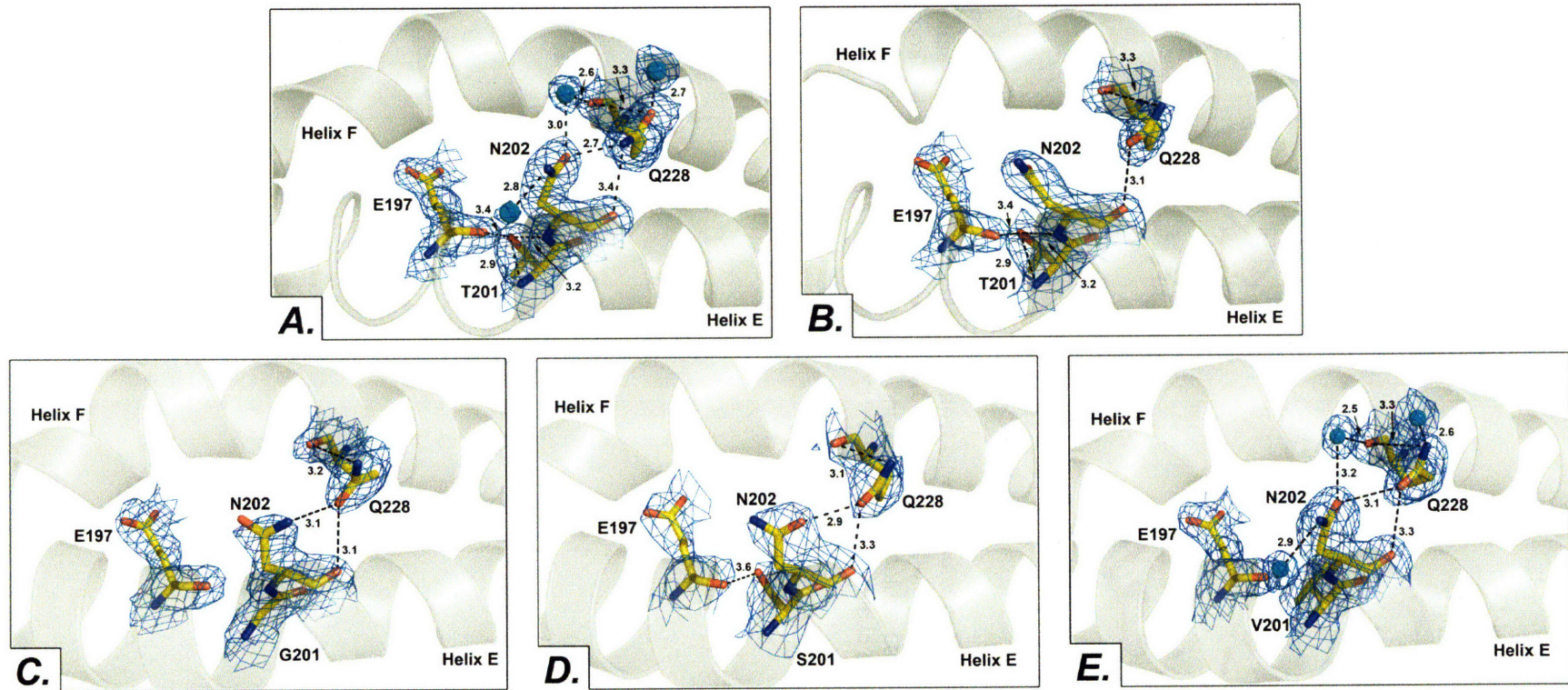


Figure 3.4. Views of the various side chain conformations, hydrogen-bonding interactions, and electron density for residues E197, T201X, N202, and Q228 from ToMOH T201G (C), ToMOH T201S (D), and ToMOH T201V (E) as compared to wild-type (A) and Mn(II)-reconstituted ToMOH (B). Iron ligating and surface exposed helices E and F are shown as translucent grey ribbons. Residues E197, T201X, N202, and Q228 are represented as sticks in yellow (carbon), blue (nitrogen), and oxygen (red). Water molecules are shown as cyan spheres. Distances are provided in angstroms. Composite omit map electron density maps contoured to 1.0 sigma are shown in light blue.

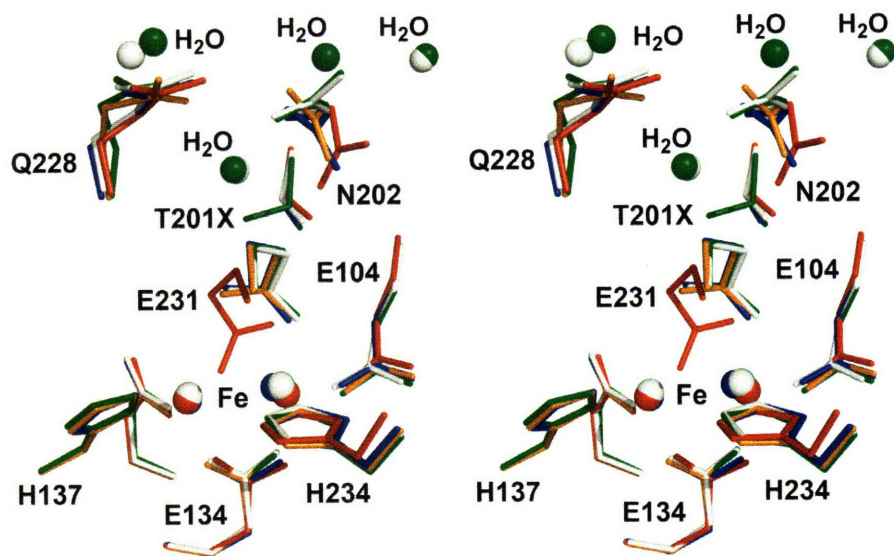


Figure 3.5. Stereo view of the overlaid structures of wild-type ToMOH (white), Mn(II)-reconstituted ToMOH (red), ToMOH T201G (orange), ToMOH T201S (blue), and ToMOH T201V (green). Iron atoms, and water molecules in hydrogen-bond contact with N202 and Q228 are depicted as spheres. Amino acid side chain ligands as well as the side chains of residues T201X, N202, and Q228 are shown as sticks.

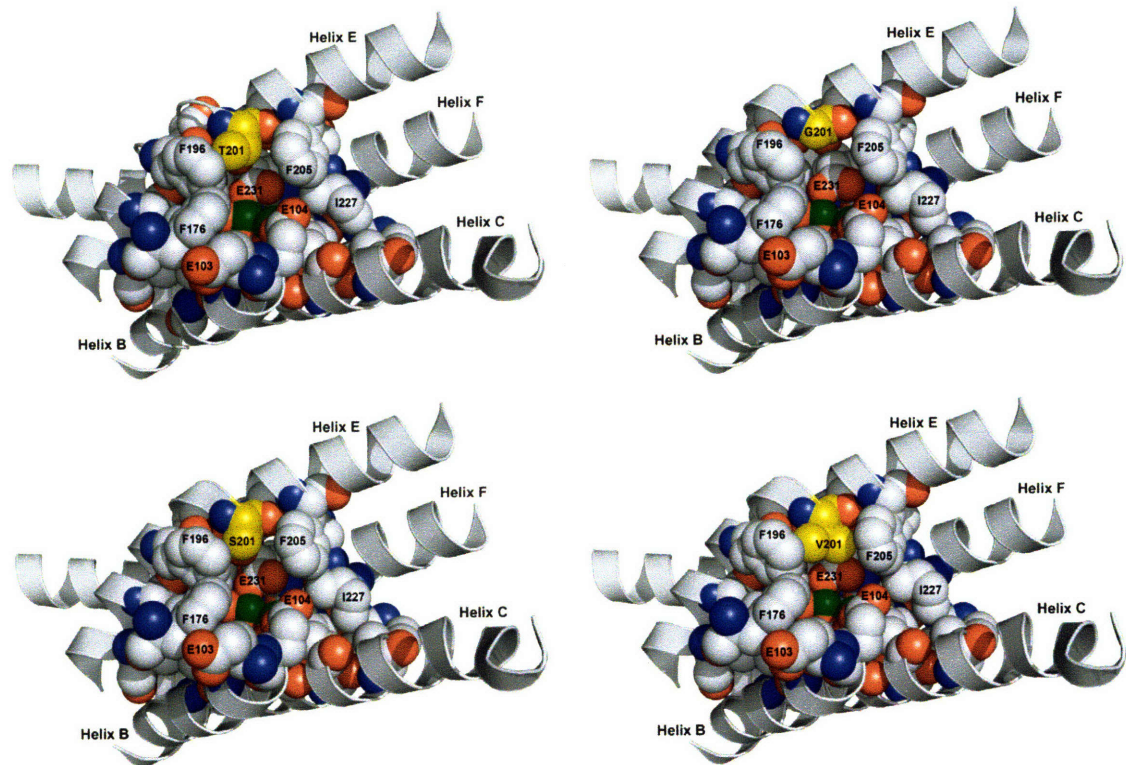


Figure 3.6. Space-filling view of the active site cavity in wild-type ToMOH, ToMOH T201G, ToMOH T201V, and ToMOH T201S (clockwise from top left), from the viewpoint of an approaching hydrocarbon substrate molecule. The mutated residue is shown in yellow (carbon), blue (nitrogen), and red (oxygen). Remaining pocket residues are similarly colored, with exception that carbons are grey. Iron atoms are shown in green.

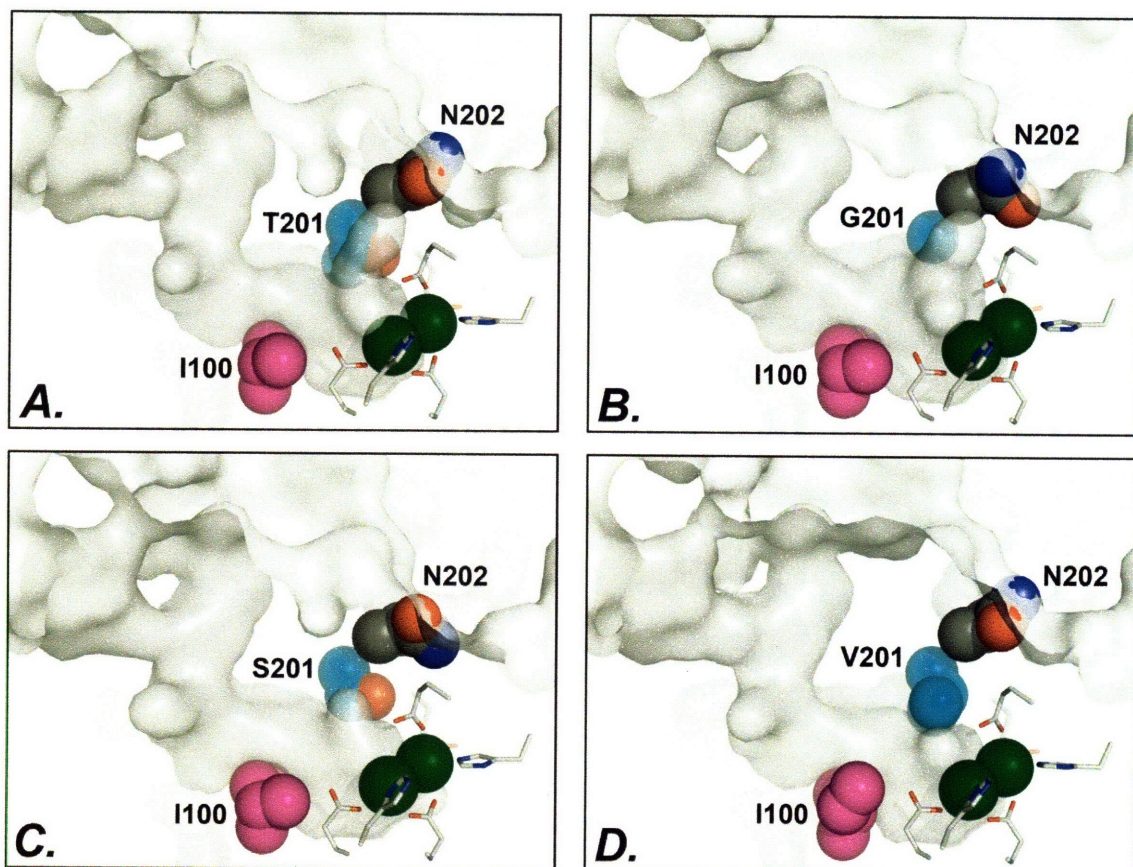


Figure 3.7. Effects of the mutation on the van Der Waals surface topology of the ToMOH channel and pore region in ToMOH T201G (B), ToMOH T201S (C), and ToMOH T201V (D) as compared to wild-type ToMOH (A). The protein van der Waals surface is shown in translucent white. Active site amino acid ligands are represented as sticks. Side chain and C_α atoms of residues I100, T201X, and N202 are represented as spheres. Iron atoms are shown as green spheres. Carbon atoms are shown in white (ligands), magenta (I100), cyan (T201X), and dark grey (N202). Nitrogen and oxygen atoms are shown in blue and red, respectively.

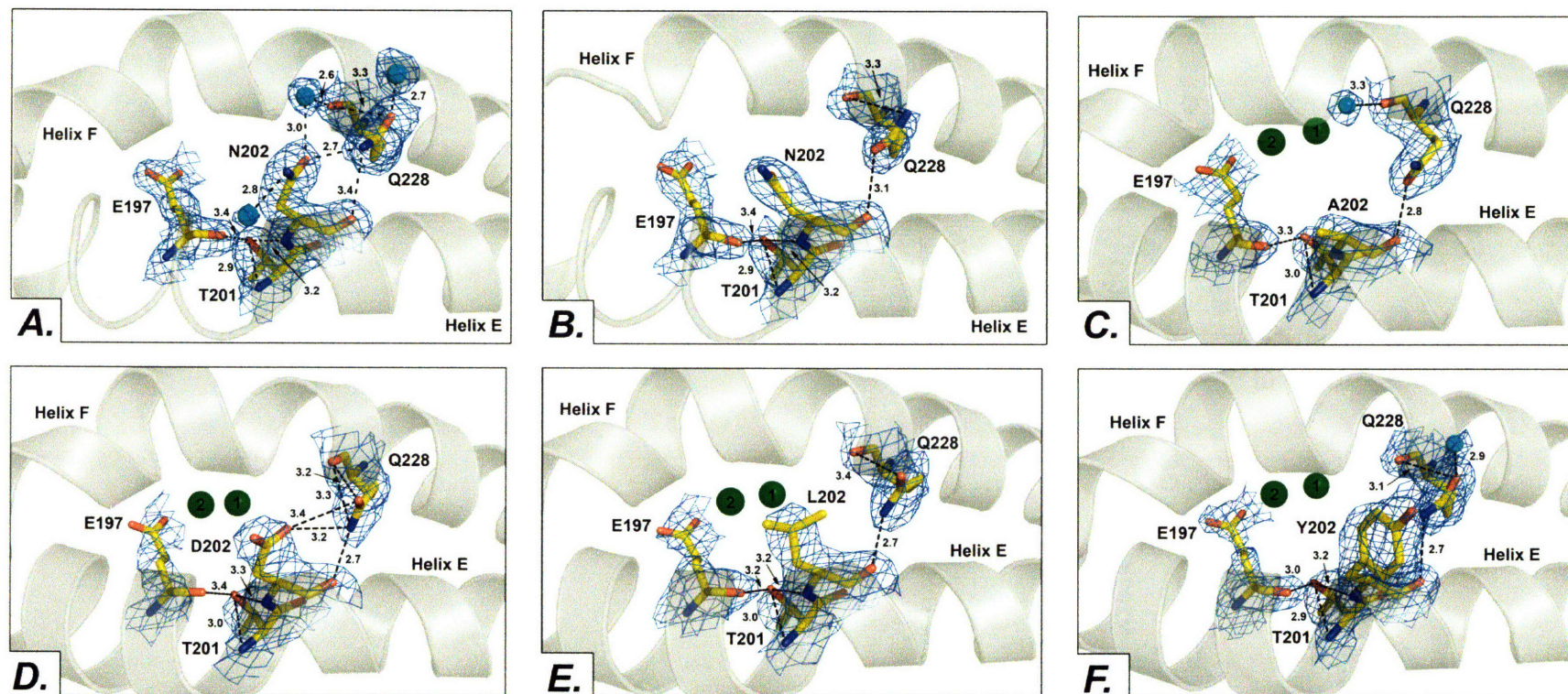


Figure 3.8. Views of the various side chain conformations, hydrogen-bonding interactions, and electron density for residues E197, T201, N202X, and Q228 from ToMOH N202A (C), ToMOH N202D (D), ToMOH N202L (E), and ToMOH N202Y (F) as compared to wild-type (A) and Mn(II)-reconstituted ToMOH (B). Iron ligating and surface exposed helices E and F are shown as translucent grey ribbons. Active site metal ions are shown as green spheres. Residues E197, T201, N202X, and Q228 are represented as sticks in yellow (carbon), blue (nitrogen), and oxygen (red). Water molecules are shown as cyan spheres. Distances are provided in angstroms. Composite omit map electron density maps contoured to 1.0 sigma are shown in light blue.

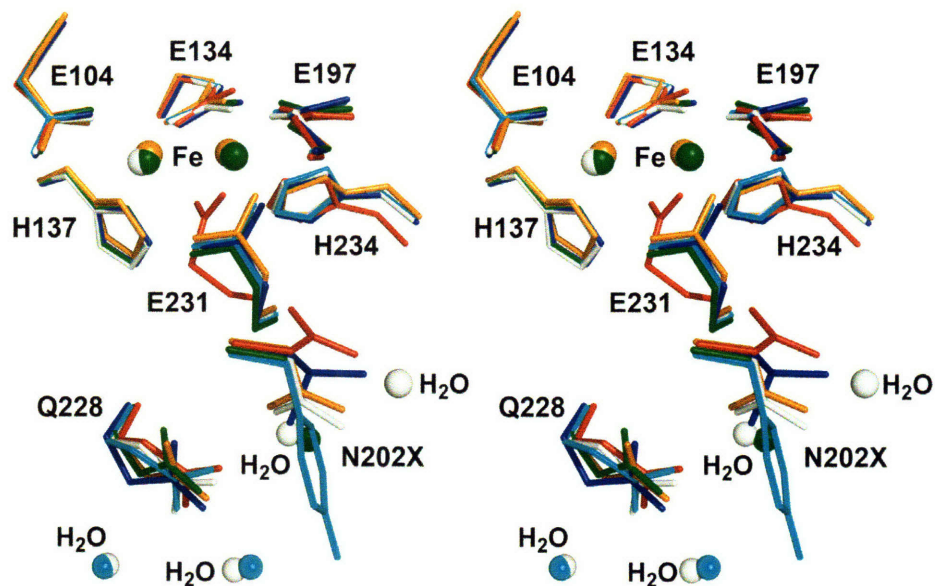


Figure 3.9. Stereo view of the overlaid structures of wild-type ToMOH (white), Mn(II)-reconstituted ToMOH (red), ToMOH N202A (green), ToMOH N202D (orange), ToMOH N202L (blue), and ToMOH N202Y (cyan). Iron atoms, and water molecules in hydrogen-bond contact with N202 and Q228 are depicted as spheres. Amino acid side chain ligands as well as the side chains of residues N202X, and Q228 are shown as sticks.

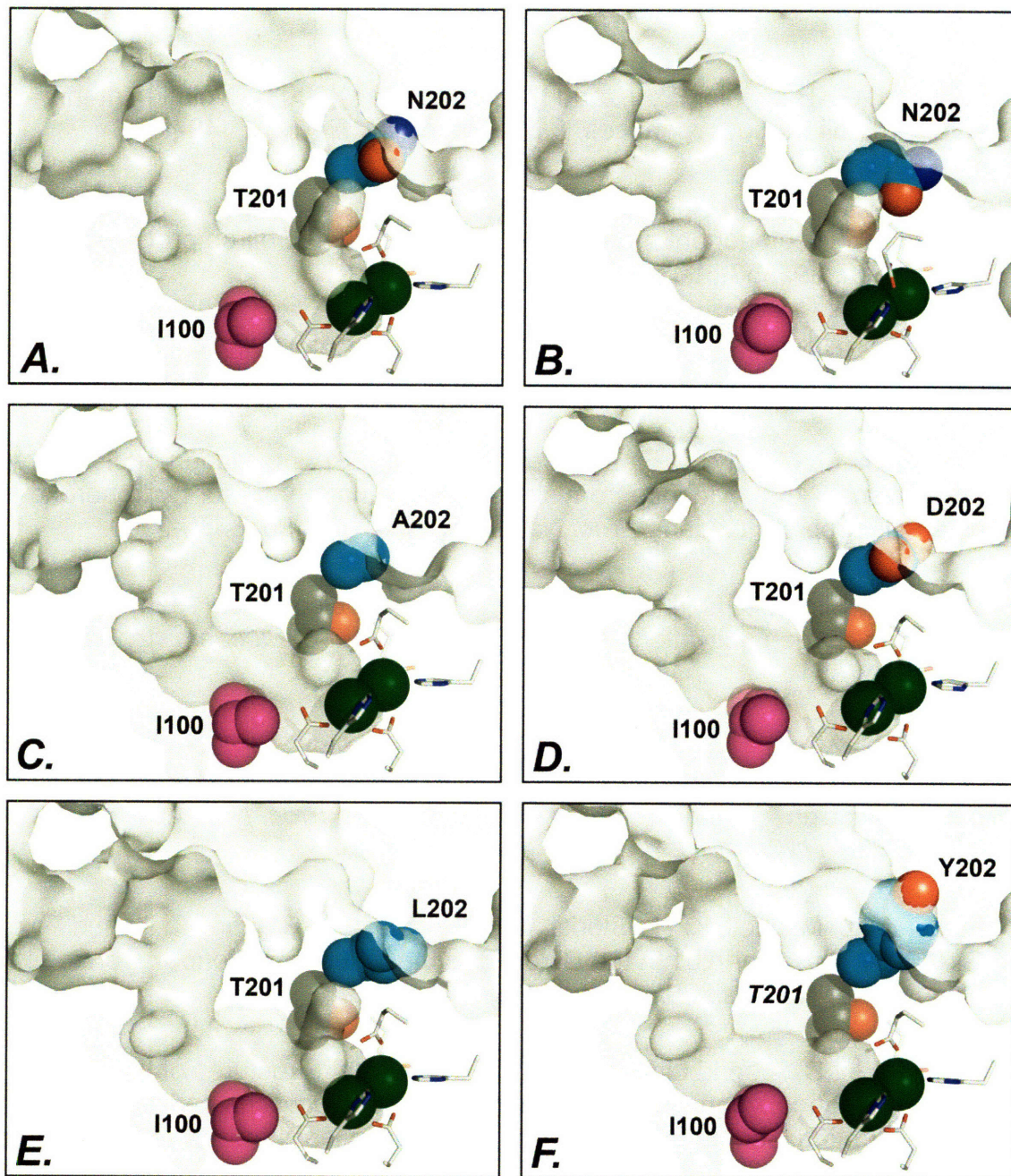


Figure 3.10. Effects of the mutation on the van der Waals surface topology of the ToMOH channel and pore region in ToMOH N202A (C), ToMOH N202D (D), ToMOH N202L (E), and ToMOH N202Y (F) as compared to wild-type (A) and Mn(II)-reconstituted (B) ToMOH. The protein van Der Waals surface is shown in translucent white. Active site amino acid ligands are represented as sticks. Side chain and C $_{\alpha}$ atoms of residues I100, T201, and N202X are represented as spheres. Iron atoms are shown as green spheres. Carbon atoms are shown in white (ligands), magenta (I100), dark grey (T201), and cyan (N202X). Nitrogen and oxygen atoms are shown in blue and red, respectively.

References

1. Leahy, J. G., Batchelor, P. J., and Morcomb, S. M. (2003) Evolution of the soluble diiron monooxygenases. *FEMS Microbiol. Rev.* 27, 449-479.
2. Sazinsky, M. H., and Lippard, S. J. (2006) Correlating structure with function in bacterial multicomponent monooxygenases and related diiron proteins. *Acc. Chem. Res.* 39, 558-566.
3. Lee, S. K., Nesheim, J. C., and Lipscomb, J. D. (1993) Transient intermediates of the methane monooxygenase catalytic cycle. *J. Biol. Chem.* 268, 21569-21577.
4. Vaz, A. D., McGinnity, D. F., and Coon, M. J. (1998) Epoxidation of olefins by cytochrome P450: evidence from site-specific mutagenesis for hydroperoxo-iron as an electrophilic oxidant. *Proc. Natl. Acad. Sci. USA* 95, 3555-3560.
5. Yeom, H., Sligar, S. G., Li, H., Poulos, T. L., and Fulco, A. J. (1995) The role of Thr268 in oxygen activation of cytochrome P450BM-3. *Biochemistry* 34, 14733-14740.
6. Guy, J. E., Abreu, I. A., Moche, M., Lindqvist, Y., Whittle, E., and Shanklin, J. (2006) A single mutation in the castor Delta 9-18:0-desaturase changes reaction partitioning from desaturation to oxidase chemistry. *Proc. Natl. Acad. Sci. USA* 103, 17220-17224.
7. Pikus, J. D., Mitchell, K. H., Studts, J. M., McClay, K., Steffan, R. J., and Fox, B. G. (2000) Threonine 201 in the Diiron Enzyme Toluene 4-Monooxygenase Is Not Required for Catalysis. *Biochemistry* 39, 791-799.
8. Whittington, D. A., and Lippard, S. J. (2001) Crystal Structures of the Soluble Methane Monooxygenase Hydroxylase from *Methylococcus capsulatus* (Bath) Demonstrating Geometrical Variability at the Dinuclear Iron Active Site. *J. Am. Chem. Soc.* 123, 827-838.
9. Song, W. J., and Lippard, S. J. unpublished results.
10. McPhillips, T. M., McPhillips, S. E., Chiu, H. J., Cohen, A. E., Deacon, A. M., Ellis, P. J., Garman, E., Gonzalez, A., Sauter, N. K., Phizackerley, R. P., Soltis, S. M., and Kuhn, P. (2002) Blu-Ice and the Distributed Control System: software for data acquisition and instrument control at macromolecular crystallography beamlines. *J. Synchrotron Radiat.* 9, 401-406.

11. Otwinowski, Z., and Minor, W. (1997) Processing of x-ray diffraction data collected in oscillation mode. *Methods Enzymol.* 276, 307-326.
12. Kissinger, C. R., Gehlhaar, D. K., and Fogel, D. B. (1999) Rapid automated molecular replacement by evolutionary search. *Acta Crystallogr. D55*, 484-491.
13. Emsley, P., and Cowtan, K. (2004) Coot: model-building tools for molecular graphics. *Acta Crystallogr. D60*, 2126-2132.
14. Murshudov, G. N., Vagin, A. A., and Dodson, E. J. (1997) Refinement of macromolecular structures by the maximum-likelihood method. *Acta Crystallogr. D53*, 240-255.
15. Anonymous. (1994) The CCP4 suite: programs for protein crystallography. *Acta Crystallogr.* 50, 760-763.
16. Brunger, A. T., Adams, P. D., Clore, G. M., DeLano, W. L., Gros, P., Grosse-Kunstleve, R. W., Jiang, J.-S., Kuszewski, J., Nilges, M., Pannu, N. S., Read, R. J., Rice, L. M., Simonson, T., and Warren, G. L. (1998) Crystallography & NMR System: a new software suite for macromolecular structure determination. *Acta Crystallogr. D54*, 905-921.
17. Kleywegt, G. J., and Jones, T. A. (1998) Databases in protein crystallography. *Acta Crystallogr.* 54, 1119-1131.
18. Laskowski, R. A., MacArthur, M. W., Moss, D. S., and Thornton, J. M. (1993) PROCHECK: a program to check the stereochemical quality of protein structures. *J. Appl. Crystallogr.* 26, 283-291.
19. Rosenzweig, A. C., Brandstetter, H., Whittington, D. A., Nordlund, P., Lippard, S. J., and Frederick, C. A. (1997) Crystal structures of the methane monooxygenase hydroxylase from *Methylococcus capsulatus* (Bath): implications for substrate gating and component interactions. *Proteins* 29, 141-152.
20. Murray, L. J., and Lippard, S. J. (2007) Substrate trafficking and dioxygen activation in bacterial multicomponent monooxygenases. *Acc. Chem. Res.* 40, 466-474.
21. Sazinsky, M. H., Bard, J., Di Donato, A., and Lippard, S. J. (2004) Crystal Structure of the Toluene/*o*-Xylene Monooxygenase Hydroxylase from *Pseudomonas stutzeri* OX1: Insight Into the Substrate Specificity, Substrate Channeling, And Active Site Tuning of Multicomponent Monooxygenases. *J. Biol. Chem.* 279, 30600-30610.

22. Gherman, B. F., Lippard, S. J., and Friesner, R. A. (2005) Substrate Hydroxylation in Methane Monooxygenase: Quantitative Modeling via Mixed Quantum Mechanics/Molecular Mechanics Techniques. *J. Am. Chem. Soc.* 127, 1025-1037.
23. Murray, L. J., Naik, S. G., Ortillo, D. O., Garcia-Serres, R., Lee, J. K., Huynh, B. H., and Lippard, S. J. (2007) Characterization of the Arene-Oxidizing Intermediate in ToMOH as a Diiron(III) Species. *J. Am. Chem. Soc.* 129, 14500-14510.
24. Vardar, G., and Wood, T. K. (2005) Protein engineering of toluene-*o*-xylene monooxygenase from *Pseudomonas stutzeri* OX1 for enhanced chlorinated ethene degradation and *o*-xylene oxidation. *Appl. Microbiol. Biotechnol.* 68, 510-517.
25. Vardar, G., and Wood, T. K. (2004) Protein engineering of toluene-*o*-xylene monooxygenase from *Pseudomonas stutzeri* OX1 for synthesizing 4-methylresorcinol, methylhydroquinone, and pyrogallol. *Appl. Environ. Microbiol.* 70, 3253-3262.

CHAPTER 4

Exploring Voids in BMM Hydroxylase α -subunits: X-ray Crystallographic Characterization of the Xenon-Pressurized Hydroxylase Component of Phenol Hydroxylase from *Pseudomonas sp.* OX1, and Computational Analyses of the Hydroxylase Components of Phenol Hydroxylase, Toluene/*o*-xylene Monooxygenase, and Methane Monooxygenase.

Introduction

Phenol hydroxylase (PH) from *Pseudomonas sp.* OX1 belongs to a class of non-heme diiron carboxylate proteins that convert hydrocarbons to alcohols and epoxides, which are known as bacterial multicomponent monooxygenases (BMMs).(1, 2) These systems employ two to three accessory protein components to effect dioxygen activation and subsequent hydrocarbon substrate oxidation at the diiron active site located within a hydrophobic cavity in the α -subunits of the 220-250 kDa $(\alpha\beta\gamma)_2$ heterodimeric hydroxylase protein. A ~38 kDa Fe_2S_2 reductase protein and a 10-15 kDa cofactorless regulatory protein comprise the universal accessory proteins in BMMs, whereas a ~10 kDa Rieske-type reductase that assists in shuttling electrons from NADH oxidation by the Fe_2S_2 reductase to the hydroxylase exists as an additional electron-transport protein in the four-component BMM systems. As a result of the amazing chemistry performed by BMMs, host bacterial are conferred with the ability to obtain all of their carbon and energy needs from hydrocarbon metabolism, which begins with BMM substrate oxidation.(3)

In addition to that from PH(4), the hydroxylase protein components of soluble methane monooxygenase (sMMO) from *Methylococcus capsulatus* (Bath)(5-12) and *Methylosinus Trichosporium* OB3b(13) (MMOH), and toluene/*o*-xylene monooxygenase (ToMO) from *Pseudomonas sp.* OX1(14, 15) (ToMOH) have been characterized by X-ray crystallography. The structures of all three BMM hydroxylases indicate extensive homology in the diiron site coordination environment and surrounding residues. In addition to similarities within the BMM class, the carboxylate bridged diiron site in the hydroxylase is similar to that utilized in functionally dissimilar enzymes such as ribonucleotide reductase R2 subunit(16), ferritin(17), and steroyl-acyl carrier protein

$\Delta 9$ -desaturase(18), suggesting that the reactivity differences observed among BMMs and in related systems results from the structures adopted by the surrounding protein scaffold and oxygenated active site intermediates generated during catalysis.

A central question in the study of bacterial multicomponent monooxygenases (BMMs), as well as that of many enzymes, is how the protein scaffold controls substrate and product access to the catalytic site while maintaining precise control of the catalytic chemistry.(19) BMM hydroxylase proteins are adept at this process, for they must precisely govern the movement of four substrates: hydrocarbons, molecular oxygen, electrons, and protons in the form of H_3O^+ cations, to the active site and two products: alcohols or epoxides and water, from the active site while simultaneously binding to and dissociating from accessory protein components during catalysis.(2, 19) Our crystallographic studies of BMM hydroxylase proteins suggest that the various cavities, channels, and pores (generalized herein as *voids*) that trace pathways from the protein exterior to the active site in their α -subunits are the primary means of molecular substrate and product transport to and from the diiron center within. As we continue to investigate this hypothesis we recall that voids in protein structures usually fall into one of two classes: functional, or adventitious as a consequence of the protein fold. We do not discount the possibility that the latter rather than the former could be the case for some of the voids in BMM hydroxylases, despite mounting evidence to the contrary.

Early crystallographic work on MMOH revealed the presence of a series of hydrophobic cavities leading from the α -subunit surface to the active site pocket (Figure 4.1).(6) These cavities have since been examined crystallographically through analysis of product(12) and product-analog(8) bound structures as well as two xenon-pressurized structures.(11) These data suggested that the hydrophobic cavities in

MMOH may constitute the route of methane access to the diiron site during *in vivo* catalysis. Later structures of ToMOH(15) and PHH(4) indicated the presence of homologous hydrophobic cavities in their respective α -subunit interiors. In contrast to MMOH, however, these structures exhibit additional open channel access routes to the diiron center designated as a channel in ToMOH(15) and an open-pore in PHH (Figure 4.1). ToMOH has also been crystallographically characterized with molecules of bromophenol bound to the interior of its 40 Å long channel, suggesting that it is the route of hydrocarbon access in that system.(15) In lieu of a ToMOH-like channel, the open-pore route to the active site cavity in PHH traces the shortest solvent accessible route to the diiron center observed in any BMM hydroxylase, directly between the two surface exposed iron-ligating α -helices, and may represent the route of active site hydrocarbon access in that system.(4) Of note with regard to the open pore in PHH, however, is the presence of a similar but considerably more constricted PHH pore-like region in both MMOH(6) and ToMOH(19), which seems to vary in size with the oxidation state of the active site iron atoms and in the presence of bound product analogs.(8) Provided with knowledge of three active site access routes in the structurally characterized BMM hydroxylases, the hydrophobic cavities, the channel in ToMOH, and the open-pore in PHH, we address the question of why each of these pathways is present and why only the first appears to be fully conserved. Intuition leads us to suggest that the one conserved pathway in BMMs, the hydrophobic cavities, is present to selectively effect translocation of the one molecular substrate that is common to all BMMs, dioxygen. In the present work we set out to investigate this hypothesis through computational analyses of the three structurally characterized hydroxylase α -subunits,

as well as by determining and subsequently analyzing a xenon-pressurized PHH x-ray crystal structure (Xe-PHH).

Since early studies of myoglobin,(20) scientists have attempted to probe the roles of voids in proteins using crystallography and other creative methods. Examples of studies where site-directed mutagenesis and kinetic analysis have been used to investigate protein voids include native to cysteine mutations throughout a peptide-gated transmembrane sodium transport channel,(21) and the channel-blocking mutant of toluene/*o*-xylene monooxygenase.(22) Others have used small molecule probes for this purpose, including fluorescence analysis of site-specifically labeled lysozymes with the probe monobromobimane to examine protein solvent accessibility,(23) and the aforementioned crystallographic characterization of product-analog bound structures of MMOH(8, 12) and ToMOH.(15) Computational approaches are also established,(24-27) and in many cases show remarkably good correlation with related crystallographic data. An example of such correlation is exhibited in studies of the bifunctional carbon monoxide dehydrogenase/acetyl-coA synthase complex.(28)

A currently popular experimental method of examining protein voids is the crystallographic characterization of samples pressurized with a heavy gas such as krypton or xenon.(29) This method is relatively inexpensive and easily accessible for most synchrotron users, does not perturb the protein structure, and can potentially provide a considerable amount of information about the accessibility and hydrophobicity of voids in protein sample. Moreover, because heavy gas pressurized structures are isomorphous with their native equivalents, they may also be used for MAD, MIR, or SAD phasing of the native diffraction data.(30-34) Taking advantage of the spin $\frac{1}{2}$ nucleus of ^{129}Xe , xenon-pressurized protein structure analysis has also been extended to include

NMR studies that allow identification and analysis of hydrophobic binding sites within proteins in the solution state.(35-41) Heavy gas pressurization studies afford many similar structures for comparative analysis as a result of their attractive properties.

In the present work, we have employed two methods to analyze BMM hydroxylase voids: xenon gas pressurization protein crystallography and computational analyses of this and previously obtained structures of PHH, ToMOH, and MMOH. Among heavy gasses used in protein crystallography, xenon is an excellent choice as a probe for dioxygen binding within the protein because it is similar to oxygen in size, hydrophobicity, and polarizability (Table 4.1). These properties make xenon ideal for highlighting potential dioxygen binding sites in protein voids, in addition to the convenient fact that its 54 electrons render it highly visible in difference Fourier electron density maps. Crystallographic studies of myoglobin have indicated that many small molecules, including dinitrogen, bind to the same sites as xenon in its heme-containing active site cavity.(42) Additional precedent for the use of xenon as a probe for small gas binding in macromolecular voids include that for dioxygen binding in copper amine oxidases(43), and the aforementioned work on carbon monoxide binding in the interior of a bifunctional carbon monoxide dehydrogenase/acetyl-coA synthase complex(28) and methane translocation to the active site of MMOH(11).

Analysis of BMM hydroxylase protein surfaces was performed by using PyMOL(44), and calculation of the surface to active site voids was conducted within CAVER.(27) The CAVER software package allows the identification of routes leading from cavities in the interior of proteins to bulk solvent outside the protein matrix, via a reciprocal distance search algorithm. Data output from CAVER includes the cross section diameter of all calculated pathways at multiple points along their trajectories,

allowing for the identification of both the location and size of points of interest along each pathway. In combination with results from the Xe-PHH structure, these data collectively yield information about the means of substrate and product transport in BMM hydroxylases, providing information about why the various surface-to-diiron site voids may have evolved in each system.

Materials and Methods

General Considerations. The PHH sample used to obtain the xenon-pressurized X-ray crystal structure of PHH was expressed as described previously.(1) PHH used for Michaelis-Menten kinetic analysis in the presence of varying dioxygen and xenon concentrations was expressed using a new plasmid that excludes the genes for expression of the reductase (PHP) and regulatory (PHM) protein components of the PH system, and includes the gene for expression of the putative iron insertase PHK (PH Δ P Δ M).(45) All PHH samples were purified as described elsewhere.(4) PHP, PHM, and catechol 2,3-dioxygenase (C2,3O) samples used were expressed and purified as described previously.(46) PHM samples used in Michaelis-Menten kinetic analysis were refolded by thermal reconstitution to improve activity (vide infra).(47) Iron content by FerroZine assay(48) and enzyme activity by coupled calorimetric assay with C2,3O(1) were also conducted as previously described.

Crystallization, Xenon Pressurization, and Diffraction Data Collection. PHH crystallization was accomplished by the hanging drop vapor diffusion method at 18 °C, with some modifications of the previously published conditions(4), as described below. Protein solution contained 35 μ M PHH and 28 μ M PHM (0.8 equivalents of added PHM) in 10 mM MES pH 7.1 and 10% glycerol. Precipitant solution contained 150 mM

$\text{Na}_2\text{MoO}_4 \cdot 2\text{H}_2\text{O}$, 100 mM Tris HCl pH 7.0, 5% (v/v) glycerol, and 17-25% PEG 8,000 (v/v). Precipitant solution was prepared individually for each well in the crystallization tray from concentrated stocks of the solution components. Following preparation of the precipitant solutions, the 24-well tray was incubated at 4 °C and shaken for approximately 15 min before addition of the hanging drops and cover slides. This step was required for proper mixing of the precipitant components because of the high solution viscosity. Hanging drops comprised 2 μL of protein solution combined with 2 μL of precipitant solution. Cryogenic solution for data collection contained the precipitant solution with added 20% (v/v) glycerol.

Crystalline samples of PHH were shipped to SSRL at ambient temperature in a centrifuge (Eppendorf) tube containing 500 μL cryo solution. Many of these crystalline samples were individually subject to xenon pressurization. At ambient temperature, single crystals were mounted on cryo loops that were subsequently placed in the gas pressurization cell(49) along with 500 μL distilled water to prevent crystal dehydration. Following, the sample was subject to 2.1×10^6 Pa xenon gas pressure for 2 to 15 min before the pressure was released and the crystal immediately frozen in liquid nitrogen. After freezing, the crystals were transferred to the Stanford Automated Mounting robot cassette(50) and screened for diffraction quality.

X-ray diffraction data were collected at the Stanford Synchrotron Radiation Laboratory (SSRL) on beam line 9-2 using the BLU-ICE data collection suite.(51) Crystal annealing was conducted as described for 1.85 Å native ToMOH, however, different lengths of annealing time were investigated, ranging from 1 to 10 s. Diffraction data were integrated and scaled in HKL2000.(52)

Structure Determination and Refinement. Phasing of the xenon PHH-PHM data was accomplished by using EPMR(53) and 2.7 Å resolution native PHH-PHM coordinates (PDB code 2INN)(4) in which all non-protein atoms and the side chains of the iron coordinating ligands removed as a starting model. An additional attempt at phasing was also conducted using the above-described model minus the coordinates for PHM. Following phasing, subsequent models were built in Coot(54) and refined using REFMAC5(55) in CCP4.(56) PHM and Xe atom occupancies as well as simulated annealing composite omit maps were calculated in CNS.(57) Xenon atoms were located by manually fitting them into heavy atom peaks in the simulated annealing composite omit $2F_o - F_c$ electron density map. PHM molecule and xenon atom occupancy refinements were performed by fixing the B-factors of the refined atoms to the 49 Å³ average for the α -, β -, and γ -subunits. MSDchem ideal coordinates as well as CNS topology and parameter files for glycerol, HEPES, and MOPS heterocompounds were obtained from the HIC-UP database (residue codes GOL, HPE, and MPO, respectively).(58)

PH Michaelis-Menten Kinetics with Dioxygen and Xenon. Data on the Michaelis-Menten kinetics of PH with dioxygen and xenon were obtained using a modification of the previously published coupled assay with C2,3O.(1) In this assay PH steady state activity was determined by monitoring the formation of 2-hydroxymuconic acid from C2,3O catalysis following phenol oxidation to catechol by PH. Production of the final product of this coupled assay, 2-hydroxymuconic acid, was measured by analysis of the absorbance change at 410 nm ($\epsilon_{410} = 12,620 \text{ M}^{-1}\text{cm}^{-1}$) with time. In the case of the present analysis of PH Michaelis-Menten activity with dioxygen and xenon, steady-state assays were performed in the presence of varying amounts of nitrogen, dioxygen, and

xenon gas and combined to ultimately provide the desired Michaelis-Menten kinetic data.

The individual steady-state experiments with PH in the presence of dioxygen and/or xenon were conducted using a dual cell UV-vis spectrophotometer (Cary) and septa-capped sample and reference quartz cuvettes. Final concentrations of PHH, PHM, PHP, NADH, phenol, and C2,3O in each individual steady-state experiment were 0.5 μ M, 1.0 μ M, 1.0 μ M, 1.0 mM, 1.0 mM, and \sim 2.5 μ M, respectively, in buffer containing 100 mM Tris HCl at pH 7.5. Saturated solutions of nitrogen, dioxygen, and xenon were prepared by purging the gasses into individual 100 mL aliquots of Tris buffer for \sim 30 min. Prior to each experiment, phenol, NADH, and all proteins less PHP were added as concentrated aliquots to the sample cell and purged of dioxygen using \sim 20 nitrogen/vacuum purge cycles and schlenck glassware. Subsequently, the nitrogen and xenon gas aliquots were added to the reaction mixture by injecting the appropriate volumes of nitrogen and xenon saturated buffer into the sample cuvette using gas-tight syringes (Hamilton). Immediately thereafter, the sample cell was placed in the UV-vis instrument and data collection at 410 nm was started. Upon observing a stable baseline, the sample cell was removed from the instrument, PHP and then dioxygen saturated buffer were added (again using gas-tight syringes), and finally, the cuvette was inverted multiple times to effect proper mixing and replaced in the instrument sample cell. In all cases the saturated nitrogen buffer was used as the reference solution and to normalize the final volume of the individual samples. Following addition of PHP and dioxygen, an expected increase in absorbance with time corresponding to PH and C2,3O coupled activity was observed, and the most linear portion of the resulting spectra (where substrate concentration is saturating) was used to extract the

slope of the reaction and determine steady-state activity at each concentration of added dioxygen and xenon gas.

Analysis of BMM Hydroxylase Voids Using PyMOL. The popular macromolecular structure visualization program PyMOL provides accurate representations of structure van der Waals surfaces.(44) Utilizing this feature, prominent voids in the crystallographically characterized BMM hydroxylases are readily observed. Provided with this information, each and every protein residue that contributes to the surface of the various BMM hydroxylase voids was identified for comparative study. The results reported here were obtained from analysis of 1.85 Å resolution ToMOH_{ox} (PDB code 2INC), 1.70 Å resolution MMOH_{ox} (PDB code 1MTY), and the 1.95 Å resolution Xe-PHH coordinates.

Analysis of BMM Hydroxylase Voids Using CAVER. The starting point for each surface-to-diiron center pathway search was the center of the active site cavity, which was manually chosen on the basis of van der Waals surface calculations initially conducted in PyMOL.(44) CAVER parameters were set to compute ten independent pathways from the starting position to the protein exterior via available space in the static protein interior. Each of the ten calculated pathways was output as coordinates spaced at 0.8 Å intervals along the trajectory. Furthermore, trajectory coordinates also contained precise radii, allowing for accurate width measurement essentially anywhere along the calculated pathways. Structures of MMOH (PDB code 1MTY), ToMOH (PDB code 1T0Q), and PHH-PHM (PDB Code 2INN) were subjected to CAVER analysis with the above parameters, following deletion of all non-protein atoms from the structure coordinate list. In the case of the PH analysis, the protomer not bound to PHM in the PHH-PHM structure (hereto referred to as *protomer A*) was chosen to represent PHH in

the absence of PHM. Conversely, the protomer bound to PHM (hereto referred to as *protomer B*) was analyzed for information about PHH in the presence of bound regulatory protein.

BMM Hydroxylase α -subunit Protein Sequence Alignments. Protein sequence alignments to analyze hydroxylase α -subunit residue conservation were performed using ClustalW. The protein sequences of PHH and ToMOH from *Pseudomonas sp.* OX1 (AAO47358 and CAA06654, respectively), MMOH from *Methylococcus capsulatus* (Bath) (AAB62392), T4MOH from *Pseudomonas mendocina* (AAS66660), alkene monooxygenase epoxidase from *Rhodococcus sp.* RHA1 (YP700435), and butane monooxygenase hydroxylase from *Pseudomonas butanovora* (AAM19727) were used for the sequence alignments.

Results and Discussion

Iron Content and Activity. The PHH sample used for crystallization and subsequent xenon pressurization contained 3.6 Fe atoms/dimer and exhibited an activity of 470 ± 40 milliunits $\text{min}^{-1} \text{mg}^{-1}$. That used for Michaelis-Menten analysis with dioxygen and xenon contained 4.4 ± 0.3 Fe atoms/dimer and exhibited an activity of $1,300 \pm 60$ milliunits $\text{min}^{-1} \text{mg}^{-1}$. The reason that the sample used for Michaelis-Menten analysis exhibits ~3 fold higher steady-state activity than that used for xenon pressurization is due to the different plasmids used for PHH expression, the former of which includes the gene for PHK expression but excludes those for PHP and PHM expression.(45)

Crystallization, Xenon Pressurization, and Data Collection. PHH crystals formed in 2 – 3 days. Among those crystals subjected to xenon pressurization and diffraction

screening, the best quality data came from one that crystallized from 19% PEG 8,000, was pressurized with xenon for 5 min, and subject to a 2 sec annealing time. Diffraction data processing gave a 1.95 Å data set with statistics shown in Table 4.2.

Structure Determination and Refinement. Molecular replacement phasing followed by extensive model fitting and refinement gave the structure with refinement statistics shown in Table 4.2. Although the data could be phased by molecular replacement with PHM present in or absent from in the initial model, considerably better refinement and coordinate geometry statistics were subsequently obtained without PHM in the Xe-PHH coordinates. Refined coordinates with PHM present indicated that the regulatory protein occupancy was $\leq 40\%$, and as in the case of the previous PHH-PHM structure, only exhibited bound PHM on one side of the dimer. As a result of the low PHM occupancy observed in this structure, modeling the protein into the corresponding weak electron density proved extremely difficult and consistently resulted in poor protein backbone and side chain geometry statistics following many rounds of structure refinement. Furthermore, comparison of the two PHH protomers in this structure indicated high structural homology between the two and corresponding C_α-to-C_α root-mean squared differences (RMSDs) of 0.23 and 0.14 Å³ for the individual monomers and α-subunits of the dimer, respectively (Figure 4.2). The previously observed rearrangements in Helix F that are believed to be a result of bound PHM(4) were also not observed in this structure, providing evidence to suggest that the partially occupied PHM has not affected the structure of the hydroxylase to the same degree in these data.

These findings with respect to the PHM content in the xenon-pressurized crystals can be rationalized by recent findings that solution samples of recombinantly expressed

PHM contain both inactive and active form of the protein, on the basis of native PAGE analysis of purified PHM samples (Figure 4.3) and solution isothermal titration calorimetry studies of PHH-PHM complex formation.(59) Considering that PHM samples containing the inactive form of the protein were added (0.8 equivalents in the case of the crystal used for structure determination) to samples of PHH expressed from the plasmid which co-expresses PHM in the crystallization setup, it is possible that the presence of the inactive form caused PHM disassociation from PHH during crystallization, through dimer formation or an equilibrium shift favoring a misfolding pathway. Considering our collective results regarding the bound PHM molecule we decided to omit the regulatory protein from the final coordinates and consider the structure to represent the lone hydroxylase. Regardless, we do note that the regulatory protein is partially present in the crystal used for data collection.

The global folds of the α -, β -, and γ -subunits of PHH are essentially identical to those of the previously determined structure of the PHH-PHM complex(4), save the aforementioned differences in the conformations of helices E and F in protomer B, with a C_{α} -to- C_{α} RMSDs of 0.74 \AA^3 for the hydroxylase and 0.26 \AA^3 for the protomer B α -subunit alone. Similarly, the diiron centers in Xe-PHH are also geometrically homologous to those of the wild-type protein, again resembling the mixed-valent MMOH diiron site(10) and exhibiting a lack of solvent-derived ligands bridging the iron atoms (Figure 4.4). Notably different about the diiron sites in Xe-PHH with respect to the native structure, however, is the presence of a presumably deprotonated glycerol molecule bound exclusively to Fe1 on both sides of the dimer and in place of a terminal water molecule observed in the previous structure.(4) This assignment is strongly supported by the $2F_o - F_c$ composite omit electron density (Figure 4.5), and furthermore, exhibits a

diiron site hydrocarbon coordination not previously observed in any BMM hydroxylase. Specifically, all other structures of alcohol bound BMM hydroxylase diiron sites indicate an asymmetrically bridging mode of hydrocarbon coordination which suggests the possibility of a different mechanism of substrate binding, oxidation, or product release in PHH with respect to MMOH and ToMOH.

Also unperturbed in comparison to the previously reported PHH structure is the structural zinc site located in the α -subunit, near the protein-protein interface with the γ -subunit. As in the previous structure of PHH(4) this site exhibits nearly perfect tetrahedral geometry and $2.3 \pm 0.1 \text{ \AA}$ Zn—S bond distances that are typical for a metalloprotein site of this type (Figures 6 and 7, top).

In addition to the diiron and zinc sites in Xe-PHH, a newly observed and considerably unusual third metal binding site is present in the structure, on the surface of the α -subunit near the dimer interface (Figures 6 and 7, bottom). The monomeric binding site appears in the structure electron density comprising only a transition metal and two histidine imidazole ligands coordinated in a nearly linear fashion to yield 172° and 178° $\text{His}_{\text{N}_\epsilon}\text{-M}^{\text{n}+}\text{-His}_{\text{N}_\delta}$ bond angles for protomers A and B, respectively. Additional ligands on this metal may be present, but are not observed in the electron density as a result of disorder or $\text{His}_{\text{N}}\text{-M}^{\text{n}+}$ bond rotation. Comparison of the coordination bond angles and distances in this structure with some inorganic model complexes suggests that metal is most likely Cu(I). (60, 61) We believe that this surface bound metal ion is not functional, and is simply a consequence of an impurity in one of the protein purification or crystallization reagents.

Twenty-four xenon atoms, twelve in each protomer, were located in the structure including fourteen in the MMOH-like hydrophobic cavities (Table 4.3 and Figure 4.8).

The refined xenon occupancies range from 0.3 to 1 and average 0.8 (Table 4.3). In cases where the occupancy refined to a value greater than or equal to 1 the occupancy was subsequently fixed at 1 and the B-factor allowed to refine. Images of the ten xenon sites found in the Xe-PHH α -subunit are shown in Figure 4.9. Distances between the xenon atoms in the hydrophobic cavities and the active site iron atoms are summarized in Table 4.4.

As is typical for a xenon-bound protein structure, a large majority of the residues contributing the various binding sites have hydrophobic side chains and are positioned 4 – 5 Å from the bound xenon atom (Table 4.3). A notable trend in the occupancies of the xenon atoms bound to the hydrophobic cavities is a significant decrease as the proximity to the buried iron center increases (Table 4.3). Also important regarding the xenon binding sites is the lack of ordered water molecules observed at or near the xenon atom sites in the structure of PHH not pressurized with xenon.(4)

PH Michaelis-Menten Kinetics with Dioxygen and Xenon. PH Michaelis-Menten kinetics in various concentrations of dioxygen indicate classic saturation behavior that reveals the system's requirement for as much as 100-200 equivalents of dioxygen in solution for optimal activity under the conditions tested. The addition of 1.0 mM xenon gas to assays containing 10 and 500 μ M dioxygen revealed no clear evidence for a decrease in steady-state activity. Results are summarized in Figure 4.10.

Analysis of BMM Hydroxylase Voids Using PyMOL. The results of our analysis of BMM hydroxylase α -subunit voids using PyMOL are summarized in Figures 4.11, 4.12, 4.13, and Table 4.5. From the figures we can clearly see that each of the three hydrophobic cavities, as well as the pore region, are present and spatially defined in the α -subunit of PHH (Figure 4.11), MMOH (Figure 4.12), and ToMOH (Figure 4.13). Also

apparent in the images is how the orientation of the cavity and pore voids are maintained in each protein with respect to the iron atoms (grey spheres) and putative electron-transfer hydrogen-bonding network (yellow residues). Reviewing the residues contributing to the interior surface of the cavities, as labeled in the figures and listed in Table 4.5, reveals that a large majority are hydrophobic and that few polar side chains face the interior spaces. Comparison of the individual cavities one (green), two (cyan), and three (magenta) in the three hydroxylases indicates that: (1) cavity one is considerably larger in PHH than in ToMOH or MMOH, (2) cavity two is similarly sized and isolated from cavities one and three in all three hydroxylases, (3) cavity three is largest in MMOH but solvent accessible in PHH and ToMOH. Considering that the structure and hydrophobicity of these cavities are conserved but without strict conservation of the contributing residues, along with the fact that they are known to bind xenon in MMOH and PHH, the suggested notion that they exist to facilitate dioxygen transport to the active site is further supported.

Comparing the pore region (orange in Figures 4.11, 4.12, and 4.13) in each protein we see that the residues contributing to its surface are the most conserved of any particular void region in the three proteins. The pore access pathway is consistently defined in part by the strictly conserved surface asparagine (PHH N204; MMOH N214; ToMOH N202), conserved surface glutamine/glutamate (PHH Q230; MMOH E240; ToMOH Q228), strictly conserved active site pocket threonine (PHH T203; MMOH T213; ToMOH T201), and carboxylate-shift iron ligating glutamate (PHH E233; MMOH E243; ToMOH E231). In all cases the remaining residues that contribute to this void space in the three proteins are hydrophobic. These findings, in the context of our knowledge that all of the conserved pore region residues other the active site pocket

threonine change conformation with active site reduction in MMOH and ToMOH suggest that it is present, at least in part, to effect the translocation of some substrate, probably protons, into the active site cavity in a time-dependent manner with respect to electron transfer. The observation that the carboxylate-shift iron ligand contributes to the pore region surface indicates that the coordination change adopted by this residue is linked to a change in the active site solvent accessibility during catalysis.

Looking at the channel void in ToMOH (Figure 4.13, grey), and in particular where it first extends away from cavities one and two toward the protein surface, we observe how it links the first two cavities in extending away from them in its trajectory. Comparing this buried region of the channel to the analogous area in PHH, we find that it is somewhat conserved, and the result is the relatively large cavity one in that system. In MMOH we find no such void space in the analogous region, and instead see hydrophobic side chains including F188, F236, and L110 projecting into the area to prevent any such expansion in cavity one. Considering these findings about the channel void in the context of the substrate specificities of PHH, ToMOH, and MMOH, one can imagine how the channel may have opened through evolution in ToMOH to accommodate its wide substrate range but closed in the other two systems to limit active site solvent access and affect hydroxylation of their preferred substrates.

BMM Hydroxylase α -subunit Protein Sequence Alignments. In the context of the PyMOL analysis of the BMM voids the sequence alignment data indicates conservation in the hydrophobicity of the residues contributing to the xenon-binding sites Xe-PHH. ClustalW sequence alignment results are summarized in Figure 4.14, where residues that have side chain contributions to the α -subunit xenon binding sites in PHH are highlighted in blue, and the protein ligands on iron are highlighted in magenta.

Analysis of BMM Hydroxylase Voids Using CAVER. Active site pocket-to-protein exterior trajectory calculation results from CAVER on all three hydroxylases as determined in this study each include three or four pathways identical to that with the largest cross section, along with one or two unreasonable pathways with extremely small average cross sections. These redundant and unreasonable pathways are excluded from the following discussion of the results.

Substrate access calculations with CAVER on the PHH-PHM structure(4) reveal: (1) there are three likely routes of small molecule access from the surface to the diiron center in the α -subunit of PHH, (2) the route exhibiting the largest cross section is the pore region, which changes in length and trajectory in the presence of PHM, and (3) all the three determined pathways are conserved among known BMM hydroxylase α -subunit structures. These features are detailed in Figure 4.15. The substrate access route in PHH with the greatest cross section is the pore region, with a reported diameter of 2.8 Å at its narrowest point near T203, F207, and E233 (Figure 4.15A, yellow). A pathway through the hydrophobic cavities of PHH is an additional route, which is narrowest near P106, H166, and Q113 at 2.2Å (Figure 4.15A, magenta). This pathway contains a majority of the xenon atoms in the structure of Xe-PHH (*vide supra*). The third and most constricted path identified in PHH wraps around protein interior side of helix E and exits between helices E and H (Figure 4.15A, cyan), tracing a pathway similar to the channel in ToMOH. In the presence of PHM, the trajectories of the pore and channel trajectories deviate significantly (Figure 4.15B). The pore exit opening is almost completely blocked by the regulatory protein when bound, causing its calculated trajectory to shift around the four-strand beta sheet of PHM toward the γ -subunit of the regulatory component bound protomer (Figure 4.15B, yellow). The alteration in this

pathway lengthens the pore trajectory by approximately 12 Å, but does not cause an expansion or contraction in its narrowest cross section. Most interesting about the change in this pathway is that the trajectory shift and lengthening begins at the point of the previously noted hydrogen-bonding interaction between PHH N204 and PHM S72.(4) The channel trajectory is similarly forced to lengthen, by approximately 10 Å, and shift toward the γ -subunit in the same direction as the pore trajectory (Figure 4.15B, cyan). The effects on both the pore and channel trajectories are exaggerated by the conformational shift in helix F that occurs in conjunction with regulatory component binding to the hydroxylase.(4)

Comparing these results to those similarly obtained from analysis of the MMOH (PDB code 1MTY) and ToMOH (PDB code 1T0Q) α -subunits reveals additional information regarding substrate access in BMMs. Most notably, the pore, hydrophobic cavity, and channel pathways calculated by CAVER for PHH are similarly observed in MMOH and ToMOH (Figure 4.15C and 15D, respectively). These results reveal that access to the active site via the pathway delineated by the channel in ToMOH or the open-pore in PHH are unique to those systems. The relative sizes of each structural feature instead reveal new similarities and differences between the structurally characterized hydroxylases. In both PHH and MMOH, for example, the pore pathway (Figure 4.15C and 15D, yellow) represents the most accessible route to the active site cavity, while the channel pathway (Figure 4.15C and 15D, cyan) is the most restricted. Accordingly, the MMOH pore pathway is narrowest near E243, E114, and T213, with a diameter of 2.4 Å (Figure 4.15C, yellow). Conversely, the channel in ToMOH (Figure 4.15D, cyan) is the most open pathway observed among all calculated diiron center access routes, with its narrowest cross sectional diameter at 3.2 Å, near F293, D211,

and M277. This is considerably larger than the analogous channel in PHH (Figure 4.15A and 15B, cyan), or that in MMOH (Figure 4.15C, cyan), that latter of which measures 1.6 Å in diameter at its narrowest dimension, near F290, W308, and W301.

The angstrom diameters of the cross-sectional pathways calculated by CAVER must be considered only in relation to one another and not as precise measurements. These values instead represent statistical averages for the diameters adopted in the crystalline state of the protein, and invariably expand to yield larger cross sections in solution as a result of protein breathing motions. Insight into the established concept of protein breathing, at different temperatures and concentrations, has recently been obtained through computational work on a variety of proteins of differing size, fold, and function.⁽⁶²⁾ Results from this work suggest that at protein concentrations typical for laboratory solution work and in cellular environments, the interatomic distances that separate secondary structural elements increase by 1.0 to 1.5 Å as a result of the protein breathing vibrational modes, and without perturbing the native fold of the macromolecule or inter-residue hydrogen-bonds. Provided that BMM α -subunits are almost entirely α -helical in secondary structure, it is reasonable to assume on the basis of the theoretical work that the relative cross-sectional sizes of the various voids calculated through CAVER analysis are maintained, but considerably larger than the actual numeric values provided.

Conclusions and Prospects

Results from the 1.95 Å resolution structure of Xe-PHH highlight the hydrophobic gas binding affinity of a series of highly conserved hydrophobic cavities within the α -subunit, reiterate many of our previous findings about the structure of PH hydroxylase

protein and geometry of the metal-binding sites, and provide further evidence to support our hypothesis that the conserved hydrophobic cavities in BMM hydroxylases are the route of dioxygen entry into the catalytic site.

Among the xenon binding sites observed in PHH, over 80% are localized entirely in the α -subunit, and 70% of those are found in the hydrophobic cavities, despite the fact that the α -subunit comprises only ~54% of the total hydroxylase molecular weight. According to our sequence alignments, the hydrophobicity of a large majority of residue side chains contributing to the xenon binding sites in the PHH α -subunit is conserved among BMMs, and similarly observed in the structures of xenon-bound MMOH (Figure 4.16). These observations and statistics alone strongly implicate the hydrophobic cavities in BMM hydroxylase function rather than as a physical consequence of imperfect folding. The similarities in size, hydrophobicity, and polarizability of xenon and dioxygen gas (Table 4.1) suggest that the xenon sites are utilized for dioxygen transport to the diiron center during catalysis. Precedent for this assignment extends back to early high-resolution crystallographic studies of small molecule binding in the interior of myoglobin, which show various small molecules and hydrophobic gasses occupying the same binding sites as xenon in the active site cavity.(42) Countless examples of xenon as a crystallographic probe for dioxygen and other small gas binding to protein voids have subsequently been reported. Interesting examples of which include xenon as a probe for dioxygen translocation in copper amine oxidase(63) and 3-hydroxybenzoate hydroxylase(64), and carbon monoxide transport between the two catalytic sites of a bifunctional carbon monoxide dehydrogenase/acetyl-coA synthase complex.(28)

Provided that the hydrophobic cavities in BMMs are the route of dioxygen access to the diiron site, the question then arises of how hydrocarbons access the active site

cavity. One possibility is that substrate and product transport in BMMs other than MMOH is accomplished using surface to active site pathways not fully conserved such as the channel in ToMOH and the open-pore in PHH. MMOH would accordingly not require such an additional access pathway because its natural substrate is hydrophobic gas like dioxygen (Table 4.1) and could therefore use the same access pathway. This logical conclusion is further supported by the fact that all BMMs appear to have evolved from a common ancestor.⁽³⁾ Accordingly, the PHH open-pore and ToMOH channel pathways may have been carved into these BMM hydroxylase α -subunit structures through divergent evolution to accommodate their natural aromatic substrates. This may have occurred in exchange for the loss of some oxidizing power in the oxygenated diiron intermediates, possibly as a result of increased active site solvent exposure, to result in systems fit to initiate aromatic substrate metabolism but not capable of oxidizing methane. This conclusion is also consistent with the results from PyMOL and CAVER discussed here.

Acknowledgement

Tzanko Doukov of SSRL is acknowledged for training the author on the use of the xenon-pressurization device. Viviana Izzo prepared the PH Δ P Δ M plasmid and expressed the PHM added to the Xe-PHH crystallization setup. Matt Sazinsky expressed and purified the PHH sample used for Xe-PHH crystallization and structure determination. Christine Tinberg optimized PHH expression from the PH Δ P Δ M plasmid and provided advise in conducting the Michaelis-Menten kinetic analysis. Mihai Duduta assisted in the collection of the Michaelis-Menten data with oxygen and xenon and conducted the PAGE analysis reported in Figure 4.3.

Table 4.1. Size and Polarizability of Dioxygen, Xenon, and Methane Gas.

	dioxygen	xenon	methane
<i>van der Waals radius (Å)</i>	3.0 - 4.3	4.3	2.2
<i>polarizability</i>	1.6	4.0	2.6

Table 4.2. X-ray Data Collection and Refinement Statistics for Xe-PHH.

Xe PHH	
Data Collection	
Beamline	SSRL 9-2
Wavelength (Å)	0.979
Space Group	P212121
Unit cell dimensions (Å)	83.9 x 141.8 x 181.2
Resolution range (Å)	50.0 - 1.95
Total Reflections	145806
Unique Reflections	94048
Completeness (%) ^a	92.5 (82.1)
$I/\sigma(I)$ ^{a,b}	21.0 (2.2)
R_{sym} (%) ^a	6.7 (53.5)
Refinement	
R_{cryst} (%) ^c	18.0
R_{free} (%) ^d	22.6
Average B-value (Å ²)	29.6
RMSD bond length (Å)	0.018
RMSD bond angles (°)	1.71
Number of Atoms/Molecules^e	
Protein ^e	15336 (29.1)
Non-Protein ^e	703 (39.8)
Iron ^e	4 (38.8)
Zinc ^e	2 (22.8)
Copper ^e	2 (34.8)
Xenon ^e	24 (37.6)
Water ^e	637 (38.6)
Glycerol ^e	9 (42.9)
MOPS ^e	1 (70.2)
HEPES ^e	1 (67.3)

^aValues in parentheses are for the highest resolution shell. ^b $R_{\text{sym}} = \sum_i \sum_{hkl} |I_i(hkl) - \langle I(hkl) \rangle| / \sum_{hkl} \langle I(hkl) \rangle$, where $I_i(hkl)$ is the i th measured diffraction intensity and $\langle I(hkl) \rangle$ is the mean intensity for the Miller index (hkl) . ^c $R_{\text{cryst}} = \sum_{hkl} ||F_o(hkl)| - |F_c(hkl)|| / \sum_{hkl} |F_o(hkl)|$. ^d $R_{\text{free}} = R_{\text{cryst}}$ for a test set of reflections (5% in each case). ^eValues in parentheses are for the average B-factor, in Å², for the atoms or molecules listed.

Table 4.3. Xenon Atom Details from 1.95 Å Resolution Xe-PHH Structure. *B-factors for xenon atoms with occupancies less than unity were fixed at the 29.1 Å² average for the hydroxylase protein atoms.

Atom	Location	Occupancy		B-factor (Å ²)		Nearby Residues, Atoms, and Average Distances (Å)
		Protomer A	Protomer B	Protomer A	Protomer B	
Xe 1	Active Site	0.26	0.30	fixed*	fixed	F100 (Ce2, 4.0); I104 (Cg2, 4.7); E108 (Oe1, 4.0); Q145 (Ne2, 4.7); L206 (Cg, 4.0); F207 (Cd2, 4.4); M211 (Ce, 3.7); F225 (Ce2, 4.7); H2O-1 (3.4); H2O-4 (3.9); H2O-620 (3.6); H2O-176 (3.6)
Xe 2a	Cavity 1	0.38	-	fixed	fixed	F178 (Cz, 4.9); F198 (Ce1, 2.9); L202 (Cb, 4.2); L206 (Cd2, 4.5); G269 (O, 3.9); L272 (Cd2, 4.1); L273 (Cg, 3.8)
Xe 2b	Cavity 1	-	0.33	fixed	fixed	L99 (Cg, 4.5); G103 (Ca, 4.4); I104 (Cd1, 3.8); P175 (Cg, 4.5); L272 (Cd1, 4.6); L275 (Cd1, 3.5)
Xe 3	Cavity 2	0.43	0.41	fixed	fixed	W170 (Cz3, 4.3); Y171 (Cb, 4.0); V174 (Cg2, 4.2); L275 (Cd2, 4.0); L335 (Cd2, 4.4); F339 (Cz, 3.5); I404 (Cg2, 4.0); P405 (Cg2, 4.0)
Xe 4	Cavity 3	1.00	1.00	33.6	38.1	W170 (Cd2, 3.7); Y342 (Cd2, 3.8); A345 (Cb, 4.7); L395 (Cd2, 4.0); P396 (Cd, 3.9); Xe-5 (4.6); Xe-6 (4.4)
Xe 5	Cavity 3	1.00	1.00	43.5	47.0	W170 (Cd1, 4.6); A345 (Cb, 3.9); L395 (Cd2, 4.2); I457 (Cd1, 3.9); L467 (Cg, 4.5); V470 (Cg, 4.7); V471 (Cg2, 4.4); Y475 (Ce2, 4.0); Xe-4 (4.6)
Xe 6	Cavity 3	1.00	1.00	41.9	46.4	Y342 (Cd2, 4.2); Q344 (Oe1, 4.4); N393 (C, 3.9); T394 (C, 4.1); L395 (Cd2, 3.9); L467 (Cd1, 4.2); Xe-4 (4.4)
Xe 7	Cavity 3 Surface	1.00	1.00	49.4	50.9	Q344 (O, 3.6); L467 (Cg, 4.7); E468 (Ca, 4.5); V471 (Cg2, 4.5); I479 (Cd1, 4.3); N483 (Od1, 4.2); F484 (Cz, 4.5)
Xe 8	Helices B, C, & F	0.72	0.67	fixed	fixed	F100 (Ce1, 4.0); Q145 (Cg, 4.0); A148 (Cb, 4.0); M149 (Ce, 3.8); T222 (Og1, 4.0); F225 (Cd2, 4.3)
Xe 9	Helices E, G, & H	1.00	1.00	37.7	41.7	F196 (Ce2, 4.2); S197 (Og, 3.5); V201 (Cg, 4.1); I262 (Cg2, 4.6); F266 (Ca, 4.0); F307 (Cz, 4.4); P318 (Cg, 4.6)
Xe 10	Helices C, E, & F	1.00	1.00	42.7	44.7	W47 (Ch2, 3.9); W50 (Cz3, 4.1); F122 (Cz, 4.4); A127 (Cb, 4.8); F188 (Ce2, 4.0); L191 (Cd2, 4.1); V243 (Cg2, 4.6); F246 (Cd2, 4.2); I247 (Cg1, 4.5)
Xe 11	a/b Subunit Interface	0.60	0.65	fixed	fixed	A22 (Cb, 4.8); W23 (Cd2, 4.3); F34 (Cz, 4.8); R128 (Nh2, 4.9); L131 (Cd2, 4.8); M135 (Sd, 4.2); L206 (Cd1, 4.2); H2O-433 (4.2); H2O-208 (3.3); H2O-539 (3.8)
Xe 12	b-Subunit Surface	1.00	1.00	43.4	50.9	Y227 (Cb, 4.5); P228 (Ca, 4.2); Y231 (Cb, 4.1); D232 (Cb, 4.4); R254 (Cg, 4.1); Y257 (Cd2, 3.8)

Table 4.4. Fe-Xe and Xe-Xe Distances in 1.95 Å Xenon-PHH X-ray Structure (Å)

Atom	Xe 1		Xe 2		Xe 3		Xe 4		Xe 5		Xe 6		Xe 7		Fe 1		Fe 2	
	Protomer		Protomer		Protomer		Protomer		Protomer		Protomer		Protomer		Protomer		Protomer	
	A	B	A	B	A	B	A	B	A	B	A	B	A	B	A	B	A	B
Xe 1	-	-	10.1	9.9	18.4	18.2	25.6	25.6	27.0	27.0	29.6	29.6	30.0	30.0	6.1	6.1	7.6	7.5
Xe 2	10.1	9.9	-	-	14.1	8.5	22.8	18.9	25.6	17.7	26.9	20.0	30.0	21.7	11.6	13.4	11.2	15.1
Xe 3	18.4	18.2	14.1	8.5	-	-	8.8	8.9	12.2	12.3	13.0	13.2	17.3	17.3	21.8	21.7	23.3	23.1
Xe 4	25.6	25.6	22.8	18.9	8.8	8.9	-	-	4.6	4.6	4.4	4.4	10.1	10.1	28.6	28.5	30.6	30.5
Xe 5	27.0	27.0	25.6	17.7	12.2	12.3	4.6	4.6	-	-	5.0	5.1	7.8	7.7	29.5	29.4	31.8	31.8
Xe 6	29.6	29.6	26.9	20.0	13.0	13.2	4.4	4.4	5.0	5.1	-	-	8.0	8.0	32.7	32.7	34.8	34.8
Xe 7	30.0	30.0	30.0	21.7	17.3	17.3	10.1	10.1	7.8	7.7	8.0	8.0	-	-	33.2	33.1	35.8	35.8
Fe 1	6.1	6.1	11.6	13.4	21.8	21.7	28.6	28.5	29.5	29.4	32.7	32.7	33.2	33.1	-	-	3.5	3.5
Fe 2	7.6	7.5	11.2	15.1	23.3	23.1	30.6	30.5	31.8	31.8	34.8	34.8	35.8	35.8	3.5	3.5	-	-

Table 4.5. Residues Contributing to the van der Waals Surfaces of Voids in the Crystallographically Characterized BMM Hydroxylases.

Xe-PHH				MMOH (PDB Code 1MTY)				ToMOH (PDB Code 2INC)				
<i>Cavity 1</i>	<i>Cavity 2</i>	<i>Cavity 3</i>	<i>Pore</i>	<i>Cavity 1</i>	<i>Cavity 2</i>	<i>Cavity 3</i>	<i>Pore</i>	<i>Cavity 1</i>	<i>Cavity 2</i>	<i>Cavity 3</i>	<i>Pore</i>	<i>Channel</i>
L99	W170	Y342	T203	L110	W99	K98	T213	I100	L95	E166	T201	G88
F100	Y171	Q344	N202	G113	V105	E101	N214	E103	G98	W167	N202	W89
G103	L172	A345	F207	E114	V106	T102	I217	A107	A99	G334	F205	T92
I104	S173	N392	Q230	A117	F109	T174	I239	E133	A161	W338	Q228	H96
S105	V174	N393	E233	E144	M184	R175	E240	H137	I162	P340	E231	Q204
L107	S274	T394	A234	H147	L216	G178	E243	F176	A168	T341		G207
E108	L275	L395		F188	V220	P179		M180	A169	V389		L208
A111	L335	P396		F192	F236	L180		L192	A171	P390		D211
Y115	T338	V454		L204	Y281	W181		F196	A172	T392		F220
Q134	F339	I457		G208	F282	V285		E197	L268	L393		S265
E138	Q403	L467		E209	L286	M288		I227	V271	P394		F269
H141	I404	V470			L289	Y292			L272	I396		T273
Q145	P405	V471			F290	G293			P275	P403		I276
P175	I407	Y475				L346			Y280	I404		M277
F178	P453					Y347			G330	L450		T281
F179						L349			M331	V451		F293
A193						A350			H332	I459		
I194						L353			V335	L464		
S197						W354			W342	A467		
F198						T356			W343	L468		
E199						G357			P346	M471		
L202						W354			L402			
L205						T356						
L206						G357						
F210						F358						
M211						F359						
F225						R360						
A229						L361						
W265						L362						
G269						P424						
L272						A497						
L273						Q498						
V276						V501						

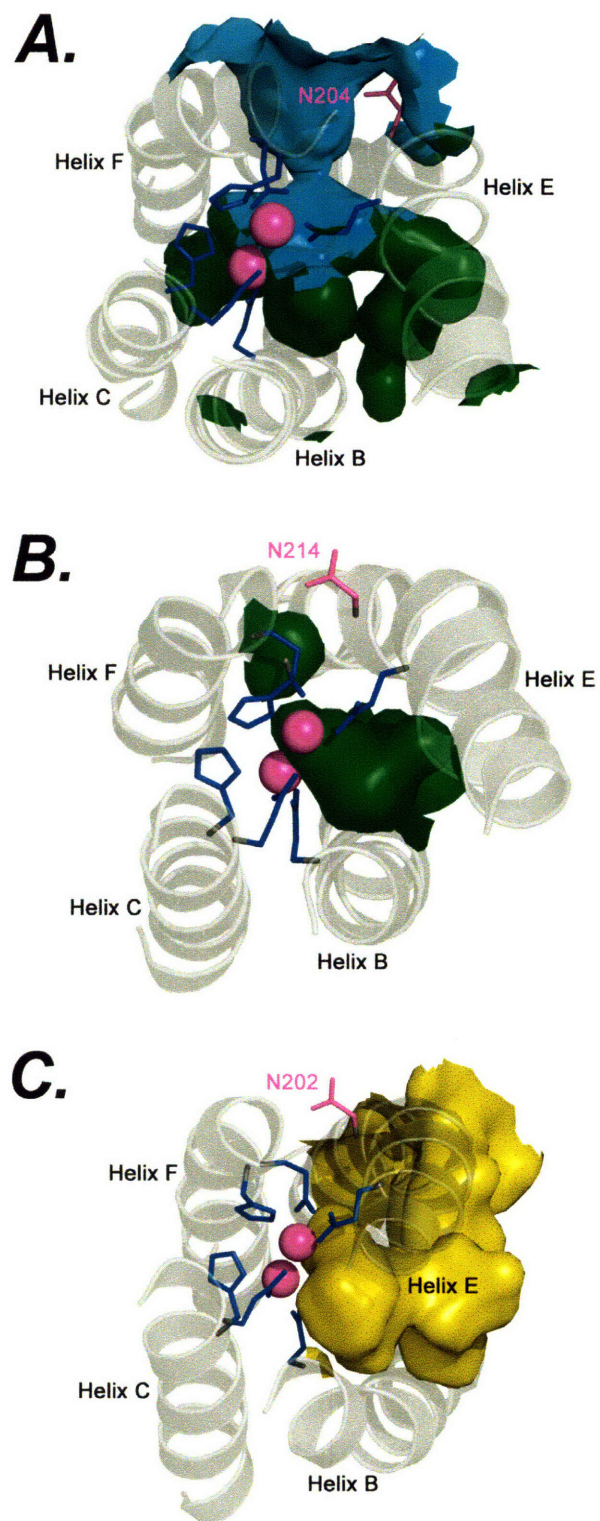


Figure 4.1. A view down the four-helix bundle (grey ribbons) in PHH (A), MMOH (B), and ToMOH (C). The active site pocket (green) and pore region (cyan) in PHH, cavity 1 (green) in MMOH, and the channel (yellow) in ToMOH are shown as van der Waals surfaces. Iron atoms and ligands are shown as spheres (magenta) and sticks (blue), respectively.

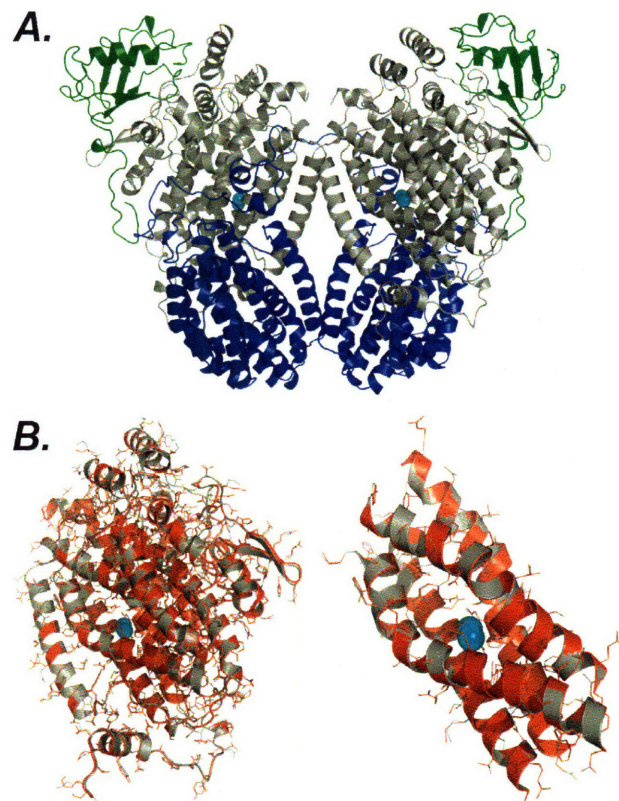


Figure 4.2. Global view of the dimer structure (A) and comparison of the α -subunits (B, left) and four-helix bundles (B, right) from protomers A and B in Xe-PHH. In (A) the α -subunits (grey), β -subunits (blue), and γ -subunits (green) are shown as ribbons. In (B) the protein backbone is shown as ribbons and side chains are shown as sticks in grey (protomer A) and red (protomer B). In all cases iron atoms are shown as spheres in cyan.

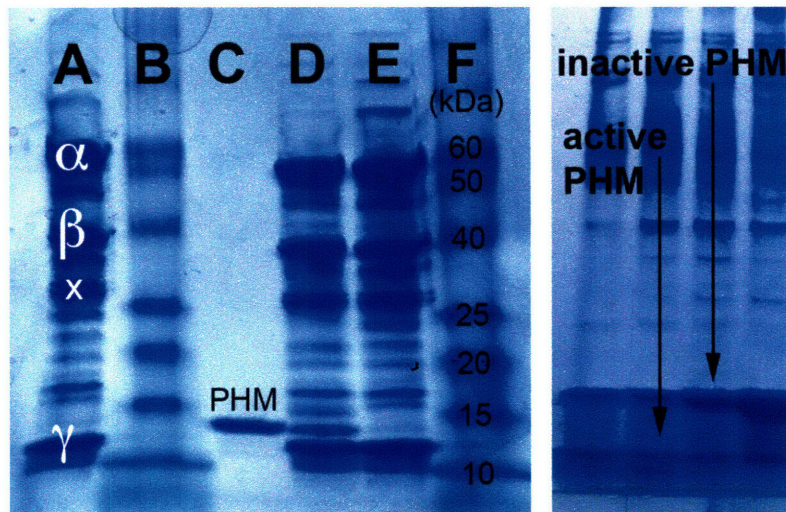


Figure 4.3. SDS-PAGE analysis of purified PHH and PHM expression products (left), and native PAGE analysis of PHM purification fractions (right). The SDS-PAGE gel shows purified PHH from expression using the plasmid containing the genes for PHH and PHK in lane A and E; bands corresponding to the PHH α -, β -, and γ -subunits, as well as an unidentified impurity (x) are labeled in lane A. Protein molecular weight standards are shown in lanes B and F; kDa values corresponding to the molecular weight standards are labeled in lane F. Purified PHM is shown in lane C. PHH from expression using the plasmid containing the genes for PHH, PHP, and PHM. The native PAGE gel shows the active fast-running and inactive slow-running forms of PHM.

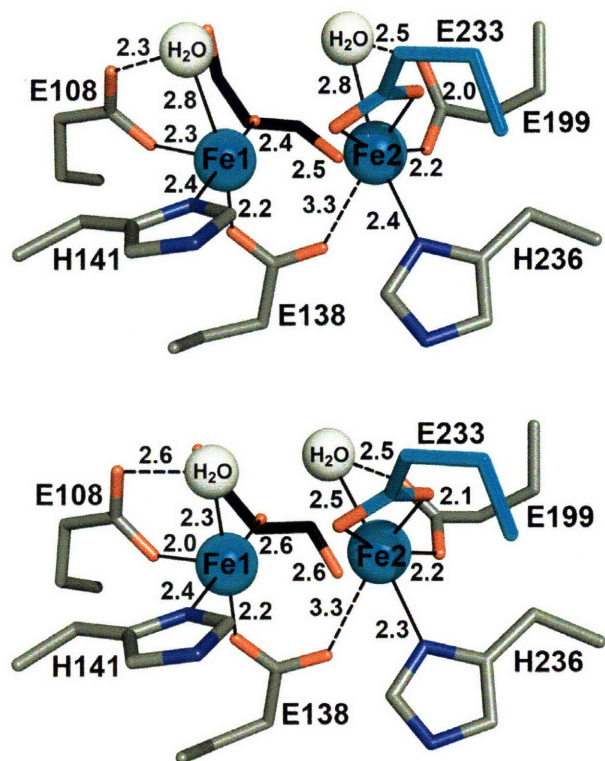


Figure 4.4. Active site coordination and geometry in PHH protomers A (top) and B (bottom). Iron atoms (cyan) and water molecules (white) are shown as spheres. Protein and glycerol ligands are shown as sticks in grey (carbon; protein ligands), cyan (carbon; E233), black (carbon; glycerol), red (oxygen), and blue (nitrogen). Interatomic distances are provided in angstroms.

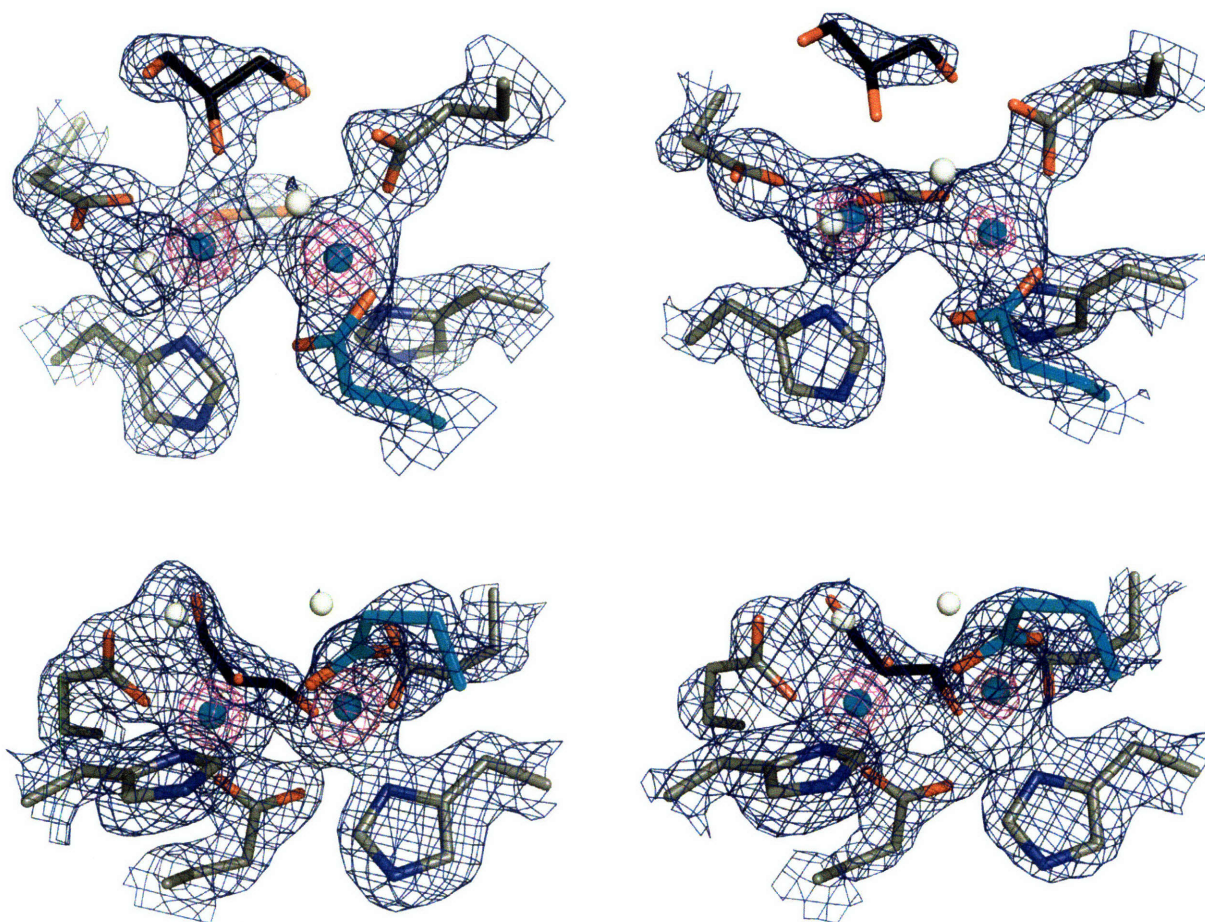


Figure 4.5. Composite omit map electron density, contoured to 1.5 sigma (blue) and 6.0 sigma (magenta) in the iron coordination environments of Xe-PHH protomers A (left) and B (right). The density and model are depicted from two views (top and bottom), which are related by a 90° rotation about the Fe–Fe vector. Iron ligands are depicted as sticks in grey/cyan (carbon), red (oxygen), and blue (nitrogen). Iron atoms and solvent derived ligands are shown as spheres in cyan and white, respectively.

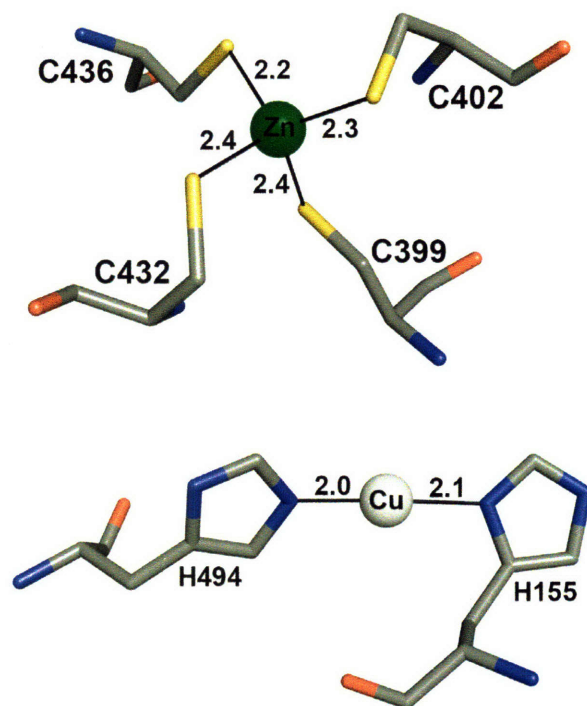


Figure 4.6. Zinc (top) and copper (bottom) binding sites in PHH. Zinc and copper atoms are shown as spheres in green and white, respectively. Protein ligands are shown as sticks in grey (carbon), yellow (sulfur), red (oxygen), and blue (nitrogen). Interatomic distances are provided in angstroms.

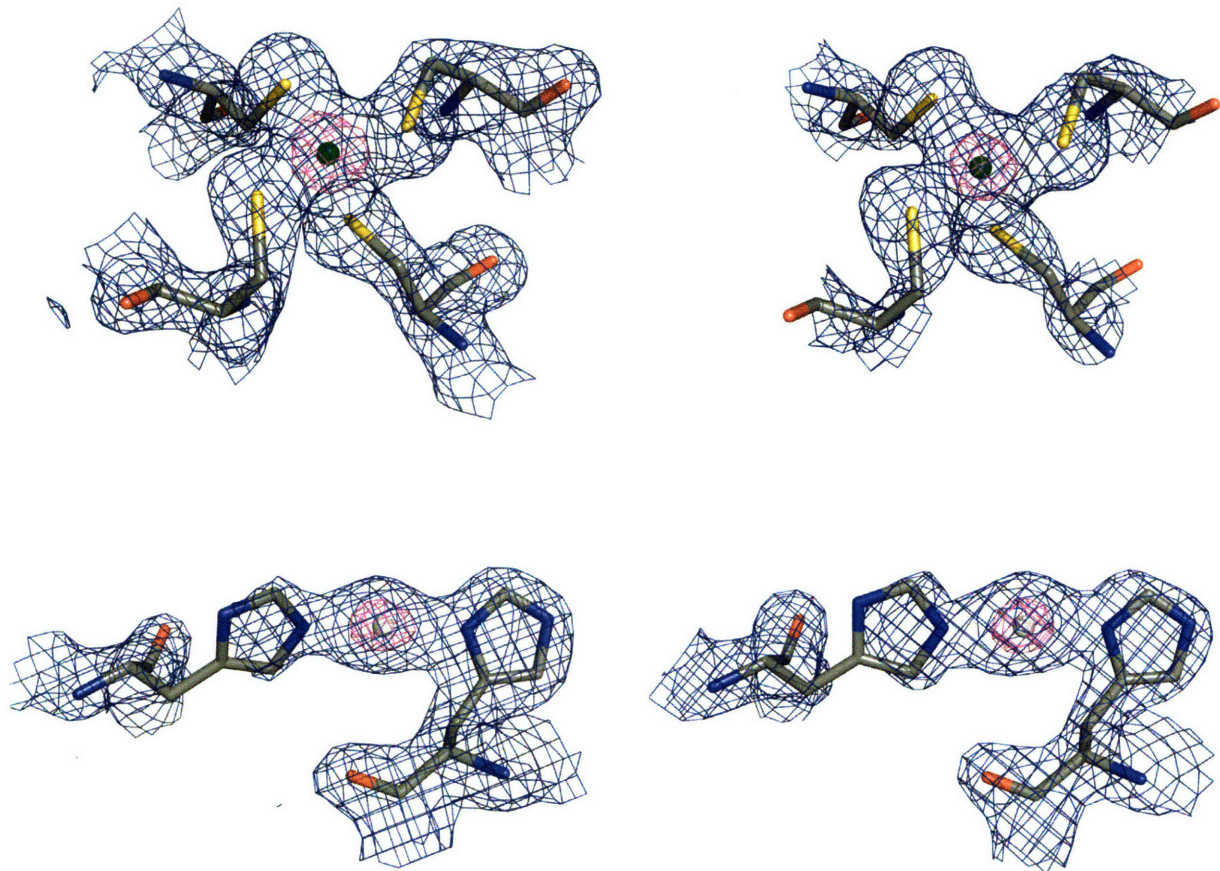


Figure 4.7. Composite omit map electron density, contoured to 1.5 sigma (blue) and 6.0 sigma (magenta) in the zinc (top) and copper (bottom) coordination environments of Xe-PHH protomers A (left) and B (right). Metal ligands are depicted as sticks in grey (carbon), red (oxygen), blue (nitrogen), and yellow (sulfur). Zinc and copper ions are shown as spheres in green and white, respectively.

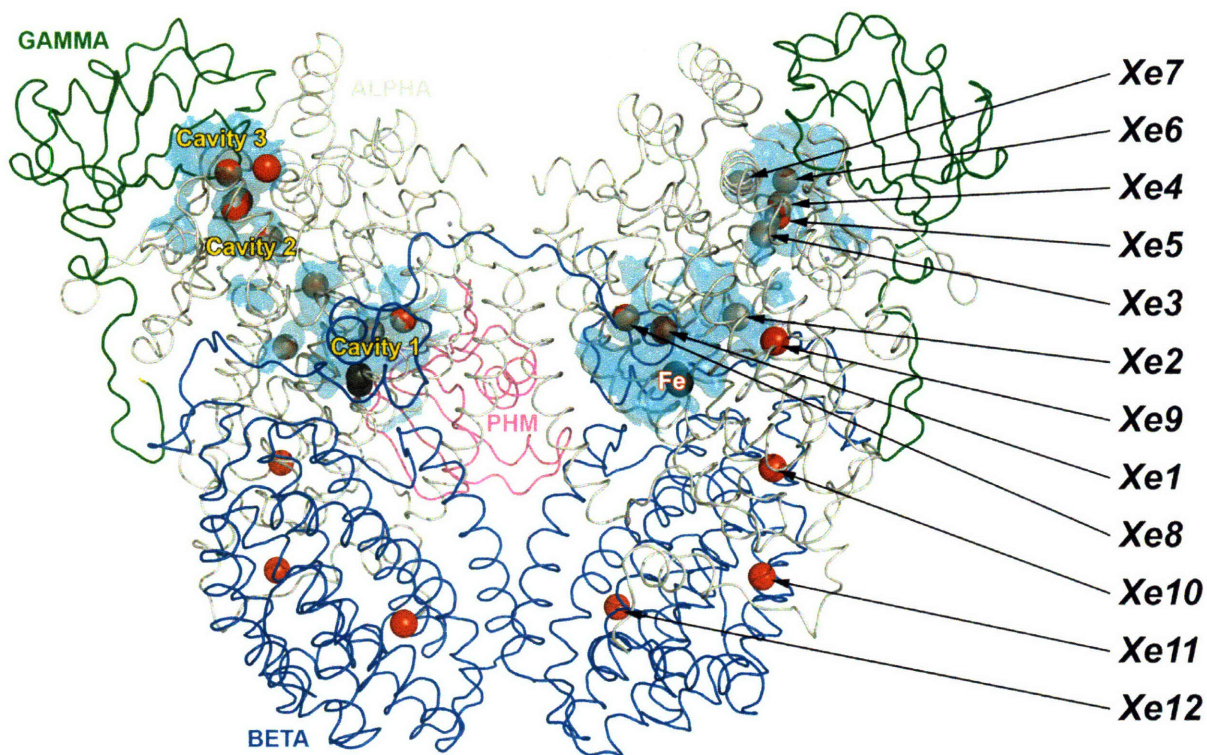
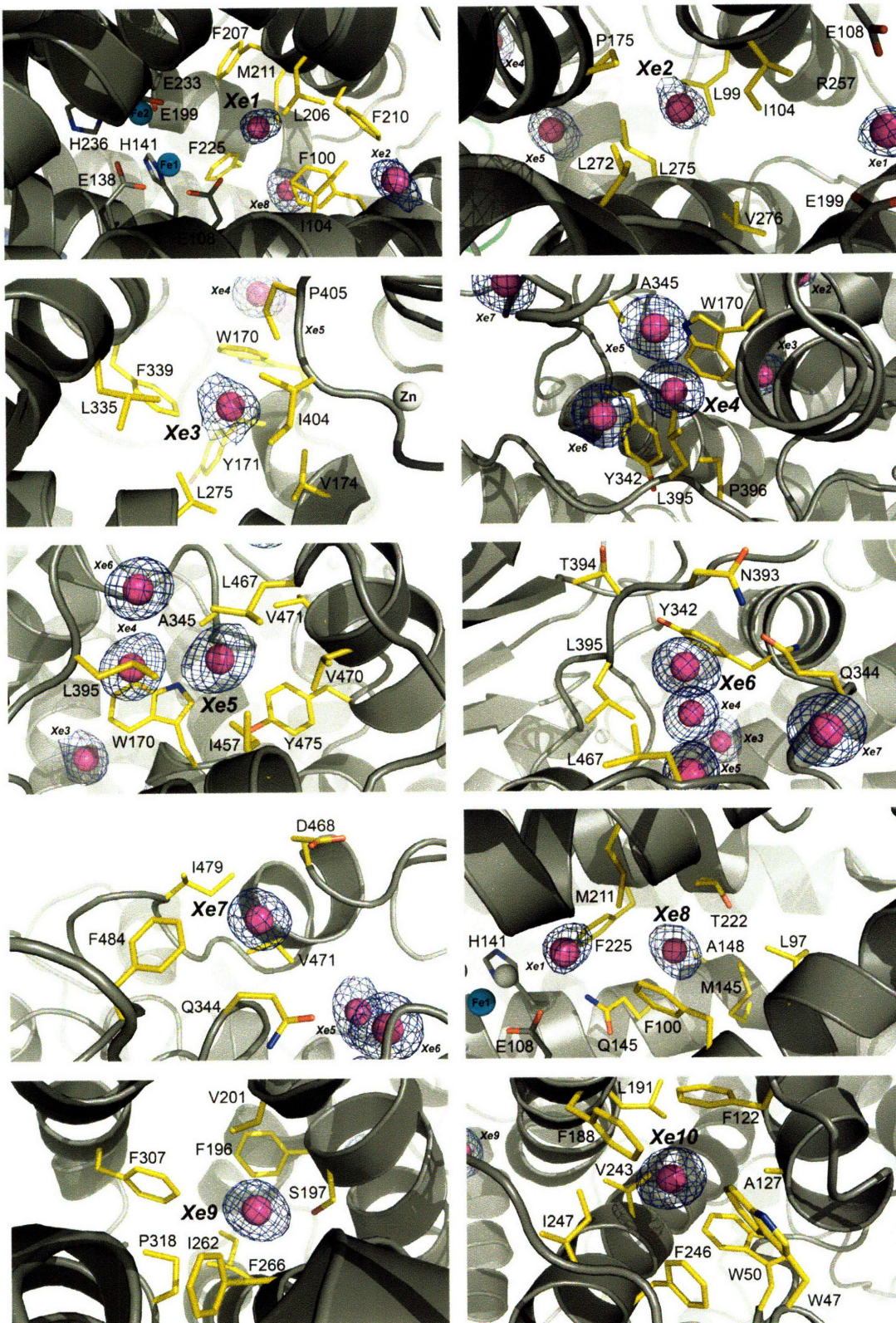


Figure 4.8. Overview of the xenon binding locations in Xe-PHH. Protein C_α trace is shown as ribbons in grey (α -subunit), blue (β -subunit), green (γ -subunit), and magenta (PHM). Iron and xenon atoms are depicted as black and red spheres, respectively. Xenon-binding hydrophobic cavities are represented as translucent van der Waals surfaces in cyan.

Figure 4.9. (Next Page) Detailed view of xenon binding sites in the α -subunit of Xe-PHH. Xenon (magenta), iron (cyan), and zinc (white) atoms are shown as spheres. Residues within 5 Å of xenon atoms are shown as sticks in yellow (carbon), red (oxygen), and blue (nitrogen). Composite omit electron density contoured to 5.0 sigma is shown in dark blue. The protein backbone is shown as grey ribbons.



Michaelis-Menten Kinetics: Oxygen vs. Xenon in PHH

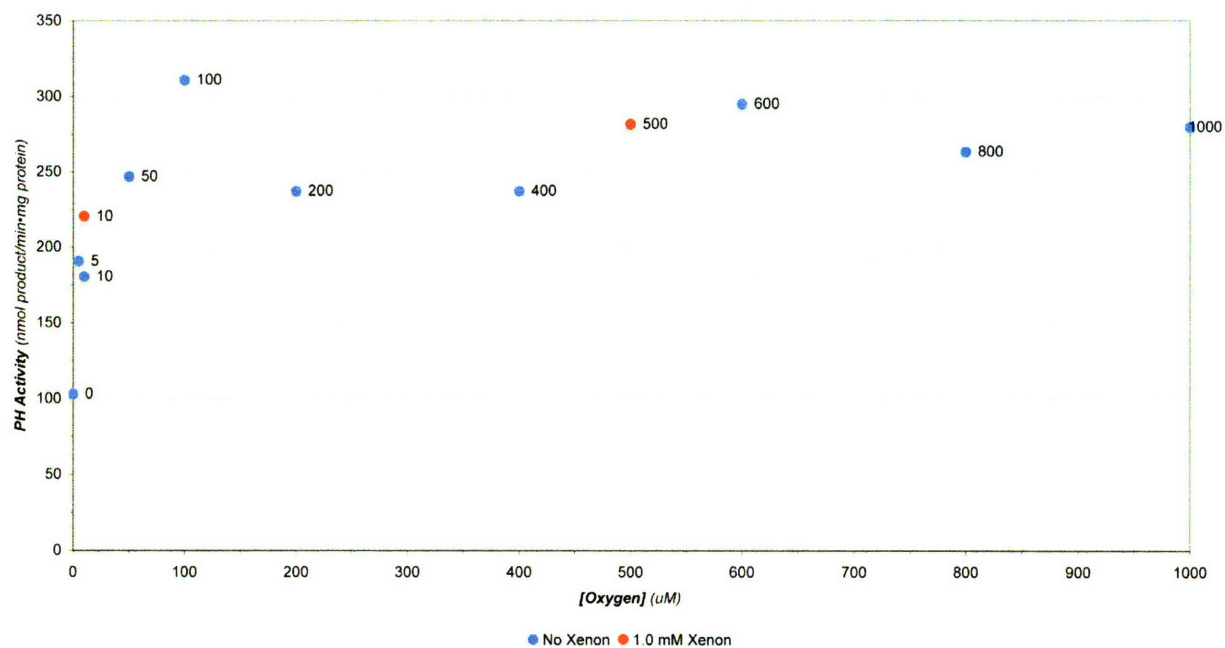


Figure 4.10. Michaelis-Menten plot of PH activity at various concentrations of dioxygen and xenon gas. Data point labels indicate the micromolar concentration of dioxygen used.

PHH

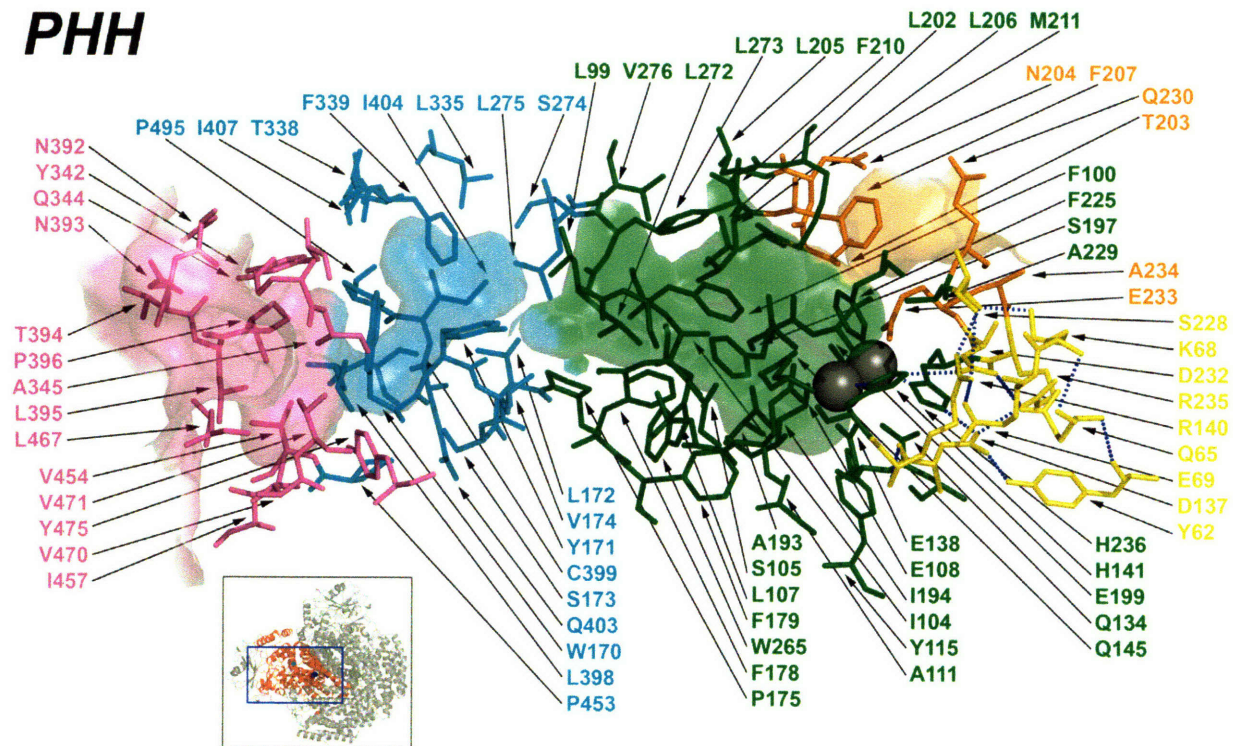


Figure 4.11. Surface-to-active site voids in the α -subunit of PHH. Hydrophobic cavities and pore region voids are represented as van der Waals surfaces in magenta (cavity 3), cyan (cavity 2), green (cavity 1), and orange (pore region). Protein residues that contribute to the van der Waals surface are shown as sticks using the same color scheme as the surface representations. The putative electron-transport hydrogen-bonding network residues are shown as yellow sticks. Iron atoms are represented as dark grey spheres. The inset indicates the orientation of the hydroxylase dimer (grey ribbons) and α -subunit (red ribbons) in the primary figure.

MMOH

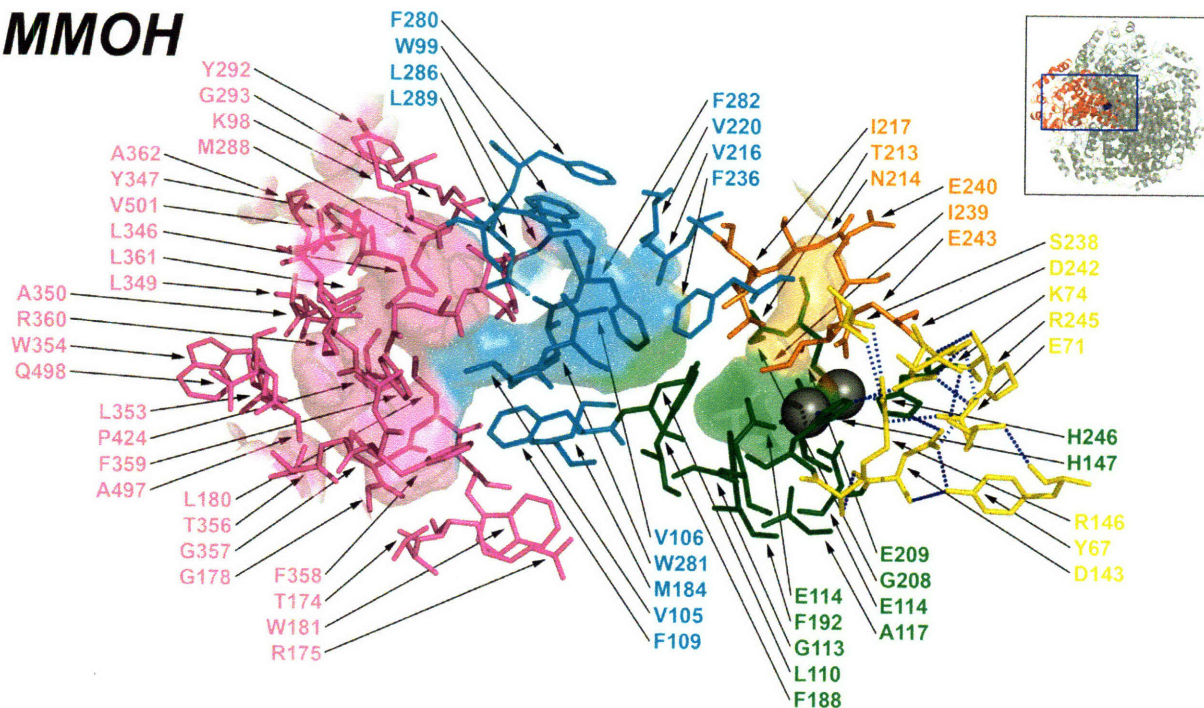


Figure 4.12. Surface-to-active site voids in the α -subunit of MMOH. Hydrophobic cavities and pore region voids are represented as van der Waals surfaces in magenta (cavity 3), cyan (cavity 2), green (cavity 1), and orange (pore region). Protein residues that contribute to the van der Waals surface are shown as sticks using the same color scheme as the surface representations. The putative electron-transport hydrogen-bonding network residues are shown as yellow sticks. Iron atoms are represented as dark grey spheres. The inset indicates the orientation of the hydroxylase dimer (grey ribbons) and α -subunit (red ribbons) in the primary figure.

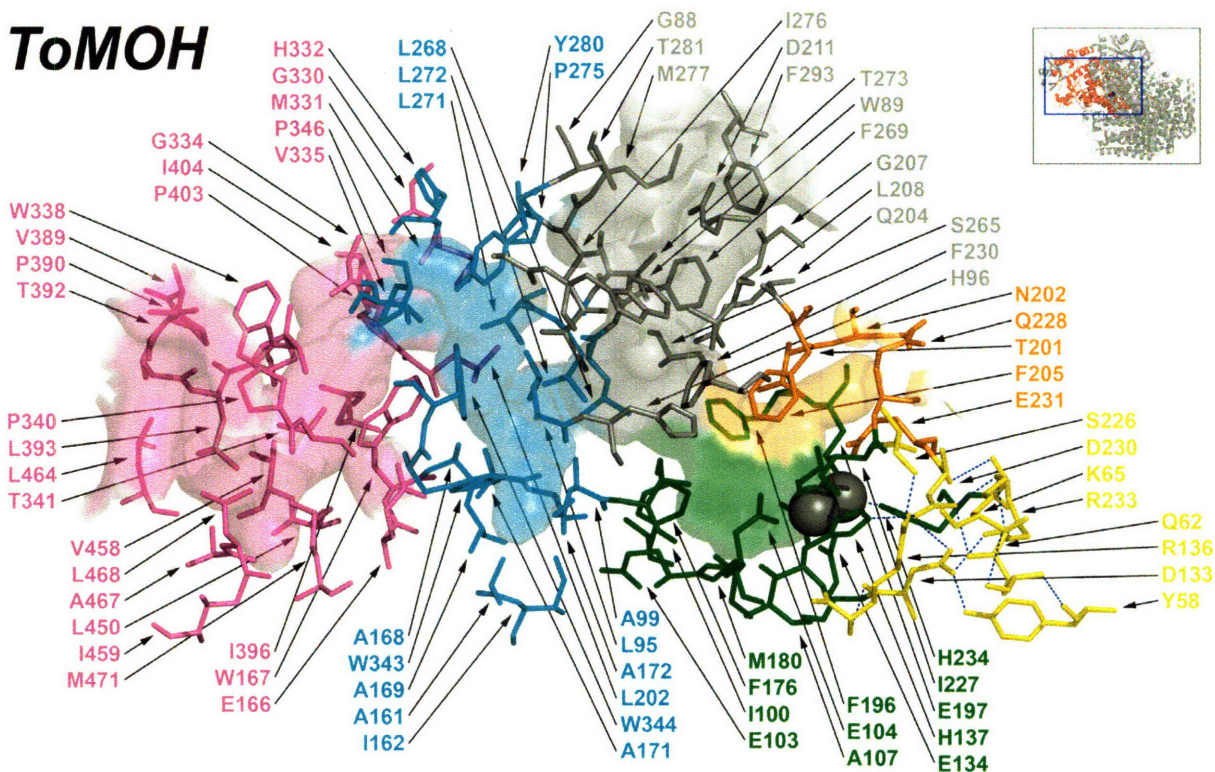


Figure 4.13. Surface-to-active site voids in the α -subunit of ToMOH. Hydrophobic cavities, pore region, and channel voids are represented as van der Waals surfaces in magenta (cavity 3), cyan (cavity 2), green (cavity 1), orange (pore region), and grey (channel). Protein residues that contribute to the van der Waals surface are shown as sticks using the same color scheme as the surface representations. The putative electron-transport hydrogen-bonding network residues are shown as yellow sticks. Iron atoms are represented as dark grey spheres. The inset indicates the orientation of the hydroxylase dimer (grey ribbons) and α -subunit (red ribbons) in the primary figure.

Figure 4.14. (next two pages) Results from BMM hydroxylase sequence alignments. Diiron site ligands are highlighted magenta and residues with side chain contributes to xenon binding sites in Xe-PHH are highlighted blue.

Phenol Hydroxylase (Pseudomonas sp. OX1)	M V S K N K K L N L K D K Y Q Y L T R D M A W E P T Y Q D K K D I F P - - - - - E E D F	39
Methane Monooxygenase (Methylococcus Capsulatus)	- - - - - M A L S T A T K A A T D A L A A N R A P T S V N A Q E V H R W L Q S F N W D F K N N R T K	45
Toluene/o-Xylene Monooxygenase (Pseudomonas sp. OX1)	- - - - - M S M L K R E D W Y D L T R T T N W T P K Y V T E N E L F P - - - - - E E M S G A	36
Toluene-4-Monooxygenase (Pseudomonas Mendocina)	- - - - - M A M H P R K D W Y E L T R A T N W T P S Y V T E E Q L F P - - - - - E R M S G H	36
Alkene Monooxygenase (Rhodococcus sp. RHA1)	- - - - - M S R Q S L T K A H A K I T E L S W D P T F A T P - - - - - - - - - - - A T R	28
Butane Monooxygenase (Pseudomonas butanovora)	- - - - - M S A N M A V K Q A L K A N P V P S S V D P Q E V H K W L Q D F T W D F K G K T A K	42

Phenol Hydroxylase (Pseudomonas sp. OX1)	E G I K I T D W S Q - W E D P F R L T M D A Y W K Y Q A E K E K K L Y A I F D A F A Q N N G H Q N I	88
Methane Monooxygenase (Methylococcus Capsulatus)	Y A T K Y K M A N E - T K E Q F K L I A K E Y A R M E A V K D E R Q F G S L Q D A L T R L N A G V R	94
Toluene/o-Xylene Monooxygenase (Pseudomonas sp. OX1)	R G I S M E A W E K - Y D E P Y K I T Y P E Y V S I Q R E K D S G A Y - S I K A A L E R D G F V D R	84
Toluene-4-Monooxygenase (Pseudomonas Mendocina)	M G I P L E K W E S - Y D E P Y K T S Y P E Y V S I Q R E K D A G A Y - S V K A A L E R A K I Y E N	84
Alkene Monooxygenase (Rhodococcus sp. RHA1)	F G T D Y T F E K A P K K D P L K Q I M R S Y F P M E E E K D N R V Y G A M D G A I R G - N M F R Q	77
Butane Monooxygenase (Pseudomonas butanovora)	Y P T K Y E M D V N - T R E Q F K L T A K E Y A R M E S I K E E R Q Y G T L L D G L D R L D A G N K	91

Phenol Hydroxylase (Pseudomonas sp. OX1)	S D A R Y V N A L K L F I S G I S P L E H A A F Q G Y S K V G R Q F S G A G A R V A C Q M Q A I D E	138
Methane Monooxygenase (Methylococcus Capsulatus)	V H P K W N E T M K V V S N F L E V G E Y N A I A A T G M L W D S A Q A A E Q K N G Y L A Q V L D E	144
Toluene/o-Xylene Monooxygenase (Pseudomonas sp. OX1)	A D P G W V S T M Q L H F G A I A L E E Y A A S T A E A R M A R F A K A P G N R N M A T F G M M D E	134
Toluene-4-Monooxygenase (Pseudomonas Mendocina)	S D P G W I S T L K S H Y G A I A V G E Y A A V T G E G R M A R F S K A P G N R N M A T F G M M D E	134
Alkene Monooxygenase (Rhodococcus sp. RHA1)	V Q Q R W L E W Q K L F L S I I P F P E I S A A R A M P M A I D A V P N P E I H N G L A V Q M I D E	127
Butane Monooxygenase (Pseudomonas butanovora)	V H P K W G E V M K L V S N F L E T G E Y G A I A G S A L L W D T A Q S P E Q R N G Y L A Q V I D E	141

Phenol Hydroxylase (Pseudomonas sp. OX1)	L R H S Q T Q Q H A M S H Y N K H - - - F N G L H D G P H M H D R V W Y L S V P K S F F D D A R S A	185
Methane Monooxygenase (Methylococcus Capsulatus)	I R H T H Q C A Y V N Y Y F A K N G Q D P A G H N D A R R T R T I G P L W K G M K R V F S D G F I S	194
Toluene/o-Xylene Monooxygenase (Pseudomonas sp. OX1)	N R H G Q I Q L Y F P Y A N V K R - - S R K W D W A H K A I H T N E W A A I A A R S F F D D M M M T	182
Toluene-4-Monooxygenase (Pseudomonas Mendocina)	L R H G Q L Q L F F P H E Y C K K - - D R Q F D W A W R A Y H S N E W A A I A A K H F F D D I I T G	182
Alkene Monooxygenase (Rhodococcus sp. RHA1)	V R H S T I Q M N L K K L Y M N N Y I D P A G F D M T E K A F A N N Y A G - T I G R Q F G E G F I T	176
Butane Monooxygenase (Pseudomonas butanovora)	I R H V N Q T A Y V N Y Y Y G K H Y Y D P A G H T N M R Q L R A I N P L Y P G V K R A F G E G F L A	191

	Helix E	Helix F	
Phenol Hydroxylase (Pseudomonas sp. OX1)	G P F E F L T - - A I S F S F E Y V L T N L L F V P F M S G A A Y N G D M A T V T F G F S A Q S D E	233	
Methane Monooxygenase (Methylococcus Capsulatus)	G D A V E C S - L N L Q L V G E A C F T N P L I V A V T E W A A A N G D E I T P T V F L S I E T D E	243	
Toluene/o-Xylene Monooxygenase (Pseudomonas sp. OX1)	R D S V A V S - I M L T F A F E T G F T N M Q F L G L A A D A A E A G D H T F A S L I S S I Q T D E	231	
Toluene-4-Monooxygenase (Pseudomonas Mendocina)	R D A I S V A - I M L T F S F E T G F T N M Q F L G L A A D A A E A G D Y T F A N L I S S I Q T D E	231	
Alkene Monooxygenase (Rhodococcus sp. RHA1)	G D A I T A A N I Y L T V V A E T A F T N T L F V A M P D E A A A N G D Y L L P T V F H S V Q S D E	226	
Butane Monooxygenase (Pseudomonas butanovora)	G D A V E S S - I N L Q L V G E A C F T N P L I V S L T E W A A A N G D E I T P T V F L S I E T D E	240	

	Helix F	
Phenol Hydroxylase (Pseudomonas sp. OX1)	A R H M T L G L E V I K F I L E Q H E D N V P I V Q R W I D K W F W R G F R L L S L V S - M M M D Y	282
Methane Monooxygenase (Methylococcus Capsulatus)	L R H M A N G Y Q T V V S I A N D P - A S A K Y L N T D L N N A F W T Q Q K Y F T P V L G M L F E Y	292
Toluene/o-Xylene Monooxygenase (Pseudomonas sp. OX1)	S R H A Q Q G G P S L K I L V E N - - G K K D E A Q Q M V D V A I W R S W K L F S V L T G P I M D Y	279
Toluene-4-Monooxygenase (Pseudomonas Mendocina)	S R H A Q Q G G P A L Q L L I E N - - G K R E E A Q K K V D M A I W R A W R L F A V L T G P V M D Y	279
Alkene Monooxygenase (Rhodococcus sp. RHA1)	S R H I S N G Y S I L L M A L A D E - R N R P L L E R D L R Y A W W N N H C V D A A I G T F I E Y	275
Butane Monooxygenase (Pseudomonas butanovora)	L R H M A N G Y Q T I V S I M N N P - E T M K Y L Q T D L D N A F W T Q H K F L T P F V G V A L E Y	289

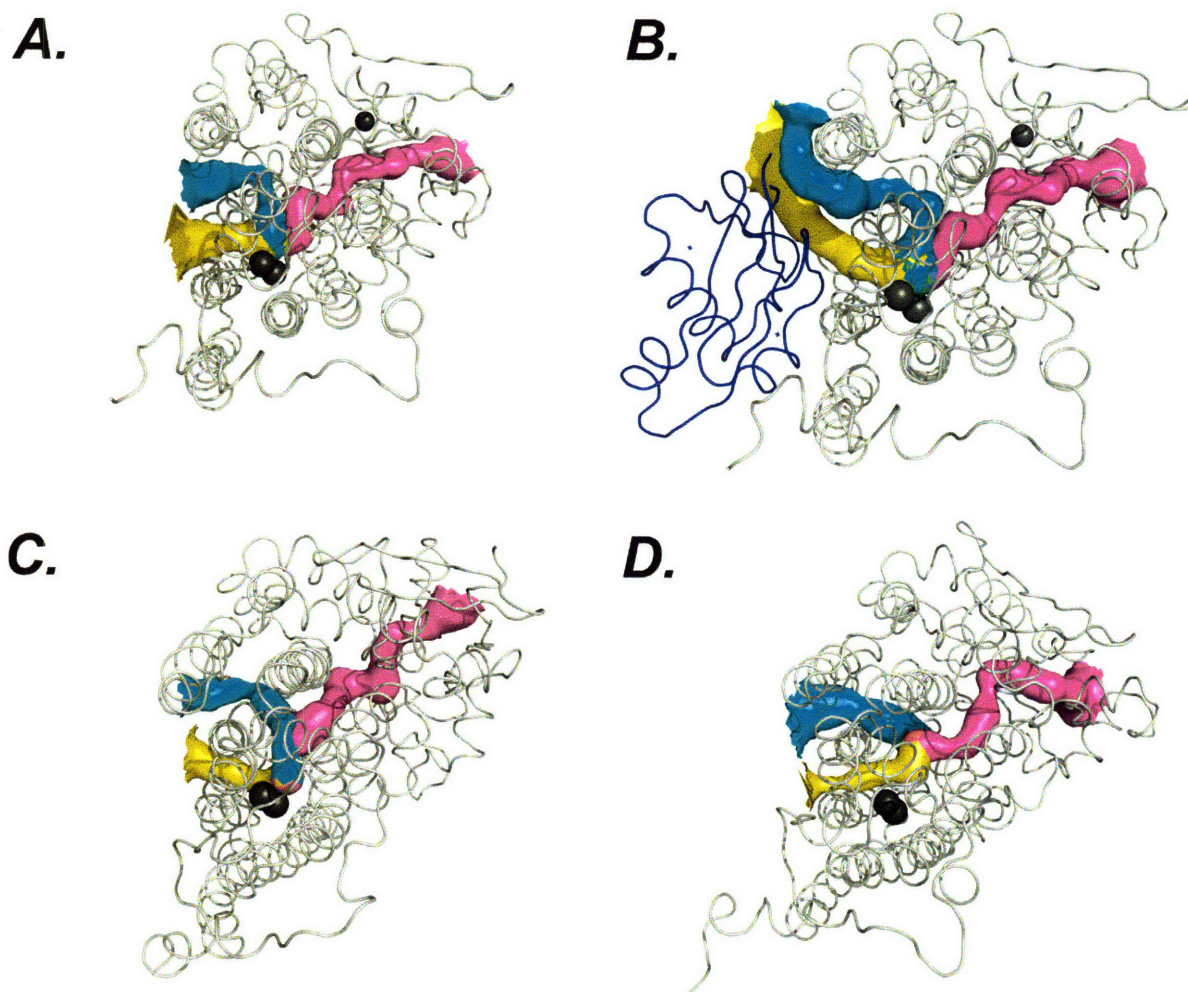


Figure 4.15. Diiron center access routes in the α -subunit of PHH (A), PHH-PHM (B), MMOH (C), and ToMOH (D) as calculated by CAVER. Substrate pathways are represented as surfaces in magenta (hydrophobic cavities), yellow (pore region), and cyan (channel). Hydroxylase α -subunit is shown as grey ribbons; PHM is shown as blue ribbons (B only). Iron and zinc (A and B only) atoms are shown as black spheres.

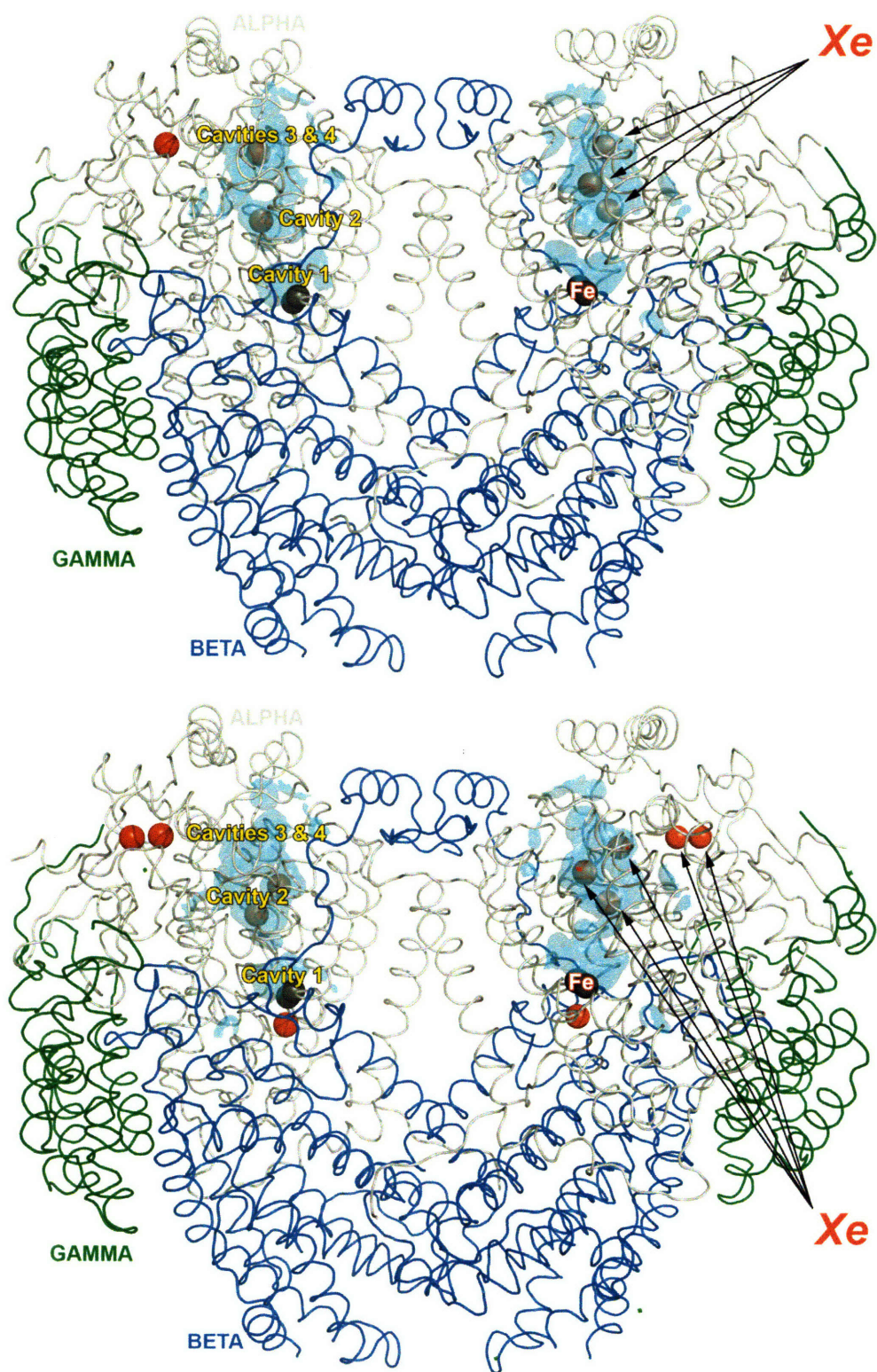


Figure 4.16. Overview of the xenon binding locations in MMOH form I (top) and form II (bottom) crystals. Protein C_α trace is shown as ribbons in grey (α -subunit), blue (β -subunit), and green (γ -subunit). Iron and xenon atoms are depicted as black and red spheres, respectively. Xenon-binding hydrophobic cavities are represented as translucent van der Waals surfaces in cyan.

References

1. Cafaro, V., Izzo, V., Scognamiglio, R., Notomista, E., Capasso, P., Casbarra, A., Pucci, P., and Di Donato, A. (2004) Phenol hydroxylase and toluene/*o*-xylene monooxygenase from *Pseudomonas stutzeri* OX1: interplay between two enzymes. *Appl. Environ. Microbiol.* 70, 2211-2219.
2. Sazinsky, M. H., and Lippard, S. J. (2006) Correlating structure with function in bacterial multicomponent monooxygenases and related diiron proteins. *Acc. Chem. Res.* 39, 558-566.
3. Leahy, J. G., Batchelor, P. J., and Morcomb, S. M. (2003) Evolution of the soluble diiron monooxygenases. *FEMS Microbiol. Rev.* 27, 449-479.
4. Sazinsky, M. H., Dunten, P. W., McCormick, M. S., DiDonato, A., and Lippard, S. J. (2006) X-ray Structure of a Hydroxylase-Regulatory Protein Complex from a Hydrocarbon-Oxidizing Multicomponent Monooxygenase, *Pseudomonas sp.* OX1 Phenol Hydroxylase. *Biochemistry* 45, 15392-15404.
5. Rosenzweig, A. C., Brandstetter, H., Whittington, D. A., Nordlund, P., Lippard, S. J., and Frederick, C. A. (1997) Crystal structures of the methane monooxygenase hydroxylase from *Methylococcus capsulatus* (Bath): implications for substrate gating and component interactions. *Proteins* 29, 141-152.
6. Rosenzweig, A. C., Frederick, C. A., Lippard, S. J., and Nordlund, P. (1993) Crystal structure of a bacterial non-heme iron hydroxylase that catalyzes the biological oxidation of methane. *Nature* 366, 537-543.
7. Rosenzweig, A. C., Nordlund, P., Takahara, P. M., Frederick, C. A., and Lippard, S. J. (1995) Geometry of the soluble methane monooxygenase catalytic diiron center in two oxidation states. *Chem. Biol.* 2, 632.
8. Sazinsky, M. H., and Lippard, S. J. (2005) Product Bound Structures of the Soluble Methane Monooxygenase Hydroxylase from *Methylococcus capsulatus* (Bath): Protein Motion in the alpha-Subunit. *J. Am. Chem. Soc.* 127, 5814-5825.
9. Sazinsky, M. H., Merckx, M., Cadieux, E., Tang, S., and Lippard, S. J. (2004) Preparation and x-ray structures of metal-free, dicobalt and dimanganese forms of soluble methane monooxygenase hydroxylase from *Methylococcus capsulatus* (Bath). *Biochemistry* 43, 16263-16276.
10. Whittington, D. A., and Lippard, S. J. (2001) Crystal Structures of the Soluble Methane Monooxygenase Hydroxylase from *Methylococcus capsulatus* (Bath)

Demonstrating Geometrical Variability at the Dinuclear Iron Active Site. *J. Am. Chem. Soc.* 123, 827-838.

11. Whittington, D. A., Rosenzweig, A. C., Frederick, C. A., and Lippard, S. J. (2001) Xenon and Halogenated Alkanes Track Putative Substrate Binding Cavities in the Soluble Methane Monooxygenase Hydroxylase. *Biochemistry* 40, 3476-3482.

12. Whittington, D. A., Sazinsky, M. H., and Lippard, S. J. (2001) X-ray Crystal Structure of Alcohol Products Bound at the Active Site of Soluble Methane Monooxygenase Hydroxylase. *J. Am. Chem. Soc.* 123, 1794-1795.

13. Elango, N., Radhakrishnan, R., Froland, W. A., Wallar, B. J., Earhart, C. A., Lipscomb, J. D., and Ohlendorf, D. H. (1997) Crystal structure of the hydroxylase component of methane monooxygenase from *Methylosinus trichosporium* QB3b. *Protein Sci.* 6, 556-568.

14. McCormick, M. S., Sazinsky, M. H., Condon, K. L., and Lippard, S. J. (2006) X-ray crystal structures of manganese(II)-reconstituted and native toluene/o-xylene monooxygenase hydroxylase reveal rotamer shifts in conserved residues and an enhanced view of the protein interior. *J. Am. Chem. Soc.* 128, 15108-15110.

15. Sazinsky, M. H., Bard, J., Di Donato, A., and Lippard, S. J. (2004) Crystal Structure of the Toluene/o-Xylene Monooxygenase Hydroxylase from *Pseudomonas stutzeri* OX1: Insight Into the Substrate Specificity, Substrate Channeling, And Active Site Tuning of Multicomponent Monooxygenases. *J. Biol. Chem.* 279, 30600-30610.

16. Stubbe, J. (2003) Di-iron-tyrosyl radical ribonucleotide reductases. *Curr. Opin. Chem. Biol.* 7, 183-188.

17. Carrondo, M. A. (2003) Ferritins, iron uptake and storage from the bacterioferritin viewpoint. *EMBO J.* 22, 1959-1968.

18. Lindqvist, Y., Huang, W., Schneider, G., and Shanklin, J. (1996) Crystal structure of delta9 stearoyl-acyl carrier protein desaturase from castor seed and its relationship to other di-iron proteins. *EMBO J.* 15, 4081-4092.

19. Murray, L. J., and Lippard, S. J. (2007) Substrate trafficking and dioxygen activation in bacterial multicomponent monooxygenases. *Acc. Chem. Res.* 40, 466-474.

20. Tilton, R. F., Jr., Kuntz, I. D., Jr., and Petsko, G. A. (1984) Cavities in proteins: structure of a metmyoglobin xenon complex solved to 1.9 Å. *Biochemistry* 23, 2849-2857.

21. Poet, M., Tauc, M., Lingueglia, E., Cance, P., Poujeol, P., Lazdunski, M., and Counillon, L. (2001) Exploration of the pore structure of a peptide-gated Na⁺ channel. *EMBO J.* 20, 5595-5602.
22. Murray, L. J., Garcia-Serres, R., McCormick, M. S., Davydov, R., Naik, S. G., Kim, S.-H., Hoffman, B. M., Huynh, B. H., and Lippard, S. J. (2007) Dioxygen Activation at Non-Heme Diiron Centers: Oxidation of a Proximal Residue in the I100W Variant of Toluene/o-Xylene Monooxygenase Hydroxylase. *Biochemistry* 46, 14795-14809.
23. Mansoor, S. E., McHaourab, H. S., and Farrens, D. L. (1999) Determination of Protein Secondary Structure and Solvent Accessibility Using Site-Directed Fluorescence Labeling. Studies of T4 Lysozyme Using the Fluorescent Probe Monobromobimane. *Biochemistry* 38, 16383-16393.
24. Damborsky, J., Petrek, M., Banas, P., and Otyepka, M. (2007) Identification of tunnels in proteins, nucleic acids, inorganic materials and molecular ensembles. *Biotechnol. J.* 2, 62-67.
25. Kleywegt, G. J., and Jones, T. A. (1994) Detection, delineation, measurement and display of cavities in macromolecular structures. *Acta Crystallogr.* 50, 178-185.
26. Petrek, M., Kosinova, P., Koca, J., and Otyepka, M. (2007) MOLE: A Voronoi Diagram-Based Explorer of Molecular Channels, Pores, and Tunnels. *Structure* 15, 1357-1363.
27. Petrek, M., Otyepka, M., Banas, P., Kosinova, P., Koca, J., and Damborsky, J. (2006) CAVER: a new tool to explore routes from protein clefts, pockets and cavities. *BMC Bioinf.* 7, 316-324.
28. Doukov, T. I., Blasiak, L. C., Seravalli, J., Ragsdale, S. W., and Drennan, C. L. (2008) Xenon in and at the End of the Tunnel of Bifunctional Carbon Monoxide Dehydrogenase/Acetyl-CoA Synthase. *Biochemistry* 47, 3474-3483.
29. Prange, T., Schiltz, M., Pernot, L., Colloc'h, N., Longhi, S., Bourguet, W., and Fourme, R. (1998) Exploring hydrophobic sites in proteins with xenon or krypton. *Proteins* 30, 61-73.
30. Cohen, A., Ellis, P., Kresge, N., and Soltis, S. M. (2001) MAD phasing with krypton. *Acta Crystallogr.* D57, 233-238.
31. Sauer, O., Schmidt, A., and Kratky, C. (1997) Freeze-trapping isomorphous xenon derivatives of protein crystals. *J. Appl. Crystallogr.* 30, 476-486.

32. Schiltz, M., Fourme, R., and Prange, T. (2003) Use of noble gases xenon and krypton as heavy atoms in protein structure determination. *Methods Enzymol.* 374, 83-119.
33. Schiltz, M., Prange, T., and Fourme, R. (1994) On the preparation and x-ray data collection and isomorphous xenon derivatives. *J. Appl. Crystallogr.* 27, 950-960.
34. Schiltz, M., Shepard, W., Fourme, R., Prange, T., de la Fortelle, E., and Bricogne, G. (1997) High-pressure krypton gas and statistical heavy-atom refinement: a successful combination of tools for macromolecular structure determination. *Acta Crystallogr. D53*, 78-92.
35. Tilton, R. F., Jr., and Kuntz, I. D., Jr. (1982) Nuclear magnetic resonance studies of xenon-129 with myoglobin and hemoglobin. *Biochemistry* 21, 6850-6857.
36. Berthault, P., Huber, G., Ha, P. T., Dubois, L., Desvaux, H., and Guittet, E. (2006) Study of the hydrophobic cavity of beta -cryptogein through laser-polarized xenon NMR spectroscopy. *ChemBioChem* 7, 59-64.
37. Brunner, E. (2005) Detection of multiple protein conformations by laser-polarized xenon. *Protein Sci.* 14, 847.
38. Cherubini, A., and Bifone, A. (2003) Hyperpolarized xenon in biology. *Prog. Nucl. Magn. Reson. Spectrosc.* 42, 1-30.
39. Rubin, S. M., Spence, M. M., Dimitrov, I. E., Ruiz, E. J., Pines, A., and Wemmer, D. E. (2001) Detection of a Conformational Change in Maltose Binding Protein by ¹²⁹Xe NMR Spectroscopy. *J. Am. Chem. Soc.* 123, 8616-8617.
40. Locci, E., Dehouck, Y., Casu, M., Saba, G., Lai, A., Luhmer, M., Reisse, J., and Bartik, K. (2001) Probing proteins in solution by ¹²⁹Xe NMR spectroscopy. *J. Magn. Reson.* 150, 167-174.
41. Saba, G., Casu, M., and Lai, A. (1996) Application of quadrupolar ¹³¹Xe-NMR relaxation to the study of macromolecular systems. *Int. J. Quant. Chem.* 59, 343-348.
42. Tilton, R. F., Jr., and Petsko, G. A. (1988) A structure of sperm whale myoglobin at a nitrogen gas pressure of 145 atmospheres. *Biochemistry* 27, 6574-6582.
43. Duff, A. P., Trambaiolo, D. M., Cohen, A. E., Ellis, P. J., Juda, G. A., Shepard, E. M., Langley, D. B., Dooley, D. M., Freeman, H. C., and Guss, J. M. (2004) Using Xenon as a Probe for Dioxygen-binding Sites in Copper Amine Oxidases. *J. Mol. Biol.* 344, 599-607.

44. DeLano, W. L. *The PyMOL Molecular Graphics System*, DeLano Scientific, San Carlos, CA, USA.
45. Tinberg, C. T., Izzo, V., and Lippard, S. J. unpublished results.
46. Cafaro, V., Scognamiglio, R., Viggiani, A., Izzo, V., Passaro, I., Notomista, E., Dal Piaz, F., Amoresano, A., Casbarra, A., Pucci, P., and Di Donato, A. (2002) Expression and purification of the recombinant subunits of toluene/*o*-xylene monooxygenase and reconstitution of the active complex. *Eur. J. Biochem.* 269, 5689-5699.
47. Izzo, V., and Lippard, S. J. unpublished results.
48. Gibbs, C. R. (1976) Characterization and application of FerroZine iron reagent as a ferrous iron indicator. *Anal. Chem.* 48, 1197-1201.
49. Soltis, S. M., Stowell, M. H. B., Wiener, M. C., Phillips, G. N., Jr., and Rees, D. C. (1997) Successful flash-cooling of xenon-derivatized myoglobin crystals. *J. Appl. Crystallogr.* 30, 190-194.
50. Cohen, A. E., Ellis, P. J., Miller, M. D., Deacon, A. M., and Phizackerley, R. P. (2002) An automated system to mount cryo-cooled protein crystals on a synchrotron beamline, using compact sample cassettes and a small-scale robot. *J. Appl. Crystallogr.* 35, 720-726.
51. McPhillips, T. M., McPhillips, S. E., Chiu, H. J., Cohen, A. E., Deacon, A. M., Ellis, P. J., Garman, E., Gonzalez, A., Sauter, N. K., Phizackerley, R. P., Soltis, S. M., and Kuhn, P. (2002) Blu-Ice and the Distributed Control System: software for data acquisition and instrument control at macromolecular crystallography beamlines. *J. Synchrotron Radiat.* 9, 401-406.
52. Otwinowski, Z., and Minor, W. (1997) Processing of x-ray diffraction data collected in oscillation mode. *Methods Enzymol.* 276, 307-326.
53. Kissinger, C. R., Gehlhaar, D. K., and Fogel, D. B. (1999) Rapid automated molecular replacement by evolutionary search. *Acta Crystallogr. D* 55, 484-491.
54. Emsley, P., and Cowtan, K. (2004) Coot: model-building tools for molecular graphics. *Acta Crystallogr. D* 60, 2126-2132.
55. Murshudov, G. N., Vagin, A. A., and Dodson, E. J. (1997) Refinement of macromolecular structures by the maximum-likelihood method. *Acta Crystallogr. D* 53, 240-255.

56. Anonymous. (1994) The CCP4 suite: programs for protein crystallography. *Acta Crystallogr.* 50, 760-763.
57. Brunger, A. T., Adams, P. D., Clore, G. M., DeLano, W. L., Gros, P., Grosse-Kunstleve, R. W., Jiang, J.-S., Kuszewski, J., Nilges, M., Pannu, N. S., Read, R. J., Rice, L. M., Simonson, T., and Warren, G. L. (1998) Crystallography & NMR System: a new software suite for macromolecular structure determination. *Acta Crystallogr. D54*, 905-921.
58. Kleywegt, G. J., and Jones, T. A. (1998) Databases in protein crystallography. *Acta Crystallogr.* 54, 1119-1131.
59. Tinberg, C. E., McCormick, M. S., Duduta, M., and Lippard, S. J. unpublished results.
60. Liang, H.-C., Kim, E., Incarvito, C. D., Rheingold, A. L., and Karlin, K. D. (2002) A Bis-Acetonitrile Two-Coordinate Copper(I) Complex: Synthesis and Characterization of Highly Soluble B(C₆F₅)₄⁻ Salts of [Cu(MeCN)₂]⁺ and [Cu(MeCN)₄]⁺. *Inorg. Chem.* 41, 2209-2212.
61. Sanyal, I., Strange, R. W., Blackburn, N. J., and Karlin, K. D. (1991) Formation of a copper-dioxygen complex (Cu₂-O₂) using simple imidazole ligands. *J. Am. Chem. Soc.* 113, 4692-4693.
62. Makowski, L., Rodi, D. J., Mandava, S., Minh, D. D. L., Gore, D. B., and Fischetti, R. F. (2008) Molecular Crowding Inhibits Intramolecular Breathing Motions in Proteins. *J. Mol. Biol.* 375, 529-546.
63. Johnson, B. J., Cohen, J., Welford, R. W., Pearson, A. R., Schulten, K., Klinman, J. P., and Wilmot, C. M. (2007) Exploring Molecular Oxygen Pathways in Hansenula polymorpha Copper-containing Amine Oxidase. *J. Biol. Chem.* 282, 17767-17776.
64. Schiltz, M., Fourme, R., Broutin, I., and Prange, T. (1995) The catalytic site of serine proteinases as a specific binding cavity for xenon. *Structure* 3, 309-316.

APPENDIX 1

X-ray Structure of a Hydroxylase-Regulatory Protein Complex from a Hydrocarbon-Oxidizing Multicomponent Monooxygenase, *Pseudomonas* sp. OX1 Phenol Hydroxylase

Author Contribution

The author was involved in many stages of the structure determination and analysis of the PHH-PHM complex. Specifically, the author assisted in diffraction data collection and the modeling of the native hydroxylase component. A majority of the analysis of the PHH-PHM interface, including the observation of the N202—S72 hydrogen bond. and preliminary structure and sequence alignments were conducted by the author. In addition, the electrostatics calculations reported in this work were also the responsibility of the author.

This appendix has been reprinted with permission from *Biochemistry* **2006**, 45, 15392-15404.

Copyright 2006 American Chemical Society.

X-ray Structure of a Hydroxylase–Regulatory Protein Complex from a Hydrocarbon-Oxidizing Multicomponent Monooxygenase, *Pseudomonas* sp. OX1 Phenol Hydroxylase^{†,‡}

Matthew H. Sazinsky,^{§,||} Pete W. Dunten,[†] Michael S. McCormick,[§] Alberto DiDonato,[@] and Stephen J. Lippard^{*,§}

Department of Chemistry, Massachusetts Institute of Technology, Cambridge, Massachusetts 02139, Stanford Synchrotron Radiation Laboratory, Stanford University, Menlo Park, California 94025, and Dipartimento di Biologia Strutturale e Funzionale, Università di Napoli Federico II and CEINGE Biotecnologie Avanzate, Napoli, Italy 80126

Received September 12, 2006; Revised Manuscript Received October 23, 2006

ABSTRACT: Phenol hydroxylase (PH) belongs to a family of bacterial multicomponent monooxygenases (BMMs) with carboxylate-bridged diiron active sites. Included are toluene/*o*-xylene (ToMO) and soluble methane (sMMO) monooxygenase. PH hydroxylates aromatic compounds, but unlike sMMO, it cannot oxidize alkanes despite having a similar dinuclear iron active site. Important for activity is formation of a complex between the hydroxylase and a regulatory protein component. To address how structural features of BMM hydroxylases and their component complexes may facilitate the catalytic mechanism and choice of substrate, we determined X-ray structures of native and SeMet forms of the PH hydroxylase (PHH) in complex with its regulatory protein (PHM) to 2.3 Å resolution. PHM binds in a canyon on one side of the ($\alpha\beta\gamma$)₂ PHH dimer, contacting α -subunit helices A, E, and F \sim 12 Å above the diiron core. The structure of the dinuclear iron center in PHH resembles that of mixed-valent MMOH, suggesting an Fe(II)Fe(III) oxidation state. Helix E, which comprises part of the iron-coordinating four-helix bundle, has more π -helical character than analogous E helices in MMOH and ToMOH lacking a bound regulatory protein. Consequently, conserved active site Thr and Asn residues translocate to the protein surface, and an \sim 6 Å pore opens through the four-helix bundle. Of likely functional significance is a specific hydrogen bond formed between this Asn residue and a conserved Ser side chain on PHM. The PHM protein covers a putative docking site on PHH for the PH reductase, which transfers electrons to the PHH diiron center prior to O₂ activation, suggesting that the regulatory component may function to block undesired reduction of oxygenated intermediates during the catalytic cycle. A series of hydrophobic cavities through the PHH α -subunit, analogous to those in MMOH, may facilitate movement of the substrate to and/or product from the active site pocket. Comparisons between the ToMOH and PHH structures provide insights into their substrate regioselectivities.

Bacterial multicomponent monooxygenases (BMMs)¹ are a diverse family of enzymes that hydroxylate and epoxidize an array of hydrocarbon substrates, including alkanes,

alkenes, and aromatics in a regio- and enantioselective fashion (1–3). This chemistry takes place at a carboxylate-bridged diiron center similar to the ones found in the R2 subunit of type I ribonucleotide reductase (RNR-R2), stearyl-acyl carrier protein (ACP) Δ^9 -desaturase, and ferritin (4, 5). Bacteria harboring different BMM family members, which include soluble methane monooxygenases (sMMOs), toluene monooxygenases (TMOs), phenol hydroxylase (PH), alkene

[†] This research was supported by National Institute of General Medical Sciences Grant GM32134 (S.J.L.) and the Italian Ministry of University and Research PRIN/2004 (A.D.). Portions of this study were carried out at the Stanford Synchrotron Radiation Laboratory, a national user facility operated by Stanford University on behalf of the U.S. Department of Energy, Office of Basic Energy Sciences. The SSRL Structural Molecular Biology Program is supported by the Department of Energy, Office of Biological and Environmental Research, and by the National Institutes of Health, National Center for Research Resources, Biomedical Technology Program, and the National Institute of General Medical Sciences.

[‡] The coordinates and structure factors for the PHH–PHM complex have been deposited in the Protein Data Bank for the native and SeMet enzyme as entries 2INP and 2INN, respectively.

* To whom correspondence should be addressed. E-mail: lippard@mit.edu. Telephone: (617) 253-1892. Fax: (617) 258-8150.

[§] Massachusetts Institute of Technology.

^{||} Current position: NRSA postdoctoral fellow (GM073457), Department of Biochemistry, Molecular and Cell Biology, Northwestern University, Evanston, IL 60202.

[†] Stanford University.

[@] Università di Napoli Federico II and CEINGE Biotecnologie Avanzate.

¹ Abbreviations: ACP, acyl carrier protein; AMO, alkene monooxygenase; APS, Advanced Photon Source; BMM, bacterial multicomponent monooxygenase; C2,3O, catechol 2,3-dioxygenase; PH, phenol hydroxylase; PHH, phenol hydroxylase hydroxylase component; PHM, phenol hydroxylase regulatory protein; PHP, phenol hydroxylase reductase; MMOB, methane monooxygenase regulatory protein; MMOH, methane monooxygenase hydroxylase; MMOR, methane monooxygenase reductase; rmsd, root-mean-square deviation; sMMO, soluble methane monooxygenase; SsoMO, hyperthermophilic toluene monooxygenase; SSRL, Stanford Synchrotron Radiation Laboratory; T4MO, toluene 4-monooxygenase; T4MOD, toluene 4-monooxygenase regulatory protein; THFMO, tetrahydrofuran monooxygenase; TMO, toluene monooxygenase; TOM, toluene *o*-monooxygenase; ToMO, toluene/*o*-xylene monooxygenase; ToMOD, toluene/*o*-xylene monooxygenase regulatory protein; ToMOH, toluene/*o*-xylene monooxygenase hydroxylase.

monooxygenase (AMO), tetrahydrofuran monooxygenase (THFMO), and hyperthermophilic toluene monooxygenase (SsoMO), use small organic compounds as their sole source of carbon and energy. The substrate transformations performed by this family of enzymes are responsible, in part, for removing atmospheric methane, a greenhouse gas, and carcinogenic halogenated solvents like TCE from the environment (6, 7). Because of the broad range of substrates oxidized by these enzymes, they have generated much interest for bioremediation and synthetic industrial applications.

BMMs like sMMO and PH consist of a 200–255 kDa dimeric hydroxylase of the form $(\alpha\beta\gamma)_2$, a cofactorless 10–16 kDa regulatory protein that enhances catalytic turnover by 30–150-fold and a FAD- and [2Fe-2S]-containing 38–40 kDa reductase that supplies the hydroxylase with electrons by consuming NADH (1–3). TMOs and SsoMOs differ slightly since they utilize an additional, Rieske protein to assist with electron transfer between the reductase and hydroxylase components (2, 3). The active sites in the resting states of the methane (MMOH) and toluene/*o*-xylene (ToMOH) monooxygenase hydroxylases contain a diiron(III) center coordinated by four glutamate and two histidine ligands from a four-helix bundle composed of helices B, C, E, and F of the protein α -subunit (8, 9). Solvent-derived water and hydroxide ions complete the octahedral coordination spheres. Sequence, spectroscopic, and structural analyses suggest that all BMM hydroxylases have nearly identical dinuclear iron centers (1, 10–12). Because AMO, TMO, SsoMO, and PH are incapable of hydroxylating alkanes, whereas sMMO and THFMO are adept at this transformation, other features of the system must control substrate reactivity at their dioxygen-activated metal centers. For sMMO, methane hydroxylation is achieved exclusively by a di- μ -oxo diiron(IV) intermediate, Q, whereas other reactions can occur at a diiron(III) peroxo precursor of Q, H_{peroxo} (1, 13, 14). A diiron(IV) intermediate has not been detected in any other BMM hydroxylase, but recent work has identified oxygenated diiron(III) species capable of oxidizing aromatic substrates (15).^{2,3}

Comparisons between the MMOH and ToMOH structures have provided insight into how the protein scaffold may tune the reactivity and substrate specificity of the diiron center by controlling the access of small molecules to the active site pocket. In particular, there is a large access channel in ToMOH linking the diiron center to the exterior environment that is absent in MMOH (8, 9). The regulatory proteins in these systems may also influence reactivity by inducing different structural changes at or near the diiron active site. In addition to enhancing the catalytic rate, the regulatory protein alters the substrate regiospecificity (16–18), influences the spectroscopic and redox properties of the diiron center (1), governs movement of the substrate and product to and from the active site pocket (5), and couples NADH consumption by the reductase with substrate hydroxylation at the diiron center (18, 19). Knowledge of the docking site on the hydroxylase and of structural changes at the diiron

center imposed by the regulatory protein is therefore essential for improving our understanding of O₂ and C–H bond activation in BMMs.

To address these questions and improve our structural knowledge about the BMM family members, we have determined in this study the X-ray crystal structure of a complex between the hydroxylase component of phenol hydroxylase, PHH, and its regulatory protein, PHM, from *Pseudomonas* sp. OX1 to 2.3 Å resolution. The information afforded provides novel insights into the functions of the regulatory protein and the tuning of the diiron active site chemistry in BMM enzyme systems.

MATERIALS AND METHODS

Purification of Phenol Hydroxylase. The hydroxylase (PHH), regulatory protein (PHM), and reductase (PHP) from *Pseudomonas* sp. OX1 were expressed simultaneously from the pJSX148 plasmid in *Escherichia coli* JM109 cells essentially as described by Cafaro et al. (20). The procedure was modified such that 100 μ M Fe(NH₄)₂SO₄·6H₂O was added to each liter of medium at induction and every hour thereafter until the cells were harvested.

The frozen cells were resuspended in a 25 mM MOPS (pH 7.0), 10% glycerol, 50 mM NaCl buffer (buffer A) supplemented with 5 mM MgCl₂, Pefabloc, 20 units of DNase, and PMSF and then lysed by sonication using 6 × 1 min pulses. Particulate debris was removed by centrifugation at 163000g for 45 min, after which the supernatant was filtered through a 0.2 μ m membrane and loaded onto a DEAE column conditioned with buffer A. A salt gradient was run from 50 to 400 mM NaCl, and the hydroxylase-containing fractions were pooled and concentrated to <5 mL using an Amicon concentrator fitted with a YM100 membrane. The concentrated protein was loaded onto an S300 column preequilibrated with 25 mM MOPS (pH 8.0), 10% glycerol, and 300 mM NaCl (buffer B) and run in that same buffer. Fractions containing PHH were pooled, loaded onto a phenyl Sepharose column conditioned with 10 mM MOPS (pH 7.0), 10% glycerol, and 100 mM NaCl, and eluted by using a 100 to 0 mM NaCl gradient. The purified PHH, which contained noticeable amounts of PHM, was concentrated, frozen in liquid N₂, and stored at –80 °C.

A selenomethionine (SeMet) derivative of PHH was generated by growing BL21(DE3) Gold *E. coli* cells transformed with the pJSX148 plasmid on LeMaster's medium supplemented with 90 mg/L Se-Met and ~5 mg/L folate, vitamin B₁₂, nicotinamide, pantothenate, thiamine, riboflavin, and *p*-aminobenzoic acid (21). The protein was expressed and purified as described above.

Activity and Iron Content. The enzyme activity, measured by using a catechol 2,3-dioxygenase (C2,3O) assay as described previously (20), was 470 ± 40 milliunits/mg. The C2,3O protein required for the assay was expressed and purified as described previously (20). The iron content of PHH was determined to be 3.6 Fe atoms/dimer by a colorimetric ferrozine assay (22).

Crystallization and Collection of X-ray Diffraction Data. Crystals were grown at 20 °C by the hanging drop vapor diffusion method. A protein solution containing 35 μ M PHH in 10 mM MES (pH 7.1) and 10% glycerol was combined with an equal volume of crystallization buffer containing 100

² V. Izzo, C. Tinberg, R. García-Serres, S. Naik, B. H. Huynh, and S. J. Lippard, unpublished results.

³ L. J. Murray, M. S. McCormick, R. García-Serres, S. Naik, B. H. Huynh, and S. J. Lippard, unpublished results.

Table 1: Data Collection, Phasing, and Refinement Statistics

	Se SAD	native
data collection		
beamline	SSRL BL9-1	NE-CAT (Sector 8)
wavelength (Å)	0.979	0.979
resolution (Å)	30–2.7	30–2.3
no. of unique observations ^a	109776	108695
total no. of observations ^a	592029	773692
completeness (%) ^a	83.0 (49.8) ^b	100 (100) ^b
redundancy ^a	5.4 (4.3) ^b	7.1 (6.9) ^b
I/σ	17.3 (5.0) ^b	16.5 (4.9) ^b
$R_{\text{sym}}^{\text{a,c}}$ (%)	5.9 (26.0) ^b	8.9 (44.8) ^b
Se sites used for phasing	71 of 77	
figure of merit (after density modification)	0.40 (0.75)	
refinement		
R_{work} (%) ^d	20.2	19.8
R_{free} (%) ^e	25.2	24.2
no. of molecules in ASU	1	1
no. of protein non-hydrogen atoms	16076	15307
no. of non-protein atoms	315	1042
rmsd for bond lengths (Å)	0.033	0.0065
rmsd for bond angles (deg)	2.55	1.28
average B value (Å ²)	36.0	37.7

^a Values for the Se SAD data were calculated considering I⁺ and I⁻ as separate reflections. ^b Values in parentheses are for the highest-resolution shell. ^c $R_{\text{sym}} = \sum_i \sum_{hkl} |I_i(hkl) - \langle I(hkl) \rangle| / \sum_{hkl} \langle I(hkl) \rangle$, where $I_i(hkl)$ is the i th measured diffraction intensity and $\langle I(hkl) \rangle$ is the mean of the intensity for the Miller index (hkl) . ^d $R_{\text{work}} = \sum_{hkl} |F_o(hkl)| - |F_c(hkl)| / \sum_{hkl} |F_o(hkl)|$. ^e $R_{\text{free}} = R_{\text{work}}$ for a test set of reflections (5%).

mM Tris (pH 7.0), 150 mM Na₂MoO₄, 5% glycerol, and 17–20% PEG 8000 (w/w). This condition was initially identified by using the Hauptman-Woodward Institute high-throughput screen. The addition of varying amounts of PHM to the crystallization buffer did not improve the occupancy of the regulatory protein in the crystals (vide infra). Before data collection, PHH crystals were frozen in a cryo solution containing the precipitant and 20% glycerol. Data at the Se peak wavelength were collected on beamline 9-1 at SSRL, and the native data set was collected at APS on the NE-CAT 8BM beamline. The data were indexed and scaled with HKL2000 (23). The space group is $P2_12_12_1$, and the unit cell dimensions are 87.8 Å × 146.3 Å × 190.0 Å. Further experimental details about data collection and refinement are given in Table 1.

Structure Determination. Molecular replacement was attempted initially by using the most structurally conserved regions of the MMOH and ToMOH α - and β -subunits. None of the starting α , α_2 , β , β_2 , $\alpha\beta$, and $\alpha_2\beta_2$ models used for molecular replacement afforded good starting phases, even though the PHH α - and β -subunits fold in a manner similar to the folding of these subunits in MMOH and ToMOH (see below).

Single-wavelength anomalous dispersion data for the selenomethionine derivative were then used to determine a set of starting phases. Attempts to determine the heavy atom substructure by using CNS (24), Solve (25), and SHELX (26) failed. SnB (27) was the only program able to locate 71 of 77 Se atoms in the asymmetric unit by using the peak wavelength. Native data were included in the phasing by refinement of both real and anomalous occupancies with MLPHARE from the CCP4 suite of programs (28). Initial phases were calculated with MLPHARE, improved, and extended to the limit of the native data by density modification with DM (28). Resolve (25) was used to autobuild

~50% of PHH, after which the remainder of the molecule was manually built in XtalView (29) and O (30) and refined with REFMAC5 (28) and CNS (24). Because of structural and occupancy differences, models for both the native and SeMet data sets were generated. The relative occupancy of PHM was estimated by refining the PHM occupancies after its B -factors were fixed to reflect the average value of the entire PHH molecule. A Ramachandran plot calculation using PROCHECK (31) indicated that 99.8% of the residues occupied allowed regions.

RESULTS AND DISCUSSION

PHH Global Fold. The PH hydroxylase component has an $(\alpha\beta\gamma)_2$ homodimeric composition with a noncrystallographic 2-fold symmetry axis similar to those in the ToMOH and MMOH structures (Figure 1A and Figure S1A–C of the Supporting Information) (8, 9). The folds of the PHH α - and β -subunits are nearly identical to those of the respective subunits in ToMOH and MMOH. The rms deviations between the α -carbon atoms are 1.5–1.6 Å for all possible α -to- α and β -to- β combinations. The largest topological differences between these evolutionarily related hydroxylase proteins occur for the γ -subunit, both in its fold and in its location. For PHH and ToMOH, the γ -subunits are positioned in the top left and right quadrants (11 and 1 o'clock, respectively) of the protein with similar ferredoxin-like folds despite having sequences that are only 13% identical (Figure S2) (9). Unlike the ToMOH γ -subunit, however, the PHH γ -subunit has an unstructured 22-amino acid N-terminus that forms extensive contacts with the α -subunit. For MMOH, the mostly α -helical γ -subunits localize to the far left- and right-hand sides of the protein (9 and 3 o'clock, respectively) and contact both the α - and β -subunits (Figure S1). Such structural differences are not surprising given the poor sequence conservation for this subunit among the different BMM family members. The function of this subunit, which is absent in some BMMs like alkene monooxygenases, is unclear (2, 3, 11).

PHM Fold and Binding Site on the Hydroxylase. The interface between the $\alpha\beta\gamma$ protomers of PHH forms a canyon, which we previously suggested would be the binding site for the BMM regulatory protein and reductase components on their hydroxylases (5, 8, 32, 33). On one face of the PHH protein, a single molecule of PHM binds in the canyon region across α -subunit helices A, E, F, and H, just 12 Å above the diiron center at its closest distance. On the opposite face of the hydroxylase, both a γ -subunit from a different, symmetry-related hydroxylase molecule in the unit cell and the N-terminus of the β -subunit occupy the space defined by the PHM binding site (Figure S3). The occupancy of the PHM component was estimated to be 40 and 50% in the native and selenomethionine (SeMet) structures, respectively. These different occupancies presumably reflect differing amounts of PHM that copurified with the hydroxylase component. We therefore generated models of the PHH–PHM complex from both the native and SeMet data.

The PHM global fold comprises three α -helices flanked by two nearly perpendicular β -sheets (Figure 1B). The fold is nearly identical to those previously reported for the NMR and crystal structures of the methane monooxygenase 159 (MMOB; PDB entries 1CKV and 2MOB) and toluene 4-monooxygenase (T4MOD; PDB entries 2BF5 and 1G10)

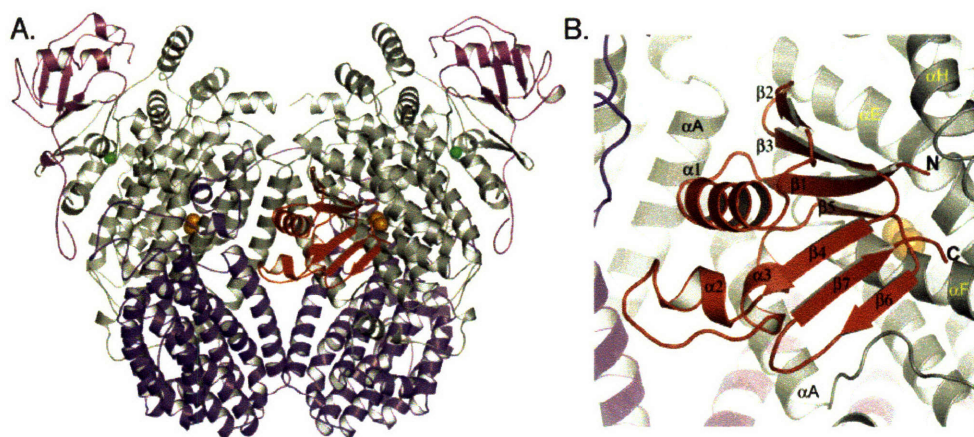


FIGURE 1: (A) Global structure of the PHH–PHM complex and (B) enlarged view of PHM in the PHH canyon. The PHH α -, β -, and γ -subunits are colored gray, purple, and pink, respectively, and PHM is colored red. Iron and zinc atoms are depicted as orange and green spheres, respectively. All figures were generated by using PyMOL (70).

regulatory proteins (34–37). The rms deviations between PHM and the T4MOD and MMOB proteins are between 1.5 and 1.6 Å for all backbone atoms (Figure S4). Comparisons between hydroxylase-bound PHM, T4MOD, and MMOB suggest there may be no significant structural rearrangements of the peptide backbone when these regulatory proteins form a complex with their respective hydroxylases.

Primarily in contact with the α -subunit of one protomer, PHM interacts with PHH helices A, E, F, and H via β -strands 1, 5, and 6, α -helix 3, the N-terminal region of α -helix 1, the loop between β -strands 2 and 3, and the peptide chain termini (Figures 1B and S5). The PHM binding site on the surface of the PHH α -subunit is formed by portions of the helices including residues 64–68 (helix A), 200–207 (helix E), and 226–245 (helix F), which collectively create a concave surface that complements the protrusive binding face of the regulatory protein. The PHH–PHM binding interaction is primarily hydrophobic, with some flanking polar and charged residues (Figure S1D). The N- and C-termini of the PHH regulatory protein are oriented away from the canyon region toward solvent and form some contacts with α -subunit helix H (Figure 1B).

Sequence alignments of the regulatory proteins from representative BMM family members indicate that very few of the amino acids are strictly conserved (Figure S5). Residues at the binding interface appear to be conserved only within a subfamily, suggesting why regulatory protein cross-reactivity with hydroxylases from different BMM subfamilies is rarely observed. Nevertheless, we generated electrostatic surface maps of what might be the homologous hydroxylase binding faces of T4MOD and MMOB from the information in Figure S5. As depicted in panels E and F of Figure S1, these protein surfaces, like that in PHM, have significant hydrophobic character, but with a somewhat greater number of charged residues. NMR line broadening, mutagenesis, cross-linking, and spin-labeling studies probing interactions of MMOB with MMOH are highly consistent with a similar surface being used by MMOB to bind its hydroxylase (Figure S5) (34, 38–40). Previously published spin-labeling experiments by our laboratory identified a different and probably incorrect MMOB binding face (41). A recent discussion of component interactions in the sMMO system is available (40).

The PHH–PHM crystal structure presented here thus serves as an excellent template for modeling interactions of the folded regulatory protein core with its cognate hydroxylase in related BMM systems. Although the unstructured N- and C-termini of some regulatory proteins (Figure S5), such as those on MMOB that affect steps in the catalytic cycle (42–45), cannot be placed on the hydroxylase surface with any degree of certainty, the specific interactions identified here (*vide infra*) should be quite valuable in guiding future mutagenesis, structural, and mechanistic studies of all the BMM enzymes.

Diiron Center. The diiron center of PHH is located in the α -subunit four-helix bundle 12 Å below the surface. Both protomers in the native and SeMet structures have nearly similar diiron active sites despite the binding of PHM to only one side of the hydroxylase. The iron atoms are coordinated by a bridging or semibridging glutamate, Glu-138, the δ -nitrogen atoms of His-141 and His-236, which lie distal to the active site pocket, and three additional glutamate residues, Glu-108, Glu-199, and Glu-233 (Figures 2 and S6). Glu-108 coordinates to Fe1 and hydrogen bonds to a terminal water molecule bound to the same iron atom. This structural motif is observed in all known BMM hydroxylase structures in their various oxidation and product-bound states (9, 33, 46–50). In the native structure and the SeMet α -subunit with bound PHM, Fe2 is coordinated by Glu-233 in a bidentate chelating mode, the geometry of which is most similar to that of the mixed-valent, Fe(II)Fe(III) form of MMOH (MMOH_{mv}) (Figure 2C). In the other SeMet protomer without bound PHM, Glu-233 appears to coordinate to Fe2 by using only one oxygen atom, the other forming a hydrogen bond to the terminal water on Fe1. For most of the active sites, Glu-199 coordinates to Fe2 via just one oxygen atom while the other dangling oxygen atom is in hydrogen bond contact with nearby residues Tyr-115 and Gln-134 (Figures 2 and 3A). This ligand appears to adopt a bidentate chelating geometry in the SeMet α -subunit without bound PHM. The final iron ligand that we could identify is a water molecule bound exclusively to Fe1. Electron density corresponding to a bridging or semibridging water-derived ligand, like hydroxide or oxide, between the iron atoms was not observed. In the higher-resolution native structure, the Fe1–Fe2 distances are 3.6 and 3.3 Å for the PHM-bound and

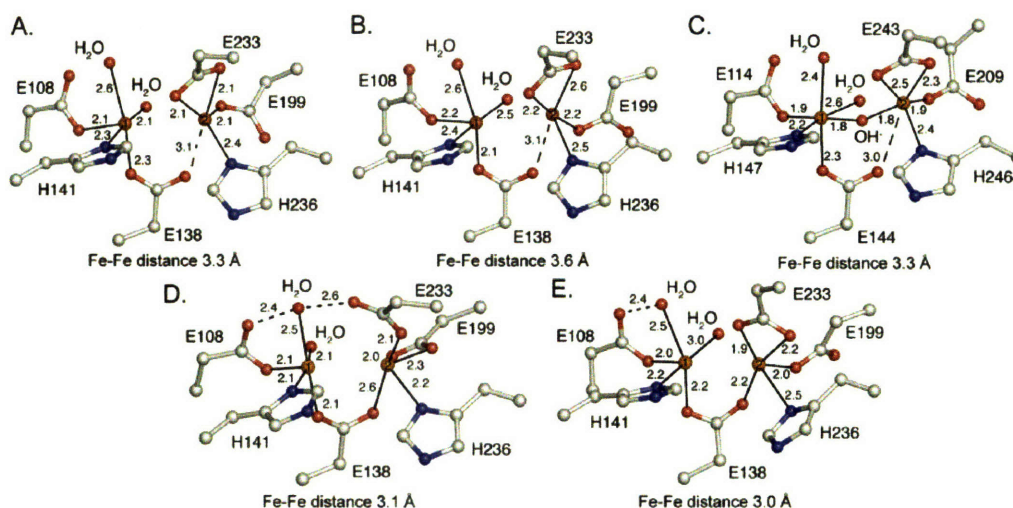


FIGURE 2: Structures of the diiron center. (A) Native PH diiron center without PHM bound. (B) Native PH diiron center with PHM bound. (C) Mixed-valent MMOH diiron center. (D) SeMet PH diiron center without PHM bound. (E) SeMet PH diiron center with PHM bound. Carbon, nitrogen, oxygen, and iron atoms are colored gray, blue, red, and orange, respectively. This color scheme will be used throughout unless otherwise noted.

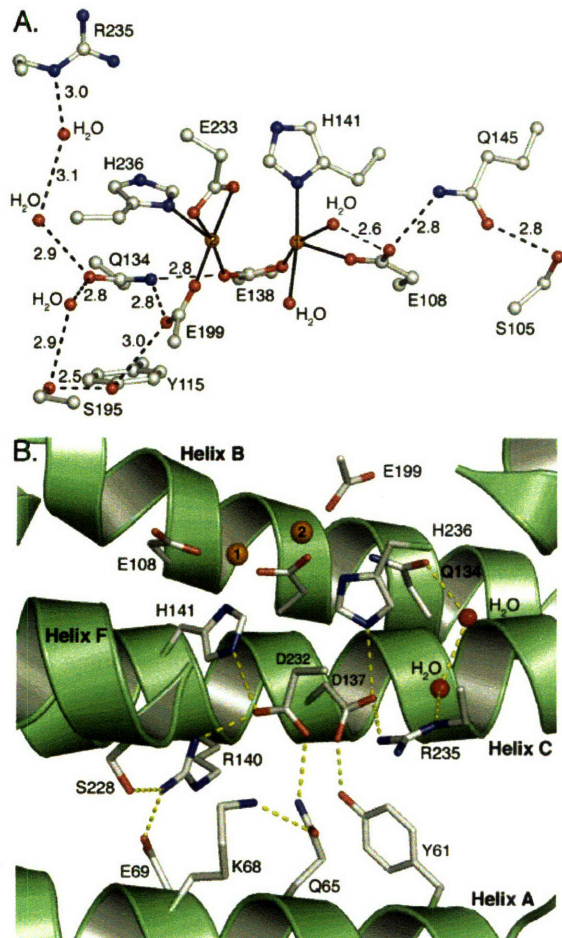


FIGURE 3: Hydrogen bonding networks in the second coordination sphere. (A) Hydrogen bonding networks flanking the diiron center. (B) Hydrogen bonding network behind the diiron center that extends to the surface of the hydroxylase canyon region where PHM binds.

unbound protomers, respectively. The Fe1–Fe2 distances in the lower-resolution SeMet structure are 3.0–3.1 Å for both 161 active sites. These shorter Fe–Fe distances may be a

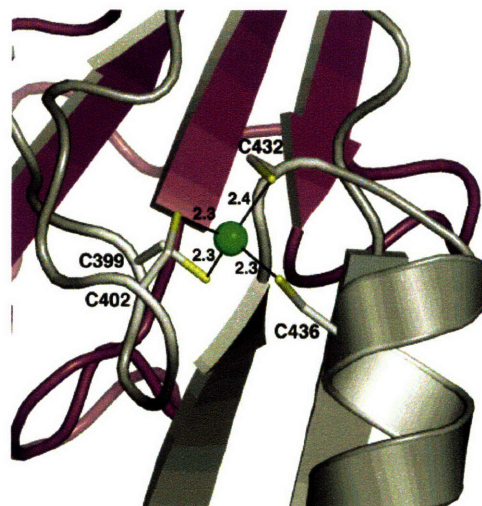


FIGURE 4: Zinc binding site in the C-terminal domain of the PHH α -subunit. Zinc is depicted as a green sphere, and sulfur atoms are colored yellow. The α -subunit is depicted as a gray ribbon and the γ -subunit as purple ribbons.

consequence of a fully bridging Glu-138 residue versus the semibringing one in the native structure. Overall, Fe1 has a five-coordinate, square-pyramidal geometry, whereas Fe2 adopts a more distorted structure.

The identity of the Fe2-coordinating histidine N-donor is notably different among the PHH, MMOH, and ToMOH dinuclear iron centers. In ToMOH, this histidine coordinates to iron by using its ϵ -nitrogen atom, whereas in MMOH and PHH, the histidine δ -nitrogen atom is employed. When the ToMOH structure was first determined, it was unclear whether this structural difference might influence the hydroxylation chemistry (9). Since PH and ToMO hydroxylate similar aromatic substrates at nearly equivalent rates (20), the structural difference is presumably of little or no consequence to this property of the dimetallic center.

At present, it is difficult to discern the true oxidation state of the different dinuclear iron centers in PHH enzymes. As purified, the enzyme has an optical band at 350 nm that is

indicative of a (μ -oxo)diiron(III) species comprising ~68–96% of the sample ($\epsilon_{350} = 4800\text{--}6000 \text{ M}^{-1} \text{ cm}^{-1}$ per dinuclear iron cluster) (12). PHH from *Pseudomonas* sp. strain CF600 is 81% identical to the *P. stutzeri* OX1 enzyme and forms a complex with its regulatory component involving the α -subunit as deduced by chemical cross-linking studies (51). Spectroscopic investigations of this enzyme indicate that the oxidized form contains both (μ -oxo)- and di- μ -(hydroxo)diiron(III) metal centers (12) and that the predominant, catalytically competent species is the oxo-bridged diiron(III) form. Preliminary EPR spectroscopic analysis of samples of *P. stutzeri* OX1 PHH in its resting and cryo-reduced states reveals that the purified protein contains a heterogeneous mixture of diiron(III) and mixed-valent Fe(II)Fe(III) species, the relative concentrations of which are at present unknown.⁴ If the PHH metal centers in these crystal structures were fully oxidized, one would expect to see either a short Fe–Fe distance of 3.0 Å and a dihydroxo-bridged dimetallic cluster (9, 48, 49) or a longer Fe–Fe distance of 3.2–3.6 Å and an oxo-bridged cluster (4, 5, 52). None of the PHH diiron centers, however, has an observable bridging oxide or hydroxide ligand. Given that the geometries of the active site metal clusters are most similar to that of the mixed-valent Fe(II)Fe(III) form of MMOH (49), one possibility is that photoreduction by synchrotron radiation occurred to produce the mixed-valent oxidation state. A similar phenomenon has been reported previously for structures of Δ^9 -desaturase and RNR-R2, although the oxidized forms of these proteins were reduced by two electrons (53–55). The structures of the PHH diiron centers presented here are not charge-balanced, however, and would require an additional negatively charged ligand, such as a bridging hydroxide ion, to achieve a neutral state similar to that observed in MMOH_{mv} (Figure 2C). Although $|2F_o| - |F_c|$ and $|F_o| - |F_c|$ simulated-annealing omit electron density maps have not allowed us to identify such a ligand, the data quality at 2.3 and 2.7 Å resolution may not be sufficient to reveal a coordinating oxygen atom between the iron atoms (56).

A second possibility is that the metal centers have each been photoreduced by two electrons to the diiron(II) state, rendering the PHH active sites charge neutral. The structures do not, however, resemble the reduced forms of MMOH and ToMOH, which both have a 3.3–3.4 Å metal–metal distance and a glutamate residue that coordinates to Fe2 in a bidentate chelating fashion and simultaneously bridges the two iron atoms with one of its O atoms (48, 49, 57). Because the active sites on the PHM-bound and unbound sides of PHH are so similar, it is unclear whether PHM affects them both in a similar manner by an allosteric effect or not at all. The incomplete PHM occupancy may also be a factor. Further spectroscopic and structural investigations are required to improve our understanding of the PHH dinuclear iron center and to discern how the diiron site geometries are influenced by the oxidation state and the presence of bound PHM.

Second-Sphere Hydrogen Bonding Patterns. The second coordination sphere is critical to the formation and stability of the BMM diiron centers, providing ligand conformational constraints in the PHH, ToMOH, and MMOH structures (5).

For PHH, the geometry of Glu-108, which coordinates to Fe1, is stabilized by a hydrogen bonding network involving Gln-145 and Ser-105 (Figure 3). A similar pattern exists in ToMOH involving Gln-141 and His-96 (9), but not in MMOH, which has a cysteine residue positioned 4.5 Å from the coordinating glutamate (8). Gln-145 is conserved among all PH and TMO family members, whereas Ser-105 and His-96 are not. Substituting the corresponding Gln with a Cys in toluene 4-monooxygenase (T4MO) resulted in a variant with a 10-fold diminished turnover rate that was still incapable of hydroxylating methane (58). A Gln-to-Val substitution in the same enzyme resulted in a 100-fold decrease in the rate of turnover compared to that of the wild-type protein. These results and the crystal structure presented here suggest that stabilization of the Fe1-coordinating terminal glutamate by hydrogen bonding may be critical for reactivity in the TMO and PH systems. The importance of such hydrogen bonding involving the analogous residue in MMOH, Glu-114, is less obvious because this residue has no hydrogen bonding partners other than an active site pocket water molecule that is not always detected in every crystal structure (49).

At the other end of the diiron center, there is extensive hydrogen bonding to conserved Gln-134, which may be essential for stabilizing the geometry by which the bridging Glu-138 and terminal Glu-199 residues coordinate to Fe2 (Figure 3). Glu-199 may also form a weak hydrogen bond with Tyr-115; this residue is a phenylalanine in homologous PH family members, however. The same general arrangement of amino acids is preserved in MMOH (9). ToMOH utilizes a water molecule (or hydronium ion) to mediate interactions between the Fe-coordinating glutamates and a second-sphere glutamate, Glu-111. In the PHH structure, hydrogen bonds between two ordered water molecules link Gln-134 with conserved Arg-235, an arrangement that differs from that in the other hydroxylase proteins (see below). It is clear through these comparisons that BMMs employ a variety of schemes to stabilize the coordination spheres around the two iron atoms, but it is unknown whether and how these different architectures might contribute to the dissimilar reactivity of the enzymes. Comparisons of the native and SeMet α -subunits with and without bound PHM do not reveal any significant alterations in these hydrogen bonding patterns.

A Conserved Mononuclear Zn²⁺ Site. In the C-terminal domain of the PHH α -subunit, 24 Å from the diiron center, there exists a four-cysteine site that coordinates a single metal ion with a tetrahedral geometry and an average metal–sulfur distance of 2.3 Å (Figures 1A and 4). Sequence homology indicates that the coordinating cysteines are conserved only among members of the PH and AMO families (Figure S7). UV–vis, EPR, and Mössbauer spectroscopic studies of recombinant PHH from *P. stutzeri* OX1 and native PHH from *Pseudomonas* sp. strain CF600 do not reveal the presence of a thiolate rich mononuclear iron center, or any other mononuclear paramagnetic metal center, in any of the protein preparations (12).^{3,4} Anomalous difference electron density maps generated from data collected at the selenium edge reveal much stronger peaks at the mononuclear metal site than at the diiron center (Table 2), suggesting that the metal at this position is a stronger absorber of X-rays at 12 660 eV than iron, the K-edge of which is 7111 eV. The K-edge of zinc occurs at 9659 eV. Given the ligand content,

⁴ V. Izzo, R. Davydov, M. H. Sazinsky, S. J. Lippard, and B. M. Hoffman, unpublished results.

Table 2: Heavy Atom Anomalous Peak Intensities^a

subunit	atom	peak height	subunit	atom	peak height
α1	Fe1	11.3	α2	Fe1	11.4
	Fe2	9.62		Fe2	8.9
	Zn	20.2		Zn	22.9

^a Peak intensities were determined by using CCP4 (28).

geometry, and absence of a spectroscopic signal, Zn²⁺ is most likely bound to this position. In addition, it was observed previously that the toluene 2-monooxygenase hydroxylase, a PH family member, is purified with two zinc and four iron atoms (59). In light of this information, we conclude that zinc is the physiologically preferred metal ion bound to the four-cysteine site and suggest that it may be important for stabilizing the fold of the α-subunit C-terminal domain.

Conserved Active Site Residues and Changes in Helix E. Situated just above the diiron center on helix E in PHH are two highly conserved residues found in every BMM, Thr-203 and Asn-204 (Thr-213 and Asn-214 in MMOH, respectively). Thr-203 is positioned at the interface between helices E and F above the Fe2-coordinating Glu-233 (Figure 5A), which undergoes oxidation state-dependent carboxylate shifts in MMOH and ToMOH (48, 49, 57). Asn-204 is located on the surface of the protein, 12 Å from the diiron site. Several ordered water molecules link these Thr and Asn residues to the diiron center by hydrogen bonds. In MMOH and ToMOH, the Thr residue forms the “roof” of the active site pocket. The Asn residue lies between helices E and F just above the iron-coordinating Glu that undergoes a carboxylate shift upon reduction of the diiron center (Figure 5B) (48, 49). The rotameric conformation of this Asn also changes with the active site oxidation state; it points inward toward the diiron center in the mixed-valent and reduced forms and away from it when the iron atoms are oxidized (Figure 5B) (48, 49). Mutagenesis studies on TMOs suggest that the Thr is not essential for catalysis under steady state conditions (60), whereas the Asn is important for turnover and protein component interactions.⁵

The positions of this pair of Thr and Asn residues in both protomers from the native and SeMet PHH structures differ significantly from what has been observed for oxidized, reduced, and mixed-valent MMOH (8, 46, 48, 49) as well as for oxidized and Mn²⁺-substituted ToMOH (9, 57). The alternative positions that we observe here are the consequence of a different helix E peptide backbone configuration (Figure 5D). Residues 193–202 form a π-helix; residues 205–217 are α-helical, and Thr-203 and Asn-204 mark the transition from the π- to the α-helical forms. In MMOH and ToMOH, the backbone atoms of Thr-213 and Asn-214 assume an α-helical configuration (Figure 5B,F), whereas the residues preceding these two form a π-helix. The alternative configuration of helix E in PHH has been observed once before, in a 6-bromohexan-1-ol-bound structure of MMOH (Figure 5C,E) (33). In this particular MMOH crystal structure, residues 212–216 adopt a π-helical configuration to accommodate the bound product analogue by increasing the volume of the active site pocket. As a result, the orientation of the conserved Thr and Asn residues changes to adopt a config-

uration nearly identical to the one observed in PHH. We previously hypothesized that such a helical reconfiguration in MMOH may reflect one way by which the regulatory protein induces a change in the active site pocket to alter substrate regiospecificity and accommodate larger substrates. The PHH structure marks the second time that this alternative configuration of helix E has been observed and strongly supports our previous suggestion that the flexibility exhibited by this segment of the α-subunit may play a significant, and largely unexplored, role in the functions of BMMs. Because helix E in all of the PHH α-subunits adopts this configuration, we cannot conclude that PHM is directly responsible for this perturbation without further investigation. If both the conformational changes in helix E and the conserved Asn are relevant to the functions of BMMs, an additional challenge will be to understand when these conformational changes take place during the catalytic cycle.

Structural Changes in Helix F. The electron density for helix F residues 225–231 in the SeMet PHH α-subunit where PHM is bound at higher occupancy is different than that in the other α-subunits (Figure S8), suggesting that PHM may induce a slight reconfiguration, or disordering, of this helix when it is bound to the hydroxylase. The best interpretation of the electron density in this region, which may be a combination of the PHM-bound and unbound forms, is presented in Figure 6. In most α-subunits, F227 and Q230 comprise part of the canyon surface and typically point toward solvent. When the regulatory protein binds, PHM side chains Q10 and I71 occupy the former positions of Q230 and F227, respectively (Figure 6B), and presumably force helix F to reconfigure. The occupancy of PHM in the native structure is insufficient for observation of these differences or identification of the positions of the specific PHM side chains. The major consequences of the helix F rearrangement are the movement of Q230 toward the diiron center, such that it lies above Fe2-coordinating E233, and a shift in the position of the F207 side chain, such that it is closer to the terminal water ligand on Fe1. Residue Q230 is highly conserved among all of the different BMM subfamilies except that of sMMO, where it is a Glu in MMOH and butane monooxygenase (BMOH). It is unknown how mutations of this Gln would affect hydroxylation, electron transfer, or proton transfer chemistry. Residue F207 is conserved among the aromatic hydroxylating BMMs but is a Leu or Ile in the other BMM systems. The conformational changes in helix F do not alter any of the second-sphere hydrogen bonding networks, but they do decrease slightly the solvent accessibility of the diiron center.

Possible Consequences of Regulatory Protein Binding on Transfer of Electrons to the Hydroxylase. Behind the diiron center is an extensive hydrogen bonding network extending from the active site to the surface of the hydroxylase canyon at α-subunit helix A (Figure 3B). Most of the residues contributing to this network are strictly conserved among the different BMM families (3), suggesting that they are critical to the function and folding of the protein. Several other diiron proteins, including bacterioferritin and rubrerythrin, have similar hydrogen bonding patterns that extend 10–14 Å to a redox active cofactor, such as a porphyrin or mononuclear iron–sulfur center (61, 62). In the R2 subunit of RNR, a tryptophan residue in an analogous hydrogen bonding network behind the diiron center facilitates genera-

⁵ E. Cadieux, L. J. Murray, M. S. McCormick, M. H. Sazinsky, and S. J. Lippard, unpublished results.

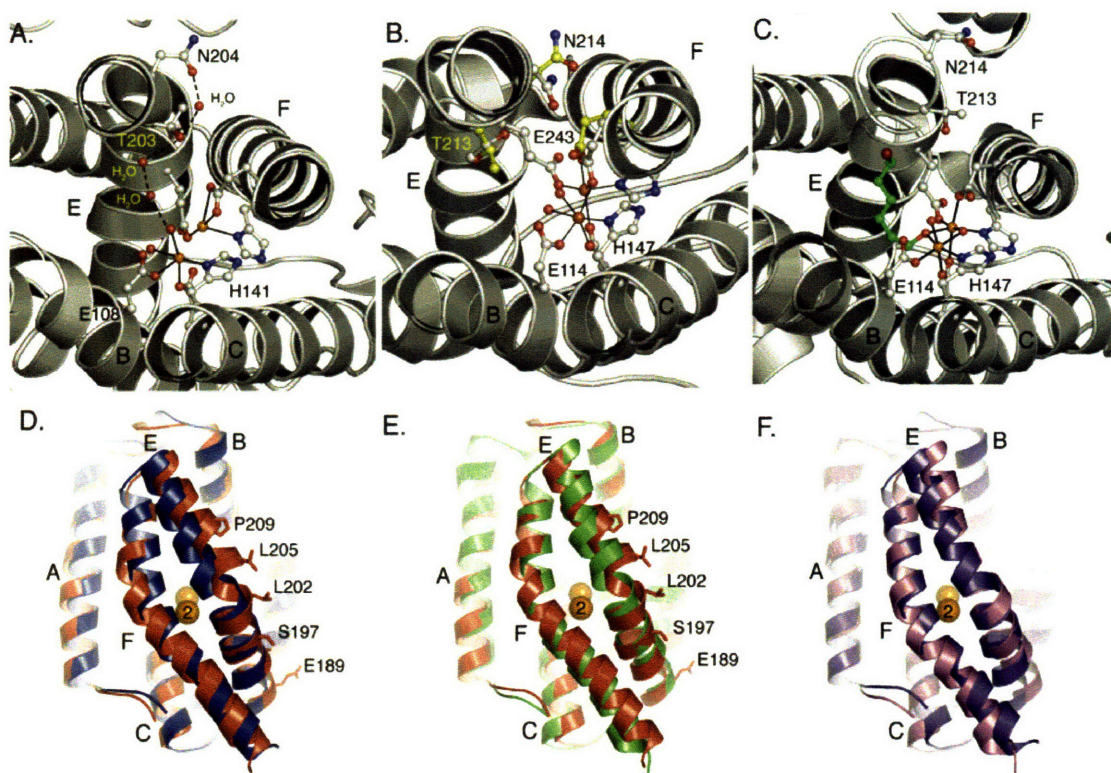


FIGURE 5: Structural differences in conserved helix E residues. (A) Positions of conserved Thr-203 and Asn-204 in PHH. (B) Redox-dependent structural changes in the positions of Thr-213, Asn-214, and Glu-243 in MMOH. Carbon atoms for the reduced and oxidized forms of MMOH are colored gray and yellow, respectively. (C) Positions of conserved Thr-213 and Asn-214 in the 6-bromohexan-1-ol-bound form of MMOH in which helix E adopts a more π -helical character. (D) Superimposition of the PHH (red) and ToMOH (blue) four-helix bundles. Helices A–F are labeled accordingly. (E) Superimposition of the four-helix bundle from the 6-bromohexan-1-ol-bound form of MMOH (green) with the PHH (red) four-helix bundle. (F) Superimposition of the ToMOH (violet) and MMOH (pink) four-helix bundles.

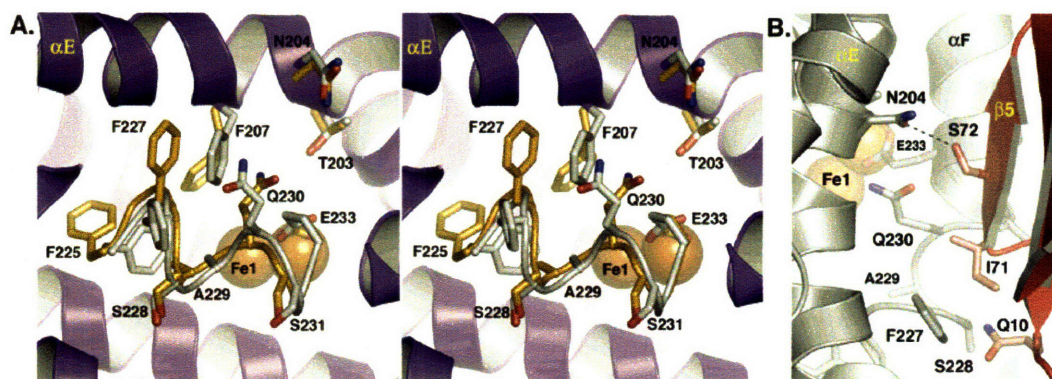


FIGURE 6: Structural changes in α -subunit helix F in the SeMet structure. (A) Comparison between PHM-altered (orange) and unaltered (gray) helix F in stereo. (B) PHH (gray) and PHM (red) binding interface at α -subunit helices E and F.

tion of the catalytically important Fe(III)Fe(IV) X intermediate and tyrosyl radical (63). More recently, this pathway in Δ^9 -desaturase has been implicated in electron transfer (64). On the basis of these observations, we hypothesized that this hydrogen bonding network in BMMs may represent the electron transfer pathway from the reductase to the diiron center (5). Investigations of the electron transfer reactions between MMOH and its reductase, MMOR, indicate the [2Fe-2S] cluster of the latter and the MMOH diiron center may be 11–14 Å apart when this protein complex forms (65). Using this distance constraint, an analysis of the PHH

164 to that of the PHM component. If our assumptions about the relative location of reductase binding site are correct, the PH regulatory and regulatory proteins must share a similar binding site on both faces of the hydroxylase surface.

This finding has important implications for how the regulatory protein influences the properties of the hydroxylase diiron center. One attractive scenario is that in which regulatory protein binding prevents the reductase from binding to the hydroxylase and donating extra electrons to the dioxygen-activated diiron center, quenching the peroxo or Q intermediates before they can achieve their hydroxylation chemistry. Such uncoupling, or premature reduction

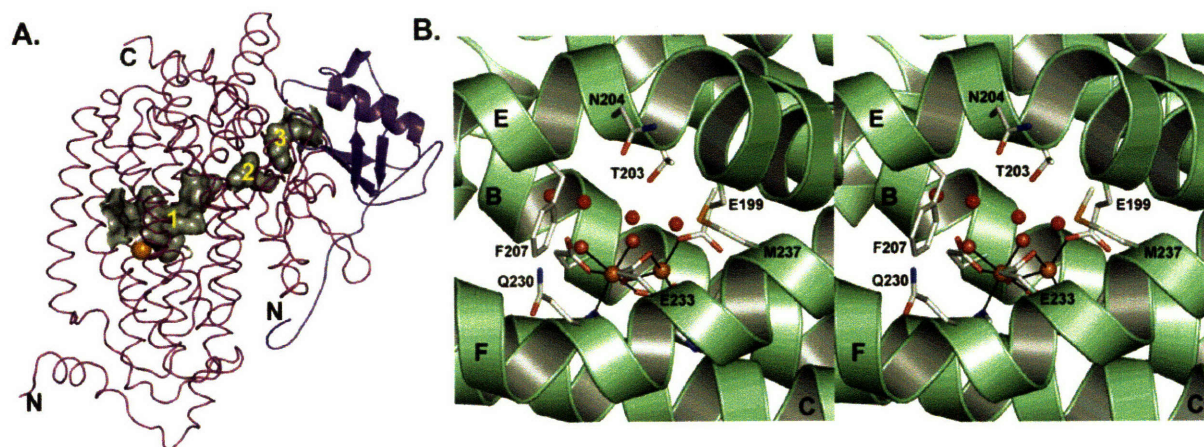


FIGURE 7: Cavities and pores in the PHH α -subunit. (A) α -Subunit cavities (gray) that extend from the diiron center to the γ -subunit (blue). (B) Stereoview of the conserved residues and water molecules (red spheres) contributing to the pore through the α -subunit four-helix bundle.

of the oxygenated metal cluster, would not only consume the reactive diiron species but also wastefully deplete the NADH supply of the cell. After completion of the hydroxylation reaction, the regulatory protein may temporarily dissociate from the hydroxylase so that the reductase can bind and reinitiate the catalytic cycle. This scenario would explain why, in the sMMO system, binding of MMOB to MMOH shifts the redox potentials to disfavor reduction of the diiron center, whereas reductase binding shifts the potentials so that reduction is favored (65–68). It is also possible that BMMs function via half-sites reactivity. During the catalytic cycle, the regulatory protein may bind on one face of the hydroxylase to facilitate catalysis while the reductase binds temporarily to the other side to reinitiate the cycle. Such a model may explain why excess regulatory protein often inhibits BMM hydroxylation chemistry, whereas substoichiometric amounts lead to uncoupling (18, 19). Pinning down the exact function of the regulatory protein has been a difficult task. Often, it has been termed a “coupling protein” because it couples hydroxylation with electron transfer and an “effector protein” because it effects substrate hydroxylation. The PHH–PHM structure demonstrates how it may carry out both functions.

Access of Substrate to the Diiron Center. The α -subunit scaffold is important for controlling the entrance and egress of small molecules to and from the diiron center. The pathway for substrate entrance, such as the hydrophobic cavities or channels that we previously identified in MMOH and ToMOH, may play an important role in determining the substrate specificity and reactivity of these enzymes (8, 9, 33, 69). Surface calculations of the PHH α -subunits using PyMOL (70) reveal the presence of three cavities leading from the active site pocket (cavity 1) to the protein surface near the γ -subunit (cavity 3) (Figure 7A). Cavities 1 and 3 have direct access to the exterior environment of the protein, whereas access to cavity 2 is gated by Leu-107 and Leu-272 at one end near the active site pocket and Leu-399 and Val-455 on the other near cavity 3. This putative route for the access of small molecules to the active site involves mostly hydrophobic residues. It traverses the α -subunit in a manner that is analogous to the pathway defined by the cavities in MMOH and ToMOH but different from the 40 Å channel in ToMOH (9, 33, 57, 69). Although the PHH

cavities are large enough to accommodate aromatic substrates, in the absence of structures containing bound product or substrate, it is difficult to know whether these cavities are relevant to the function of PHH.

Surface calculations of the PHH α -subunits without bound PHM reveal a large pore between helices E and F that offers the most direct route for access of small molecules to the active site pocket. This pore is ~ 6 Å in diameter, lies above the diiron center, and is lined with the side chains of Thr-203, Asn-204, Phe-207, Glu-233, and Met-237 (Figure 7B), all of which are conserved among the different PH enzymes. The pore diameter may be large enough to accommodate phenol and alternative substrates like xylene, dimethylcat-echol, and naphthalene, which have diameters between 5.0 and 7.0 Å. Several water molecules occupy the pore and delineate how a substrate may move through the four-helix bundle in the absence of PHM. The 6-bromohexanol-bound form of MMOH, which has a helix E configuration similar to that in PHH, does not have such an obvious mode of entry through helices E and F. The absence of an analogous pore in the MMOH structure may reflect the fact that the peptide backbones of helices E and F near the diiron center are closer together by approximately 2.0 Å, measuring from the C α atoms of Asn-214 and Gln-240 (Figure 5E). In some, but not all, crystal structures of reduced MMOH in which helix E has its typical configuration, a pore with a narrow 2.0 Å diameter forms as a result of Asn-214 (Asn-204 in PHH) shifting to point inward, toward the diiron center (33). This pore may become large enough to accommodate small substrates like methane, dioxygen, and protons in the form of H₃O⁺.

Surface calculations of the PHH α -subunits with bound PHM reveal that direct access to the diiron center through helices E and F is restricted in this conformation of the complex (Figure 8). Binding of the regulatory protein also induces F207 and Q230 to reposition as described above, further limiting access to the diiron center. Previously, we suggested a similar barrier-like role for MMOB in the sMMO system because it significantly slowed the rate of diffusion of iron into and out of the active site during metal reconstitution studies (32). Investigations of *Methylosinus trichosporium* OB3b MMOB mutants in which residues 108–111 were changed to Ala revealed variable substrate

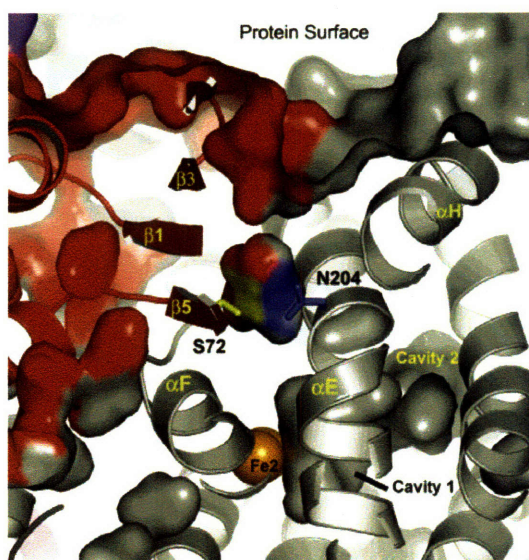


FIGURE 8: Access of the substrate to the diiron center at the PHH–PHM interface. PHH (gray) and PHM (red) surfaces and cavities are depicted. Interactions between conserved N204 (blue) and S72 (yellow) and how they may gate access to the metal center are also shown.

access to the diiron center. On the basis of these results, MMOB was proposed to generate a size-selective pore on the hydroxylase surface that would serve as a substrate-specific “sieve” (44, 71, 72). We find no evidence for a PHM-generated substrate-specific pore in the PHH–PHM complex or in models of the MMOH–MMOB structure (not shown), suggesting that the MMOB mutations, which correspond to residues 70–73 in PHM (Figures 6B and S5), may simply decrease the diffusion barrier at the MMOH–MMOB interface to modify the access of the substrate and product to and from the diiron center. Kinetic and computational studies of the reactions of intermediate Q with a variety of substrates have revealed two mechanistic limits, depending upon whether access to the diiron center is rate-determining (73). These results suggest how the regulatory protein might be responsible for controlling the kinetics of these processes in the sMMO system.

The PHM equivalent of S110 in *M. trichosporium* MMOB is S72. The side chain of this residue forms a hydrogen bond to conserved Asn-204 in both the native and SeMet crystal structures (Figures 6B and 8) and is highly conserved among the different BMM regulatory proteins. The link between these two residues has not yet been fully explored. Given that the PH enzymes act on substrates larger than MMOH and that only a deep crevice is observed on the surface of the PHH–PHM complex (Figure 8), the aromatic substrates may enter the PH hydroxylase by an alternative route, possibly via cavity 3. If a pore through the E and F helices of the α -subunits forms at specific stages of the catalytic cycle, such as when the diiron center is reduced and Asn-204 undergoes a rotameric shift, it may allow passage of O_2 , H_2O , or H_3O^+ to or from the active site. Collectively, these findings reveal how the regulatory protein may control the access of small molecules and ions to the diiron center and possibly offers some type of protection of the dioxygen-activated metal center as it traverses the reaction cycle.

Active Site Pocket and Substrate Specificity. The arrangement of side chains in the active site pockets of BMMs is

crucial for determining substrate specificity. Phenol hydroxylases, for the most part, are ortho-hydroxylating enzymes, whereas toluene monooxygenases hydroxylate in the para position (58, 74). PHH and ToMOH from *P. stutzeri* OX1, however, have relaxed regioselectivities and typically afford 70% *o*-cresol and 45% *p*-cresol, respectively (20, 75, 76). For alternative substrates, PH and ToMO perform highly regioselective reactions. For example, PH and ToMO yield 96% 3-methylcatechol and 95% 4-methylcatechol, respectively, when *m*-cresol is used as the substrate (76, 77). The hydrophobic residues that line the active site pockets of PHH and ToMOH are mostly conserved among their specific subfamilies (Table 3) (3). A superimposition of the PHH and ToMOH active sites indicates that the side chains occupy nearly identical positions except for those residues on helix E because of its alternative conformation (Figure 9). Single-ring aromatic substrates can be most effectively docked manually into the active site by orienting their ring plane perpendicular to the Fe–Fe vector. A similar orientation for the aromatic ring has been suggested previously for ToMOH (77). On the basis of DFT calculations and structural investigations of MMOH, substrate hydroxylation presumably occurs at a bridging position between the two iron atoms (78). By docking the oxygen atom of a pentamethylphenol at such a position, we readily see that ortho hydroxylation is favored if a ring substituent points above or below the plane of the iron atoms and bridging oxygen (carbons 2 and 6 in Figure 9), whereas para and meta hydroxylation are favored only if the ring substituent is positioned at the back of the active site pocket. Para hydroxylation may be disfavored in PH enzymes because of steric interaction between Leu-107 and the substituent on the C4 atom (Figure 9). For TMOs, the residue analogous to Leu-107 is typically a glycine or a glutamate (Glu-103) in ToMOH that points away from the active site pocket. A smaller residue at this position would provide enough space to orient a substituent on C4 toward the back of the active site pocket to favor hydroxylation of the para carbon atom. Mutants of both T4MOH and ToMOH in which this residue was changed to leucine afforded 55–60% ortho hydroxylation (58, 77), suggesting that the space occupied by this residue is important for steering substrates. Conversely, mutagenesis studies on a related phenol hydroxylase family member demonstrated that changing the residue analogous to Leu-107 to an alanine produced an enzyme that yielded 50% *o*-cresol, compared to 98% for the wild-type form (74). Moreover, this variant was capable of hydroxylating naphthalene, anthracene, fluorene, and phenanthrene at increased rates. Thus, increasing the depth of the active site pocket promotes hydroxylation of larger substrates.

In essence, the PHH active site pocket is shallower than that of ToMOH. Because the regulatory proteins in these different BMM systems alter the product distributions by influencing the structure of the active site pocket (17, 18), possibly by changing the configuration of helix E, it is difficult to account fully for all of the residues and structural features that are responsible for orienting substrates in the absence of a crystal structure of the hydroxylase–regulatory protein complex at higher occupancy and in different oxidation states. Nevertheless, our structures of PHH and ToMOH, in addition to revealing the two different configurations of helix E, provide an improved understanding of the

Table 3: Residues Comprising the BMM Active Site Substrate Binding Pocket^a

PHH	I104	L107	A111	Q145	F179	R183 ^b	I194	F198	T203	L206	F207
CF600	V105	L108	A112	Q146	F180	R184 ^b	V195	F199	T204	L207	F208
TOMH	V106	L109	A113	E147	F181	A185 ^b	V196	F200	T205	L208	F209
ToMOH	I100	E103	A107	Q141	F176	M180	L192	F196	T201	Q204	F205
T4MOH	I100	G103	A107	Q141	F176	I180	L192	F196	T201	Q204	F205
AMOH	L91	A94	A98	E133	G167	F172	L184	A188	T193	L196	L197
MMOH	L110	G113	A117	C151	F188	F192	L204	G208	T213	L216	I217

^a Abbreviations: PHH, *Pseudomonas* sp. OX1 PHH; CF600, *Pseudomonas* sp. strain CF600 PHH; TOMH, *Burkholderia cepacia* G4 toluene *o*-monooxygenase hydroxylase; ToMOH, *Pseudomonas* sp. OX1 ToMOH; T4MOH, *Pseudomonas medonica* KR1 T4MOH; AMOH, *Rhodococcus corallinus* B-276 alkene monooxygenase hydroxylase; MMOH, *Methylococcus capsulatus* (Bath). ^b A side chain that does not contribute to the active site pocket yet has a homologous BMM family member with a side chain that does.

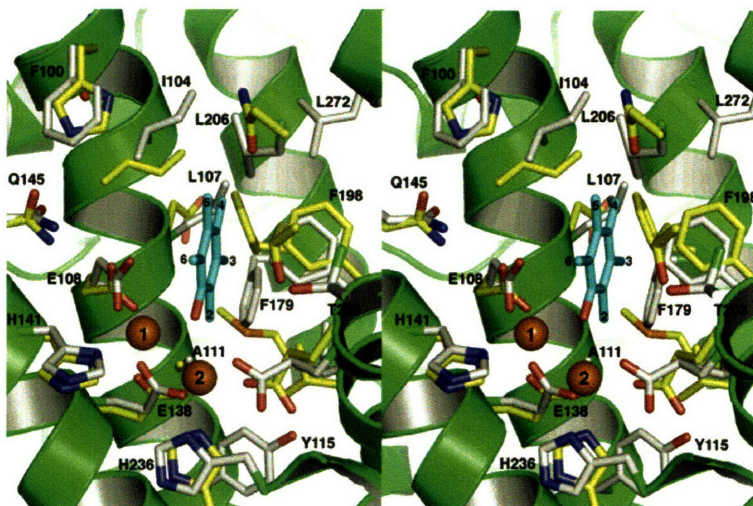


FIGURE 9: Stereoview of the superimposed PHH and ToMOH substrate binding pockets. The PHH and ToMOH carbon atoms are colored gray and yellow, respectively, and helices of PHH are depicted in green. Pentamethylphenol (cyan) is docked manually into the active site pocket. The aromatic carbon atoms of the docked aromatics as well as the PHH residues contributing to the active site are labeled. The identity of the ToMOH residues can be obtained from Table 3.

active site pockets and an initial structural basis from which one can proceed to rationally engineer these enzymes for industrial and bioremediation applications.

CONCLUSIONS AND PROSPECTS

The fundamental properties that are responsible for controlling the substrate reactivity of the BMM diiron centers lie within the protein scaffold of the hydroxylase subunit. The structure of the PHH–PHM complex represents a key step toward unraveling the principles that underlie the chemistry performed by the carboxylate-bridged diiron centers of these proteins. The structure indicates that PHM functions to block the entrance of the solvent and substrate to the diiron active site through the four-helix bundle, alter the configuration of helices E and F in a manner that could enhance the overall activity of the metal cluster, shape the active site cavity to control product distributions, and most likely affect electron transfer from the reductase by partially or wholly covering its binding site on the hydroxylase canyon walls. Sharing of the hydroxylase surface by the reductase and regulatory protein components would imply that a critical role for the regulatory proteins in all BMMs is to prevent reduction of the dioxygen-activated diiron center at inappropriate times during the catalytic cycle. The recombinant PH enzyme system is ideal for testing the various structural control features, such as hydrogen bonding networks, cavity gates, active site pores, and helix rearrangements, that we

suggest may be functionally significant for substrate entrance, electron transfer, and component interactions. Moreover, the PH system will allow future testing of mechanistic theories related to the different reactivities of BMMs.

ACKNOWLEDGMENT

We thank Dr. Viviana Izzo (Università di Napoli Federico II) for providing the plasmids and protein-expressing strains as well as Eugenio Notomista (Università di Napoli Federico II) and Leslie Muray (Massachusetts Institute of Technology) for useful discussions about substrate regiospecificity and electron transfer.

SUPPORTING INFORMATION AVAILABLE

BMM hydroxylase and regulatory protein structures and their electrostatic surfaces (Figures S1 and S2), packing of the β -subunit N-terminus and a γ -subunit from an adjacent molecule in the PHH canyon (Figure S3), comparison of known regulatory protein structures (Figure S4), sequence alignments of the different regulatory proteins (Figure S5), models of the PHH diiron center in electron density maps (Figure S6), comparison of the hydroxylase zinc-binding sequences (Figure S7), and electron density maps around helix F (Figure S8). This material is available free of charge via the Internet at <http://pubs.acs.org>.

REFERENCES

1. Merckx, M., Kopp, D. A., Sazinsky, M. H., Blazyk, J. L., Müller, J., and Lippard, S. J. (2001) Dioxygen activation and methane

- hydroxylation by soluble methane monooxygenase: A tale of two irons and three proteins, *Angew. Chem., Int. Ed.* **40**, 2783–2807 (and references cited therein).
2. Notomista, E., Lahm, A., Di Donato, A., and Tramontano, A. (2003) Evolution of bacterial and archaeal multicomponent monooxygenases, *J. Mol. Evol.* **56**, 435–445.
 3. Leahy, J. G., Batchelor, P. J., and Morcomb, S. M. (2003) Evolution of the soluble diiron monooxygenases, *FEMS Microbiol. Rev.* **27**, 449–479.
 4. Kurtz, D. M., Jr. (1997) Structural similarity and functional diversity in diiron-oxo proteins, *J. Biol. Inorg. Chem.* **2**, 159–167.
 5. Sazinsky, M. H., and Lippard, S. J. (2006) Correlating structure with function in bacterial multicomponent monooxygenases and related diiron proteins, *Acc. Chem. Res.* **39**, 558–566.
 6. Fox, B. G., Borneman, J. G., Wackett, L. P., and Lipscomb, J. D. (1990) Haloalkene oxidation by the soluble methane monooxygenase from *Methylosinus trichosporium* OB3b: Mechanistic and environmental implications, *Biochemistry* **29**, 6419–6427.
 7. Hanson, R. S., and Hanson, T. E. (1996) Methanotrophic bacteria, *Microbiol. Rev.* **60**, 439–471.
 8. Rosenzweig, A. C., Frederick, C. A., Lippard, S. J., and Nordlund, P. (1993) Crystal structure of a bacterial non-haem iron hydroxylase that catalyses the biological oxidation of methane, *Nature* **366**, 537–543.
 9. Sazinsky, M. H., Bard, J., Di Donato, A., and Lippard, S. J. (2004) Structure of the toluene/*o*-xylene monooxygenase hydroxylase from *Pseudomonas stutzeri* OX1: Substrate channeling and active site tuning of multicomponent monooxygenases, *J. Biol. Chem.* **279**, 30600–30610.
 10. Pikus, J. D., Studts, J. M., Achim, C., Kauffmann, K. E., Münck, E., Steffan, R. J., McClay, K., and Fox, B. G. (1996) Recombinant toluene-4-monooxygenase: Catalytic and Mössbauer studies of the purified diiron and Rieske components of a four-protein complex, *Biochemistry* **35**, 9106–9119.
 11. Gallagher, S. C., Cammack, R., and Dalton, H. (1997) Alkene monooxygenase from *Nocardia corallina* B-276 is a member of the class of dinuclear iron proteins capable of stereospecific epoxidation reactions, *Eur. J. Biochem.* **247**, 635–641.
 12. Cadieux, E., Vrajmasu, V., Achim, C., Powlowski, J., and Münck, E. (2002) Biochemical, Mössbauer, and EPR studies of the diiron cluster of phenol hydroxylase from *Pseudomonas* sp. strain CF 600, *Biochemistry* **41**, 10680–10691.
 13. Valentine, A. M., Stahl, S. S., and Lippard, S. J. (1999) Mechanistic studies of the reaction of reduced methane monooxygenase hydroxylase with dioxygen and substrates, *J. Am. Chem. Soc.* **121**, 3876–3887.
 14. Beauvais, L. G., and Lippard, S. J. (2005) Reactions of the peroxo intermediate of soluble methane monooxygenase hydroxylase with ethers, *J. Am. Chem. Soc.* **127**, 7370–7378.
 15. Murray, L. J., Garcia-Serres, R., Naik, S., Huynh, B. H., and Lippard, S. J. (2006) Dioxygen activation at non-heme diiron centers: Characterization of intermediates in a mutant form of toluene/*o*-xylene monooxygenase hydroxylase, *J. Am. Chem. Soc.* **128**, 7458–7459.
 16. Green, J., and Dalton, H. (1989) Substrate specificity of soluble methane monooxygenase: Mechanistic implications, *J. Biol. Chem.* **264**, 17698–17703.
 17. Froland, W. A., Andersson, K. K., Lee, S. K., Liu, Y., and Lipscomb, J. D. (1992) Methane monooxygenase component B and reductase alter the regioselectivity of the hydroxylase component-catalyzed reactions, *J. Biol. Chem.* **267**, 17588–17597.
 18. Mitchell, K. H., Studts, J. M., and Fox, B. G. (2002) Combined participation of hydroxylase active residues and effector protein binding in a *para* to *ortho* modulation of toluene 4-monooxygenase regioselectivity, *Biochemistry* **41**, 3176–3188.
 19. Gassner, G. T., and Lippard, S. J. (1999) Component interactions in the soluble methane monooxygenase system from *Methylococcus capsulatus* (Bath), *Biochemistry* **38**, 12768–12785.
 20. Cafaro, V., Izzo, V., Scognamiglio, R., Notomista, E., Capasso, P., Casbarra, A., Pucci, P., and Di Donato, A. (2004) Phenol hydroxylase and toluene/*o*-xylene monooxygenase from *Pseudomonas stutzeri* OX1: Interplay between two enzymes, *Appl. Environ. Microbiol.* **70**, 2211–2219.
 21. LeMaster, D. M., and Richards, F. M. (1985) ^1H – ^{15}N heteronuclear NMR studies of *Escherichia coli* thioredoxin in samples isotopically labeled by residue type, *Biochemistry* **24**, 7263–7268.
 22. Gibbs, C. R. (1976) Characterization and application of ferrozine iron reagent as a ferrous iron indicator, *Anal. Chem.* **48**, 1197–1201.
 23. Otwinowski, Z., and Minor, W. (1997) HKL Suite of programs, *Methods Enzymol.* **276**, 307–326.
 24. Brünger, A. T., Adams, P. D., Clore, G. M., Delano, W. L., Gros, P., Grosse-Kunstleve, R. W., Jiang, J.-S., Kuszewski, J., Nilges, N., Pannu, N. S., Read, R. J., Rice, L. M., Simonson, T., and Warren, G. L. (1998) Crystallography and NMR system (CNS): A new software system for macromolecular structure determination, *Acta Crystallogr. D54*, 905–921.
 25. Terwilliger, T. C., and Berendzen, J. (1999) Automated MAD and MIR structure solution, *Acta Crystallogr. D55*, 849–861.
 26. Sheldrick, G. M., and Uson, I. (1999) Advances in direct methods for protein crystallography, *Curr. Opin. Struct. Biol.* **9**, 643–648.
 27. Weeks, C. M., and Miller, R. (1999) The design and implementation of *SnB* v2.0, *J. Appl. Crystallogr.* **32**, 120–124.
 28. Collaborative Computational Project Number 4 (1995) The CCP4 suite: Programs for protein crystallography, *Acta Crystallogr. D50*, 760–763.
 29. McRee, D. E. (1999) XtalView/Xfit: A versatile program for manipulating atomic coordinates and electron density, *J. Struct. Biol.* **125**, 156–165.
 30. Jones, T. A., Zou, J.-Y., Cowan, S. W., and Kjeldgaard, M. (1991) Improved methods for the building of protein models in electron density maps and the location of errors in these models, *Acta Crystallogr. A47*, 110–119.
 31. Laskowski, R. A., MacArthur, M. W., Moss, D. S., and Thornton, J. M. (1993) PROCHECK: A program to check the stereochemical quality of protein structures, *J. Appl. Crystallogr.* **26**, 283–291.
 32. Sazinsky, M. H., Merckx, M., Cadieux, E., Tang, S., and Lippard, S. J. (2004) Preparation and X-ray structures of metal-free, dicobalt and dimanganese forms of soluble methane monooxygenase hydroxylase from *Methylococcus capsulatus* (Bath), *Biochemistry* **43**, 16263–16276.
 33. Sazinsky, M. H., and Lippard, S. J. (2005) Product bound structures of the soluble methane monooxygenase hydroxylase from *Methylococcus capsulatus* (Bath): Protein motion in the α -subunit, *J. Am. Chem. Soc.* **127**, 5814–5825.
 34. Walters, K. J., Gassner, G. T., Lippard, S. J., and Wagner, G. (1999) Structure of the soluble methane monooxygenase regulatory protein B, *Proc. Natl. Acad. Sci. U.S.A.* **96**, 7877–7882.
 35. Chang, S.-L., Wallar, B. J., Lipscomb, J. D., and Mayo, K. H. (1999) Solution structure of component B from methane monooxygenase derived through heteronuclear NMR and molecular modeling, *Biochemistry* **38**, 5799–5812.
 36. Hemmi, H., Studts, J. M., Chae, Y. K., Song, J., Markley, J. L., and Fox, B. G. (2001) Solution structure of the toluene 4-monooxygenase effector protein (T4moD), *Biochemistry* **40**, 3512–3524.
 37. Lountos, G. T., Mitchell, K. H., Studts, J. M., Fox, B. G., and Orville, A. M. (2005) Crystal structures and functional studies of T4moD, the toluene 4-monooxygenase catalytic effector protein, *Biochemistry* **44**, 7131–7142.
 38. Brazeau, B. J., Wallar, B. J., and Lipscomb, J. D. (2003) Effector proteins from P450cam and methane monooxygenase: Lessons in tuning nature's powerful reagents, *Biochem. Biophys. Res. Commun.* **312**, 143–148.
 39. Chang, S., Wallar, B. J., Lipscomb, J. D., and Mayo, J. D. (2001) Residues in *Methylosinus trichosporium* OB3b methane monooxygenase component B involved in molecular interactions with reduced- and oxidized-hydroxylase component: A role for the N-terminus, *Biochemistry* **40**, 9539–9551.
 40. Zhang, J., Wallar, B. J., Popescu, C. V., Renner, D. B., Thomas, D. D., and Lipscomb, J. D. (2006) Methane monooxygenase hydroxylase and B component interactions, *Biochemistry* **45**, 2913–2926.
 41. MacArthur, R., Sazinsky, M. H., Kühne, H., Whittington, D. A., Lippard, S. J., and Brudvig, G. W. (2002) Component B binding to the soluble methane monooxygenase hydroxylase by saturation recovery-EPR spectroscopy of spin-labeled MMOB, *J. Am. Chem. Soc.* **124**, 13392–13393.
 42. Lloyd, J. S., Bhambra, A., Murrell, J. C., and Dalton, H. (1997) Inactivation of the regulatory protein B of soluble methane monooxygenase from *Methylococcus capsulatus* (Bath) by proteolysis can be overcome by a Gly to Gln modification, *Eur. J. Biochem.* **248**, 72–79.

43. Brandstetter, H., Whittington, D. A., Lippard, S. J., and Frederick, C. A. (1999) Mutational and structural analyses of the regulatory protein B of soluble methane monooxygenase from *Methylococcus capsulatus* (Bath). *Chem. Biol.* 6, 441–449.
44. Wallar, B. J., and Lipscomb, J. D. (2001) Methane monooxygenase component B mutants alter the kinetic steps throughout the catalytic cycle. *Biochemistry* 40, 2220–2233.
45. Zhang, J., and Lipscomb, J. D. (2006) Role of the C-terminal region of the B component of *Methylosinus trichosporium* OB3b methane monooxygenase in the regulation of oxygen activation. *Biochemistry* 45, 1459–1469.
46. Elango, N., Radhakrishnan, R., Froland, W. A., Wallar, B. J., Earhart, C. A., Lipscomb, J. D., and Ohlendorf, D. H. (1997) Crystal structure of the hydroxylase component of methane monooxygenase from *Methylosinus trichosporium* OB3b. *Protein Sci.* 6, 556–568.
47. Rosenzweig, A. C., and Lippard, S. J. (1994) Determining the structure of a hydroxylase enzyme that catalyzes the conversion of methane to methanol in methanotrophic bacteria. *Acc. Chem. Res.* 27, 229–236.
48. Rosenzweig, A. C., Nordlund, P., Takahara, P. M., Frederick, C. A., and Lippard, S. J. (1995) Geometry of the soluble methane monooxygenase catalytic diiron center in two oxidation states. *Chem. Biol.* 2, 409–418.
49. Whittington, D. A., and Lippard, S. J. (2001) Crystal structures of the soluble methane monooxygenase hydroxylase from *Methylococcus capsulatus* (Bath) demonstrating geometrical variability at the dinuclear iron active site. *J. Am. Chem. Soc.* 123, 827–838.
50. Whittington, D. A., Sazinsky, M. H., and Lippard, S. J. (2001) X-ray crystal structure of alcohol products bound at the active site of soluble methane monooxygenase hydroxylase. *J. Am. Chem. Soc.* 123, 1794–1795.
51. Cadioux, E., and Powlowski, J. (1999) Characterization of active and inactive forms of the phenol hydroxylase stimulatory protein DmpM. *Biochemistry* 38, 10714–10722.
52. Krutz, D. M., Jr. (1990) Oxo- and hydroxo-bridged diiron complexes: A chemical perspective on a biological unit. *Chem. Rev.* 90, 585–606.
53. Lindqvist, Y., Huang, W., Schneider, G., and Shanklin, J. (1996) Crystal structure of Δ^9 stearoyl-acyl carrier protein desaturase from castor seed and its relationship to other di-iron proteins. *EMBO J.* 15, 4081–4092.
54. Logan, D. T., Su, X.-D., Åberg, A., Regnström, K., Hajdu, J., Eklund, H., and Nordlund, P. (1996) Crystal structure of reduced protein R2 of ribonucleotide reductase: The structural basis for oxygen activation at a dinuclear iron site. *Structure* 4, 1053–1064.
55. Eriksson, M., Jordan, A., and Eklund, H. (1998) Structure of *Salmonella typhimurium* nrdF ribonucleotide reductase in its oxidized and reduced forms. *Biochemistry* 37, 13359–13369.
56. Einsle, O., Tezcan, F. A., Andrade, S. L. A., Schmid, B., Yoshida, M., Howard, J. B., and Rees, D. C. (2002) Nitrogenase MoFe-protein at 1.16 Å resolution: A central ligand in the FeMo-cofactor. *Science* 297, 1696–1700.
57. McCormick, M. S., Sazinsky, M. H., Condon, K. L., and Lippard, S. J. (2006) X-ray crystal structures of manganese(II) reconstituted and native toluene/*o*-xylene monooxygenase hydroxylase reveal rotamer shifts in conserved residues and an enhanced view of the protein interior. *J. Am. Chem. Soc.* 128, 15108–15110.
58. Pikus, J. D., Studts, J. M., McClay, K., Steffan, R. J., and Fox, B. G. (1997) Changes in the regioselectivity of aromatic hydroxylation produced by active site engineering in the diiron enzyme toluene 4-monooxygenase. *Biochemistry* 36, 9283–9289.
59. Newman, L. M., and Wackett, L. P. (1995) Purification and characterization of toluene 2-monooxygenase from *Burkholderia cepacia* G4. *Biochemistry* 34, 14066–14076.
60. Pikus, J. D., Mitchell, K. H., Studts, J. M., McClay, K., Steffan, R. J., and Fox, B. G. (2000) Threonine 201 in the diiron enzyme toluene 4-monooxygenase is not required for catalysis. *Biochemistry* 39, 791–799.
61. Frolow, F., Kalb, A. J., and Yariv, J. (1994) Structure of a unique two fold symmetric heme-binding site. *Nat. Struct. Biol.* 1, 453–460.
62. deMare, F., Kurtz, D. M., Jr., and Nordlund, P. (1996) The structure of *Desulfobrio vulgaris* rubrerythrin reveals a unique combination of rubredoxin-like FeS4 and ferritin-like diiron domains. *Nat. Struct. Biol.* 3, 539–546.
63. Stubbe, J., Nocera, D. G., Yee, C. S., and Chang, M. C. Y. (2003) Radical initiation in the Class I ribonucleotide reductase: Long-range proton-coupled electron transfer? *Chem. Rev.* 103, 2167–2202.
64. Sobrado, P., Lyle, K. S., Kaul, S. P., Turco, M. M., Arabshahi, I., Marwah, A., and Fox, B. G. (2006) Identification of the binding region of the [2Fe-2S] ferredoxin in stearoyl-acyl carrier protein desaturase: Insight into the catalytic complex and mechanism of action. *Biochemistry* 45, 4848–4858.
65. Blazyk, J. L., Gassner, G. T., and Lippard, S. J. (2005) Intermolecular electron-transfer reactions in soluble methane monooxygenase: A role for hysteresis in protein function. *J. Am. Chem. Soc.* 127, 17364–17376.
66. Liu, K. E., and Lippard, S. J. (1991) Redox properties of the hydroxylase component of methane monooxygenase from *Methylococcus capsulatus* (Bath): Effects of protein B, reductase, and substrate. *J. Biol. Chem.* 266, 12836–12839.
67. Paulsen, K. E., Liu, Y., Fox, B. G., Lipscomb, J. D., Münck, E., and Stankovich, M. T. (1994) Oxidation-reduction potentials of the methane monooxygenase hydroxylase component from *Methylosinus trichosporium* OB3b. *Biochemistry* 33, 713–722.
68. Kazlauskaitė, J., Hill, H. A. O., Wilkins, P. C., and Dalton, H. (1996) Direct electrochemistry of the hydroxylase of soluble methane monooxygenase from *Methylococcus capsulatus* (Bath). *Eur. J. Biochem.* 241, 552–556.
69. Whittington, D. A., Rosenzweig, A. C., Frederick, C. A., and Lippard, S. J. (2001) Xenon and halogenated alkanes track putative substrate binding cavities in the soluble methane monooxygenase hydroxylase. *Biochemistry* 40, 3476–3482.
70. DeLano, W. L. (2002) *The PyMol Molecular Graphics System*, DeLano Scientific LLC, San Carlos, CA.
71. Zheng, H., and Lipscomb, J. D. (2006) Regulation of methane monooxygenase catalysis based on size exclusion and quantum tunneling. *Biochemistry* 45, 1685–1692.
72. Brazeau, B. J., and Lipscomb, J. D. (2003) Key amino acid residues in the regulation of soluble methane monooxygenase catalysis by component B. *Biochemistry* 42, 5618–5631.
73. Lippard, S. J. (2005) Hydroxylation of C–H bonds at carboxylate-bridged diiron centres. *Philos. Trans. R. Soc. London, Ser. A* 363, 861–877.
74. Canada, K. A., Iwashita, A., Shim, H., and Wood, T. K. (2002) Directed evolution of toluene *ortho*-monooxygenase for enhanced 1-naphthol synthesis and chlorinated ethene degradation. *J. Bacteriol.* 184, 344–349.
75. Cafaro, V., Scognamiglio, R., Viggiani, A., Izzo, V., Passaro, I., Notomista, E., Dal Piaz, F., Amoresano, A., Casbarra, A., Pucci, P., and Di Donato, A. (2002) Expression and purification of the recombinant subunits of toluene/*o*-xylene monooxygenase and reconstitution of the active complex. *Eur. J. Biochem.* 269, 5689–5699.
76. Cafaro, V., Notomista, E., Capasso, P., and Di Donato, A. (2005) Regioselectivity of two multicomponent monooxygenases from *Pseudomonas stutzeri* OX1: Molecular basis for catabolic adaption of this microorganism to methylated aromatic compounds. *Appl. Environ. Microbiol.* 71, 4736–4743.
77. Cafaro, V., Notomista, E., Capasso, P., and Di Donato, A. (2005) Mutation of glutamic acid 103 of toluene *o*-xylene monooxygenase as a means to control the catabolic efficiency of a recombinant upper pathway for degradation of methylated aromatic compounds. *Appl. Environ. Microbiol.* 71, 4744–4750.
78. Baik, M.-H., Newcomb, M., Friesner, R. A., and Lippard, S. J. (2003) Mechanistic studies on the hydroxylation of methane by methane monooxygenase. *Chem. Rev.* 103, 2385–2420.

BI0618969

X-ray Structure of a Hydroxylase-Regulatory Protein Complex from a
Hydrocarbon-Oxidizing Multicomponent Monooxygenase, *Pseudomonas stutzeri*
OX1 Phenol Hydroxylase^{†,‡}

Matthew H. Sazinsky,^{§,¶} Pete W. Dunten,[⊥] Michael S. McCormick,[§] Alberto DiDonato,^{||} and
Stephen J. Lippard^{§,*}

[§]*Department of Chemistry, Massachusetts Institute of Technology, Cambridge MA 02139;*

[⊥]*Stanford Synchrotron Radiation Laboratory, Stanford University, Menlo Park, CA 94025;*

^{||}*Dipartimento di Chimica Biologica, Universita' di Napoli Federico II, 80134 Napoli, Italy*

Running Title: Structure of a Phenol Hydroxylase-Regulatory Protein Complex

[†]This research was supported by National Institute of General Medical Sciences Grant GM32134 (S.J.L.) and the Italian Ministry of University and Research, PRIN/2002 (A.D.).

[‡]The coordinates and structure factors for the PHH-PHM complex have been deposited in the Protein Data Bank (entries XXXX and XXXX) for the native and SeMet enzyme, respectively.

[¶]Current position: NRSA postdoctoral fellow (GM073457) in the Department of Biochemistry, Molecular and Cell Biology, Northwestern University, Evanston IL 60202.

* To whom correspondence should be addressed. E-mail: lippard@mit.edu. Telephone: (617) 253-1892. Fax: (617) 258-8150.

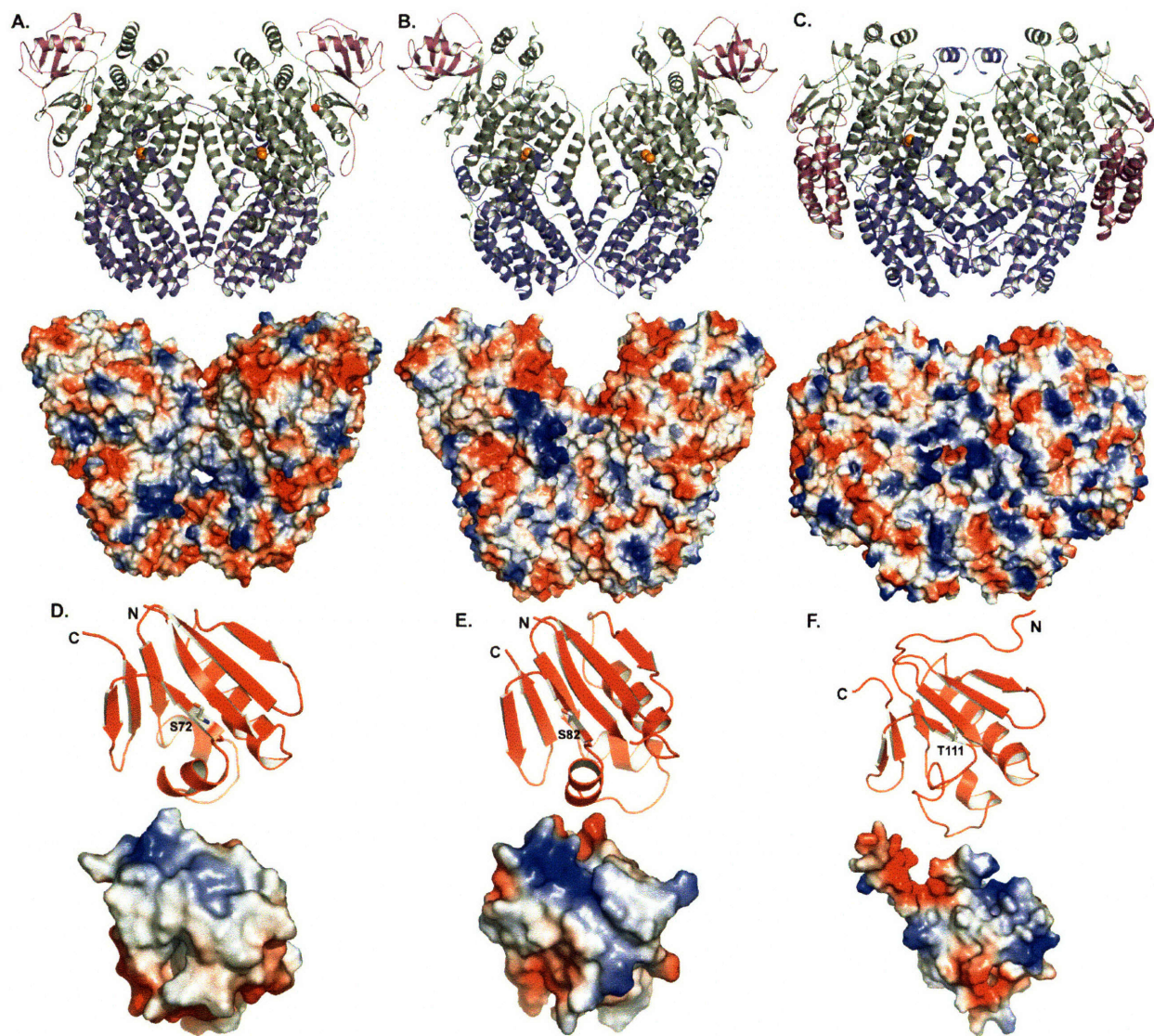


Figure S1. Structure and electrostatic surfaces of (A) PHH, (B) ToMOH, and (C) MMOH. The hydroxylase α , β , and γ subunits are colored gray, blue, and purple, respectively. Protein and electrostatic surfaces of (D) PHM, and of those predicted by homology for (E) T4MOD and (F) MMOB, that pack against the hydroxylase are also shown. Electrostatic surfaces were generated by using APBS in PyMol. Red surfaces are negatively charged and blue surfaces are positively charged.

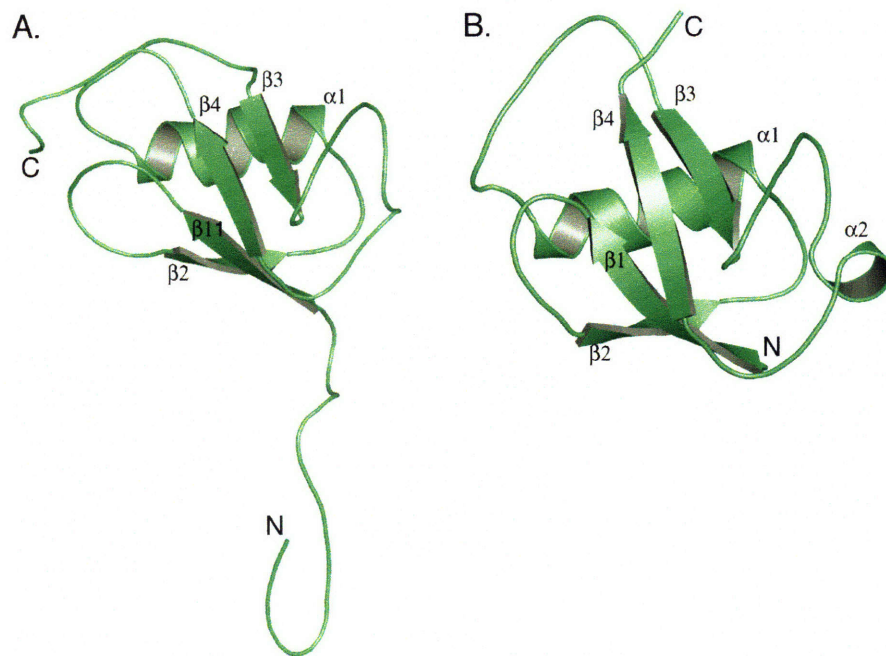


Figure S2. Structures of the (A) PHH and (B) ToMOH γ -subunits. The α -helices and β -strands are labeled accordingly.

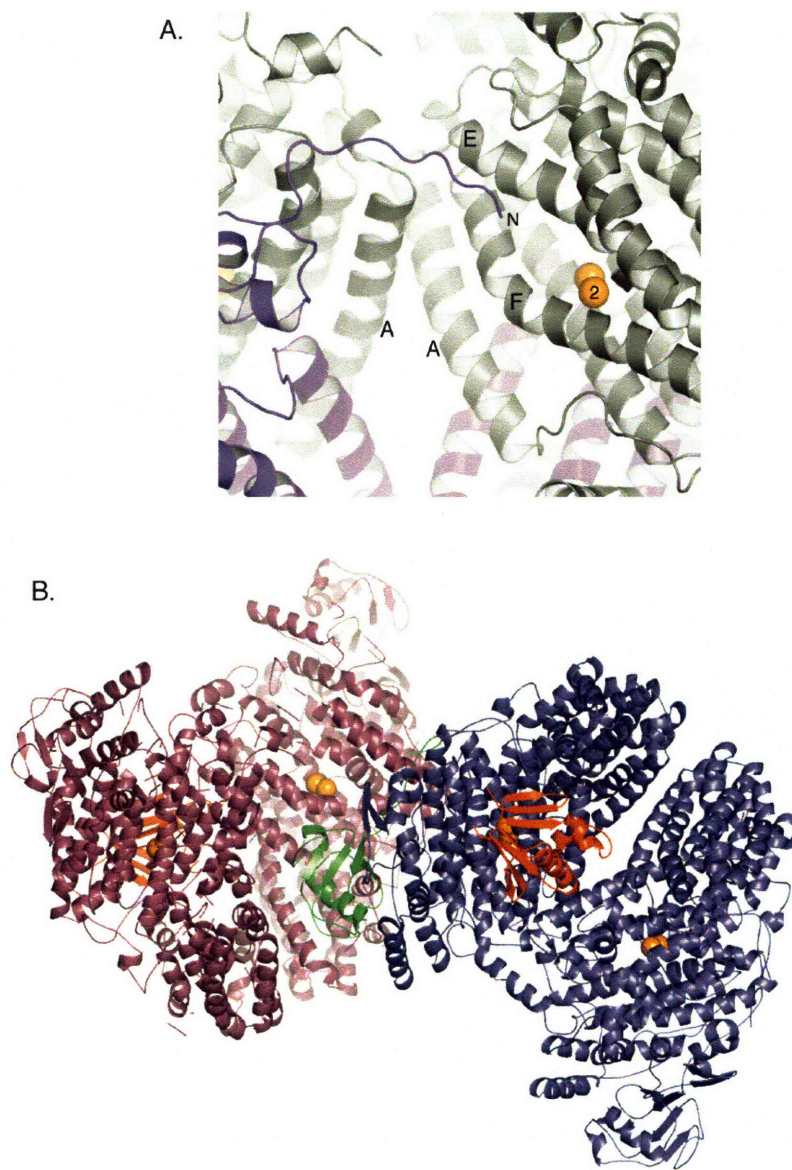


Figure S3. (A) Interaction of the PHH β -subunit N-terminus (purple) with α -subunit helices E and F (gray) on the hydroxylase surface in which PHM is not bound. (B) Packing interaction of PHH and PHM molecules in the crystal lattice. The γ -subunit (green) of one PHH molecule (blue) packs against the canyon region of an adjacent PHH molecule (purple). PHM is colored red.

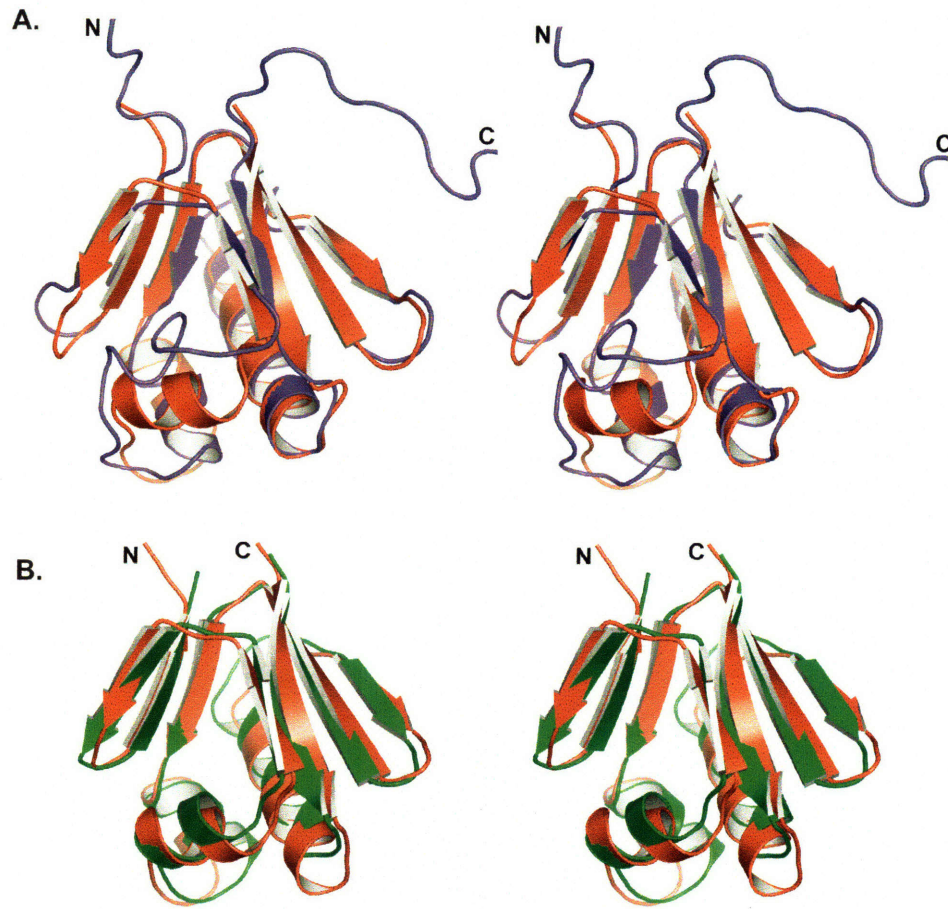


Figure S4. Structural comparisons between BMM regulatory proteins. Alignments of (A) PHM (red) and MMOH (purple) and (B) PHM and T4MOD (green) in stereo.

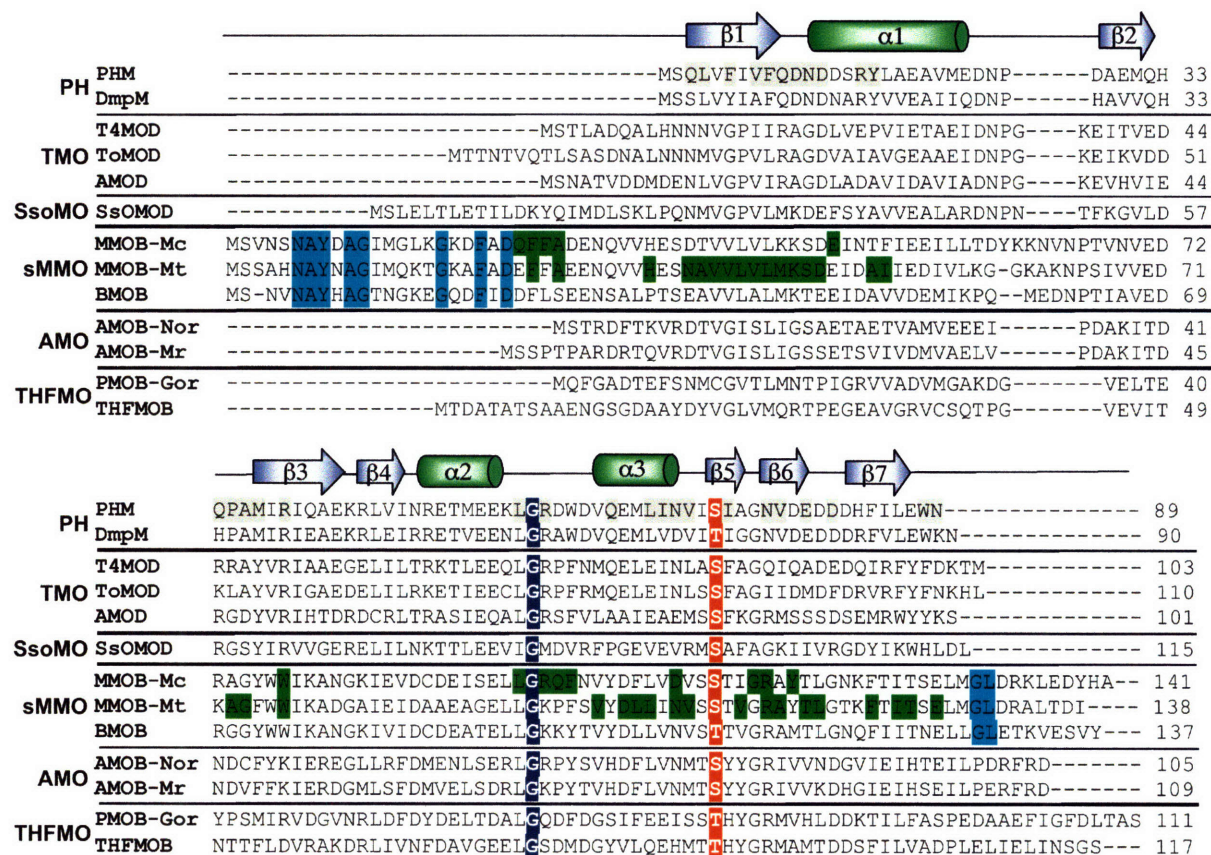


Figure S5. Sequence alignment of BMM regulatory proteins within their specific sub-families. PHM residues highlighted in gray form contacts with the PHH surface. Residues in green mark MMOB positions that experience greater than average NMR line broadening in the presence of MMOH. Teal shading denotes highly conserved sMMOH residues in the N- and C-termini that may be important for function. Blue shading denotes a strictly conserved residue while red shading marks a conserved residue having important catalytic function. The regulatory protein sequences and accession numbers used for the alignment are: PHM, *Pseudomonas stutzeri* OX1 (AAO47357), DmpM *Pseudomonas* sp. strain CF600 (P19731); T4MOD, *Pseudomonas mendocina* (2BF2_B); ToMOD, *Pseudomonas stutzeri* OX1 (AAT40434); AMOD,

Xanthobacter autotrophicus Py2 (CAA09914); SsoMOD, *Sulfolobus solfataricus* P2 (NP_342687); MMOB-Mc, *Methylococcus capsulatus* Bath (P18797); MMOB-Mt, *Methylosinus trichosporium* OB3b (P27356); BMOB, *Pseudomonas butanovora* (AAM19729); AMOB-Nor, *Nocardioides* sp. JS614 (AAV52083); AMOB-Mr, *Mycobacterium rhodesiae* (AAO48575); PMOB, *Gordonia* sp. TY-5 (BAD03959), THFMOB, *Pseudonocardia* sp. K1 (CAC10510).

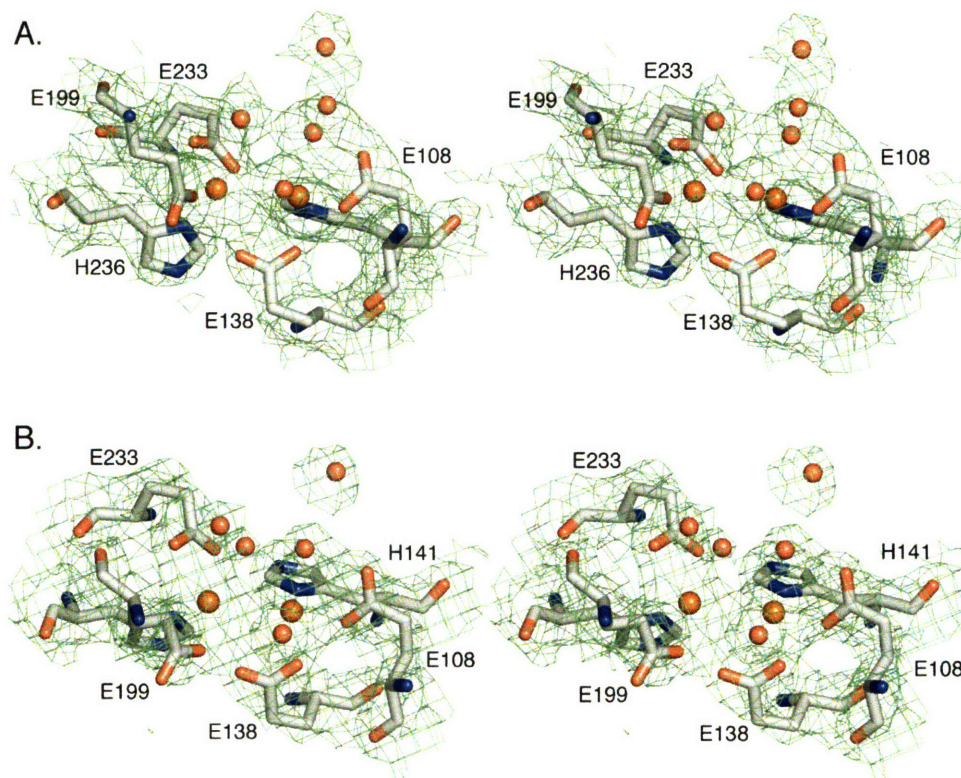


Figure S6. Stereo view of the $|2F_o| - |F_c|$ simulated-annealing omit electron density maps (green) surrounding the native PHH diiron active sites from (A) chain A and (B) PHM-bound chain B contoured to 1.2σ .

```

sMMO IYIDRVSQVP-FCPSLAKGASTLRVHE--YNGQMHTFSDQWGERM 456
-----
AMO P-MCQVQVPCVMPRLDMNAA--RIIE--FEGQKIALCSEPQRI 430
-----
PhN PQLCQVQIPIPTIFTEKD-APTMLSHRQIEHEGERYHFCSDGDCDI 439
MopN PQLCQVQIIPMTFFEMDGDPTLFSYRDSIYKDERYHTCSDGCHDI 447
PhhN PHLQVQVPAIFFEPD-DPTKLSLRSLVHEGERYHFCSDGDCDI 439
PhlD PHLQVQVPAIFFEPD-DPTKLSLRSLVHEGERYHFCSDGDCDI 439
DmpN PHLQVQVQLPVIFFEPD-DPTKLSLRSLVHEGERYQFCSDGDCDI 440
PhcN PMLCTTQIPMGFFEP-GDATKICYRESDYEGSKYHFCSDGDKHV 441
TbmD PMLCTTQIPMGFFEP-GDATKIAYRESDYFGMKYHFCSDHDKHI 440
TomA PMLCTTQIPMIFFEP-GDATKICYRESAYLGDKYHFCSDHDKHI 441
PoxD PMLCTTQIPMIFFEPD-DPTQTCYRESSYHGKMFHFCSDGDKDI 438
-----
ToMO PTICNMNLPIAHT--PGNKWNVKDYQLEYEGRLYHFGSEADRWC 435

```

Figure S7. Sequence alignment of the C-terminal portion of the PH hydroxylase α -subunit depicting the conserved cysteines contributing to the zinc binding site in PHH. The alignment was adapted from Leahy, et al. (3). Phenol hydroxylase α -subunit sequences are from *Pseudomonas stutzeri* OX1 (PhN), *Acinetobacter calcoaceticus* NCIB8250 (MopN), *Pseudomonas putida* P35X (PhhN), *Pseudomonas putida* H (PhlD), *Pseudomonas* sp. Strain CF600 (DmpN), *Comamonas testosteroni* R5 (PhcN), *Burkholderia cepacia* JS150 (TbmD), *Burkholderia cepacia* G4 (TomA3), and *Ralstonia eutropha* E2 (PoxD).

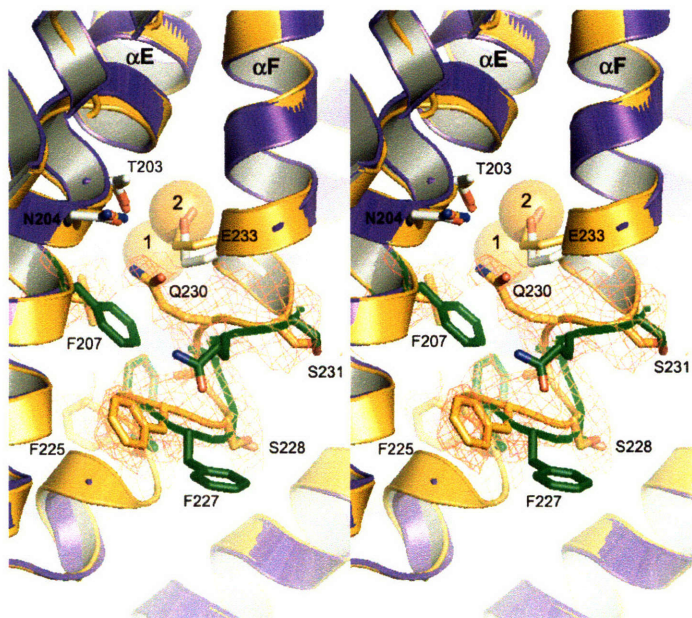


Figure S8. Structural changes in helix F. A $|2F_o| - |F_c|$ simulated annealing electron density omit map (red) contoured at 1.0σ around α -subunit helices E and F from the SeMet PHH-PHM structure (orange), depicts structural changes in stereo. Residues in green depict the unaltered conformation of helix E and F residues in the other PHH α -subunits.

APPENDIX 2

Experimental Procedures for the Expression and Purification of Monoclonal Antibodies to MMOH from Hybridoma Cell Lines

Introduction

During the previous four years, monoclonal antibodies (MAbs) to MMOH have been expressed in the lab in effort to ultimately obtain corresponding MMOH-binding Fab fragments and use them as MMO system crystallization agents. One result of this work is was development of a generalized scheme to represent the many biological and biochemical procedures involved in this project. The initial stages of this process require hybridoma cell culture, are relatively straightforward, and were successfully conducted in the lab since shortly after the project's inception. The remaining stages of the process leading up to and including screening for crystallization conditions, however, proved a much greater challenge. A majority of the problems initially encountered involve purification of the MAbs and Fab fragments. At the end of this project and upon successful purification of the MAbs, it became clear that the antibody titer from the expression cell lines is extremely low and can not be improved because it is due to poor cell fusion that occurred during the creation of the hybridoma cells at an outside laboratory. Along with a discussion of antibody technology and structure, the experimental procedures employed in this project are summarized below.

Monoclonal Antibody Structure and Technology. For a complete understanding of the challenges at hand in this project it is beneficial to keep in mind fundamentals of antibody technology and structure.(1) Antibodies are precisely identical serum proteins that fall into a class of molecules called Igs. B cells in the host organism produce antibodies as an immune response to foreign macromolecules, called antigens in this context. Upon recognition of an antigen, naïve B cells interact with specific T cells and induce cloning to yield plasma B cells, that each produces a specific MAb. Epitopes on

the surface of antigens provide binding sites to which MAb molecules are complementary. Large proteins usually have multiple epitopes, thereby inducing the production of multiple distinct and site specific MAbs. The production of antibodies by plasma B cells is notably fast, voluminous, and accurate. Moreover, this process is a highly effective immune response mechanism because antibody-antigen complexes are easily recognized and removed by the liver or spleen of the host organism.

MAbs are composed of four polypeptide chains, two heavy and two light, that are linked by disulfides and organized in an overall Y shape (Figure 1).(2) The heavy and light chains each have constant and variable domains that are so named because of the observed variance differences in the amino acid sequences of different antibodies. The variable domains of one heavy and one light chain form the two identical antigen-binding sites on each antibody. The Fab region of the antibody contains the antigen-binding site, and is composed of one light chain and the variable domain of one heavy chain. Conversely, the antibody Fc region is composed only of the constant domains of the two heavy chains, and is virtually identical in all antibodies from the same organism. MAb proteolysis with the enzyme papain occurs at the hinge region, and yields two Fab and one Fc fragment, which are each approximately 50 kDa in mass.

Antibodies to specific proteins can be isolated and mass-produced using monoclonal antibody technology. The technique begins with the immunization of an animal, typically a mouse or rabbit, with the protein to which antibodies are desired. Following an immune response from the animal, its spleen is removed, and plasma B cells are isolated from the contents. The isolated plasma B cells are then combined in suspension with cultured mutant myeloma cells in conditions that favor cell fusion.

Myeloma cells used in this preparation are engineered such that they will not grow in the presence of aminopterin. The B and myeloma cells undergo fusion to yield hybridoma cells (Figure 2), and are transferred to media containing aminopterin. Only the hybridoma cells survive the transfer to the aminopterin-containing media, allowing for selection of the hybridomas. Furthermore, by fusion with myeloma cells the plasma B cells become immortal, and will indefinitely produce single MAbs. Individual cell lines producing different antibodies are identified through diagnostic tests with the antigen molecule. Following, specific cell lines are isolated and cultured for the production of individual MAbs to the antigen of interest.

Monoclonal antibody technology provides a formidable source of tools for use in countless biochemical applications. Routine assays like ELISA and Western Blot are based entirely on this technology. One emerging application is in the structural characterization of membrane proteins, where MAb Fab fragments have been successfully employed in the solubilization of the transmembrane regions to yield crystallizable samples.⁽³⁾ Fab fragments may similarly be utilized as crystallization agents for soluble proteins by stabilizing conformationally flexible regions and aiding in crystal lattice formation, as in the case of the present study.

Experimental Methods

General Considerations. The hybridoma cell cultures were maintained and, in most cases, inoculated from DMSO cell stocks by Dianna Matthes under the supervision of the author. MAb and Fab fragment purifications were conducted using a GE Healthcare AKTA Purifier 10 fitted with inline conductivity, pH, and A₂₈₀ detectors

and an automatic fraction collector. All Native and SDS PAGE analysis was conducted using BioRad 15 well, 15 uL Ready Gels. SDS-PAGE sample buffer contained 62.5 mM Tris pH 6.8, 2% (w/v) SDS, 25% (v/v) glycerol, 0.01% (w/v) Bromphenol Blue and 5 % (v/v) b-mercaptoethanol. SDS-PAGE running buffer contained 0.1% (w/v) SDS, 25 mM Tris and 192 mM Glycine.

MAb Expression: Growth and Harvest of Antibody Cell Lines. Frozen DMSO stocks of MMOH monoclonal antibody producing hybridoma cell lines (Cell Essentials) were kept in liquid N₂ storage dewars. 1 mL stocks were removed from liquid N₂ storage and thawed quickly at 37 °C. Combined growth media consisted of 90% Utility media, 10% Fetalclone III (HyClone), and 1:100 dilution of penicillin/streptomycin antibiotics (Invitrogen). Combined growth media was prepared and sterilized with a 0.2-micron filter immediately before use. Upon thaw completion cells from the DMSO stock were added to 12 mL of combined growth media and allowed to diffuse for 5 minutes at room temperature. Cells and media were then centrifuged at 100 x g for 7 min. The cell pellet was isolated from the DMSO-containing supernatant and resuspended in 12 mL of fresh media. Cells and media were split evenly in volume and incubated at 37 °C and 5% CO₂ in T25 canted neck breathable flasks (Falcon). Cell density was monitored daily by hemacytometer cell counting. Upon reaching a density of 8 x 10⁵ to 1 x 10⁶ cells/mL growth flasks were scraped to loosen surface attached cells and the contents were transferred to sterile centrifuge tubes. Combined growth media was then exchanged by centrifuging cells and media at 100 x g for 7 minutes and resuspending the pellet in approximately three times the previous volume of fresh combined media.

Cells and media were then returned to incubation at 37 °C and 5% CO₂ in multiple T75 canted neck breathable flasks (Falcon).

Media exchange and cell proliferation continued under this protocol until a volume of approximately 500 mL of cells and media was reached. Upon reaching a volume ≥ 500 mL, cells and media incubation at 37 °C continued but media exchange was ceased. Hybridoma cell vitality was monitored daily by Trypan Blue staining. This was accomplished by combining 0.5 mL 4% (v/v) Trypan Blue, 0.3 mL Hank's balanced salt solution (HBSS), and 10 – 30 μ L hybridoma cells in combined media and incubating the resulting solution for 5 minutes at room temperature. The percentage of living cells was determined by counting the ratio of unstained cells to the total cell number using a hemacytometer. When the number of living cells reached $\leq 1\%$, cells pelleted by centrifugation at 6,000 rpm for 8 minutes. The antibody containing tissue culture supernatant (TCS) was carefully removed from the cell pellet, filtered with a 0.22 micron filter, and stored at -25 °C for later purification. Freeze/thaw cycles were avoided.

At multiple points in time during cell culture, DMSO stocks of the growing hybridoma cell lines were prepared. The stocks were prepared by pelleting cells as required for media exchange and resuspending them in a 10% (v/v) sterile DMSO solution in combined growth media using a volume such that the final cell density is approximately 5×10^6 cells/mL. Immediately following preparation the DMSO stocks were transferred to cryogenic vials in 1 mL aliquots, insulated and slowly frozen at -80 °C overnight, and finally transferred to liquid N₂ for storage.

MAb Purification: DEAE Sepharose Ion-Exchange Chromatography. TCS from antibody harvest was removed from -25 °C storage and thawed at 4 °C overnight.

Following thaw completion, the TCS was concentrated from approximately 500 mL to approximately 50 mL using a 10 kDa MWCO block concentrator (Vivaflow).

Concentrated TCS was dialyzed against (3 x 3.0 L) 10 mM Tris pH 8.0 overnight in 8 kDa MWCO dialysis tubing (Pierce). Prior to loading the dialyzed TCS onto the column, the DEAE Sepharose Fast Flow resin (GE Healthcare) was washed using 150 mL buffer A (10 mM Tris pH 8.0), followed by a 50 mL linear gradient from buffer A to 100% buffer B (10 mM Tris pH 8.0, 2.0 M NaCl), 300 mL buffer B, and finally 400 mL buffer A. The dialyzed TCS was filtered through a 0.22 micron syringe filter and loaded onto the column at 3.0 mL/min. Purified MAb was eluted from the column using 200 mL buffer A, followed by a 500 mL linear gradient of buffer A to 25% buffer B, and 200 mL 25% buffer B. Note that the fraction size was 12 mL, the wash and elution flow rate was 3.0 mL/min, and the column volume was approximately 50 mL. Sample loading, buffer flow control, and elution analysis (A_{280} , conductivity, and pH) was conducted using an AKTA Purifier 10 UPC purification system (GE Healthcare).

Elution fractions suspected to contain the purified MAb were analyzed by SDS-PAGE. Pure MAb containing fractions were pooled and concentrated using a 5 kDa MWCO centrifugal concentrator (Millipore). Yields of pure MAb were determined by A_{280} using the estimate $\epsilon = 2.25 \times 10^6$. Concentrated MAb samples were drop-frozen in liquid N_2 and stored at $-80^\circ C$ or dialyzed for subsequent fragmentation with papain (vide infra).

MAb Purification: Protein-G Affinity Chromatography. TCS from antibody harvest was removed from $-25^\circ C$ storage and thawed at $4^\circ C$ overnight. Following thaw completion, the TCS was diluted from 250 mL to 2.0 L using Binding buffer (20 mM

NaPi pH 7.0), and the resulting solution was filtered with a 0.22 micron vacuum filter and subsequently degassed for approximately 30 min. The diluted TCS sample was loaded onto the HiTrap Protein-G resin (GE Healthcare) at 1.5 mL/min overnight. After sample loading, unbound material was eluted from the column using a 50 mL Binding buffer wash, and 5.0 mL fractions were collected. The pure MAb was then eluted with 50 mL of Elution buffer (100 mM Glycine-HCl pH 2.7). Fractions collected from the Elution buffer wash were 1.0 mL in volume, and contained 200 μ L of Quench buffer (1.0 M Tris pH 9.0) which was present to return the sample pH to neutral immediately following the low pH elution from the column. Purified samples were analyzed, concentrated, and stored exactly as in the case of the DEAE purification method, and the AKTA purifier was similarly employed as well to affect sample separation.

MAb Fragmentation: Soluble Papain. Note that this procedure is a modified version of one provided by Dr. Uta Maria Ohondorf in which greater enzyme to substrate ratios were employed to effect successful fragmentation. DEAE Sepharose chromatography purified MAb was dialyzed overnight against (3 x 1.8 L) PBS pH 8.0 and concentrated or diluted to $A_{280} = 1.5$ using the dialysis buffer. Digestion samples were prepared by adding 10 mM Na_2EDTA , 10 mM Cysteine HCL, and 10 mM β -mercaptoethanol to the dialyzed MAb and incubating the resulting solution at 37 °C for 45 min. A 1 mg/mL solution of soluble papain (Worthington; 80% protein lyophilized powder), 10 mM Na_2EDTA , 10 mM Cysteine HCL, and 10 mM β -mercaptoethanol was similarly prepared in PBS and incubated at 37 °C for 45 minutes. Following incubation, the papain solution was added to the antibody sample at a 1:25 enzyme to substrate ratio, and the sample was returned to 37 °C incubation for 6 hours. Every hour after the

addition of papain to the MAb sample a 100 uL aliquot of the fragmentation sample was removed from incubation and the fragmentation was ceased by the addition of 23 mM iodoacetamide. Following completion of the 6 hour digestion time 23 mM iodoacetamide was similarly added to the entire volume of MAb sample to prevent adventitious digestion of the MAb Fab and Fc fragments then present in the sample solution.

Fab Fragment Purification: MonoQ Ion-Exchange Chromatography. MAb fragmentation samples were prepared for purification immediately following digestion with papain, by dialysis into (3 x 1.8 L) 10 mM Tris pH 7.5 at 4 °C overnight. Prior to loading the dialyzed Fab sample, the MonoQ 10/100 GL column (GE Healthcare) was washed using 16 mL buffer A (10 mM Tris pH 7.5), followed by a 4 mL linear gradient from buffer A to 100% buffer B (10 mM Tris pH 7.5, 2.0 M NaCl), 40 mL buffer B, a 4 mL linear gradient from buffer B to buffer A, and finally 80 mL buffer A. The dialyzed Fab sample was filtered through a 0.22 micron syringe filter and loaded onto the column at 2.0 mL/min. Purified Fab was eluted from the column using 32 mL buffer A, followed by an 80 mL linear gradient of buffer A to 25% buffer B, and finally 32 mL 25% buffer B. Note that the fraction size was 4 mL, the elution flow rate was 3.0 mL/min, and the column volume was approximately 8 mL. Fractions from the column were analyzed by SDS-PAGE.

Results and Discussion

MAb Expression: Growth and Harvest of Antibody Cell Lines. The results of MAb expression and hybridoma cell culture are summarized in Diana Matthes' Diploma Thesis.(4)

MAb Purification: DEAE Sepharose Ion-Exchange Chromatography. MAb purification by DEAE Sepharose chromatography was reproducible and resulted in moderately pure MAb samples, but consistently failed to effect removal of a significant portion of the BSA impurity present in all MAb TCS samples. A typical purification chromatograph and associated SDS-PAGE gel are shown in Figures 3 and 4, respectively.

MAb Purification: Protein-G Affinity Chromatography. MAb 7 purification by Protein-G chromatography yielded samples of incredible purity. The purification chromatograph and associated SDS-PAGE gel are shown in Figure 6. Unfortunately, in the case of the purification trials attempted using this method, only ~1 µg of pure MAb could be obtained from from 250 mL MAb TCS. At a late stage in this project it was determined that the poor yeild a result of low expression during hybrodoma cell culture on the basis of ELISA studies of TCS samples.

MAb Fragmentation: Soluble Papain. Although the author is convinced that the described papain fragmentation procedure works, it is difficult to draw additional conclusions or optimize the method when the DEAE purification method used beforehand resulted in samples contaminated with BSA. The SDS-PAGE gels shown in Figure 7 and similar results obtained previously are the basis for the conclusion that the fragmentation procedure is successful even in the case of samples contaminated with BSA. It is also noted here that digestion times exceeding 6 hours are believed to result in adventitious MAb proteolysis (Figure 7).

Fab Fragment Purification: MonoQ Ion-Exchange Chromatography. This method is based on that established during Uta Maria Ohndorf's experience purifying MAb Fab

fragments for use in crystallization.(3) Like the MAb fragmentation procedure, this purification would most likely work if conducted on a sample not significantly contaminated with BSA.

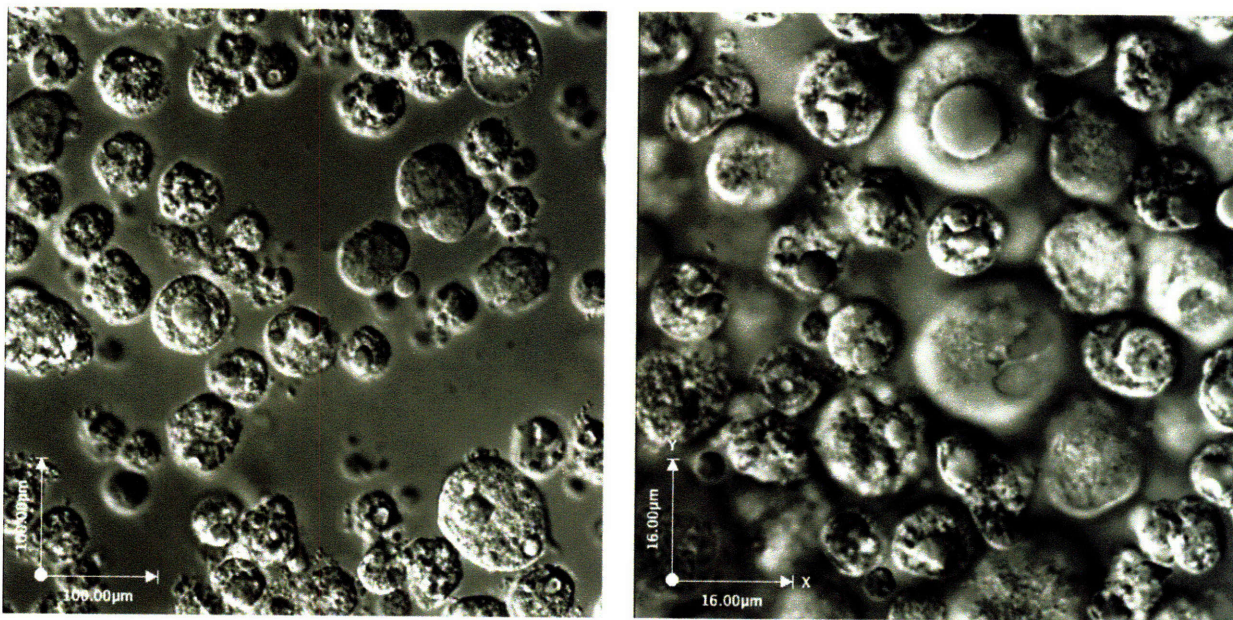


Figure 2. MMOH MAb expressing hybridoma cells at 63X (left) and 100X (right) magnification.

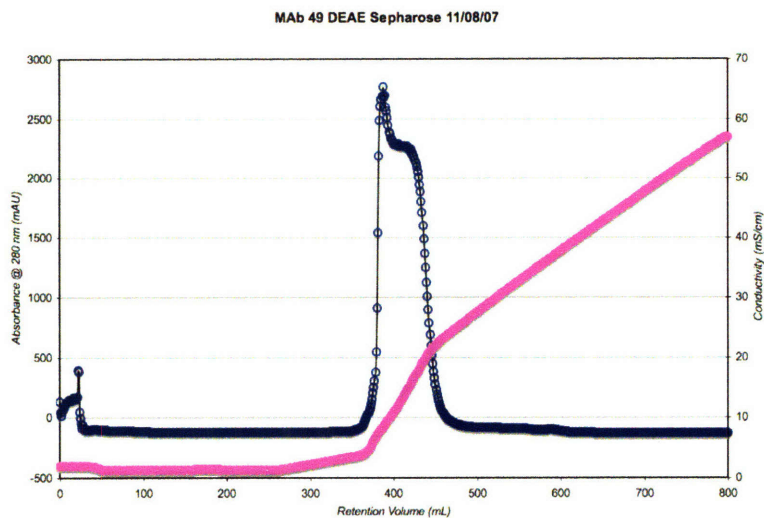


Figure 3. A₂₈₀ (blue) and conductivity (magenta) traces from the DEAE Sepharose purification of MAb 49 TCS.

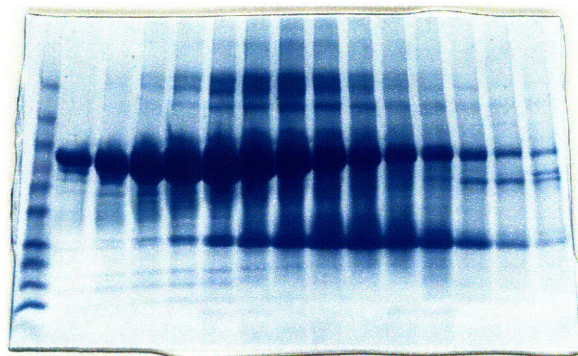


Figure 4. MAb and BSA containing fractions from DEAE purification of MAb 49 TCS.

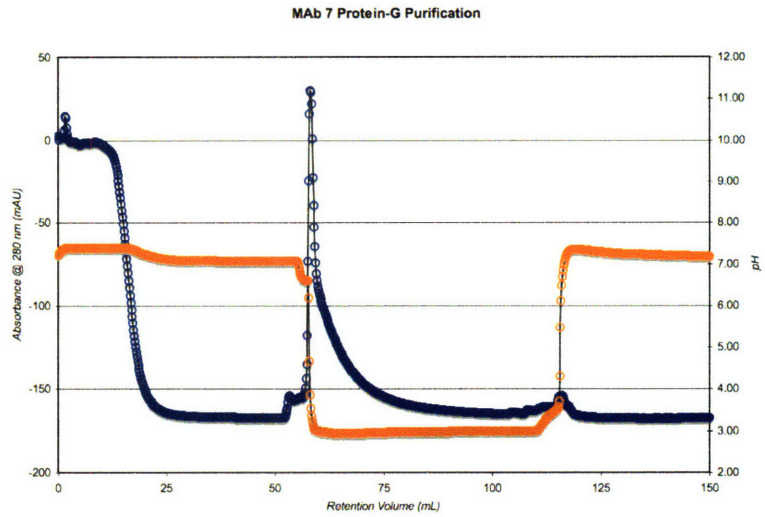


Figure 5. A₂₈₀ (blue) and pH (orange) traces from Protein-G affinity purification of MAb 7 TCS.

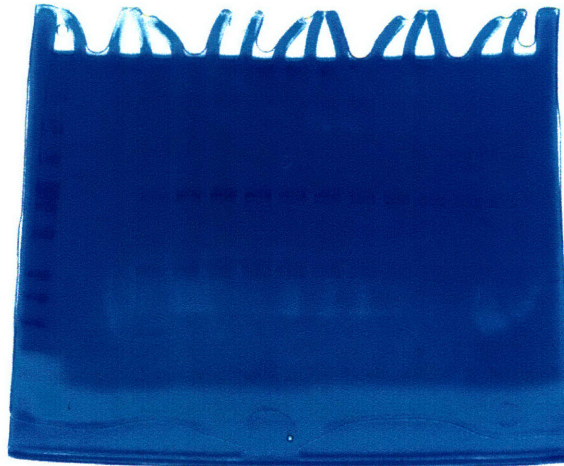


Figure 6. MAb containing fractions from Protein-G affinity purification of MAb 7 TCS.

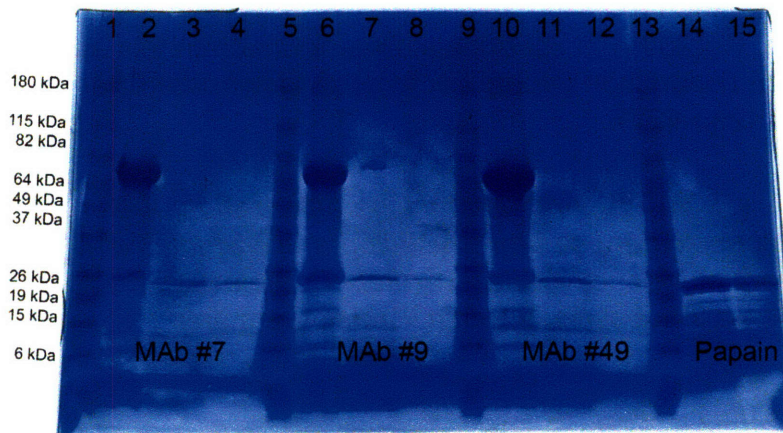


Figure 7. MAb fragmentations. Lanes 2, 6, and 10 contain MAb samples before fragmentation; Lanes 3, 4, 7, 8, 11, and 12 contain MAb samples after fragmentation, and indicate the loss of the higher molecular weight heavy chain band.

References

- (1) Harlow, E., and Lane, D. (1998) *Antibodies: A Laboratory Manual*.
- (2) Voet, D., and Voet, J. G. (1995) *Biochemistry: Second Edition*.
- (3) MacKinnon, R. (2004) Ion channels: Potassium channels and the atomic basis of selective ion conduction (Nobel Lecture). *Angewandte Chemie, International Edition* 43, 4265-4277.
- (4) Matthes, D. (2008) *Preparation and Characterization of Monoclonal Antibodies to Methane Monooxygenase and Crystallographic Studies of Bacterial Multicomponent Monooxygenase Protein Complexes.*, Doctoral thesis, Technische Fachhochschule Berlin, Berlin, Germany.

APPENDIX 3

Dioxygen Activation at Non-Heme Diiron Centers: Oxidation of a Proximal Residue in the I100W Variant of Toluene/o-Xylene Monooxygenase Hydroxylase

Author Contribution

The author was responsible for the crystallization and structure determination of the ToMOH I100W mutant..

This appendix has been reprinted with permission from *Biochemistry* **2007**, *46*, 14795-14809.

Copyright 2006 American Chemical Society.

Dioxygen Activation at Non-Heme Diiron Centers: Oxidation of a Proximal Residue in the I100W Variant of Toluene/*o*-Xylene Monooxygenase Hydroxylase[†]

Leslie J. Murray,^{||} Ricardo García-Serres,[§] Michael S. McCormick,^{||} Roman Davydov,[‡] Sunil G. Naik,[§] Sun-Hee Kim,[‡] Brian M. Hoffman,^{*‡} Boi Hanh Huynh,^{*§} and Stephen J. Lippard^{*||}

Department of Chemistry, Massachusetts Institute of Technology, Cambridge, Massachusetts 02139, Department of Physics, Emory University, Atlanta, Georgia 30322, and Department of Chemistry, Northwestern University, Evanston, Illinois 60208

Received August 22, 2007; Revised Manuscript Received September 22, 2007

ABSTRACT: At its carboxylate-bridged diiron active site, the hydroxylase component of toluene/*o*-xylene monooxygenase activates dioxygen for subsequent arene hydroxylation. In an I100W variant of this enzyme, we characterized the formation and decay of two species formed by addition of dioxygen to the reduced, diiron(II) state by rapid-freeze quench (RFQ) EPR, Mössbauer, and ENDOR spectroscopy. The dependence of the formation and decay rates of this mixed-valent transient on pH and the presence of phenol, propylene, or acetylene was investigated by double-mixing stopped-flow optical spectroscopy. Modification of the α -subunit of the hydroxylase after reaction of the reduced protein with dioxygen-saturated buffer was investigated by tryptic digestion coupled mass spectrometry. From these investigations, we conclude that (i) a diiron(III,IV)–W^{*} transient, kinetically linked to a preceding diiron(III) intermediate, arises from the one-electron oxidation of W100, (ii) the tryptophan radical is deprotonated, (iii) rapid exchange of either a terminal water or hydroxide ion with water occurs at the ferric ion in the diiron(III,IV) cluster, and (iv) the diiron(III,IV) core and W^{*} decay to the diiron(III) product by a common mechanism. No transient radical was observed by stopped-flow optical spectroscopy for reactions of the reduced hydroxylase variants I100Y, L208F, and F205W with dioxygen. The absence of such species, and the deprotonated state of the tryptophanyl radical in the diiron(III,IV)–W^{*} transient, allow for a conservative estimate of the reduction potential of the diiron(III) intermediate as lying between 1.1 and 1.3 V. We also describe the X-ray crystal structure of the I100W variant of ToMOH.

Metal-activated dioxygen species are capable of oxidizing a broad range of substrates (1–4). In synthetic systems, these units are generated in a solvent that is inert to oxidation. The peptide matrix surrounding the active site protects reactive intermediates in protein systems. Enzymes are able to coordinate reduction of an active metal center and dioxygen activation with substrate binding, thereby assuring that reactive metal–oxygen units are generated only when the substrate is available (5, 6). The active sites in carboxylate-bridged diiron (CBDI¹) proteins are housed within a four-helix bundle and shielded by the protein framework (7–9). As a consequence, reactive intermediates such as Q, an oxo-bridged diiron(IV) center, in MMOH and X, a mixed-valent diiron(III,IV) cluster, in RNR-R2 can accumulate and be characterized by a number of spectroscopic methods (10, 11).

The primary coordination spheres of the diiron centers in the CBDI enzyme superfamily are remarkably similar, yet the high-valent intermediates Q and X are observed only in MMOH and RNR-R2, respectively (12). Although the capacity to form these iron(IV)-containing units is reserved for these two enzymes, proteins in the superfamily activate dioxygen by analogous mechanisms. The reduced diiron(II) core reacts rapidly with O₂ to generate a peroxo-bridged diiron(III) species as the first observable intermediate. No other oxygenated intermediates are observed in Ft and Δ^9 D, and the peroxodiiron(III) unit is detectable in Δ^9 D only when the substrate–carrier protein conjugate is bound to the desaturase. This behavior has been ascribed to stearyl-ACP blocking access to the active site via a large substrate channel (13). To date, no oxygenated intermediates have been reported for reactions of diiron(II) or diiron(III) forms of rubrerythrin with either dioxygen or hydrogen peroxide,

[†] This study was supported by NIH Grants GM32134 (to S.J.L.), GM47295 (to B.H.H.), and HL13531 (to B.M.H.). L.J.M. was supported in part by a fellowship from the Martin Society (M.I.T.).

[‡] Crystallographic coordinates for ToMOH I100W have been deposited into the RCSB Protein Databank with accession code 2RDB.

* Authors to whom correspondence should be addressed: E-mail: lippard@mit.edu. Phone: 617-253-1892. Fax: 617-258-8150. E-mail: vhuynh@physics.emory.edu. Phone: 404-727-4295. Fax: 404-727-0873. E-mail: bmh@northwestern.edu. Phone: 847-491-3104. Fax: 847-491-7713.

^{||} Massachusetts Institute of Technology.

[§] Emory University.

[‡] Northwestern University.

¹ Abbreviations: CBDI, carboxylate-bridged diiron; Δ^9 D, stearyl-ACP Δ^9 desaturase; Ft, ferritin; MMOH, hydroxylase component of methane monooxygenase; ToMO, toluene/*o*-xylene monooxygenase; ToMOC, Rieske component of ToMO; ToMOD, regulatory component of ToMO; ToMOF, NADH oxidoreductase component of ToMO; ToMOH, hydroxylase component of ToMO; H_{mv}, diiron(II,III) form of the hydroxylase; H_{peroxo}, peroxodiiron(III) intermediate of the hydroxylase; H_{red}, diiron(II) form of the hydroxylase; Q, di(μ -oxo)-diiron(IV) transient of MMOH; RNR-R2, ribonucleotide reductase R2 subunit (Class I); SSRL, Stanford Synchrotron Radiation Laboratories; X, mixed-valent diiron(III,IV) intermediate formed in RNR-R2.

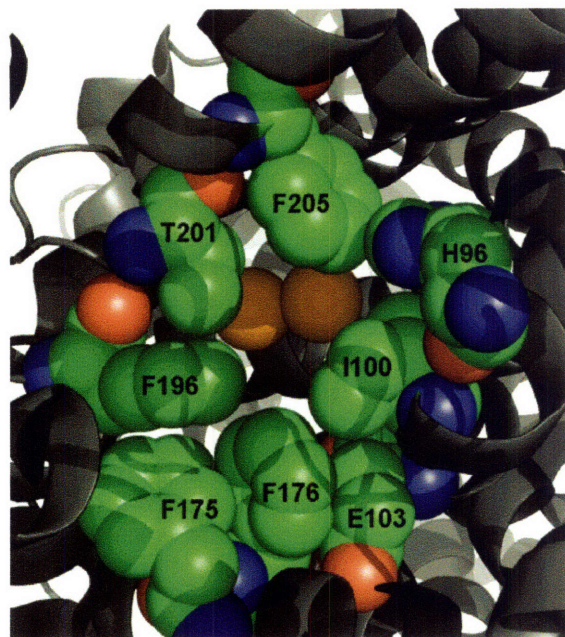


FIGURE 1: View of the active site pocket of ToMOH from the substrate access channel. The diiron atoms and the hydroxylase polypeptide backbone are depicted as orange spheres and as a gray ribbon diagram, respectively. The opening to the pocket is bordered by residues I100, T201, F205, and F196. I100 is analogous to the proposed leucine gate, L110, in MMOH.

respectively. From its crystal structure, the active site of rubrerythrin appears to be more accessible to solvent and buffer components than those of other enzymes in the family (14). The accumulation of reactive oxygenated iron(III) and iron(IV) intermediates would therefore appear to be correlated with accessibility of the diiron center to potential quenching moieties in the medium.

At the beginning of the present study, no transient species with UV-visible absorption bands had been detected kinetically for the reaction of reduced ToMOH with dioxygen. In the crystal structure of the native enzyme, a large channel for substrate access and/or product egress, extending from the protein surface to the active site pocket, was identified (15). Site-directed mutagenesis studies of residues within the channel of ToMOH were therefore undertaken to evaluate the possibility that reactive intermediates might accumulate if solvent or buffer components were occluded from the active site in this system. Residues I100, F196, F205, and H96 form a hydrophobic portal to the active site at the end of the solvent-accessible channel in ToMOH (Figure 1). Of these residues, I100 is especially noteworthy. The analogous residue in MMOH, L110, has been proposed to function as a gate for substrate entry to, and/or product egress from, the active site during catalysis (7). Residue L98 in hemerythrin might perform a similar function, controlling solvent access to the diiron core (16). We therefore wondered whether mutation of I100 would sufficiently isolate the active site pocket from the channel to shield the dimetallic center from buffer components or solvent, allowing accumulation of reactive intermediates to observable levels. Residue F205, which is on the opposite side of the channel from I100, and L208, which is farther from the active site pocket, were also selected as targets for mutagenesis (Figure 2). We substituted I100 with tyrosine and tryptophan, L208 with phenylalanine, and F205 with tryptophan. Modeling structures of these

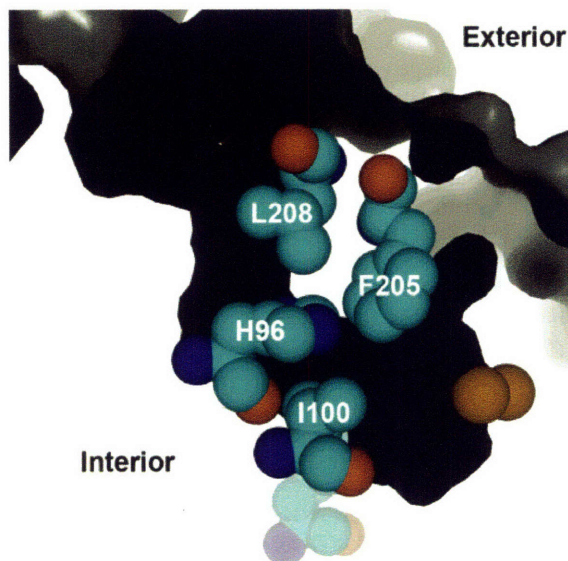


FIGURE 2: A substrate access channel (black) in ToMOH extends from the protein surface to the diiron active site. Residues H96, I100, and F205 form a hydrophobic region that joins the active site pocket to the channel. Residue L208 resides farther from the diiron active site, forming part of the channel wall. The iron atoms are depicted as orange spheres in the lower right portion of the figure.

variant hydroxylases using the native crystal structure suggested that they would afford maximal closure of the channel without disrupting the protein fold of the surrounding matrix.

Preliminary investigations of reaction of ToMOH I100W with dioxygen were reported previously (17). From this initial study, dioxygen activation at the diiron(II) core was discovered to produce an optically transparent diiron(III) intermediate that could be identified by Mössbauer spectroscopy. This intermediate oxidizes the nearby W100 to form a mixed-valent diiron(III,IV) unit coupled to a protein-based tryptophanyl radical. This species subsequently decays to the resting, oxidized diiron(III) state. The process by which the diiron(III) intermediate oxidizes the nearby W residue and the subsequent decay of the mixed-valent center and the protein-based radical have been investigated in considerable detail and form the basis for this report. The reactivity of other channel-blocking mutations, I100Y, L208F, and F205W, was also investigated under pre-steady-state and steady-state conditions. We include these results because they provide additional insight into the nature of the important diiron(III) transient.

EXPERIMENTAL METHODS

General Considerations. Plasmids containing the genes for the ToMO components were supplied by the laboratory of Professor Alberto Di Donato, Naples, Italy. Recombinant expression and preparation of the ToMO component proteins were carried out as described elsewhere (15). ToMOH variant proteins were prepared by the same protocol as used for the native enzyme. The iron content, measured by the ferrozine assay, ranged from 4.2 to 4.6 iron atoms per ToMOH dimer for all samples. Isotopically enriched ToMOH I100W protein for Mössbauer and ENDOR spectroscopy was obtained by expression in LeMaster's media containing $^{57}\text{FeCl}_3$ or

tryptophan-*d*₅, selectively labeled on the indole ring (Cambridge Isotope Labs, Andover, MA) (18). The solution of ⁵⁷FeCl₃ was prepared by dissolving ⁵⁷Fe powder (96.7% isotopic purity, Advanced Materials Technologies Ltd., Nes-Ziona, Israel) in concentrated hydrochloric acid. Deuterium oxide was purchased from Cambridge Isotope Labs, and all other reagents were acquired from Aldrich Chemical Co. HPLC experiments were carried out with a Vydac protein & peptide C18 column connected to a Waters 600S controller and a Waters 2487 dual wavelength absorbance detector. Optical absorption spectra were recorded with an HP8452 diode-array spectrophotometer.

Crystallization and Data Collection. Crystallization conditions for ToMOH I100W were as published (19). Purified ToMOH I100W protein was exchanged into buffer containing 10 mM MES, pH 7.5, and 10% (v/v) glycerol to a final concentration of 50 μM. A 2 μL aliquot of this solution was mixed with 1 μL of a native ToMOH micro seed stock solution containing 2.3 M (NH₄)₂SO₄, 100 mM HEPES, pH 7.5, and 2% (v/v) PEG 400, as well as 1 μL of precipitant solution. The precipitant solution contained 2.0–3.0 M (NH₄)₂SO₄, 100 mM HEPES, pH 7.5, and 2% (v/v) PEG 400. Cryogenic solutions for data collection contained the precipitant solution with added 20% (v/v) glycerol. X-ray diffraction data were collected at the SSRL on beam line 9-2 using the BLU-ICE data collection suite (20). Crystal annealing was conducted as described for 1.85 Å native ToMOH, using a 5.0-s pause in the cryostream flow (19). Diffraction data were integrated and scaled in HKL 2000 (21).

Structure Determination and Refinement. Phasing of the ToMOH I100W data was accomplished by using EPMR and 1.85 Å native ToMOH coordinates (PDB code 2INC) in which all non-protein atoms and the side chains of the iron coordinating ligands and residues I100, T201, N202, Q228, S232, and R233 were removed as a starting model (15, 22). Subsequent models were built in Coot and refined using REFMAC5 in CCP4 (23–25). Simulated annealing composite omit maps were generated in CNS (26). MSDchem ideal coordinates as well as CNS topology and parameter files for glycerol, PEG 400, and MOPS heterocompounds were obtained from the HIC-UP database (residue codes GOL, P6G, and MPO, respectively) (27).

Site-Directed Mutagenesis of the ToMOH α-Subunit. The mutations were introduced by site directed mutagenesis on the parent pET-22b(+)/touBEA plasmid with an MJ Research MiniCycler using DNA polymerase pfU Turbo, dNTPs, and reaction buffer (Stratagene, La Jolla, CA) according to the manufacturer's protocol. The sequences for oligonucleotides (Invitrogen, Carlsbad, CA) used as primers are given in Table S1 (Supporting Information). Primers for the mutation I100W were as reported previously (17). PCR products were transformed into *E. coli* XL-1 Blue super-competent cells (Stratagene, La Jolla, CA) by heat-shock as described by the manufacturer and grown overnight on LB-Agar plates containing ampicillin (300 μg/mL). Five colonies from each plate were picked and grown in 5 mL cultures (LB media, 300 μg ampicillin /mL) for 20 h. Cells were pelleted at 3500 rpm for 15 min and the plasmids were isolated with a Qiagen Mini-Prep kit. Isolated plasmids were submitted for sequencing in the forward and reverse directions to the Biopolymers core facility in the Center for Cancer Research (M.I.T.).

Steady-State Activity Assays and Product Determinations for ToMOH Variants. A colorimetric assay was used to detect catechol that formed during steady-state hydroxylation of phenol by these variant hydroxylases (28). Catechol-2,3-dioxygenase cleaves catechol to form 2-hydroxyruconic semialdehyde, which can be monitored by measuring the absorption at 410 nm ($\epsilon = 1260 \text{ M}^{-1}\text{cm}^{-1}$). Assays were conducted at 25 °C in 0.1 M Tris/HCl pH 7.5 in a final volume of 1 mL. Reaction mixtures contained 0.15 μM ToMOH, 10 μM ToMOD, 4 μM ToMOC, 30 nM ToMOF, and saturating amounts of catechol-2,3-dioxygenase. Steady-state hydroxylation of phenol (1 mM) was initiated with NADH to a final concentration of 1 mM.

To determine if the regiospecificity of hydroxylation was altered by these mutations, products of steady-state turnover for phenol were identified by HPLC. The ToMO protein component concentrations were 0.3 μM ToMOH, 2 μM ToMOD, 4 μM ToMOC, and 30 nM ToMOF in 0.1 M Tris/HCl pH 7.5 (150 μL). Assay solutions contained 1 mM phenol, and were initiated with NADH to a final concentration of 2 mM. Reaction mixtures were incubated at 25 °C for 15 min, quenched with 50 μL TFA, centrifuged for 10 min at 14000 × *g*, frozen in liquid nitrogen, and stored at –20 °C. Samples were thawed and 100 μL of the supernatant was injected on to the Vydac column. HPLC conditions for separation of hydroxylated products from phenol were 0% buffer B for 7 min, 0% to 40% B for 1 min (linear gradient), 40% to 100% for 7 min (linear gradient), and 100% B for 3 min (A: 1% acetonitrile, 98.8% ddH₂O, 0.2% TFA; B: 49.9% acetonitrile, 49.9% ddH₂O, 0.2% TFA). Absorption at 280 nm was monitored with time for all samples. Retention times for catechol, resorcinol, and hydroquinone were determined under these conditions.

Stopped-Flow Optical Spectroscopy. A HiTech DX2 stopped flow instrument was made anaerobic by treatment with an anaerobic solution of sodium dithionite (> 4 mM). This solution was allowed to stand in the drive syringes and flow lines for at least 15 min to ensure complete scavenging of dioxygen. The instrument was then flushed with anaerobic 25 mM MOPS buffer at the appropriate pH immediately prior to use. Solutions containing the hydroxylase and regulatory protein were made anaerobic by cycles of vacuum gas exchange with nitrogen and transferred to a Vacuum Atmospheres MO-20 anaerobic chamber, where they were reduced with excess sodium dithionite in the presence of methyl viologen. The reduced protein was dialyzed (8000 MWCO) twice against 25 mM MOPS at specific pH values. Samples were then transferred either into tonometers or Hamilton gastight sample-lock syringes and loaded into the anaerobic stopped-flow instrument and mixed against O₂-saturated 25 mM MOPS buffer at a specific pH. The software packages KinetAsyst 3.14 (HiTech Scientific, UK) and Kaleidagraph 3.5 (Synergy Software, Reading, PA) were used to fit the time dependence of the optical data.

Reaction of ToMOH_{red} I100Y, F205W, and L208F with O₂. Concentrations of the variant hydroxylases after mixing varied from 25 μM to 150 μM. Reaction mixtures contained three equivalents of ToMOD to one equivalent of ToMOH. The reduced hydroxylase pre-complexed with the regulatory protein was dialyzed against buffer, pH 7.0, and allowed to react with dioxygen-saturated buffer of the same pH. The temperature of the stopped-flow instrument was maintained

at 4.0 ± 0.1 °C. Multiwavelength data were collected between 350 and 750 nm with a xenon arc lamp and a diode array detector.

Solvent Kinetic Isotope Effect (SKIE) for Formation and Decay of the ToMOH I100W Transient. After reduction, protein mixtures were dialyzed anaerobically against either 25 mM MOPS buffer pD 6.61 in D₂O or pH 7.0 in H₂O and allowed to react with dioxygen. The reaction was carried out over the temperature range 4.0 and 36.0 °C. The concentration of ToMOH I100W:3ToMOD varied from 25 to 60 μM in the optical cell. The optical traces collected in single-wavelength mode at 500 nm were fit to an A→B→C model to determine the formation and decay rate constants.

Effect of pH on the Reaction of ToMOH_{red} I100W with O₂. In these experiments, the pH of the reaction mixture was adjusted either by using double-mixing mode to set the pH after dialysis and prior to oxygenation in the second push, or in single-mixing mode with dialysis carried out using buffers at specific pH values. For double-mixing experiments, the concentrations of the hydroxylase and regulatory protein after mixing were 94 μM and 282 μM, respectively. The reduced protein was dialyzed against buffer with a pH value of 6.6. In the first push, the solution of the hydroxylase and regulatory protein was mixed with anaerobic buffer, pH 6.6 or 8.0, and allowed to age for 1 min. In the second push, the aged protein solution was allowed to react with oxygenated buffer, pH 6.6 or 7.2, and data were collected in multi- and single-wavelength modes. The instrument temperature was maintained at 4.0 °C. For single-mixing experiments, the concentrations of the hydroxylase and regulatory protein in the optical cell were 18 μM and 45 μM, respectively. After reduction, the first dialysis was carried out against 25 mM MOPS pH 7.0. The pH of the buffer was 6.5, 7.0, or 7.5 for the second dialysis. The reduced anaerobic samples were mixed at 4.0 °C with oxygenated 25 mM MOPS buffer at the appropriate pH values. Data were collected at 500 nm for 100 to 200 s.

Effect of Substrates on the Decay Rate of the ToMOH I100W Transient. This double-mixing experiment was carried out at 4.0 °C monitoring the absorption 500 nm. The concentration of ToMOH I100W:3ToMOD after mixing was 25 μM. Reduced ToMOH I100W:3ToMOD was dialyzed against buffer at pH 7.0, and loaded into the anaerobic stopped-flow instrument. In the first push, the reduced hydroxylase was reacted with dioxygen-saturated buffer (pH 7.0) for 3.9 s. The aged solution was subsequently mixed with 25 mM MOPS pH 7.0 containing phenol, acetylene, or propylene. The concentration of phenol after mixing ranged from 25 μM to 5.2 mM. For acetylene and propylene, an aliquot (10 mL) of buffer was sparged with the gas for 1.5 h to obtain saturated solutions of the substrate (7.7 mM or 42.4 mM, respectively) (29). Optical data were collected for 10 to 200 s and fit to either one or two exponential functions.

Rapid-Freeze Quench Sample Preparation. Protein solutions of ToMOH I100W:3ToMOD were reduced and dialyzed against 25 mM MOPS buffer pH 7.0 as described for stopped-flow experiments. Reduced mixtures were loaded into gastight syringes for an Update Instruments 1000 ram drive system connected to a model 705A computer controller. The RFQ instrumentation has been described in detail elsewhere (30). Reduced protein was mixed with dioxygen-saturated buffer and allowed to age for reaction times

between 0.03 and 900 s, after which the protein solution was quenched in isopentane at -140 °C. The frozen protein solutions were packed into X-band EPR tubes and Mössbauer sample cups. Samples for ENDOR spectroscopy were quenched 4 s after mixing with dioxygen-saturated buffer, and packed into Q-band EPR tubes. All RFQ samples were stored in liquid nitrogen until spectra were acquired.

Mössbauer Spectroscopy. ToMOH I100W isotopically enriched with ⁵⁷Fe was used to generate RFQ samples for Mössbauer spectroscopy. The concentration of ToMOH I100W:3ToMOD after mixing was 290 μM. Mössbauer spectra were recorded at 4.2 K in a magnetic field of either 50 mT or between 1 and 8 T applied parallel to the γ -beam on instrumentation described elsewhere (30). The zero velocity refers to the centroid of a room-temperature spectrum of an Fe foil.

X-Band EPR Spectroscopy. Samples were generated with ToMOH I100W that contained either ⁵⁶Fe or ⁵⁷Fe. The concentration of ToMOH I100W:3ToMOD in the quenched reaction mixtures was 198 μM. EPR spectra at $g = 2.00$ were recorded at 30 K with the following parameters: power = 0.02 mW; frequency = 9.65 GHz; modulation frequency = 100 kHz; modulation amplitude = 5 G; gain = 6.3×10^4 . EPR spectra at $g = 16$ were recorded at 8 K with the following parameters in parallel mode: power = 20 mW; frequency = 9.39 GHz; modulation frequency = 100 kHz; modulation amplitude = 10 G; gain = 6.3×10^4 .

ENDOR Spectroscopy. Samples were prepared either with 25 mM MOPS in D₂O (pD 6.6) or H₂O (pH 7.0), and the hydroxylase contained either natural abundance ⁵⁶Fe or was isotopically enriched with ⁵⁷Fe. For samples prepared with D₂O-containing buffers, the reduced protein was dialyzed against deuterated buffers. The concentration of ToMOH I100W:3ToMOD in ENDOR samples ranged from 250 μM to 350 μM. ¹H- and ²H-Mims ENDOR spectra were recorded on instrumentation described elsewhere (31).

Enzymatic Digestion and Mass Spectrometry of ToMOH I100W. Reduced ToMOH I100W was prepared as described above for the stopped-flow experiments. A 10-μL control aliquot of the ToMOH I100W:3ToMOD mixture was removed prior to making the protein anaerobic. The remainder of the protein was reduced with excess sodium dithionite and dialyzed under anaerobic conditions against 25 mM MOPS pH 7.0. The reduced protein was mixed with buffer oxygenated with either natural abundance ¹⁶O₂ or enriched ¹⁸O₂ (95%, Cambridge Isotope Labs, Andover, MA) in the stopped-flow instrument. The polypeptide chains of reacted and unreacted oxidized protein solutions were separated on a 4–20% Tris/HCl SDS-PAGE gel run at 200 V for 45 min. The band corresponding to the α -subunit was excised and digested with trypsin according to the manufacturer's protocol (New England Biolabs, Ipswich, MA). Positive ion MALDI-TOF mass spectrometry of digests was carried out with a Voyager DE-STR MALDI-TOF mass spectrometer (Applied Biosystems, Foster City, CA), installed in the Biopolymers Core Facility of the M.I.T. Center for Cancer Research. The instrument was operated in reflector mode with an accelerating potential of 20 kV and mass resolution of at least 1:10000. The MALDI matrix was α -cyano-4-hydroxybenzoic acid. Protein digest samples were mixed with a 10 mg/mL matrix solution in a 1:1 ratio and were deposited on the MALDI plate. Mass spectra were obtained using a

nitrogen UV laser (337 nm). Each mass spectrum is the average of 50 laser shots. The mass spectrometer was calibrated as per the manufacturer's standard operating protocols, with a mixture of peptides of known mass that were spotted on the MALDI plate adjacent to the sample. Mass spectra were processed using the Applied Biosystems Data Explorer software.

LC-MS analyses of the protein digests were carried out using a Tempo nano HPLC system (Applied Biosystems, Foster City, CA) coupled on-line to a QSTAR Elite quadrupole-time-of-flight tandem mass spectrometer (MDS Sciex/Applied Biosystems, Foster City, CA), installed in the Proteomics Core Facility of the M.I.T. Center for Cancer Research. The mass spectrometer was calibrated as per the manufacturer's standard operating protocols, with the fragment ions from a peptide of known sequence. Separation of proteolytic peptides was carried out on a C18 capillary HPLC column (Michrom Bioresources, Auburn, CA) and a water-acetonitrile (with 0.1% formic acid) solvent gradient at a flow rate of 300 nL/min. Mass spectral data were acquired and processed with the Applied Biosystems Analyst QS software. Data acquisition was performed using the software "Information Dependent Acquisition" mode with each MS scan, where peptide ion m/z values were measured, followed by four MS/MS scans, where fragment ion spectra of the four most abundant precursor ions were acquired. A temporary exclusion list was generated by the software after each MS/MS data acquisition to minimize the generation of duplicate MS/MS spectra from the same precursor ion.

RESULTS

X-ray Crystal Structure of ToMOH I100W. ToMOH I100W crystallization conditions and morphology matched that published for the native and Mn(II)-substituted protein (19). The best-diffracting I100W crystal yielded a 2.1-Å resolution data set, which was used for the structure determination. Successful phasing followed by multiple rounds of model fitting and refinements afforded the current structure with statistics shown in Table S2. The diffraction data exhibit a moderately low overall completeness of 84.7%, but there are high I/σ ratios and redundancy counts in all resolution shells. The global folds of the α -, β -, and γ -subunits of ToMOH I100W are the same as those for the native protein, except for predicted differences in the channel interior, with a C_α -to- C_α rmsd of 0.173 Å. The indole ring of the W100 side chain was modeled in two different rotameric forms, as required by the observed electron density. One position orients the plane of the indole ring almost parallel to the Fe-Fe vector (Figure 3, Position A), whereas the second position directs $C_{\zeta 3}$ and $C_{\epsilon 3}$ of the indole side chain toward the diiron active site (Figure 3, Position B). The two rotamers were assigned equal occupancies of 50%, which led to average refined Debye-Waller factors for the two W100 side chains of 44.7 Å² for Position A and 40.1 Å² for Position B; the average B-value for all atoms in the α -subunit is 50.8 Å². Both positions of the W100 side chain block direct access to the active site, as can be seen from van der Waals surface renderings of the channel interior (Figure 4). Distances between the indole ring and the active site iron atoms range from 6.0 to 11.9 Å, with average values of 10.6 and 8.0 Å for W100 positions A and B, respectively (Table S3). The shortest distance is that between $C_{\zeta 3}$ (Position

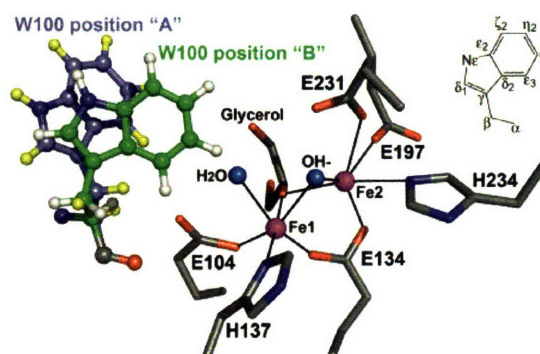


FIGURE 3: Conformations adopted by W100 in the crystal structure. The aromatic side-chain occupies two positions with populations of 50% for positions A and B. The indole ring in A is oriented parallel to the diiron center whereas $C_{\zeta 3}$ and $C_{\epsilon 3}$ are pointed toward the diiron center in second conformation. The inset shows the labeling scheme referred to for the atoms in the indole ring.

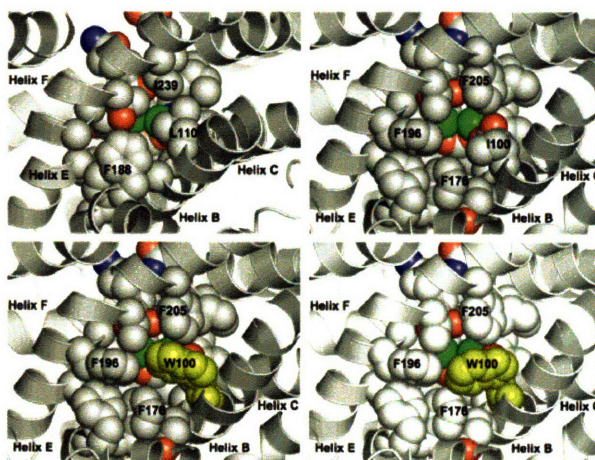


FIGURE 4: Diiron center blocking effect of W100 in ToMOH I100W (bottom) in comparison to MMOH (top, left) and native ToMOH (top, right). Amino acids in the region of the active site pocket and iron atoms are shown as spheres (carbon) in gray, red (oxygen), blue (nitrogen), and green (iron). The two partially occupied positions of the W100 side chain in the variant ToMOH structure are highlighted in yellow.

B) and Fe1 at 6.0 Å, and the longest is that between $C_{\zeta 2}$ (Position A) and Fe2 at 11.9 Å.

Flanking the W100 side chain are two molecules of glycerol, presumably derived from the purification or cryo buffers used in sample preparation. These glycerol molecules, together with the W100 indole ring, occupy the space containing hexaethylene glycol encountered in the recent crystal structures of ToMOH (19). One of these two glycerol molecules resides in the active site cavity and, in a manner similar to that observed for ethanol in MMOH, asymmetrically bridges the active site iron atoms, replacing the hydroxide ion typically found syn to the ligating histidine residues (Figure 3) (32). With exception of this $\{\mu^- \text{OCH}(\text{CH}_2\text{OH})_2\}$ bridging glycerol anion, the diiron center in ToMOH I100W is otherwise identical to that in native ToMOH_{ox} (15, 19). The B-factors for atoms in the coordinated and fully occupied glycerol molecule average 56.9 Å².

Steady-State Product Distribution and Activity of ToMOH Variants with Phenol as Substrate. The steady-state specific activities of the ToMOH variants for phenol were lower than that observed for wild-type hydroxylase as determined by

the coupled assay with catechol-2,3-dioxygenase. The I100W variant had a specific activity of 80 mU/mg compared to 1250 mU/mg for the wild-type protein. ToMOH I100Y, L208F, and F205W showed no activity under the conditions of this assay. Catechol, resorcinol, hydroquinone, and phenol are well separated by the method described in the Experimental Section, with retention times of 13, 11, 6.5, and 15 min, respectively. The peak corresponding to the enzymatic product had a retention time co-incident with that of catechol (Figure S1). No peaks corresponding to resorcinol or hydroquinone were observed. Product analyses for the variant hydroxylases revealed catechol to be the only product formed. A trace amount of catechol was observed in assay mixtures for ToMOH I100Y, F205W, and L208F.

Stopped-Flow Optical Study of the Reaction of ToMOH Variants with O₂-Saturated Buffer. No transient absorption bands between 350 and 750 nm were observed after mixing solutions of chemically reduced hydroxylase variants I100Y, F205W, or L208F in complex with ToMOD against dioxygen-saturated buffer.

Reaction of Reduced ToMOH I100W with O₂ Monitored by Mössbauer Spectroscopy. An initial spectroscopic characterization of the dioxygen activation reaction by the reduced I100W ToMOH variant revealed two transient species, an EPR-silent, optically transparent diiron(III) intermediate that exhibits Mössbauer spectra characteristic of ferric iron ($\delta = 0.54$ mm/s and $\Delta E_Q = 0.67$ mm/s) and a spin-coupled diiron(III,IV)-W^{*} chromophore that displays an absorption band at 500 nm, an EPR signal in the $g = 2.0$ region, and Mössbauer spectral characters indicative of a mixed-valent diiron(III,IV) cluster (17). The magnetic field dependence of the Mössbauer spectrum of the diiron(III,IV)-W^{*} intermediate confirmed a dipolar spin-spin interaction between the diiron(III,IV) cluster and W^{*}. To gain further insight into dioxygen activation by reduced ToMOH I100W variant and to obtain time evolution profiles of Fe species generated in the reaction, Mössbauer and EPR spectra of samples freeze-quenched during the reaction were collected and analyzed.

Figure 5 shows Mössbauer spectra of reduced protein before (A) and after (B–F) mixing with O₂. Because the parameters of these iron intermediates had been determined previously (17), decomposition of the spectra into components corresponding to different Fe species was possible (Figure 5, colored lines). Percentages of Fe-absorption corresponding to species generated at different time points, including others not depicted here, were thereby obtained. On the basis of the Fe/protein ratio determined for the freeze-quenched samples, 3.88 Fe atoms/ToMOH dimer, these relative percentages were converted to accumulation amounts of diiron cluster/protomer for the diiron species at various time points. The results (diamonds) are presented in Figure 6, which shows clearly the formation and decay of the various diiron species. Before mixing with O₂, the reduced protein sample contains mainly diiron(II) clusters, 0.96 diiron clusters/ToMOH protomer, the spectrum of which can be modeled as two unresolved quadrupole doublets (Figure 5A, green lines) with parameters given in the figure caption. After mixing with O₂-saturated buffer, approximately 40% of the diiron(II) sites react rapidly to form the diiron(III) intermediate (Figure 5, red lines) with a rate constant of ~ 18 s⁻¹. Accumulation of the diiron(III) intermediate reaches a

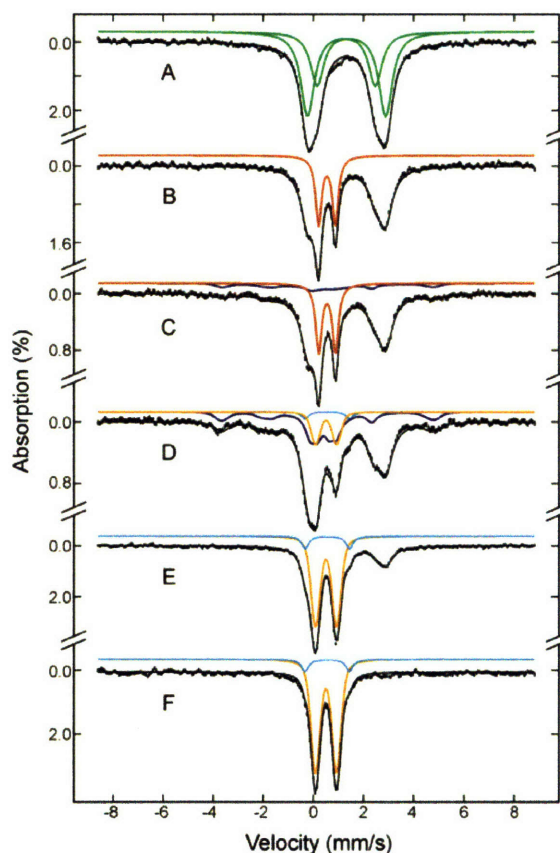


FIGURE 5: Mössbauer spectra of freeze-quenched samples from the reaction of ToMOH_{red} I100W:3ToMOD with O₂. The samples were frozen before mixing (A) and after (B–F) mixing with O₂. The samples were frozen before mixing (A) and 0.07 s (B), 0.44 s (C), 3.5 s (D), 37 s (E), and 900 s (F) after mixing. The spectra (vertical bars) are collected at 4.2 K in a 50 mT field applied parallel to the γ -beam. The diiron(II) spectrum (A) was simulated as a superposition of two unresolved quadrupole doublets (green lines in A) with an intensity ratio of 1.6:1 for doublet 1:doublet 2. The parameters are $\delta = 1.32$ mm/s, $\Delta E_Q = 3.11$ mm/s, and line width = 0.65 mm/s for doublet 1, and $\delta = 1.31$ mm/s, $\Delta E_Q = 2.32$ mm/s, and line width = 0.65 mm/s for doublet 2. In B–F, the red, blue, orange, and cyan lines are simulated spectra of the diiron(III) transient, diiron(III,IV)-W^{*} intermediate, major diiron(III) and minor diiron(III) products, respectively. The spectra of the diiron(III) transient and diiron(III,IV)-W^{*} intermediate are simulated with parameters reported previously (17). The spectrum of the major diiron(III) product is modeled with a single quadrupole doublet with $\delta = 0.51$ mm/s, $\Delta E_Q = 0.84$ mm/s, and line width = 0.35 mm/s. The spectrum of the minor diiron(III) product is simulated with $\delta = 0.56$ mm/s, $\Delta E_Q = 1.77$ mm/s, and line width = 0.33 mm/s. For clarity, the diiron(II) spectral component is not shown specifically in B–F. The simulated spectra are plotted at the following absorption intensity: red, 29% and 27% in B and C, respectively; blue, 16% and 34% in C and D, respectively; orange, 14%, 60%, and 65% in D, E, and F, respectively; cyan, 3%, 8%, and 8% in D, E, and F, respectively. The black lines overlaid with the experimental spectra are composite spectra including the diiron(II) and all other species mentioned above. Approximately 25% of the total Fe in F appears in the form of broad, featureless absorptions, indicative of ill-defined paramagnetic ferric species. We therefore did not include this iron in the composite spectra.

maximum of 0.32 clusters/protomer at 0.14 s and then decays at a rate of ~ 1.1 s⁻¹ (Figure 6, red line and diamonds). The decay of the diiron(III) intermediate parallels the formation of the diiron(III,IV)-W^{*} species (Figure 6, blue line and diamonds), while the unreacted diiron(II) sites stay relatively

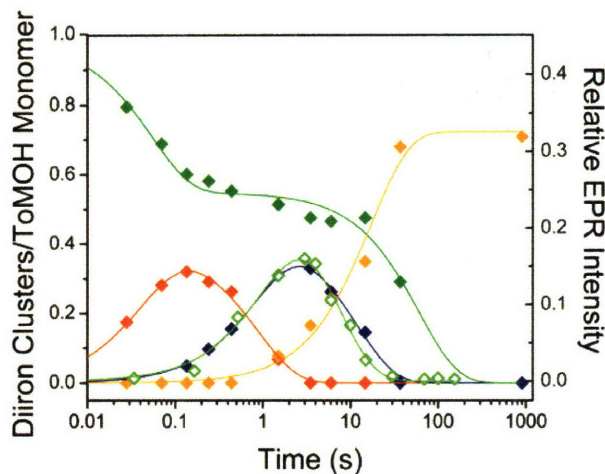


FIGURE 6: Speciation plot for the reaction of ToMOH_{red} I100W:3ToMOD with dioxygen. The diiron(II) starting material (green diamonds) rapidly converts to a diiron(III) intermediate (red diamonds) at $\sim 18 \text{ s}^{-1}$. The diiron(III) transient evolves to the mixed-valent species (blue diamonds) at $\sim 1 \text{ s}^{-1}$. The formation and decay rates of the $g = 2.0$ signal (open green diamonds) from RFQ EPR experiments are within error of the rates for mixed-valent species determined by Mössbauer. The diiron(III) resting state (orange diamonds) is formed as the mixed-valent species decays at $\sim 0.08 \text{ s}^{-1}$. III-defined ferric species formed during reaction of the reduced hydroxylase with dioxygen (see caption to Figure 5) are omitted from this kinetic analysis. The diiron(II) starting material (green line), the diiron(III) intermediate (red line), mixed-valent diiron(III,IV) transient (blue line), $g = 2.0$ EPR signal (light-green line), and the diiron(III) product (orange line) were fit to two-exponential functions.

Table 1: Formation and Decay Rate Constants of the Mixed-Valent Diiron(III,IV)-W* Species Measured by Optical, Mössbauer, and EPR Spectroscopy

rate constant	optical	Mössbauer	EPR
$k_f (\text{s}^{-1})$	0.804(1)	1.1	0.77
$k_d (\text{s}^{-1})$	0.054(2)	0.08	0.15

stable (Figure 6, green line and diamonds) during this decay phase of the diiron(III) intermediate. This result establishes unambiguously that the diiron(III) transient is a true precursor to diiron(III,IV)-W*. The data also reveal that the diiron(III,IV)-W* species reaches a maximum accumulation of 0.33 clusters/protomer at 3.5 s and decays with a rate constant of $\sim 0.08 \text{ s}^{-1}$ to generate the diiron(III) product (Figure 6, orange line). The formation and decay rates of the optically silent diiron(III,IV) cluster are linked to that of the optically active W*, because the rates of the former, determined from Mössbauer spectroscopy, agree with those of the latter, determined from optical studies (17, also, see Table 1). Slow oxidation ($\sim 0.01 \text{ s}^{-1}$) of residual unreacted diiron(II) species accompanies the second phase formation of the diiron(III) product and the generation of other minor, unidentified ferric species. A previously unreported, minor oxidation product (Figure 5, cyan lines) can be detected as forming around 1 to 2 s after mixing with O₂. After 5 s its accumulation reaches a constant value of $\sim 8\%$ of the total iron in the samples. Its Mössbauer parameters ($\delta = 0.56 \text{ mm/s}$ and $\Delta E_Q = 1.77 \text{ mm/s}$) and diamagnetism, revealed by high-field Mössbauer measurements, indicate a diiron(III) cluster. Its kinetic profile suggests that it is a final

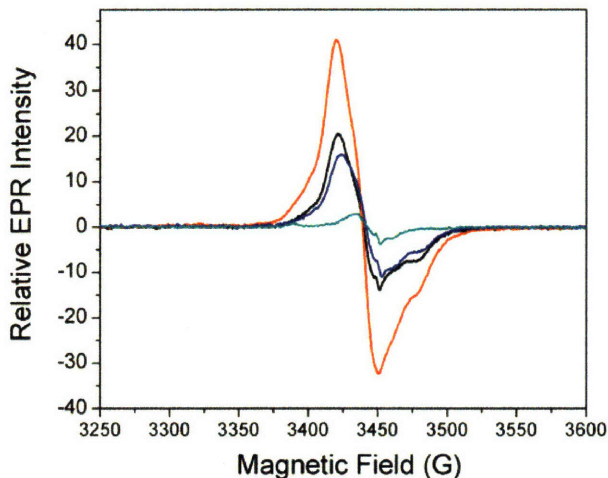


FIGURE 7: Selected EPR spectra for the transient formed during the reaction of ToMOH_{red} I100W:3ToMOD with O₂. The intensity of the signal at $g = 2.0$ maximizes 4 s (red) after mixing reduced protein with dioxygen-saturated buffer. Spectra for samples that were allowed to react for 520 ms (black), 10 s (blue), and 100 s (cyan) are also shown.

product. A definitive identification cannot be made, however, due to the small amount of material that accumulates.

Reaction of Reduced ToMOH I100W with O₂ Monitored by EPR Spectroscopy. As reported previously (17), two EPR signals were observed during the reaction of the reduced I100W variant hydroxylase with dioxygen, a signal at $g = 16$, corresponding to diiron(II) centers, and a transient $g = 2.0$ signal, associated with the diiron(III,IV)-W* intermediate. The $g = 16$ signal decays in a biphasic manner. The first phase is rapid and could not be simulated accurately with the data collected. This initial decay is complete by $\sim 0.17 \text{ s}$, which is consistent with the decay kinetics of the rapidly interacting diiron(II) sites observed in the Mössbauer measurements (*vide supra*). The second phase was slower and incomplete by 150 s. Figure 7 displays EPR spectra of selected freeze-quenched samples in the $g = 2.0$ region, showing the rise and fall of the transient EPR signal. The intensity of this transient signal appeared and decayed with rate constants of 0.77 s^{-1} and 0.15 s^{-1} , maximizing at approximately 4 s (Figure 6, green open diamonds and line, respectively). The rate constants for formation and decay agree with those reported from the stopped-flow optical and Mössbauer experiments, confirming that this EPR active species corresponds to the spin coupled mixed-valent diiron(III,IV)-W* intermediate (Table 1). The time-dependent EPR data indicate that the fast-reacting diiron(II) protein and the mixed-valent species are not kinetically linked because the rate of decay of the former is much faster than the rate of formation of the latter. This result indicates the presence of an intervening EPR-silent species, namely, the diiron(III) intermediate observed in the Mössbauer spectra of RFQ samples quenched between 0.03 and 4 s, described above.

Prior to carrying out the ¹H and ²H-Mims ENDOR measurements, X-band EPR spectra were recorded on samples quenched 4 s after mixing solutions of ToMOH_{red} I100W:3ToMOD with dioxygen-saturated buffer. The $g = 2.0$ signal has two contributions, as previously mentioned, one from the diiron(III,IV) cluster and the other from the tryptophan radical. The radical signal is visible at temper-

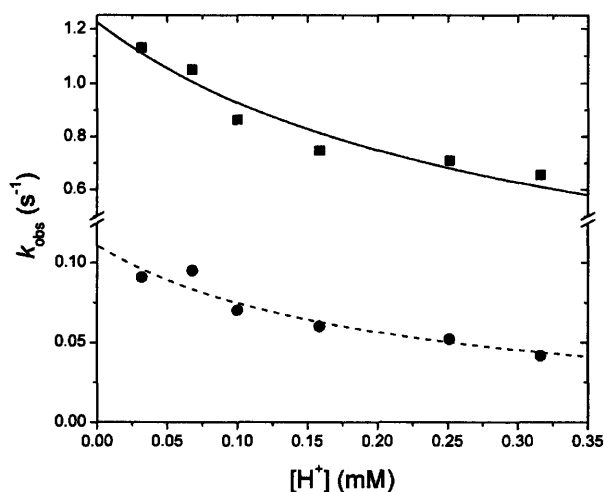


FIGURE 8: Effect of proton concentration on formation and decay of the diiron(III,IV)-W^{*} species. Increasing pH increases k_f and k_d of the ToMOH 1100W transient. The rate constants both increase with decreasing $[H^+]$, with k_f (■) and k_d (●) increasing ~ 2 -fold between pH 6.5 and 7.5. The y-axis scales differ above and below the break.

atures up to ~ 77 K, whereas the diiron signal is visible only below ~ 40 K (Figure S4). The peak width of the mixed-valent diiron(III,IV)-W^{*} transient is smaller than that reported elsewhere for tryptophan cation and neutral radicals (33).

Kinetic Isotope Effects for Formation and Decay of the Diiron(III,IV)-W^{*} Species. Both the rates of formation, k_f , and decay, k_d , were sensitive to the hydrogen isotope concentration with normal isotope effects, $k_H > k_D$, observed over the examined temperature range (Table S4). The ratio of k_H/k_D decreased with increasing temperature from 2.51 to 1.97 for k_f and from 3.2 to 1.72 for k_d . From Arrhenius plots, the formation activation energy is greater in deuterated, 15.6 ± 0.5 kcal/mol, than in protic, 13.5 ± 0.1 kcal/mol, solvent as expected from the ratio of k_H/k_D (Figure S2). The solvent kinetic isotope effect (SKIE) for the formation process is weakly dependent on temperature and contrasts with the stronger, nonlinear dependence for the decay process. The magnitude and sensitivity to temperature of the SKIEs indicate that hydrogen atom transfer or tunneling does not occur in the transition state during the reaction of the diiron(III) intermediate with W100, or for subsequent decay of the mixed-valent diiron(III,IV)-W^{*} species.

Effect of pH on Reaction of ToMOH 1100W with O₂-Saturated Buffer. As the pH increased from 6.5 to 7.5, the rates of oxidation of W100 by the diiron(III) intermediate and decay of the diiron(III,IV)-W^{*} species also increased (Table S5). From data collected in diode array mode, the absorption maximum of the tryptophanyl radical was unchanged over the examined pH range. To explain the pH dependence, we propose a model in which a rate-limiting deprotonation precedes a fast oxidation reaction. The pH dependence data agree reasonably well with this model to give a calculated proton-independent electron-transfer rate of 1.22 s^{-1} (Figure 8). The decay rate of the transient is also sensitive to pH, following a similar trend as observed for the formation rate. Values of k_d increase almost 2-fold with an order of magnitude decrease in proton concentration. The data were adequately fit with the model applied to the

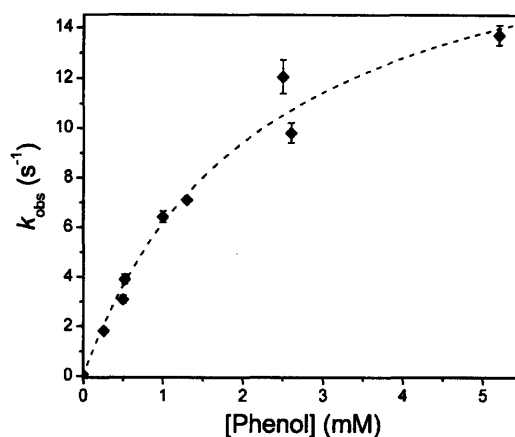


FIGURE 9: Phenol increases the decay rate of the tryptophanyl radical. The dependence of the observed rate on phenol concentration is well modeled by saturation kinetics. The determined reaction rate of the transient, k_{rxn} , with phenol and the substrate binding constant, K_d , are $20 \pm 2 \text{ s}^{-1}$ and $2.3 \pm 0.5 \text{ mM}$, respectively.

formation rate, rate-limiting deprotonation followed by oxidation, yielding a rate constant of 0.12 s^{-1} for the rapid second step of the reaction (Figure 8).

Effect of Substrates on the Decay Rate of the ToMOH 1100W Transient. The presence of phenol increased the decay rate constant of the tryptophanyl radical from 0.054 s^{-1} to $13.7 \pm 0.4 \text{ s}^{-1}$. The concentration dependence of k_d was modeled with a saturation binding model applied to the reaction of oxygenated intermediates in MMOH with alternative substrates, where a substrate-enzyme complex forms prior to reaction (eq 1) (34). From this analysis, the rate

$$k_{\text{obs}} = \frac{k_{\text{rxn}}[S]}{K_d + [S]} \quad (1)$$

constant for reaction with phenol, k_{rxn} , and the substrate-enzyme dissociation constant, K_d , are $20 \pm 2 \text{ s}^{-1}$ and $2.3 \pm 0.5 \text{ mM}$, respectively (Figure 9). In double-mixing experiments employing phenol, the absorbance over all wavelengths increased after decay of the transient. This growth in absorption was modeled as an independent exponential function in all data for which phenol was the substrate. The decay rate of W^{*} is also accelerated in the presence of propylene. The observed decay rate constants are $0.239 \pm 0.003 \text{ s}^{-1}$ and $2.8 \pm 0.1 \text{ s}^{-1}$ for propylene concentrations of $19 \mu\text{M}$ and 3.8 mM , respectively. Addition of acetylene to the tryptophanyl radical had little influence on the decay process, increasing the rate constant from $0.079 \pm 0.002 \text{ s}^{-1}$ to $0.114 \pm 0.006 \text{ s}^{-1}$ (Figure S3).

¹H- and ²H-ENDOR Spectra of the Mixed Valent Diiron(III,IV)-W^{*} Couple. To confirm that the protein-based radical resides on a tryptophan residue, ^{1,2}H-ENDOR spectra were recorded of this transient in H₂O/D₂O buffers using enzymes that contained either natural abundance tryptophan or the tryptophan selectively deuterated on the indole ring. Although the radical EPR signal overlaps that of the diiron center, the spectrum of the latter is substantially broader. Signals from the two can therefore be distinguished by their field dependence as well as by their different relaxation properties.

The ¹H-CW ENDOR spectra collected at fields associated with the radical for samples containing natural abundance tryptophan residues are dominated by signals from the C_β

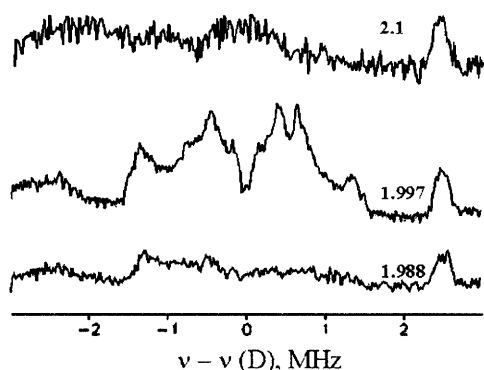


FIGURE 10: ^2H -Mims ENDOR spectra of the tryptophanyl radical. Protein in this sample was expressed in media containing isotopically enriched tryptophan(d_5 -indole). Saturation of the transition corresponding to the radical signal at $g \sim 2.00$ (middle) yields ^2H signals from the labeled indole ring. These peaks disappear upon saturation at higher (top) or lower (bottom) g -values. Magnetic fields scanned are reported as g -values in the figure.

protons of the residue, with strong hyperfine couplings of ~ 20 MHz, and by those from the indole ring, with smaller couplings (Figure S5). Additional features near ν_{H} have been assigned to protein matrix protons in other systems (35). To determine that the radical is centered at tryptophan, we collected ^2H -Mims ENDOR spectra from natural-abundance and selectively deuterated, tryptophan(d_5 -indole), hydroxylase.

The sample prepared with isotopically enriched tryptophan shows ^2H -Mims ENDOR signals with hyperfine couplings corresponding to $A_{\text{H}} > 10$ MHz when the field of observation is where the radical signal is strongest (Figure 10). These signals arise from the aromatic protons of the indole ring because they are absent at fields outside the EPR envelope of the radical signal. The signals unequivocally confirm that the protein-based radical resides on a tryptophan residue.

^1H -CW ENDOR spectra collected at the field corresponding to the maximum intensity of the radical are similar for the diiron(III,IV)- W^{\bullet} transient generated with unlabeled protein in deuterated and protic buffers, but such comparisons are difficult because of strong signals from nonexchangeable protons (Figure S5). As a result, the presence of potentially exchangeable protons was investigated by ^2H Mims ENDOR measurements. ^2H -Mims ENDOR signals corresponding to ^1H coupling of $A_{\text{H}} \sim 4$ –8 MHz were observed in samples generated in deuterated buffer (Figure 11). Because these signals are observed at fields across the EPR envelope of the diiron center, and outside that of the tryptophanyl radical, they can be assigned to the diiron center (compare Figures 10 and 11). By analogy to the diiron centers of intermediate X and MMOH_{mv} , for which ENDOR signals from terminal water molecules on the iron(III) ion correspond to species with $A_{\text{H}} \sim 7$ –9 MHz, the signals observed in the diiron(III,IV)- W^{\bullet} transient can be assigned to a terminal water molecule or hydroxide ion on the ferric ion (35, 36).

If the tryptophanyl radical were protonated at the indole nitrogen atom, one would expect an additional ^2H signal, with $A_{\text{H}} > 10$ MHz, at fields associated with this radical (37–41). No such ^2H signals are observed, however (Figure 11). The absence of an exchangeable proton associated with the protein radical is consistent with our interpretation of

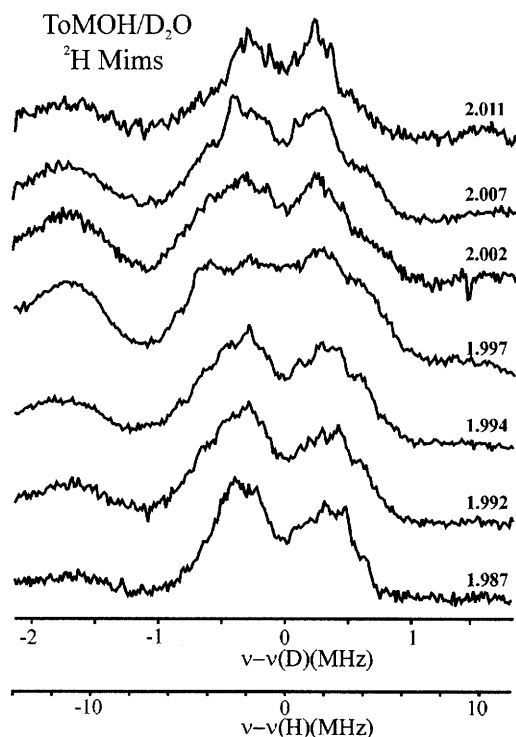


FIGURE 11: ^2H -Mims ENDOR spectra of the diiron(III,IV)- W^{\bullet} species generated in deuterated buffers. Signals arising from protonated species are observed over the swept magnetic fields. The signal shows minor changes upon saturation at $g = 1.9875$ to 2.0 and does not correlate with the tryptophan radical. The corresponding proton scale is shown for comparison.

the stopped-flow optical data, where a band with λ_{max} of 500 nm indicated a deprotonated tryptophanyl radical.

Tryptic Digestion and Mass Spectrometric Analyses of ToMOH I100W and its Oxidation Product. The most intense ion envelopes in the MALDI-TOF(+) spectra are between 700 and 2500 m/z for the in-gel tryptic digested α -subunit of as-isolated and O_2 -reacted $\text{ToMOH}_{\text{red}}$ I100W. The expected tryptic peptide containing W100, $_{85}\text{ADPGWVSTM-QLHFGAWALEEYAASTAEAR}_{113}$, has a predicted monoisotopic mass of 3165.5 Da for the $[\text{M} + \text{H}]^+$ parent ion. The ion envelope at $m/z = 3166$ in the as-isolated sample is well separated from other ions in the spectrum and is assigned to this 29mer peptide containing W100 (Figure 12). Two additional envelopes of lower intensity are present at m/z values of 3182 and 3198. The relative intensities of these latter two envelopes in the reacted sample increase markedly, with that at $m/z = 3182$ becoming the most intense. The envelopes at $m/z = 3182$ and 3198 were unchanged in MALDI-TOF spectra of digestion products of reduced ToMOH I100W reacted with $^{18}\text{O}_2$ -saturated buffer.

The tryptic peptide of interest also contains other residues sensitive to oxidation, such as methionine and histidine. To determine the decay pathway chemistry for the W^{\bullet} species, we attempted to identify the specific residue that is oxidized. Fragmentation of the tryptic peptide was carried out by ESI(+)-MS/MS. Ions resulting from the $[\text{M} + \text{H}]^{3+}$ ion were assigned to respective b and y peptides by considering the fragment ion mass and the peak-to-peak separation within the ion envelope (Figure S6) (42). We could not identify the ions corresponding to every possible fragment because

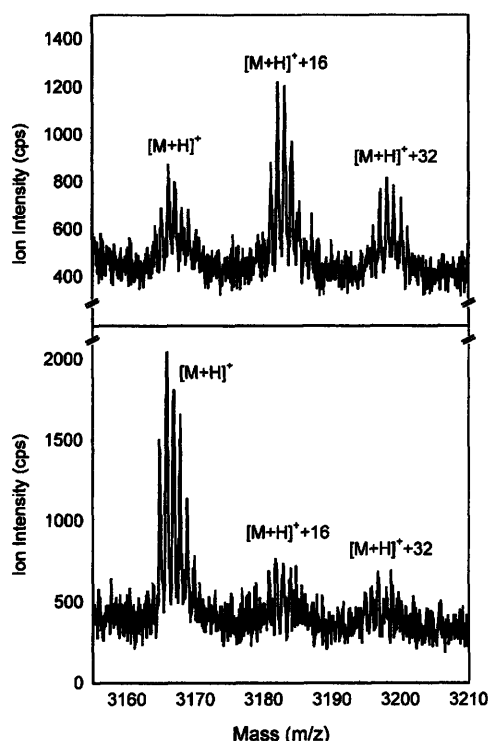


FIGURE 12: MALDI-TOF spectra of tryptic peptides for the α -subunit of O_2 -reacted (top) and as-isolated (bottom) ToMOH I100W. The mass of the $[M + H]^+$ ion at 3166 m/z agrees with the predicted mass for the 29mer peptide. Two additional envelopes of 16 and 32 Da higher mass are also present. The relative intensity of these three envelopes changes in the reacted sample, with $[M + H]^+$ less abundant than $[M + H]^+ + 16$.

the peak intensities were below our detection threshold. From the ions that were isolated, the b ions limit the site of modification to lie between S91 and E104, a region that includes two other possible sites of oxidation, M93 and H96. The y fragment ions further narrowed the possible region of oxidation, excluding M93. Probable sites of oxidation are therefore limited to H96 and W100.

DISCUSSION

Mixed-Valent Diiron(III,IV)-W Species as an Entry to Identifying Oxygenated Intermediates in ToMOH.* Dioxygen reacts rapidly, $k_{obs} \sim 18 \text{ s}^{-1}$, with reduced diiron(II) ToMOH I100W preincubated with ToMOD to yield a diiron(III) intermediate that was only disclosed because it generated the tryptophan neutral radical chromophore. One-electron reduction of this diiron(III) transient by W100 gives rise to a mixed-valent diiron(III,IV) center. The peroxodiiron(III) species in RNR-R2 reacts in a similar manner. Oxidation of W48 and protonation of one of the oxygen atoms in the peroxy-adduct of RNR-R2 facilitates O–O bond cleavage to form intermediate X (43, 44). The proposed mechanism for dioxygen activation in cytochrome P450 enzymes requires protonation of the distal oxygen atoms in the peroxoiron(III) intermediate by a conserved threonine-aspartic acid pair (6, 31). Residue T201 in the active site cavity of ToMOH, which is strongly conserved among the BMMs, could function in a proton shuttle pathway to the diiron core. In MMOH, this threonine is proposed either to deliver protons to the peroxodiiron(III) species directly or, more plausibly, by strategically holding a hydronium ion for

proton transfer during reduction of the oxidized diiron(III) center (45, 46). Conversion of the diiron(III) intermediate in ToMOH to the mixed-valent diiron center could proceed by an analogous pathway as that in the heme systems and RNR-R2. In the I100W variant, T201 could help to provide a crucial proton to facilitate cleavage of the O–O bond to form the mixed-valent transient. Protons would be consumed during the oxidative phase of the ToMOH catalytic cycle, which would contrast with MMOH where protons are proposed to be required during reduction of the oxidized diiron(III) core (47). In the native system, T201 may be important for steady-state catalysis if substrate radical generation is a pathway for arene hydroxylation. Pre-steady-state studies of a series of variants at this position would be valuable in discerning its possible role in the mechanism of substrate oxidation.

An investigation of T201 variants of T4MOH demonstrated that this residue does not affect steady-state catalysis (48). For an observable effect under steady-state conditions, however, T201 must be involved in the rate-determining step. Product release is believed to be rate-limiting for hydroxylation by MMOH (49). The products catechol and phenol can bind to the diiron center in $ToMOH_{ox}$ isolated after purification or following single-turnover experiments (50). Lack of knowledge of the rate-determining step under steady-state catalysis prevents us from making a meaningful comparison between the earlier steady-state and current pre-steady-state analyses.

Values of δ and ΔE_Q for the mixed-valent diiron(III,IV) transient in ToMOH I100W are comparable to those of the Fe(III)Fe(IV) centers of intermediate X in RNR-R2 and Q_X in MMOH (43, 51). In addition, the 2H -ENDOR spectra of the ToMOH diiron(III,IV) species prepared in deuterated buffer suggest that an exchangeable proton-containing species is coordinated to the iron(III) ion. The observed hyperfine couplings for this protonated ligand are within the range of those reported for terminal water molecules on the ferric centers in $MMOH_{mv}$ and intermediate X (36, 44). This terminal hydroxide ion or water molecule may arise by a mechanism similar to that proposed for RNR-R2 (44). Protonation-aided cleavage of the O–O bond in the diiron(III) species would yield a water molecule that coordinates to the ferric ion. Despite the differences between the diiron(III) intermediate in ToMOH and those of other CBDI enzymes, the ability to form high-valent transients with similar spectroscopic parameters might arise from the homologous primary coordination spheres that these enzymes share.

Our preliminary assignment of the protein-based radical as W^* was based on stopped-flow optical experiments. In these studies, a λ_{max} was measured to be 500 nm, within the previously reported range for tryptophanyl radicals (52–54). Since the species (λ_{max} 500 nm) was observed only in the tryptophan variant, this specific residue seemed to be critical for transient formation. 1H - and 2H -Mims ENDOR spectra of this species containing unlabeled and selectively deuterated tryptophan residues firmly establish the presence of a tryptophanyl radical. Samples made in protic and deuterated buffers displayed similar 1H -Mims ENDOR spectra, providing evidence that the tryptophanyl radical is deprotonated, confirming unequivocally our initial assignment that the optically active intermediate observed in stopped-flow studies is a neutral tryptophanyl radical.

The redox potentials of the aromatic side chains of tyrosine and tryptophan are pH dependent with lower proton concentrations favoring oxidation (52, 54). In the present study, we observed the deprotonated form of the radical, the λ_{\max} value of which was invariant across the examined pH range of 6.5 to 7.5. We were unable to access pH values near the reported pK_a values for the N–H group of the indole ring and the cationic indolyl radical because of protein instability (54, 55). Nonetheless, deprotonation of the indole nitrogen is tightly coupled to electron abstraction because the tryptophan cation radical is not observed. We exclude mechanisms such as hydrogen atom transfer from W100 to the diiron center or a proton tunneling event during the rate-determining step for formation and decay of the diiron(III,IV)–W* transient because of the small magnitude and temperature dependence of the kinetic isotope effects. In enzymes where hydrogen-atom transfer or proton tunneling are proposed to occur, the isotope effects range from 3 to >100 and are temperature independent (56, 57). The isotope effects observed here are <3.2 for either rate constant and temperature dependent, both of which are atypical of hydrogen-atom transfer or tunneling.

Disruption of electron-transfer pathways from W48 and Y122 to oxygenated diiron intermediates in RNR-R2 results in oxidation of phenylalanine and tyrosine residues near the dimetallic center (58–60). Models of the I100Y mutation estimate the distance between the diiron center and this tyrosine at 7 to 10 Å, positioning this residue for possible oxidation (61). Absorption bands corresponding to tyrosyl radicals or iron-catecholate species were not observed during or after the reaction of ToMOH_{red} I100Y with dioxygen. Absence of these bands suggests that if oxidation of the tyrosine residue were to occur, a stable radical species is not formed and the L-dopa product is unable to coordinate to the diiron center. Alternatively, the diiron(III) intermediate may not be a strong enough oxidant to abstract an electron from Y100. This limitation may arise from the redox potential of tyrosine or from other parameters that affect ET, such as the distance.

As mentioned in the Results section, a model whereby a slow reversible equilibrium precedes fast oxidation provides the most satisfactory explanation for the pH dependence data. Deprotonation of the tryptophan residue, the diiron(III) intermediate, or an amino acid side chain required to accept the proton from the tryptophan residue could limit the oxidation rate. The tryptophan cation radical is not observed in our optical studies, implying that proton loss must occur upon oxidation of this residue. Deprotonation of the indole nitrogen before electron abstraction by the diiron(III) intermediate is expected to be unfavorable because the pK_a value for this proton is estimated to be 17 (55). Oxidation of W100 prior to proton loss would yield a transient tryptophan cation radical, the pK_a of which is 3.7 (54). Deprotonation of the radical cation is therefore predicted to be facile within the examined pH range. Proton loss from the indole ring could limit the oxidation rate if it is required to occur prior to this reaction. Alternatively, if loss occurs after oxidation, the rate-limiting deprotonation event might involve either the diiron(III) intermediate or nearby amino acid residues.

A Novel Diiron(III) Intermediate Oxidizes W100. The mechanism for arene hydroxylation by the native hydroxylase 208 could proceed by either one- or two-electron oxidation

pathways. If the reaction occurs by initial electron abstraction from substrate, the hydroxylation mechanism could involve generation of a species similar to the mixed-valent diiron(III,IV)–W* center in ToMOH I100W. However, oxidation of the aromatic substrate by electrophilic attack on the π -system would be comparable to the reactions of MMOH_{peroxo} with electron-rich substrates, bypassing stable radical intermediates (62).

Both radical- and cation-derived products were observed for oxidation of RCS probes by T4MO, implying that one- and two-electron oxidation mechanisms might occur in this system (63). Formation of both of these products could reflect two competing mechanisms for substrate oxidation depending upon the ease of approach of these unnatural substrates to the diiron site. If substrate is bound close to the reactive intermediate, then oxidation might proceed by hydride abstraction to generate a substrate cation. Ring-opening of the substrate would give rise to the observed cation-derived product. On the other hand, if the hydrocarbon were not able to approach the oxidizing intermediate, electron abstraction may predominate to generate substrate-radical intermediates. If the diiron(III) species is the only iron-based transient formed during dioxygen activation in the native hydroxylase, the preference for electron-rich substrates, such as the indole ring of W100 or aromatic compounds, by this transient in ToMOH would be similar to the observed reactivity of MMOH_{peroxo} and the peroxodiiron(III) species in RNR-R2. The formation of both radical- and cation-derived RCS products could arise from two distinct intermediates that react with these substrates. In MMOH, Q is proposed to carry out one-electron oxidations and MMOH_{peroxo} by hydride abstraction and epoxidation mechanisms (62). The diiron(III) intermediate observed in ToMOH I100W is the only observed precursor to the mixed-valent diiron(III,IV) center, yet we cannot exclude formation of a short-lived oxo-bridged diiron(IV) intermediate. Formation of such a Q-type intermediate would facilitate electron abstraction pathways and the diiron(III) intermediate would allow for two-electron oxidation mechanisms. We recently reported a detailed examination of dioxygen activation in the native system where a similar diiron(III) intermediate forms and is kinetically competent for substrate hydroxylation (50).

The Mössbauer parameters and lack of optical absorption features in the near-IR region for the diiron(III) transient species are unique among intermediates at this oxidation level in the CBDO enzyme family (4). Specifically, values for λ_{\max} near 700 nm, $\delta > 0.6$ mm/s, and $\Delta E_Q > 1$ mm/s are characteristic parameters of μ -1,2-peroxodiiron(III) clusters in synthetic and enzyme systems (12). This intermediate is EPR-silent, like other peroxo-bridged diiron(III) clusters. We tentatively assign this intermediate as a peroxodiiron(III) species based on the similarities of the proposed reactivity to other peroxo-intermediates and by analogy to the mechanism of dioxygen activation at synthetic and enzymatic CBDO centers.

The differences between the Mössbauer parameters for this intermediate and other peroxodiiron(III) species might arise from an alternate binding geometry of the peroxide moiety to the diiron core. Binding modes, such as μ - η^1 : η^2 - and μ -1,1-, of peroxide fragments at diiron(III) centers are proposed to occur during formation of MMOH_{peroxo} and X (64–66). The peroxide fragment here might adopt such a conformation. The protonation state of the peroxide ion may

also differ. Hydroperoxoiron(III) intermediates reported in heme systems are proposed to be electrophilic oxidants, similar to the observed reactivity of peroxodiiron(III) centers (6, 67). Structural investigations of this intermediate in the native system by ENDOR and XAS would provide insight into the structure of this species.

The redox potential of the diiron(III) intermediate can be estimated by Marcus theory (eq 2). The variable k_{ET} is the

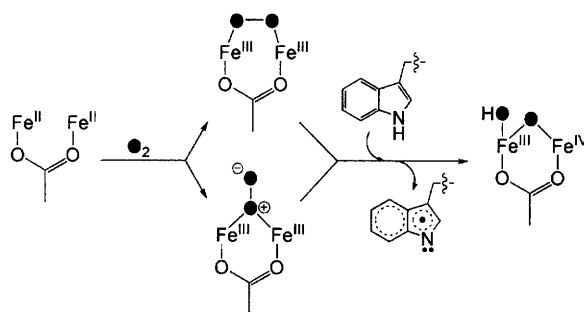
$$k_{ET} = k_0 e^{-\beta(r-r_0)} e^{-(\Delta G + \lambda)^2/(4\lambda RT)} \quad (2)$$

electron-transfer rate, k_0 is the characteristic frequency of the nuclei, usually assigned a value of 10^{13} , R is the gas constant, and T is the temperature in K (68). The term β , fixed at 1.1 \AA^{-1} , is related to the nature of the intervening medium between the redox partners. The distance between the tryptophan residue and the diiron center, r , was determined from the crystal structure to be 6.5 \AA , and r_0 is the contact distance, which is generally set to 3 \AA . Reorganization energies, λ , of 1.0 and 0.1 V were used to calculate a range for the reduction potential of the diiron(III) intermediate. The driving force, ΔG , is the sum of the reduction potentials for the forward reaction. Since we did not observe a transient tyrosyl radical in the I100Y variant, the reduction potential of the diiron(III) intermediate might lie between that of Y and W. Depending on whether deprotonation of the indole ring occurs before or after electron abstraction, the potential may be further limited to between those of the W^+/W^- and the $W^{•-}/W$ half reactions. To obtain a conservative estimate of the oxidizing power of the diiron(III) intermediate, we assumed that proton loss must occur prior to electron transfer because the energetic cost is less for oxidation of the deprotonated versus neutral indole ring. The foregoing analysis was used to estimate the potential for the $Fe_2^{III}/Fe_2^{III,IV}$ half reaction, assuming that the W^+/W^- couple is 0.73 V, which corresponds to deprotonation of 50% of the tryptophan residues (54). To negate the inhibitory effect of protons on the oxidation rate, the calculated proton-independent oxidation rate of 1.22 s^{-1} determined from the variable pH data was used for k_{ET} . With these assumptions, we estimate the reduction potential of the intermediate to lie between 1.1 and 1.3 V versus NHE. This range is close to the reduction potentials of oxidants such as hydrogen peroxide (0.878 V), manganese dioxide (1.224 V), and chromate (1.35 V). The latter two oxidants, MnO_2 and CrO_4^- , are commonly employed for the conversion of hydroxyl groups to either carbonyl or carboxylate functionalities. The peroxodiiron(III) intermediate in MMOH is proposed to carry out similar oxidation reactions, albeit via hydride abstraction (62).

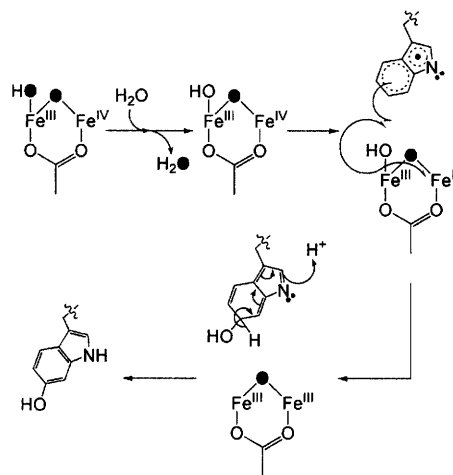
Mechanism of Dioxygen Activation and W100 Oxidation. Scheme 1 depicts our proposed mechanism for formation of the mixed-valent diiron(III,IV)- W^{\bullet} transient. Dioxygen binding to the reduced diiron(II) enzyme would yield a peroxodiiron(III) intermediate, two possible geometries for which are shown. Electron abstraction from W100 by the diiron(III) center is accompanied by protonation-aided cleavage of the O-O bond to form the mixed-valent diiron(III,IV)- W^{\bullet} transient. The structure of the mixed-valent diiron core is similar to that proposed for intermediate X, where the oxygen atoms derived from dioxygen (filled circles in Scheme 1) become an oxo-bridge and either a terminal hydroxide ion or water molecule.

The diiron(III,IV) cluster and W^{\bullet} radical decay at the same rate as measured by Mössbauer, EPR, and optical spectro-

Scheme 1: Proposed Mechanism for Formation of the Diiron(III,IV)- W^{\bullet} Transient



Scheme 2: Proposed Mechanism for Decay of the Diiron(III,IV)- W^{\bullet} Transient



copy. The two $S = 1/2$ centers are therefore likely to share a common mechanism to restore the oxidized diiron(III) cluster and quench the protein radical. In reacted ToMOH I100W, the installed tryptophan appears to be oxidized, as demonstrated by the 16 Da increase in mass of the tryptic peptide containing W100 and the fragmentation peptides thereof. In the crystal structure of ToMOH I100W, the indole ring adopts conformations in which the six-membered ring of the indole side chain vector is oriented either away from or toward the active site. We predict either C_{ζ_3} or C_{η_2} to be the site of oxidation, based on the distances between these two carbon atoms and the diiron core in the oxidized crystal structure. Oxidation of W^{\bullet} arising from attack by dioxygen is unlikely, since the mass of the predicted products would be 32 Da greater than the parent $[M + H]^+$ ion of the unmodified peptide, in disagreement with the experimental results. Dioxygen attack on W^{\bullet} gives rise to a transient tryptophan peroxyl radical, which results in cleavage of the pyrrole ring (69). The peak at $m/z = 3198$ in the MALDI-TOF spectra is of weak intensity and is attributed to further oxidation of the W100 from multiple turnovers of the hydroxylase, instead of oxidation of the indolyl radical by O_2 . In addition, such a pathway would not explain the simultaneous decay of the mixed-valent diiron(III,IV) center. Instead, we propose a radical recombination mechanism, where an oxygen atom species on the diiron(III,IV) cluster is transferred to the indolyl radical (Scheme 2).

The terminal hydroxide or water molecule must be exchangeable to explain the insensitivity of the mass of the tryptic peptide and its fragments containing W100 to the

isotopic content of the dioxygen source. ^2H -ENDOR spectra of the transient in deuterated buffers identified an exchangeable species with hyperfine coupling constants similar to those reported for terminal water ligands on the ferric ion in X and MMOH_{mv} (35, 36). The exchange rate of this labile species must be significantly faster than the rate of the decay of the transient species to prevent incorporation of ^{18}O -atoms into the tryptic peptide. Rapid exchange of oxygen atom ligands at high-valent iron centers has been reported for bridging and terminal ligands in intermediate X and terminal oxo-groups at mononuclear iron centers (44, 70, 71). Hydroxyl radical transfer from the diiron center to W* followed by rearomatization of the indole ring gives rise to an oxo-bridged diiron(III) cluster and a hydroxyindole side chain at W100. Addition of water to the diiron core reforms the di(μ -hydroxo)diiron(III) resting state.

The decay reaction is sensitive to proton concentration. The active site of ToMOH is charge neutral, and depending on the ligand type and binding geometries in the diiron(III,IV) transient, the terminal ligand could be either a bound water or hydroxide ion. If the terminal species is a bound water molecule, deprotonation might be required prior to hydroxyl radical transfer. Alternatively, the protonation state of residues within the active site cavity or channel near W100 may be important for stabilizing the diiron(III,IV) cluster or W*. Deprotonation of these residues could favor decay of these transient species. More detailed structural information on the transient species formed during dioxygen activation in the native and I100W variant of the hydroxylase is required to determine the source of this proton dependence.

Potential substrates for BMMs, such as propylene and phenol, accelerate decay of the tryptophanyl radical in stopped-flow optical studies. In the steady state, the activity of ToMOH I100W is more than an order of magnitude lower than that of the wild type enzyme, possibly due to retardation of substrate access or product egress in the variant hydroxylase. The ability of phenol and propylene to accelerate the decay rate is interesting. Phenol could quench the tryptophanyl radical by hydrogen atom transfer from the O–H group to form a phenoxyl radical. Similar reactivity is observed in small molecule chemistry where analogues of phenol are used as radical scavengers. Neutral and cationic tryptophanyl radicals reportedly abstract hydrogen atoms from the hydroxyl group of *p*-methoxyphenol at rates exceeding 10^5 s^{-1} (72). No absorption bands were observed at 410 nm during our double-mixing optical experiments, which indicates that any phenoxyl radical formed by hydrogen-atom abstraction must be short-lived. To explain the sensitivity of the decay rate on propylene and acetylene, we consider the bond dissociation energies of the weakest C–H bonds in these molecules. The BDE of the phenolic O–H bond is similar to that of the methyl sp^3 C–H bond in propylene, $\sim 87 \text{ kcal/mol}$ (73, 74). Acetylene, by comparison, has a C–H BDE almost 50 kcal/mol greater than that of phenol or propylene. The tryptophanyl radical is capable of abstracting a hydrogen atom from the weak O–H bond in phenol and C–H bond in propylene, accelerating the decay of this transient. Because the same reaction with acetylene requires more energy, the decay rate is not appreciably perturbed upon mixing the radical with this substrate.

The reaction of phenol with the neutral tryptophan radical is a pathway distinct from hydroxylation of this substrate to

yield catechol under steady-state conditions where the diiron centers are distributed into populations of reduced, diiron(III) intermediate, diiron(III,IV)–W* transient, and diiron(III) product species. The presence of W100 effectively outcompetes the phenolic substrate for the diiron(III) intermediate, if substrate binding occurs after dioxygen activation. Substrate could conceivably bind to the active site in either the reduced state, prior to dioxygen binding and activation, or in the oxidized state after oxidation of W100 or phenol. The reduced capacity of the I100W hydroxylase to oxidize phenol reflects the retarded access of substrate into the active site pocket afforded by the mutation. Considering the location of residue 100 in the ToMOH α -subunit, separating the active site pocket from the rest of the channel and cavity 2, it is reasonable to propose that it may serve to gate substrate entry, product egress, or solvent access to the diiron center as proposed for L110 in MMOH and L98 in hemerythrin (16, 32). Evidence supporting this proposal is illustrated by the two conformations of the indole side chain in the crystal structure of I100W, which allow different levels of access to the diiron center of ToMOH.

CONCLUSIONS

The reaction of diiron(II) ToMOH I100W with dioxygen yields a diiron(III) intermediate, which subsequently abstracts an electron from W100 to form a chromophoric mixed-valent diiron(III,IV)–W* species. This coupled species could decay by transfer of an O-atom from the diiron core to the protein-based radical. The one-electron redox chemistry afforded by the diiron(III) intermediate resembles that of the peroxodiiron(III) intermediate in RNR-R2. No other high-valent diiron species were observed, suggesting that oxidation of hydrocarbons in this system occurs at the diiron(III) level. This diiron(III) intermediate is spectroscopically different from that of μ -1,2-peroxodiiron(III) clusters in CBDI enzymes and model compounds. These differences suggest that this intermediate in ToMOH may have an alternate binding geometry or protonation state of the dioxygen-derived fragment. The oxidation of W100 to form a deprotonated tryptophanyl radical has allowed us to estimate the reduction potential of the diiron(III) intermediate as 1.1–1.3 V. The mixed-valent diiron(III,IV) center has spectroscopic parameters similar to those of intermediates X and Q_x, although the diiron(III) precursors differ spectroscopically.

ACKNOWLEDGMENT

X-ray data were collected at the Stanford Synchrotron Radiation Laboratory (SSRL), which is funded by the Department of Energy (BES, BER) and the National Institutes of Health (NCRR, NIGMS). Crystallographic figures were generated using PyMOL (75). We thank Dr. Ioannis Papayannopoulos (Center for Cancer Research, M.I.T.) for collection, acquisition, and analysis of the MS data.

SUPPORTING INFORMATION AVAILABLE

Distances between the atoms of the indole ring of W100 and the diiron center, HPLC traces from the steady-state product determination for phenol, data for the effect of pH on k_f and k_d , the effect of propylene and acetylene on k_d , selected ENDOR spectra, and ESI-MS/MS data. This

information is available free of charge via the Internet at <http://pubs.acs.org>.

REFERENCES

- Song, W. J., Seo, M. S., George, S. D., Ohta, T., Song, R., Kang, M.-J., Tosha, T., Kitagawa, T., Solomon, E. I., and Nam, W. (2007) Synthesis, characterization, and reactivities of manganese(V)-oxo porphyrin complexes, *J. Am. Chem. Soc.* *129*, 1268–1277.
- Nam, W. (2007) High-valent iron(IV)-oxo complexes of heme and non-heme ligands in oxygenation reactions, *Acc. Chem. Res.* *40*, 522–531.
- Mirica, L. M., Vance, M., Jackson Rudd, D., Hedman, B., Hodgson, K. O., Solomon, E. I., and Stack, T. D. P. (2005) Tyrosinase reactivity in a model complex: an alternative hydroxylation mechanism, *Science* *308*, 1890–1892.
- Lippard, S. J. (2005) Hydroxylation of C-H bonds at carboxylate-bridged diiron centres, *Phil. Trans. R. Soc. A* *363*, 861–877.
- Sinnecker, S., Svendsen, N., Barr, E. W., Ye, S., Bollinger, J. M., Jr., Neese, F., and Krebs, C. (2007) Spectroscopic and computational evaluation of the structure of the high-spin Fe(IV)-oxo intermediates in taurine: α -ketoglutarate dioxygenase from *Escherichia coli* and its His99Ala ligand variant, *J. Am. Chem. Soc.* *129*, 6168–6179.
- Denisov, I. G., Makris, T. M., Sligar, S. G., and Schlichting, I. (2005) Structure and chemistry of cytochrome P450, *Chem. Rev.* *105*, 2253–2277.
- Rosenzweig, A. C., Brandstetter, H., Whittington, D. A., Nordlund, P., Lippard, S. J., and Frederick, C. A. (1997) Crystal structures of the methane monooxygenase hydroxylase from *Methylococcus capsulatus* (Bath): implications for substrate gating and component interactions, *Proteins* *29*, 141–152.
- Logan, D. T., Su, X.-D., Åberg, A., Regnström, K., Hajdu, J., Eklund, H., and Nordlund, P. (1996) Crystal structure of reduced protein R2 of ribonucleotide reductase: the structural basis for oxygen activation at a dinuclear iron site, *Structure* *4*, 1053–1064.
- Lindqvist, Y., Huang, W., Schneider, G., and Shanklin, J. (1996) Crystal structure of Δ^9 stearoyl-acyl carrier protein desaturase from castor seed and its relationship to other di-iron proteins, *EMBO J.* *15*, 4081–4092.
- (a) Lee, S.-K., Fox, B. G., Froland, W. A., Lipscomb, J. D., and Münck, E. (1993) A transient intermediate of the methane monooxygenase catalytic cycle containing an Fe(IV)Fe(IV) cluster, *J. Am. Chem. Soc.* *115*, 6450–6451. (b) Liu, K. E., Wang, D., Huynh, B. H., Edmondson, D. E., Salifoglou, A., and Lippard, S. J. (1994) Spectroscopic detection of intermediates in the reaction of dioxygen with the reduced methane monooxygenase hydroxylase from *Methylococcus capsulatus* (Bath), *J. Am. Chem. Soc.* *116*, 7465–7466.
- Sturgeon, B. E., Burdi, D., Chen, S., Huynh, B. H., Edmondson, D. E., Stubbe, J., and Hoffman, B. M. (1996) Reconsideration of X, the diiron intermediate formed during cofactor assembly in *E. coli* ribonucleotide reductase, *J. Am. Chem. Soc.* *118*, 7551–7557.
- Merkx, M., Kopp, D. A., Sazinsky, M. H., Blazyk, J. L., Müller, J., and Lippard, S. J. (2001) Dioxygen activation and methane hydroxylation by soluble methane monooxygenase: a tale of two irons and three proteins, *Angew. Chem., Int. Ed.* *40*, 2782–2807.
- Broadwater, J. A., Ai, J., Loehr, T. M., Sanders-Loehr, J., and Fox, B. G. (1998) Peroxidiferic intermediate of stearoyl-acyl carrier protein Δ^9 desaturase: oxidase reactivity during single turnover and implications for the mechanism of desaturation, *Biochemistry* *37*, 14664–14671.
- Jin, S., Kurtz, D. M., Jr., Liu, Z.-J., Rose, J., and Wang, B.-C. (2002) X-ray crystal structures of reduced rubrerythrin and its azide adduct: a structure-based mechanism for a non-heme diiron peroxidase, *J. Am. Chem. Soc.* *124*, 9845–9855.
- Sazinsky, M. H., Bard, J., Di Donato, A., and Lippard, S. J. (2004) Crystal structure of the toluene/*o*-xylene monooxygenase hydroxylase from *Pseudomonas stutzeri* OX1: insight into the substrate specificity, substrate channeling, and active site tuning of multicomponent monooxygenases, *J. Biol. Chem.* *279*, 30600–30610.
- Farmer, C. S., Kurtz, D. M., Jr., Phillips, R. S., Ai, J., and Sanders-Loehr, J. (2000) A leucine residue “gates” solvent but not O₂ access to the binding pocket of *Phascolopsis gouldii* hemerythrin, *J. Biol. Chem.* *275*, 17043–17050.
- Murray, L. J., García-Serres, R., Naik, S., Huynh, B. H., and Lippard, S. J. (2006) Dioxygen activation at non-heme diiron centers: characterization of intermediates in a mutant form of toluene/*o*-xylene monooxygenase hydroxylase, *J. Am. Chem. Soc.* *128*, 7458–7459.
- LeMaster, D. M., and Richards, F. M. (1985) ¹H-¹⁵N heteronuclear NMR studies of *Escherichia coli* thioredoxin in samples isotopically labeled by residue type, *Biochemistry* *24*, 7263–7268.
- McCormick, M. S., Sazinsky, M. H., Condon, K. L., and Lippard, S. J. (2006) X-ray crystal structures of manganese(II)-reconstituted and native toluene/*o*-xylene monooxygenase hydroxylase reveal rotamer shifts in conserved residues and an enhanced view of the protein interior, *J. Am. Chem. Soc.* *128*, 15108–15110.
- McPhillips, T. M., McPhillips, S. E., Chiu, H.-J., Cohen, A. E., Deacon, A. M., Ellis, P. J., Garman, E., Gonzalez, A., Sauter, N. K., Phizackerley, R. P., Soltis, S. M., and Kuhn, P. (2002) *Blu-Ice* and the *Distributed Control System*: software for data acquisition and instrument control at macromolecular crystallography beamlines, *J. Synchrotron Rad.* *9*, 401–406.
- Orwinowski, Z., and Minor, W. (1997) Processing of x-ray diffraction data collected in oscillation mode, *Methods Enzymol.* *276*, 305–326.
- Kissinger, C. R., Gehlhaar, D. K., and Fogel, D. B. (1999) Rapid automated molecular replacement by evolutionary search, *Acta Crystallogr. D55*, 484–491.
- Murshudov, G. N., Vagin, A. A., and Dodson, E. J. (1997) Refinement of macromolecular structures by the maximum-likelihood method, *Acta Crystallogr. D53*, 240–255.
- Collaborative Computational Project, Number 4 (1994) The CCP4 suite: programs for protein crystallography, *Acta Crystallogr. D50*, 760–763.
- Emsley, P., and Cowtan, K. (2004) *Coot*: model-building tools for molecular graphics, *Acta Crystallogr. D60*, 2126–2132.
- Brünger, A. T., Adams, P. D., Clore, G. M., DeLano, W. L., Gros, P., Grosse-Kunstleve, R. W., Jiang, J.-S., Kuszewski, J., Nilges, M., Pannu, N. S., Read, R. J., Rice, L. M., Simonson, T., and Warren, G. L. (1998) *Crystallography & NMR Systems*: a new software suite for macromolecular structure determination, *Acta Crystallogr. D54*, 905–921.
- Kleywegt, G. J., and Jones, T. A. (1998) Databases in protein crystallography, *Acta Crystallogr. D54*, 1119–1131.
- Cafaro, V., Scognamiglio, R., Viggiani, A., Izzo, V., Passaro, I., Notomista, E., Dal Piaz, F., Amoresano, A., Casbarra, A., Pucci, P., and Di Donato, A. (2002) Expression and purification of the recombinant subunits of toluene/*o*-xylene monooxygenase and reconstitution of the active complex, *Eur. J. Biochem.* *269*, 5689–5699.
- Wilhelm, E., Battino, R., and Wilcock, R. J. (1977) Low-pressure solubility of gases in liquid water, *Chem. Rev.* *77*, 219–262.
- Ravi, N., Bollinger, J. M., Jr., Huynh, B. H., Edmondson, D. E., and Stubbe, J. (1994) Mechanism of assembly of the tyrosyl radical-diiron(III) cofactor of *E. coli* ribonucleotide reductase. 1. Mössbauer characterization of the diferric radical precursor, *J. Am. Chem. Soc.* *116*, 8007–8014.
- Davydov, R., Perera, R., Jin, S., Yang, T.-C., Bryson, T. A., Sono, M., Dawson, J. H., and Hoffman, B. M. (2005) Substrate modulation of the properties and reactivity of the oxy-ferrous and hydroperoxy-ferrous intermediates of cytochrome P450cam as shown by cryoreduction-EPR/ENDOR spectroscopy, *J. Am. Chem. Soc.* *127*, 1403–1413.
- Whittington, D. A., Sazinsky, M. H., and Lippard, S. J. (2001) X-ray crystal structure of alcohol products bound at the active site of soluble methane monooxygenase hydroxylase, *J. Am. Chem. Soc.* *123*, 1794–1795.
- Lendzian, F. (2005) Structure and interactions of amino acid radicals in class I ribonucleotide reductase studied by ENDOR and high-field EPR spectroscopy, *Biochim. Biophys. Acta* *1707*, 67–90.
- Abundo, E. A., Friesner, R. A., and Lippard, S. J. (2002) Reactions of methane monooxygenase intermediate Q with derivatized methanes, *J. Am. Chem. Soc.* *124*, 8770–8771.
- Willems, J.-P., Lee, H.-I., Burdi, D., Doan, P. E., Stubbe, J., and Hoffman, B. M. (1997) Identification of the protonated oxygenic ligands of ribonucleotide reductase intermediate X by Q-Band ^{1,2}H CW and pulsed ENDOR, *J. Am. Chem. Soc.* *119*, 9816–9824.
- Smoukov, S. K., Kopp, D. A., Valentine, A. M., Davydov, R., Lippard, S. J., and Hoffman, B. M. (2002) Product binding to the diiron(III) and mixed-valence diiron centers of methane monooxy-

- genase hydroxylase studied by ^2H and ^{19}F ENDOR spectroscopy, *J. Am. Chem. Soc.* **124**, 2657–2663.
37. Himo, F., and Eriksson, L. A. (1997) Theoretical study of model tryptophan radicals and radical cations: comparison with experimental data of DNA photolyase, cytochrome *c* peroxidase, and ribonucleotide reductase, *J. Phys. Chem. B* **101**, 9811–9819.
 38. Huyett, J. E., Doan, P. E., Gurbel, R., Houseman, A. L. P., Sivaraja, M., Goodin, D. B., and Hoffman, B. M. (1995) Compound ES of cytochrome *c* peroxidase contains a Trp π -cation radical: characterization by CW and pulsed Q-band ENDOR spectroscopy, *J. Am. Chem. Soc.* **117**, 9033–9041.
 39. Walden, S. E., and Wheeler, R. A. (1996) Distinguishing features of indolyl radical and radical cation: implications for tryptophan radical studies, *J. Phys. Chem.* **100**, 1530–1535.
 40. Rigby, S. E. J., Jünemann, S., Rich, P. R., and Heathcote, P. (2000) Reaction of bovine cytochrome *c* oxidase with hydrogen peroxide produces a tryptophan cation radical and a porphyrin cation radical, *Biochemistry* **39**, 5921–5928.
 41. O'Malley, P. J., and Ellison, D. A. (1996) The calculation of ^1H , ^{13}C , ^{14}N isotropic and anisotropic hyperfine interactions for the 3-methyl indole cation and neutral radicals using hybrid density functional methods models for in vivo tryptophan-based radicals, *Chem. Phys. Lett.* **260**, 492–498.
 42. Papayannopoulos, I. A. (1995) The interpretation of collision-induced dissociation tandem mass spectra of peptides, *Mass Spectrom. Rev.* **14**, 49–73.
 43. Krebs, C., Chen, S., Baldwin, J., Ley, B. A., Patel, U., Edmondson, D. E., Huynh, B. H., and Bollinger, J. M., Jr. (2000) Mechanism of rapid electron transfer during oxygen activation in the R2 subunit of *Escherichia coli* ribonucleotide reductase. 2. Evidence for and consequences of blocked electron transfer in the W48F variant, *J. Am. Chem. Soc.* **122**, 12207–12219.
 44. Burdi, D., Willems, J.-P., Riggs-Gelasco, P., Antholine, W. E., Stubbe, J., and Hoffman, B. M. (1998) The core structure of X generated in the assembly of the diiron cluster of ribonucleotide reductase: $^{17}\text{O}_2$ and H_2^{17}O ENDOR, *J. Am. Chem. Soc.* **120**, 12910–12919.
 45. Lee, S.-K., and Lipscomb, J. D. (1999) Oxygen activation catalyzed by methane monooxygenase hydroxylase component: proton delivery during the O-O bond cleavage steps, *Biochemistry* **38**, 4423–4432.
 46. Lovell, T., Li, J., and Noodleman, L. (2001) Energetics of oxidized and reduced methane monooxygenase active site clusters in the protein environment, *Inorg. Chem.* **40**, 5267–5278.
 47. Murray, L. J., and Lippard, S. J. (2007) Substrate trafficking and dioxygen activation in bacterial multicomponent monooxygenases, *Acc. Chem. Res.* **40**, 466–474.
 48. Pikus, J. D., Mitchell, K. H., Studts, J. M., McClay, K., Steffan, R. J., and Fox, B. G. (2000) Threonine 201 in the diiron enzyme toluene 4-monooxygenase is not required for catalysis, *Biochemistry* **39**, 791–799.
 49. Lipscomb, J. D. (1994) Biochemistry of soluble methane monooxygenase, *Annu. Rev. Microbiol.* **48**, 371–399.
 50. Murray, L. J., Naik, S. G., Ortillo, D. O., García-Serres, R., Lee, J. K., Huynh, B. H., and Lippard, S. J. (2007) Characterization of the arene-oxidizing intermediate in ToMOH as a diiron(III) species, *J. Am. Chem. Soc.*, ASAP.
 51. Valentine, A. M., Tavares, P., Pereira, A. S., Davydov, R., Krebs, C., Hoffman, B. M., Huynh, B. H., and Lippard, S. J. (1998) Generation of a mixed-valent Fe(III)Fe(IV) form of intermediate Q in the reaction cycle of soluble methane monooxygenase, an analogue of intermediate X in ribonucleotide reductase R2 assembly, *J. Am. Chem. Soc.* **120**, 2190–2191.
 52. Reece, S. Y., Stubbe, J., and Nocera, D. G. (2005) pH dependence of charge transfer between tryptophan and tyrosine in dipeptides, *Biochim. Biophys. Acta* **1706**, 232–238.
 53. Aubert, C., Vos, M. H., Mathis, P., Eker, A. P. M., and Brettel, K. (2000) Intraprotein radical transfer during photoactivation of DNA photolyase, *Nature* **405**, 586–590.
 54. Tommos, C., Skalicky, J. J., Pilloud, D. L., Wand, A. J., and Dutton, P. L. (1999) De novo proteins as models of radical enzymes, *Biochemistry* **38**, 9495–9507.
 55. Yagil, G. (1967) The proton dissociation constant of pyrrole, indole, and related compounds, *Tetrahedron* **23**, 2855–2861.
 56. Aikens, J., and Sligar, S. G. (1994) Kinetic solvent isotope effects during oxygen activation by cytochrome P-450cam, *J. Am. Chem. Soc.* **116**, 1143–1144.
 57. Kohen, A. (2003) Kinetic isotope effects as probes for hydrogen tunneling, coupled motion and dynamics contributions to enzyme catalysis, *Prog. React. Kinet. Mech.* **28**, 119–156.
 58. Baldwin, J., Voegtli, W. C., Khidekel, N., Moënné-Loccoz, P., Krebs, C., Pereira, A. S., Ley, B. A., Huynh, B. H., Loehr, T. M., Riggs-Gelasco, P. J., Rosenzweig, A. C., and Bollinger, J. M., Jr. (2001) Rational reprogramming of the R2 subunit of *Escherichia coli* ribonucleotide reductase into a self-hydroxylating monooxygenase, *J. Am. Chem. Soc.* **123**, 7017–7030.
 59. Parkin, S. E., Chen, S., Ley, B. A., Mangravite, L., Edmondson, D. E., Huynh, B. H., and Bollinger, J. M., Jr. (1998) Electron injection through a specific pathway determines the outcome of oxygen activation at the diiron cluster in the F208Y mutant of *Escherichia coli* ribonucleotide reductase protein R2, *Biochemistry* **37**, 1124–1130.
 60. Ormö, M., deMaré, F., Regnström, K., Åberg, A., Sahlin, M., Ling, J., Loehr, T. M., Sanders-Loehr, J., and Sjöberg, B.-M. (1992) Engineering of the iron site in ribonucleotide reductase to a self-hydroxylating monooxygenase, *J. Biol. Chem.* **267**, 8711–8714.
 61. McCormick, M. S., and Lippard, S. J., unpublished results.
 62. Beauvais, L. G., and Lippard, S. J. (2005) Reactions of the peroxo intermediate of soluble methane monooxygenase hydroxylase with ethers, *J. Am. Chem. Soc.* **127**, 7370–7378.
 63. Moe, L. A., Hu, Z., Deng, D., Austin, R. N., Groves, J. T., and Fox, B. G. (2004) Remarkable aliphatic hydroxylation by the diiron enzyme toluene 4-monooxygenase in reactions with radical or cation diagnostic probes norcaradiene, 1,1-dimethylcyclopropane, and 1,1-diethylcyclopropane, *Biochemistry* **43**, 15688–15701.
 64. Gherman, B. F., Baik, M.-H., Lippard, S. J., and Friesner, R. A. (2004) Dioxygen activation in methane monooxygenase: a theoretical study, *J. Am. Chem. Soc.* **126**, 2978–2990.
 65. Baldwin, J., Krebs, C., Saleh, L., Stelling, M., Huynh, B. H., Bollinger, J. M., Jr., and Riggs-Gelasco, P. J. (2003) Structural characterization of the peroxodiiron(III) intermediate generated during oxygen activation by the W48A/D84E variant of ribonucleotide reductase, *Biochemistry* **42**, 13269–13279.
 66. Brunold, T. C., Tamura, N., Kitajima, N., Moro-oka, Y., and Solomon, E. I. (1998) Spectroscopic study of $[\text{Fe}_2(\text{O}_2)(\text{OBz})_2(\text{HB}(\text{pz})_3)_2]$: nature of the μ -1,2 peroxide-Fe(III) bond and its possible relevance to O_2 activation by non-heme iron enzymes, *J. Am. Chem. Soc.* **120**, 5674–5690.
 67. Nam, W., Ryu, Y. O., and Song, W. J. (2004) Oxidizing intermediates in cytochrome P450 model reactions, *J. Biol. Inorg. Chem.* **9**, 654–660.
 68. Blazyk, J. L., Gassner, G. T., and Lippard, S. J. (2005) Inter-molecular electron-transfer reactions in soluble methane monooxygenase: a role for hysteresis in protein function, *J. Am. Chem. Soc.* **127**, 17364–17376.
 69. Candéias, L. P., Wardman, P., and Mason, R. P. (1997) The reaction of oxygen with radicals from oxidation of tryptophan and indole-3-acetic acid, *Biophys. Chem.* **67**, 229–237 and references cited therein.
 70. Dorovska-Taran, V., Posthumus, M. A., Boeren, S., Boersma, M. G., Teunis, C. J., Rietjens, I. M. C. M., and Veeger, C. (1998) Oxygen exchange with water in heme-oxo intermediates during H_2O_2 -driven oxygen incorporation in aromatic hydrocarbons catalyzed by microperoxidase-8, *Eur. J. Biochem.* **253**, 659–668.
 71. Seo, M. S., In, J.-H., Kim, S. O., Oh, N. Y., Hong, J., Kim, J., Que, L., Jr., and Nam, W. (2004) Direct evidence for oxygen-atom exchange between nonheme oxoiron(IV) complexes and isotopically labeled water, *Angew. Chem., Int. Ed.* **43**, 2417–2420.
 72. Jovanovic, S. V., Steenken, S., and Simic, M. G. (1991) Kinetics and energetics of one-electron-transfer reactions involving tryptophan neutral and cation radicals, *J. Phys. Chem.* **95**, 684–687.
 73. Blanksby, S. J., and Ellison, G. B. (2003) Bond dissociation energies of organic molecules, *Acc. Chem. Res.* **36**, 255–263.
 74. da Silva, G., Chen, C.-C., and Bozzelli, J. W. (2006) Bond dissociation energy of the phenol O-H bond from ab initio calculations, *Chem. Phys. Lett.* **424**, 42–45.
 75. DeLano, W. L. (2002), DeLano Scientific, San Carlos, CA.

BI7017128

Supporting Information

Dioxygen Activation at Non-Heme Diiron Centers: Oxidation of a Proximal Residue in the I100W Mutant of Toluene/*o*-Xylene Monooxygenase Hydroxylase

*Leslie J. Murray,¹ Ricardo García-Serres,² Michael S. McCormick,¹ Roman Davydov,³ Sunil Naik,²
Sun-Hee Kim,³ Brian M. Hoffman,³ Boi Hanh Huynh,² and Stephen J. Lippard¹*

¹Department of Chemistry, Massachusetts Institute of Technology, Cambridge, MA, ²Department of Physics, Emory University, Atlanta, GA, and ³Department of Chemistry, Northwestern University, Evanston, IL

lippard@mit.edu; vhuynh@physics.emory.edu; and bmh@northwestern.edu

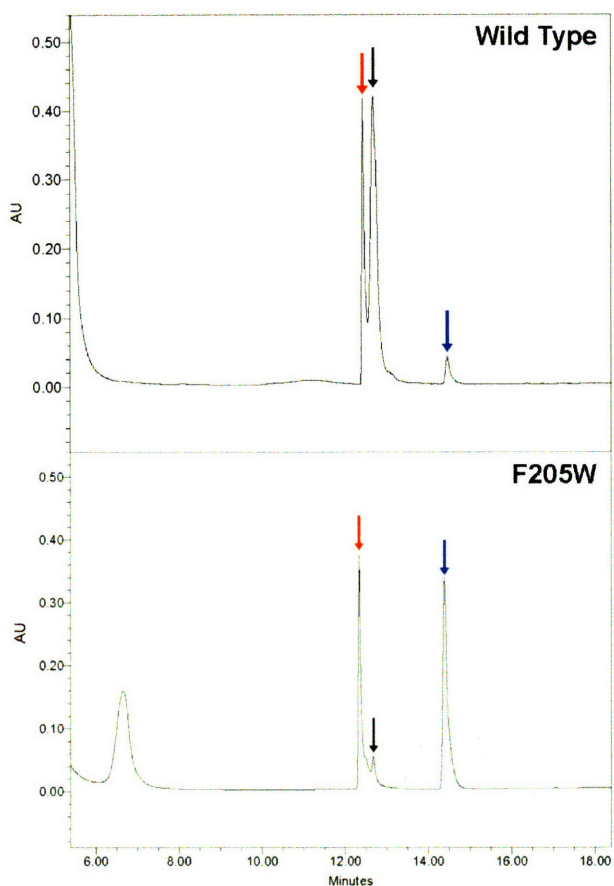


Figure S1. HPLC traces at 280 nm of steady-state reaction mixtures for wild-type and F205W mutant hydroxylases. Catechol (black arrow) is the only observed product in reactions. The peak corresponding to phenol (blue arrow), the substrate used in these assays, was of a lower intensity in the reaction containing the F205W mutant, consistent with the reduced steady-state activity of this hydroxylase. The compound eluting at 6 min does not arise from hydroquinone, as determined by HPLC traces for samples doped with this compound. A background peak at ~ 12.5 min (red arrow) appears in all traces with equal intensity.

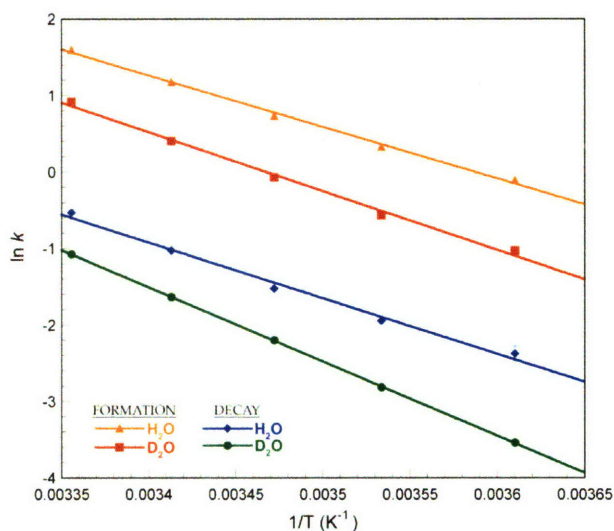


Figure S2. Arrhenius plots for formation and decay rates of the mixed-valent diiron(III,IV)-W^{*} formed during the reaction of ToMOH_{red} I100W:3ToMOD with dioxygen. The difference in activation energy for both phases in protic versus deuterated buffers is non-zero as determined from the Arrhenius plots (right). The temperature dependence of k_H/k_D is therefore non-zero for both processes with the decay exhibiting a stronger dependence than formation. This data imply that hydrogen atom transfer or tunneling from W100 to the diiron(III) intermediate does not occur during formation.

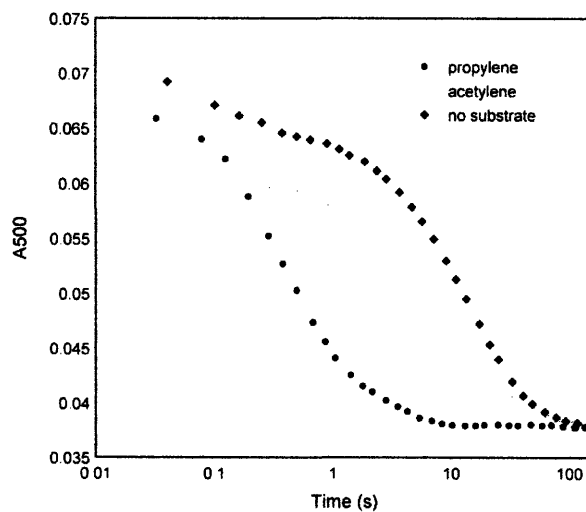


Figure S3. Effect of propylene and acetylene on the decay rate of the tryptophanyl radical. Propylene, a substrate for $\text{MMOH}_{\text{peroxo}}$, accelerates k_d by more than 50-fold to 2.8 s^{-1} whereas acetylene has only a minor effect.

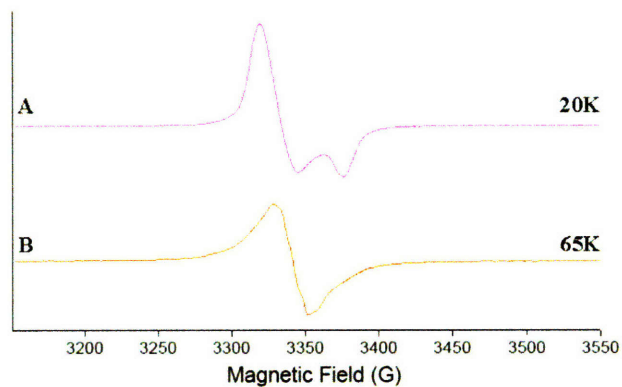


Figure S4. X-band EPR spectra of the diiron(III,IV)-W' species at (A) 20 K and (B) 65 K. (A) The spectrum at 20 K contains the anisotropic features associated with the diiron center with the radical signal saturated. (B) The spectrum at 65 K of the intermediate predominantly arises from the W' radical. The diiron center is not saturated below 60 K.

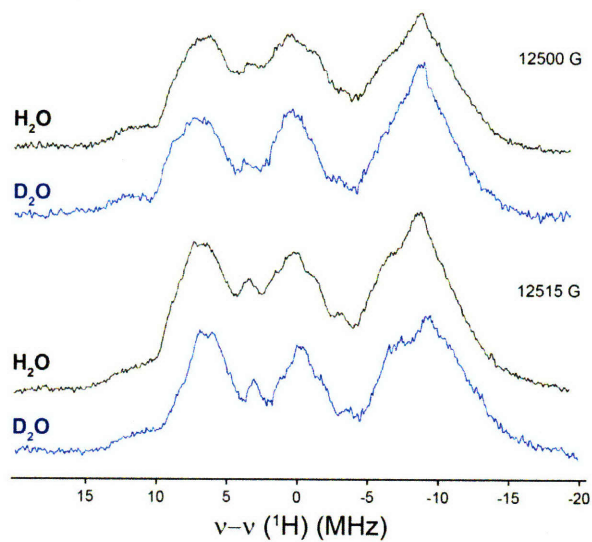


Figure S5. ¹H-Mims ENDOR spectra of the tryptophan radical in buffers containing H₂O (black) and D₂O (blue). The two spectra are superimposable indicating that there are no exchangeable protons on the radical. The spectra, as for the ²H-Mims spectra, are dominated by signals from the indole protons.



Ion	Mass (m/z)	Charge	Ion	Mass (m/z)	Charge
b4	341.2	+1	y1	175.1	+1
b5	527.2	+1	y2	246.2	+1
b6	626.3	+1	y3	375.2	+1
b6	313.2	+2	y4	446.3	+1
b7	713.3	+1	y5	547.3	+1
<i>b20</i>	<i>1122.5</i>	+2	y6	634.3	+1
<i>b22</i>	<i>1239.6</i>	+2	y7	705.4	+1
			y8	776.4	+1
			y9	939.5	+1
			y12	1320.6	+1
			<i>y19</i>	<i>1055.8</i>	+2
			<i>y23</i>	<i>1278.6</i>	+2
			<i>y27</i>	<i>1328.2</i>	+2
			<i>y27</i>	<i>999.1</i>	+3

Figure S6. ESI-MS/MS fragment ions arising from the tryptic peptide containing W100. The fragment peptide ions of the tryptic peptide of interest are labeled using the b and y ion nomenclature (top). W100 is in red font. The $[M+H]^{3+}$ parent ion was fragmented. The fragment peptide ions were assigned based on mass and isotopic spacing of the individual envelopes. The fragment ions containing the modified residue are shown in italics. This analysis revealed that the 16 Da increase observed for the reacted sample results from modification of a residue situated between H96 and E104.

Table S1. Sequences for Mutagenic Primers for the α -Subunit of ToMOH

MUTATION	PRIMER	SEQUENCE (5' to 3')
I100W	sense	caacttcacttcggagcg TGG gcacttgaagaatcg
	antisense	cgtattctcaagtgc CCA cgctccgaagtgaagtg
I100Y	sense	ggtagcactatgcaacttcacttcggagcg TAT gcacttgaagaatcg
	antisense	cgtattctcaagtgc ATA cgctccgaagtgaagtgcatagtctaacc
F205W	sense	ggcttcaccaatatgcag TGG ctcggttgccg
	antisense	cggccaaaccgag CCA ctgcatattggtgaagcc
L208F	sense	gcagtttctcgg TTC cgccgctgacgctgctgaggccg
	antisense	cggcctcagcagcgtcagcggc GAA accgagaaactgc

Table S2. Data Collection and Refinement Statistics for ToMOH I100W

	ToMOH _{ox}
Data Collection	
Beamline	SSRL 9-2
Wavelength (Å)	0.979
Space Group	P3 ₁ 21
Unit cell dimensions (Å)	182.4 x 182.4 x 68.0
Resolution range (Å)	50 - 2.1
Total Reflections	449931
Unique Reflections	70195
Completeness (%)*	84.7 (83.6)
I/s(I)	27.2 (19.4)
Rsym (%)	6.4 (54.1)
Phasing method	Molecular Replacement
Refinement	
Rcryst (%)	21.7
Rfree (%)	28.4
No. Protein Atoms	7352
No. Non-Protein Atoms	204
r.m.s deviation bond length (Å)	0.034
r.m.s deviation bond angles (°)	2.76
Average B-value (Å ²)	50.8

Table S3. Distances Between the Atoms of the Side-Chain of W100 and the Diiron Active Site

Position <u>A</u> Distances (Å)	C _α	C _β	C _γ	C _{δ1}	C _{δ2}	C _{ε2}	C _{ε3}	C _{ζ2}	C _{ζ3}	C _{η2}	N _ε
Fe1	8.8	8.1	9.0	9.7	9.3	10.3	9.2	11.1	10.1	11.0	10.5
Fe2	10.6	10.0	10.6	11.4	10.6	11.5	10.1	11.9	10.7	11.6	11.9
μ-OH (hydroxide)	10.3	9.5	10.1	10.8	10.4	11.2	10.2	11.8	10.9	11.7	11.4
μ-OH (glycerol)	8.5	7.8	8.5	9.4	8.6	9.6	8.2	10.2	8.9	9.9	10.0
H ₂ O (terminal on Fe1)	8.3	7.3	7.9	8.5	8.2	9.0	8.3	9.8	9.1	9.8	9.1
Position <u>B</u> Distances (Å)	C _α	C _β	C _γ	C _{δ1}	C _{δ2}	C _{ε2}	C _{ε3}	C _{ζ2}	C _{ζ3}	C _{η2}	N _ε
Fe1	8.7	8.2	8.0	8.9	7.2	7.7	6.3	7.5	6.0	6.7	8.7
Fe2	10.6	10.2	9.7	10.4	8.5	8.7	7.6	8.0	6.8	7.0	9.7
μ-OH (hydroxide)	10.3	9.6	9.2	9.9	8.3	8.5	7.5	8.1	7.0	7.3	9.5
μ-OH (glycerol)	8.4	8.1	7.6	8.4	6.5	6.9	5.5	6.3	4.9	5.3	8.0
H ₂ O (terminal on Fe1)	8.2	7.4	6.9	7.6	6.2	6.5	5.7	6.3	5.5	5.8	7.3

Table S4. Formation and Decay Rate Constants for I100W Transient in H₂O and D₂O Buffers

Temp (± 0.1 °C)	H ₂ O		D ₂ O		Formation k_H/k_D	Decay k_H/k_D
	k_f (s ⁻¹)	k_d (s ⁻¹)	k_f (s ⁻¹)	k_d (s ⁻¹)		
4.0	0.90 ± 0.01	0.093 ± 0.009	0.358 ± 0.002	0.029 ± 0.001	2.51 ± 0.04	3.2 ± 0.3
10.0	1.39 ± 0.02	0.143 ± 0.002	0.567 ± 0.003	0.060 ± 0.001	2.46 ± 0.03	2.36 ± 0.05
15.0	2.09 ± 0.03	0.218 ± 0.002	0.93 ± 0.04	0.111 ± 0.001	2.24 ± 0.08	1.97 ± 0.02
20.0	3.25 ± 0.05	0.359 ± 0.008	1.50 ± 0.06	0.195 ± 0.001	2.17 ± 0.09	1.84 ± 0.04
25.0	4.9 ± 0.1	0.59 ± 0.01	2.50 ± 0.07	0.342 ± 0.001	1.97 ± 0.07	1.72 ± 0.02

Table S5. Formation and Decay Rate Constants at Varying pH Values

pH	k_f (s⁻¹)	k_d (s⁻¹)
6.5	0.66 ± 0.01	0.0417 ± 0.0006
6.6	0.71 ± 0.01	0.052 ± 0.005
7.0	0.86 ± 0.04	0.070 ± 0.003
7.2	1.05 ± 0.02	0.095 ± 0.001
7.5	1.13 ± 0.02	0.091 ± 0.001

Biographical Note

The author was born in Newport News, VA, on January 15, 1981 to Scott and Margaret McCormick. He was raised along with one sister, Elizabeth, in Farmington, MI, and attended Farmington High School. After graduating from high school in 1999, he attended the University of Michigan in Ann Arbor, MI, where he conducted undergraduate research under the guidance of Vincent L. Pecoraro in the Department of Chemistry. He graduated in 2003 with a dual-degree Bachelor of Science in Chemistry and Biochemistry. Following graduation from the University of Michigan, he worked in the laboratory of Bernt Krebs at the University of Münster in Munster, Germany during the summer prior to starting graduate work at MIT in the Fall of 2003. After completion of his Ph.D., he plans to move to San Diego, CA and pursue a career in the science industry.

MICHAEL S. McCORMICK

77 Massachusetts Ave., 18-425 • Cambridge, MA 02139-4307
Phone: (617) 233-7316 • Email: msm@mit.edu

EDUCATION

Ph.D.	Massachusetts Institute of Technology <i>Inorganic Chemistry</i>	2008
B.S.	University of Michigan <i>Biochemistry</i>	2003
B.S. Chemistry	University of Michigan <i>Chemistry</i>	2003

RESEARCH EXPERIENCE

Massachusetts Institute of Technology <i>Structural investigations of bacterial multicomponent monooxygenases</i> Advisor: Prof. Stephen J. Lippard	2003-2008
Universität Münster <i>Dimanganese synthetic active site models of manganese catalase</i> Advisor: Prof. Bernt Krebs	2003
University of Michigan <i>Functional and structural models of manganese-containing redox enzymes</i> Advisor: Prof. Vincent L. Pecoraro	2000-2003

AWARDS

Merck Index Award for Outstanding Undergraduate Thesis Research <i>Awarded by the University of Michigan Department of Chemistry</i>	2003
University of Michigan Gomberg Summer Fellowship Award <i>Awarded by the University of Michigan Department of Chemistry</i>	2002
Pittsburgh Plate and Glass Summer Fellowship Award <i>Awarded by the University of Michigan Department of Chemistry</i>	2001

RESEARCH PROJECTS

Massachusetts Institute of Technology

Macromolecular X-ray crystallographic structures of bacterial multicomponent monooxygenase hydroxylases in various redox active and component protein bound states were determined and analyzed for structure-activity relationships and mechanistic insight. Extensive protein expression, purification, and site-directed-mutagenesis experiments were employed to conduct this research. Results from this work have allowed a greater understanding of biological hydrocarbon oxidation as well as general structure and mechanism in diiron carboxylate enzymes.

Universität Münster

Dinuclear manganese complexes were pursued as functional and structural active site models for manganese catalase. Tetradentate N-donor tripodal ligands provided the framework for the synthesis of μ -oxo bridged dinuclear manganese complexes. Synthesized compounds were characterized by X-ray crystallography.

University of Michigan

Trimethyl-, triisopropyl-, and diisopropyl mono carboxylate derivatives of triazacyclononane were synthesized and used as ligand frameworks in the design of active site models for manganese-containing redox active enzymes. Mono-, di-, and tetranuclear complexes with manganese were pursued as structural and functional mimics of superoxide dismutase, catalase, and the oxygen-evolving complex of photosystem II, respectively. Synthetic compounds were characterized by electron paramagnetic resonance and X-ray crystallography to probe structural and electronic similarities to the corresponding natural systems.

TEACHING EXPERIENCE

- | | |
|--|-----------|
| Diploma Thesis Mentor
<i>Expression and Purification of MMOH Monoclonal Antibodies</i>
Student: Diana Matthes | 2007-2008 |
| HHMI-MIT Undergraduate Mentoring Program
<i>Investigating the Role of Phenol Hydroxylase N204 by Site-Directed-Mutagenesis</i>
Student: Mihai Duduta | 2007-2008 |
| Undergraduate Research Opportunity Mentorship
<i>Structural Investigations of Bacterial Multicomponent Monooxygenases</i>
Student: Karen L. Condon | 2004-2006 |
| Massachusetts Institute of Technology Chemistry Department
<i>Intermediate Chemical Experimentation Laboratory Course (5.32)</i>
<i>Introductory Chemical Experimentation Laboratory Course (5.311)</i> | 2003-2004 |

PUBLICATIONS

Lovejoy, K. S., Todd, R. C., Zhang, S., **McCormick, M. S.**, D'Aquino, J. A., Reardon, J. T., Sancar, A., Giacomini, K. M., and Lippard, S. J. (2008) *cis*-Diammine(pyridine) chloroplatinum(II), a Monofunctional Platinum(II) Antitumor Agent: Uptake, Structure, Function, and Prospects, *Proc. Nat. Acad. Sci. USA*, in press.

Murray, L. J., García-Serres, R., **McCormick, M. S.**, Davydov, R., Naik, S., Kim, S.-H., Hoffman, B. M., Huynh, B. H. and Lippard, S. J. (2007) Dioxygen Activation at Non-Heme Diiron Centers: Oxidation of a Proximal Residue in the I100W Mutant of Toluene/*o*-Xylene Monooxygenase Hydroxylase, *Biochemistry* 46, 14795-14809.

Sazinsky, M. H., Duntzen, P. W., **McCormick, M. S.**, DiDonato, A., and Lippard, S. J. (2006) X-ray Structure of a Hydroxylase-Regulatory Protein Complex from a Hydrocarbon-Oxidizing Multicomponent Monooxygenase, *Pseudomonas sp.* OX1 Phenol Hydroxylase, *Biochemistry* 45, 15392–15404.

McCormick, M. S., Sazinsky, M. H., Condon, K. L., and Lippard, S. J. (2006) X-ray Crystal Structures of Manganese(II)-Reconstituted and Native Toluene/*o*-Xylene Monooxygenase Hydroxylase Reveal Rotamer Shifts in Conserved Residues and an Enhanced View of the Protein Interior, *J. Am. Chem. Soc.* 128, 15108–15110.

PRESENTATIONS

American Chemical Society 234th National Meeting, invited oral presentation, "X-ray structure of a hydroxylase-regulatory protein complex from phenol hydroxylase a hydrocarbon-oxidizing multicomponent monooxygenase", August 19, 2007.